Preserving Projectiles During Impacts on Asteroids and Planets

By

R. Terik Daly

B.S. Brigham Young University, 2012

Sc.M. Brown University, 2014

Dissertation

Submitted in partial fulfillment of the requirements for the degree of Doctor of

Philosophy in Earth, Environmental and Planetary Sciences at Brown University

PROVIDENCE, RHODE ISLAND

MAY 2017

This dissertation by R. Terik Daly is accepted in its present form by
the Department of Earth, Environmental and Planetary Sciences as satisfying the
dissertation requirement for the degree of Doctor of Philosophy.

Date _____   _____
                                            Peter H. Schultz, Advisor

Recommended to the Graduate Council

Date _____   _____
                                            Reid F. Cooper, Reader

Date _____   _____
                                            Ralph E. Milliken, Reader

Date _____   _____
                                            Alberto E. Saal, Reader

Date _____   _____
                                            Timothy J. McCoy, Reader

Approved by the Graduate Council

Date _____   _____
                                            Andrew G. Campbell, Dean of the Graduate School

R. TERIK DALY

CURRICULUM VITAE

Department of Earth, Environmental and Planetary Sciences, Brown University
324 Brook Street, Box 1846, Providence, RI 02912
terik_daly@brown.edu ▪ terikdaly.com ▪ @TerikDaly ▪ 408.455.4447

EDUCATION

2017	**Ph.D.**, Geological Sciences, Brown University
2014	**Sc.M.**, Geological Sciences, Brown University
2012	**B.S.**, Geology (*magna cum laude*); minor in Modern Dance, Brigham Young University

---

PEER-REVIEWED PUBLICATIONS

2016   **Daly, R.T.** and Schultz, P.H., 2016, Delivering a projectile component to the vestan regolith, *Icarus,* 264, 9 – 19, doi:10.1016/j.icarus.2015.08.034.

2015   **Daly, R.T.** and Schultz, P.H., 2015, Predictions for impactor contamination on Ceres based on hypervelocity impact experiments, *Geophysical Research Letters*, 42, 7890 – 7898, doi:10.1002/2015GL065601.

2013   **Daly, R.T.**, Kerby, J.D., and Austin, D.E., 2013, Electrospray charging of minerals and ices for hypervelocity impact research, *Planetary and Space Science*, 75, 182 – 187, doi:10.1016/j.pss.2012.11.012.

Barney, B.L., **Daly, R.T.**, and Austin, D.E., 2013, A multi-stage image charge detector made from printed circuit boards, *Reviews of Scientific Instruments*, 84, 114101, doi:10.1063/1.4828668.

Kerby, J.D., **Daly, R.T.**, and Austin, D.E., 2013, A novel particle source for dust accelerators and its significance for cosmic dust studies, *Earth, Planets, and Space,* 65, 157 – 165, doi:10.5047/eps.2012.08.005.

FELLOWSHIPS, AWARDS, AND GRANTS

2013 – 2017	National Science Foundation Graduate Research Fellowship
2015 – 2017	Bevan and Mary Hill French Fund for Impact Geology
2016	GSA Planetary Geology Division travel grant
2016	GSA Northeastern Section travel grant
2016	Rhode Island Space Grant Consortium travel grant
2016	Brown University Graduate Student Council travel award
2016	Travel Grant to Earth Educator Rendezvous
2015	Lunar and Planetary Institute Career Development Award
2015	Barringer Travel Grant for Bridging the Gap III Meeting
2015	Fellowship, Paul G. Benedum Graduate Travel & Research Fund
2015	Finalist, *Science Magazine's* Dance Your PhD Contest
2014	Archambault Award for Teaching Excellence with Distinction
2012	Stephen E. Dwornik Award for Best Undergraduate Poster at LPSC
2011	Barry M. Goldwater Scholarship in Sci., Mathematics, & Engineering

CONFERENCE PRESENTATIONS

*denotes oral presentations

2017   **Daly R.T.**, Schultz, P.H., Loewy, S.L., Lassiter, J.C., Thompson, L.M., Spray, J.G., 2017, Implications of the Unusually High Projectile Component at East Clearwater Crater and the Absence of an Impactor Signature at West Clearwater, Abstract no. 2428 at the 48th Lunar and Planetary Science Conference.

*Daly, R.T. and Schultz, P.H., 2017, Projectile Preservation During Oblique Hypervelocity Impacts, Abstract no. 1573 at the 48th Lunar and Planetary Science Conference.

2016   ***Daly, R.T.** and Schultz, P.H., 2016, Impact delivery of water during impacts by hydrated asteroids: Insights from hypervelocity impact experiments, Abstract no. 281035 at the GSA Annual Meeting.

*Daly, R.T. and Quintana Bouchey, S.N., 2016, How to use problem-based learning to catalyze student engagement in classes that explore exoplanets, habitability, or astrobiology, in "Implementing InTeGrate & Curriculum Design" at the Earth Educator Rendezvous 2016.

Daly, R.T. and Schultz, P.H., 2016, Hypervelocity impact experiments implicate impact melt as a host for impact-delivered water on asteroids, Abstract no. 1319 at the 47th Lunar and Planetary Science Conference.

2015 ***Daly, R.T.**, Bruck Syal, M., and Schultz, P.H., 2015, Experiments and numerical models provide complementary information about projectile survival and delivery, Abstract no. 1080 at Bridging the Gap III: Impact Cratering in Nature, Experiments, and Modeling.

Daly, R.T. and Schultz, P.H., 2015, New constraints on the delivery of impactors to icy bodies: Implications for Ceres, Abstract no. 1972 at the 46th Lunar and Planetary Science Conference.

*Daly, R.T., 2015, Dating impacts on Earth, Workshop Internacional Impactos Y Craterización (invited), June 22 – 26th, 2015, San Juan, Argentina.

*Daly, R.T., 2015, Geochemistry of impacts, Workshop Internacional Impactos Y Craterización (invited), June 22 – 26th, 2015, San Juan, Argentina.

2014 ***Daly, R.T.** and Schultz, P.H., 2014, How much of the impactor (and its water) ends up in Vesta's regolith?, Abstract no. 2070 at the 45th Lunar and Planetary Science Conference.

*Daly, R.T. and Schultz, P.H., 2014, How much of the impactor (and its water) ends up in Vesta's regolith?, Rhode Island Space Grant Annual Symposium.

Daly, R.T. and Schultz, P.H., 2014, Experimental studies into the survival and state of the projectile, Rhode Island Space Grant Annual Symposium.

2013 **Daly, R.T.** and Schultz, P.H., 2013, Experimental studies into the survival and state of the projectile, Abstract no. 2240 at the 44th Lunar and Planetary Science Conference.

2012 Gavin, P., **Daly, T.**, Chevrier, V., Ninagawa, K., Gucsik, A., and Hasegawa, S., 2012, Experimental investigation into the effects of heating and impacts on the spectral properties of phyllosilicates on Mars, Abstract no. 7048 at the 3rd International Conference on Early Mars.

Daly, R.T., Kerby, J., and Austin, D.E., 2012, Steps toward an innovative electrospray-based particle source for dust accelerators, Abstract no. 1917 at the 43rd Lunar and Planetary Science Conference.

2011 **Daly, T.**, Kerby, J.D., and Austin, D.E., 2011, Electrospray charging of minerals and ices for hypervelocity impact research, Abstract no. PS02-A052 at the Asia Oceania Geosciences Society Meeting.

Daly, T., Kerby, J., and Austin, D.E., 2011, Electrospray charging of minerals: A new method for creating and characterizing high- to hyper-velocity microparticle impacts, Abstract no. 2078 at the 42nd Lunar and Planetary Science Conference.

Daly, T., Gavin, P., and Chevrier, V., 2011, Effects of thermal alteration on the near-infrared and mid-infrared spectra of martian phyllosilicates, Abstract no. 1164 at the 42nd Lunar and Planetary Science Conference.

2010 **Daly, T.**, Call, S., and Austin, D.E., 2010, Electrospray charging of minerals: Surface chemistry and applications to high-velocity microparticle impacts, Abstract no. V31C-2338 at the Fall Meeting of the American Geophysical Union.

Daly, T., Call, S., and Austin, D.E., 2010, Electrospray charging of quartz microparticles for studies of high-velocity micrometeorite impact chemistry, Abstract no. 2270 at the 41st Lunar and Planetary Science Conference.

2009 **Daly, T.**, Radebaugh, J., and Austin, D.E., 2009, Computational study of the lunar time-of-flight mass spectrometer (LTMS): Meteorite impacts and outgassing events, Abstract no. 2411 at the 40th Lunar and Planetary Science Conference.

2008 Austin, D.E., Miller, I., **Daly, T.**, Crotts, A., Syrstad, E., Brinckerhoff, W., and Radebaugh, J., 2008, Characterizing meteorite impact vaporization and outgassing processes on the lunar surface: A new methodology and opportunity, Abstract no. 2074 at the NLSI Lunar Science Conference.

2007 **Daly, T.**, 2007, Chemical aspects of the impact process, Abstract no. P41A-0225 at the Fall Meeting of the American Geophysical Union.

DEPARTMENTAL TALKS

2017   **Daly, R.T.**, 2017, The meteoritic signature at the Clearwater craters: Insights from osmium isotopes, Brown University Planetary Geosciences Lunch Bunch.

2015   **Daly, R.T.**, 2015, Hypervelocity impact experiments predict extensive impactor contamination on Ceres, Brown University Planetary Geosciences Lunch Bunch.

2014   **Daly, R.T.** and Schultz, P.H., 2014, How much of the impactor (and its water) ends up in Vesta's regolith?, Brown University Planetary Geosciences Lunch Bunch.

2013   **Daly, R.T.**, 2013, Steps toward a novel electrospray-based particle source for dust accelerators, Brown University Planetary Geosciences Lunch Bunch.

TEACHING EXPERIENCE

2016   **Habitable Worlds: Possible Places for Life in the Solar System and Beyond**, instructor of record, Summer@Brown.

2015   **Habitable Worlds: Possible Places for Life in the Solar System and Beyond**, instructor of record, Summer@Brown.

        Planetary Geology, teaching assistant, Brown University.

2014   **Habitable Worlds: Possible Places for Life in the Solar System and Beyond**, instructor of record, Summer@Brown. Won the Archambault Award for Teaching Excellence with Distinction.

2013   **Habitable Worlds: Possible Places for Life in the Solar System and Beyond**, instructor of record, Summer@Brown.

SERVICE TO THE PROFESSION

2016   Co-Chair, "Implementing InTeGrate and Curriculum Design" session at 2016 Earth Educator Rendezvous

Technical Session Coordinator, Annual Meeting of the Geological Society of America

Judge, Stephen E. Dwornik Award

2015   Leveler, NASA Review Panel

SERVICE TO THE UNIVERSITY

2016 – 2017   Graduate Student Advisory Committee Member, Sheridan Center for Teaching and Learning at Brown University

2015 – 2017   Member, Brown University Mental Health Community Council

First Year Graduate Student Mentor, Brown University Department of Earth, Environmental and Planetary Sciences

Departmental Graduate Student Liaison, Sheridan Center for Teaching and Learning at Brown University

2015 – 2016   Discussion Leader for Brown University's New TA Orientation

2013 – 2014   Treasurer, Brown University GeoClub

PROFESSIONAL DEVELOPMENT ACTIVITIES

2017   **Brown Executive Scholars Training Program,** Brown University Graduate School. Prepares graduate students for future leadership roles in higher education administration through a semester-long, mentored education and training experience.

2016 – 2017   **Certificate IV: Teaching Consultant,** Brown University Sheridan Center for Teaching and Learning. Used principles of effective communication, inclusive learning, and reflective teaching to give formative feedback to graduate students, postdocs, and faculty instructors.

2016 – 2017   **Educational Development Reading Group,** Sheridan Center for Teaching and Learning. Prepares advanced graduate students for careers in higher educational development.

| 2016 | **Facilitating Learning Online**, Brown University School of Professional studies. Online course disseminating research-based practices for creating and facilitating effective online learning experiences. |

| 2016 | **Summer Institute for Teaching and Technology**, Brown University. Week-long intensive institute exploring best practices for integrating technology into courses. Practiced using many tools (e.g., Canvas, Panopto, Adobe Spark, Camtasia) and approaches (e.g., flipped classrooms). |

| 2016 | **LPSC Educator Professional Development Workshop: Solar System Exploration**, Lunar and Planetary Institute. Day-long workshop exploring best practices for engaging diverse learners. Included NGSS-aligned activities. |

| 2015 – 2016 | **Certificate III: Professional Development**, Brown University Sheridan Center for Teaching and Learning. Development of the teaching portfolio as a tool for cultivating a personal teaching philosophy and reflective practice. |

| 2014 – 2015 | **Certificate I: Reflective Teaching**, Brown University Sheridan Center for Teaching and Learning. Introduces fundamental teaching, assessment, and communication skills. Topics: backwards course design, student-centered learning, measuring student learning, and rhetorical practice. |

EDUCATION AND PUBLIC OUTREACH

| 2003 – 2017 | **Ask an Expert Program**, Science Buddies. Over 970,000 individuals from across the globe visit the associated website annually. |

| 2012 – 2017 | **Second Grade Science**, volunteer educator, Vartan Gregorian Elementary School. ~26 students per visit. |

| 2016 | **A Day on College Hill**, Brown University. ~25 high school seniors. |

NASA Northeast Planetary Data Center Open House, Brown University. 50+ attendees.

Museum exhibit: From Mars to Pluto, Museum of Natural History in Providence, RI and Northeast Planetary Data Center. Exhibit contributor.

	Museum exhibit: Icy Worlds & the Discoveries of Dawn and New Horizons, Northeast Planetary Data Center. Exhibit contributor.
2014	**NASA Northeast Planetary Data Center Open House**, Brown University. 50+ attendees.
	Project Idea: Using a Digital Camera to Measure Skyglow, Science Buddies. Project Ideas each have 14,000+ visitors annually. (www.sciencebuddies.org/science-fair-projects/project_ideas/Astro_p022.shtml)
	Project Idea: The Moon and Tides, Science Buddies. Project Ideas each have 14,000+ visitors annually. (www.sciencebuddies.org/science-fair-projects/project_ideas/Astro_p009.shtml)
	Exoplanets, Johnston Public Library. ~15 elementary school students.
2013	**NASA Northeast Planetary Data Center Open House**, Brown University. 50+ attendees.
	The Scale of the Solar System (invited), Lawn School. ~45 fifth graders.
2012	**Guest blog post (invited)**, Women in Planetary Blog. (womeninplanetaryscience.wordpress.com/2012/08/23/having-it-all/)
	Science Buddies blog. (www.sciencebuddies.org/blog/2012/06/pinhole-viewer-trying-again-for-the-transit.php)
2008 – 2012	**Science Fair Workshops for Students, Parents, and Teachers**, in collaboration with the Central Utah Science and Engineering Fair, Salt Lake Valley Science and Engineering Fair, and Ritchey Science and Engineering Fair. ~5 events annually, each with 15 to 30 attendees.

RELEVANT PROFESSIONAL APPOINTMENTS

2012	Scientist, Science Buddies
2008 – 2009	Intern, Science Buddies
2011 – 2012	Research Assistant, Brigham Young Univ. Dept. Geological Sciences
2008 – 2012	Research Assistant, Brigham Young Univ. Dept. Chem. & Biochem.
2010	NSF REU Intern, U. of Arkansas at Fayetteville Space Science Center
2007	Intern, Weizmann Institute of Science

PROFESSIONAL SOCIETIES

Phi Kappa Phi (inducted 2011)

Sigma Xi (inducted 2015)

American Geophysical Union

Geological Society of America

National Association of Geoscience Teachers

Acknowledgements

When I first wrote this section, it was nine pages long. In those nine pages, I individually thanked dozens of people and carefully explained why each deserved mention. I smiled upon re-reading my first draft. "It's true," I thought, "it 'takes a village to raise a child' into a grown-up scientist." But, my smile faded as I realized that I failed to thank so-and-so; I forgot to mention such-and-such. I started jotting down names. The names turned into sentences, the sentences into paragraphs, the paragraphs spilled onto new pages. It was a city, not a village, that made me into the planetary scientist I am today.

Unfortunately, that approach meant that the individuals who mattered most got lost in a sprawling cast of characters. So, I changed tack. I faced the fact that in this dissertation I cannot personally thank each person who has influenced my life for the better. Instead, I chose to do three things.

Part I:

First, I express sincere gratitude to all the family members, friends, neighbors, teachers, leaders, acquaintances, and mentors who have sculpted my life to date. Some of you know who you are. Some of you might lack the tiniest inkling of the extent to which you have altered me. To all of you: the person I am today integrates all our past encounters and conversations—thank you for the time you spent with me. Thank you for sharing so generously of your wit, advice, thoughts, fears, aspirations, strengths, foibles, reflections, faith, and dreams.

Part II:

Second, I acknowledge groups of people and organizations who influenced my academic and professional life in ways that pertain directly to this dissertation. See the bulleted list below. I thank the following for influencing my life as indicated:

- For igniting my interest in impact cratering: Gene Shoemaker and NOVA.

- For spending untold hours helping me with science fair projects (which were the seeds of this dissertation): Heidi Black, Carol Evans, and Lynn Johnson.

- For helping me realize that I could be a "real" scientist: the Synopsys Silicon Valley Science and Technology Championship, California State Science Fair, Junior Science and Humanities Symposium, Siemens Competition, Intel Science Talent Search, and Intel International Science and Engineering Fair.

- For mentoring me at BYU: Daniel Austin and Jani Radebaugh.

- For mentoring me during graduate school: Amy Barr, Reid Cooper, John Lassiter, Ralph Milliken, Jessica Metzler, Shawn Nordell, Steve Parman, Carle Pieters, Alberto Saal, Pete Schultz, Jan Tullis, and Mary Wright.

- For teaching me the ins-and-outs of various analytical methods: Joe Boesenberg, Bill Collins, Rebecca Greenberger, Taki Hiroi, John Lassiter, Staci Loewy, Tony McCormick, Laura Messier, Ralph Milliken, Dave Murray, Joe Orchardo, and Kevin Robertson.

Part III:

Third, and finally, I detail the pivotal roles of two people: Dr. Peter H. Schultz and Ms. Carol Evans.

I first met my advisor, Dr. Peter H. Schultz, in 2004. I was an enthusiastic, but somewhat naïve, high school sophomore. Pete had responded very generously to an email that I had sent. I had asked him to help me with a science fair project. Pete took an entire day out of one of his weeks at the AVGR to help me. I only now appreciate what a day at

the AVGR is worth in time, money, and productivity. Pete's help at this juncture was a critical stepping stone in my path toward becoming a scientist. Hence, I must thank Pete for taking a chance on me thirteen years ago.

I met Pete again in 2011. I was considering graduate school at the time, and I wanted to know whether Pete was taking students. With a bit of trepidation, I approached Pete during a poster session at LPSC. Surprisingly, he remembered me! He told me that I should come to Brown for graduate school. He said he was retiring soon but would wait for me. I arrived at Brown the following fall, turning down offers from six other programs including Harvard. Working with Pete felt right; I decided to follow my heart rather than hearkening to Harvard's call. I thank Pete for remembering me and urging me to continue down the path I had started on when he and I first met.

While at Brown, Pete has opened many opportunities to me. He has given advice and shared insights freely, yet he has still supported my own ideas. Our most vibrant conversations happen over food. It is a lesson I will remember as I work with students of my own. I will miss the broad-ranging conversations we have shared at restaurant tables across the globe. (If you are ever in Prescott, Arizona you absolutely must eat at a restaurant called El Gato Azul!) Thank you, Pete, for teaching me many of the nuances of hypervelocity impact experiments, impact cratering, and scientific discourse.

Now, finally, I express my enduring gratitude to Ms. Carol Evans. She taught my high school chemistry and advanced science research classes. However, Carol was far more than a teacher. She was my comrade-in-arms for four years as I pursued science fair projects that set me on the path to this doctoral degree. She was my guide and my cheerleader. She

found money to pay for my projects, chauffeured me around the San Francisco Bay Area, intervened with school administrators when science-fair-related absences nearly classified me as a high school truant, and spent a great deal of time helping me decode scientific papers. It became a running joke that whenever I gave Carol "a bit of light reading", I was handing her a dense document that would take hours to parse. But, she would read it anyway. Carol, this dissertation is the last "light reading" I will give you—it is also completely optional. I do not know how many hours Carol Evans spent helping me between 2003 and 2007. But, I know that the time she spent did not earn her additional salary or course releases. Carol Evans carved time out of her life to help me, an offering for which I am deeply grateful. Carol, more than anyone, set me on the path to defending this dissertation.

Thank you, Ms. Evans.

Introduction

Impact cratering is one of the most influential geologic processes affecting planets, moons, and small bodies in the Solar System. Indeed, impact events helped to build these objects when the solar system formed 4.6 billion years ago. Today, impacts continue to sculpt every solid object in the solar system [e.g., *Gault et al.,* 1968; *Gault et al.,* 1970]. However, impacts do more than simply shape the surfaces of objects: impacts can also be a force for compositional change. Broadly speaking, the chemical consequences of impacts take one of two forms: First, an impact can remove some chemical component from the target. Second, impacts might deliver material to the target. This latter situation is the focus of this dissertation.

A growing body of evidence indicates portions of the impacting object (the "impactor" or "projectile") are plastered on the target during impact, thereby permanently altering the composition of the target object. This evidence includes impact experiments [e.g., *Schultz and Gault,* 1990; *Daly and Schultz,* 2016] and shock physics code calculations [e.g., *Ong et al.,* 2010; *Bruck Syal et al.,* 2015; *Daly et al.,* 2015), as well as observational evidence. For example, the exogenic inclusions in several types of meteorites [e.g., *Zolensky et al.,* 1996; *Goodrich et al.,* 2015], the meteoritic fingerprints found in impactites [e.g., *Koeberl,* 2007], and the presence of impact-delivered dark material on Vesta provide additional evidence that impactors can be preserved. Experiments, models, meteorites, terrestrial samples, and spacecraft observations tell a self-consistent story.

The nature of this impactor contribution can range from subtle to stark. For instance, at large terrestrial craters the impactor contribution can only be detected by

detailed geochemical analyses. On Vesta, in contrast, the impactor component was detected by orbiting spacecraft [e.g., *McCord et al.,* 2012; *Prettyman et al.,* 2012]. In yet other cases, the impactor component affects bodies at the planetary scale—such was the case when impacts delivered water to the terrestrial planets early in their history [e.g., *Krähenbühl et al.,* 1973; *Wänke and Dreibus,* 1994; *Morbidelli et al.,* 2000].

Such findings raise questions about the *processes* by which impactors deliver material to their targets. How efficient is the delivery process? What conditions are needed for an impact to contribute an impactor component? What are the roles of impact variables, such as speed, angle, impactor properties, and target properties? What does the impactor contribution look like: that is, what is its physical state? The four chapters in this dissertation explore the answers to many of these questions. To find these answers, I leverage information provided by hypervelocity impact experiments and terrestrial impact craters, coupled with a variety of chemical, spectroscopic, and isotopic analyses.

Chapter one examines whether Ceres, the largest object in the asteroid belt, is likely to have accumulated a significant impactor component. This chapter was motivated, in part, by the observation that Vesta is peppered with impact-delivered dark material [e.g., *Prettyman et al.,* 2012; *McCord et al.,* 2012]. Experiments designed to characterize impact delivery to Vesta [*Daly and Schultz,* 2016] revealed that delivery should be a natural consequence of impact conditions in the main asteroid belt. Hence, we anticipated the arrival of the *Dawn* mission at Ceres by assessing delivery in other targets that may be relevant to Ceres, including porous ice targets [*Daly and Schultz,* 2015]. We hypothesized that Ceres, like Vesta, should be laden with a significant impactor contribution. If so, then

the surface of Ceres seen today may be markedly different from its primordial surface, even in the absence of endogenic processing. This led to a series of impact experiments that revealed that Ceres may have accumulated several hundred meters of impactor debris [*Daly and Schultz,* 2015]. Shock physics code calculations [*Daly et al.,* 2015] further supported this prediction show showing that distal materials are also delivered. *Vernazza et al.* [2017] and *Nathues et al.* [2016] have since reported detections of materials on Ceres believed to be exogenic (i.e., impact-delivered).

Chapter two assesses the effect of impact variables on projectile preservation under more extreme conditions through the use of high-impedance metal targets. Prior experiments by Schultz recognized that projectile fragments were captured on the uprange wall of impact craters in basalt and copper targets, a finding that has implications for the survival of organics and volatiles. The Long-Duration Exposure Facility (LDEF) further motivated this work by revealing that a significant fraction of the micron- to mm-scale impact craters on the LDEF spacecraft contained projectile residues [e.g., *Bunch et al.,* 1991; *Berthoud et al.,* 1995]. Since then, various groups used impact experiments to try to reproduce such residues in micro-scale craters [*Bunch et al.,* 1991; *Bunch et al.,* 1993; *Berthoud et al.,* 1995; *Hill et al.,* 1995; *Kearsley et al.,* 2007; *Burchell et al.,* 2008]. We wanted to fully document preserved projectile residues in macro-scale (cm) craters. In addition, we explored how the interplay between impact variables influences the preservation of projectile residues. We find that cm-scale craters formed during impact experiments preserve portions of the projectile under all conditions studied, including conditions relevant to the asteroid and Kuiper belts.

Chapter three approaches impact delivery from a very different perspective than the other three chapters. Whereas the first three chapters rely heavily on hypervelocity impact experiments, the third chapter is based on samples from two terrestrial impact craters. These two craters are the East and West Clearwater craters, both located in Quebec. Prior studies measured an unusually strong impactor signature in impact melts at East Clearwater, while failing to detect any impactor signature at West Clearwater [e.g., *Palme et al.,* 1978]. We revisited these craters using osmium isotopes, the most sensitive geochemical tool for characterizing impactor signatures in terrestrial impactites [e.g., *Goderis et al.,* 2013; *Koeberl,* 2007]. Even with this most sensitive method and having more than doubled the number of samples analyzed, we cannot find even a whiff of an impactor signature at West Clearwater. If present, the meteoritic component must be <0.002 wt.% in the samples analyzed, if the impactor was chondritic. Based on findings at East Clearwater, this non-detection cannot easily be attributed to heterogeneity in the melt sheet. We explore hypotheses for why these two craters have impactor signatures that set them apart from almost all other terrestrial craters that have, to date, been searched for an impactor signature.

Chapter four investigates how efficiently impacts deliver water. Based on theoretical considerations, some have argued that a late-stage, volatile-rich veneer was needed in order to account for the volatile contents of the terrestrial planets. Other studies argued that volatiles were delivered by asteroids and meteoroids and were later released [e.g., *Drake and Righter,* 2002]. Dynamical models indicate that the terrestrial planets received most of their water during impacts by water-rich objects [*Morbidelli et al.,* 2000]. Hence, knowing how efficiently impacts deliver water (whether during accretion or later

collisions) is a critical piece in the puzzle of planet formation and evolution. For example, *Schultz* [2011] hypothesized (based on experiments) that impacting volatiles could be stored in the regolith and later released. Isotopic evidence indicates that carbonaceous chondrite-like objects delivered most of the water on the Earth and Moon [*Saal et al.,* 2013]. Hence, the water delivery efficiency of impacts caused by carbonaceous chondrite-like objects, specifically, needs to be characterized. (Note that "water delivery" includes both OH and H_2O.) Although shock physics codes can calculate water delivery [e.g., *Ong et al.,* 2010; *Bruck Syal and Schultz,* 2015], the limitations of available equations of state and constitutive models introduce uncertainties in the details. Impact experiments, in contrast, can directly measure water delivery during impacts into complex geologic materials. In addition, experiments reveal how delivered water is stored on the target object, a process that current shock physics codes also cannot treat in detail. Our findings indicate for impact speeds found in the main asteroid belt, carbonaceous chondrite analogs deliver up to 36% of the total structural water in the impactor. A combination of impact glasses and projectile relics host the delivered water.

I close with an excerpt from *Palme et al.* [1978], one of the early papers that searched for impactor signatures at terrestrial craters:

> The search for meteoritic [projectile] material at large, ancient craters is only slightly more rewarding than the search for the Loch Ness monster. The success rate is low, and would be far lower still if we had not been able to capitalize on the labors of earlier workers. . . . Present understanding of the fate of meteoritic material [the projectile] is still woefully inadequate. Theoretical studies are of little help: they either slight the problem entirely or treat it in insufficient detail for comparison with observation. We must therefore rely on the sparse empirical data available (p. 319).

If you remember nothing else bound in this dissertation, remember two things. First, empirical data continue to divulge things that state-of-the-art shock physics codes cannot, even thirty nine years after Palme penned his criticism of theoretical studies. Second, and finally, today the search for meteoritic material—on Vesta, on Ceres, in meteorites, and on Earth—is far more rewarding than the search for the Loch Ness monster.

References

Berthoud, L., Mandeville, J.-C., Durin, C., Borg, J., 1995. Debris and meteoroid proportions deduced from impact crater residue analysis. Presented at the LDEF: 69 Months in Space. Third Post-Retrieval Symposium.

Bruck Syal, M., Schultz, P.H., 2015. Impact Delivery of Water at the Moon and Mercury. Presented at the Lunar and Planetary Science Conference, abstract no. 1680.

Bunch, T.E., Becker, L., Bada, J., Macklin, J., Radicati di Brozolo, F., Fleming, R.H., Erlichman, J., 1993. Hypervelocity impact survivability experiments for carbonaceous impactors. Presented at the LDEF: 69 Months in Space. Part 4: Second Post-Retrieval Symposium.

Bunch, T.E., Radicati di Brozolo, F., Fleming, R.H., Harris, D.W., Brownlee, D., Reilly, T.W., 1991. LDEF Impact Craters Formed by Carbon-Rich Impactors: A Preliminary Report. Presented at the LDEF, 69 Months in Space: First Post-Retrieval Symposium, p. 549.

Burchell, M.J., Foster, N.J., Kearsley, A.T., Creighton, J.A., 2008. Identification of mineral impactors in hypervelocity impact craters in aluminum by Raman spectroscopy of residues. *Meteorit. Planet. Sci.* 43, 135–142. doi:10.1111/j.1945-5100.2008.tb00614.x

Daly, R.T., Schultz. P.H., 2015. Predictions for impactor contamination on Ceres based on hypervelocity impact experiments. *Geophysical Research Letters,* 42, 7890 – 7898.

Daly, R.T., Bruck Syal, M., Schultz, P.H., 2015. Experiments and Numerical Models Provide Complementary Information About Projectile Survival and Delivery. Presented at Bridging the Gap III: Impact Cratering in Nature, Experiments, and Modeling, abstract no. 1080.

Daly, R.T., Schultz, P.H., 2016. Delivering a projectile component to the vestan regolith. *Icarus.* 264, 9–19. doi:10.1016/j.icarus.2015.08.034

Drake, M.J, Righter, K., 2002, Determining the composition of the Earth. *Nature,* 416, 39–44.

Gault, D., Quaide, W., Oberbeck, V., 1968. Impact cratering mechanics and structures, in: *Shock Metamorphism of Natural Materials.* Mono Book Corp., pp. 87–99.

Gault, D.E., 1970. Saturation and equilibrium conditions for impact cratering on the lunar surface: Criteria and implications. *Radio Sci.* 5, 273–291. doi:10.1029/RS005i002p00273

Goderis, S., Paquay, F.S., Claeys, P., 2013. Projectile identification in terrestrial impact structures and ejecta materials, in: *Impact Cratering: Processes and Products.* Wiley-Blackwell, pp. 223–239.

Goodrich, C.A., Hartmann, W.K., O'Brien, D.P., Weidenschilling, S.J., Wilson, L., Michel, P., Jutzi, M., 2015. Origin and history of ureilitic material in the solar system: The view from asteroid 2008 TC3 and the Almahata Sitta meteorite. *Meteorit. Planet. Sci.* 50, 782–809. doi:10.1111/maps.12401

Hill, D.C., Rose, M.F., Best, S.R., Crumpler, M.S., Crawford, G.D., Zee, R.H.-C., Bozack, M.J., 1995. The effect of impact angle on craters formed by hypervelocity particles. Presented at the LDEF: 69 Months in Space. Third Post-Retrieval Symposium.

Kearsley, A.T., Graham, G.A., McDonnell, J.A.M., Taylor, E.A., Drolshagen, G., Chater, R.J., McPhail, D., Burchell, M.J., 2007. The chemical composition of micrometeoroids impacting upon the solar arrays of the Hubble Space Telescope. *Adv. Space Res.* 39, 590–604. doi:10.1016/j.asr.2006.05.011

Koeberl, C., 2007. The Geochemistry and Cosmochemistry of Impacts, in: Holland, H.D., Turekian, K.K. (Eds.), *Treatise on Geochemistry.* Pergamon, Oxford, pp. 1–52.

Krähenbühl, U., Ganapathy, R., Morgan, J.W., Anders, E. *Proceedings of the 4th Lunar Science Conference*, 1325 – 1348.

McCord, T.B., Li, J.-Y., Combe, J.-P., McSween, H.Y., Jaumann, R., Reddy, V., Tosi, F., Williams, D.A., Blewett, D.T., Turrini, D., Palomba, E., Pieters, C.M., de Sanctis, M.C., Ammannito, E., Capria, M.T., Le Corre, L., Longobardo, A., Nathues, A., Mittlefehldt, D.W., Schröder, S.E., Hiesinger, H., Beck, A.W., Capaccioni, F., Carsenty, U., Keller, H.U., Denevi, B.W., Sunshine, J.M., Raymond, C.A., Russell, C.T., 2012. Dark material on Vesta from the infall of carbonaceous volatile-rich material. *Nature.* 491, 83–86. doi:10.1038/nature11561

Morbidelli, A., Chambers, J., Lunine, J.I., Petit, J.M., Robert, F., Valsecchi, G.B., Cyr, K.E., 2000. Source regions and timescales for the delivery of water to the Earth. *Meteorit. Planet. Sci.* 35, 1309–1320. doi:10.1111/j.1945-5100.2000.tb01518.x

Nathues, A., Hoffmann, M., Platz, T., Thangjam, G.S., Cloutis, E.A., Reddy, V., Le Corre, L., Li, J.-Y., Mengel, K., Rivkin, A., Applin, D.M., Schaefer, M., Christensen, U., Sierks, H., Ripken, J., Schmidt, B.E., Hiesinger, H., Sykes, M.V., Sizemore, H.G., Preusker, F., Russell, C.T., 2016. FC colour images of dwarf planet Ceres reveal a complicated geological history. *Planet. Space Sci.* 134, 122–127. doi:10.1016/j.pss.2016.10.017

Ong, L., Asphaug, E.I., Korycansky, D., Coker, R.F., 2010. Volatile retention from cometary impacts on the Moon. *Icarus.* 207, 578–589. doi:10.1016/j.icarus.2009.12.012

Palme, H., Janssens, M.J., Takahashi, H., Anders, E., Hertogen, J., 1978. Meteoritic material at five large impact craters. *Geochim. Cosmochim. Acta.* 42, 313–323. doi:10.1016/0016-7037(78)90184-9

Prettyman, T.H., Mittlefehldt, D.W., Yamashita, N., Lawrence, D.J., Beck, A.W., Feldman, W.C., McCoy, T.J., McSween, H.Y., Toplis, M.J., Titus, T.N., Tricarico, P., Reedy, R.C., Hendricks, J.S., Forni, O., Corre, L.L., Li, J.-Y., Mizzon, H., Reddy, V., Raymond, C.A., Russell, C.T., 2012. Elemental Mapping by Dawn Reveals Exogenic H in Vesta's Regolith. *Science.* 338, 242–246. doi:10.1126/science.1225354

Saal, A.E., Hauri, E.H., Orman, J.A.V., Rutherford, M.J., 2013. Hydrogen Isotopes in Lunar Volcanic Glasses and Melt Inclusions Reveal a Carbonaceous Chondrite Heritage. *Science.* 340, 1317–1320. doi:10.1126/science.1235142

Schultz, P.H., Gault, D.E., 1990. Prolonged global catastrophes from oblique impacts. *Geol. Soc. Am. Spec. Pap. 247*, 239–262. doi:10.1130/SPE247-p239

Schultz, P. H., 2011, Possible sources of polar volatiles. American Geophysical Union Fall Meeting, abstract no. P12C-04.

Syal, M.B., Schultz, P.H., Riner, M.A., 2015. Darkening of Mercury's surface by cometary carbon. *Nat. Geosci.* 8, 352–356. doi:10.1038/ngeo2397

Vernazza, P., Mothé-Diniz, T., Barucci, M.A., Birlan, M., Carvano, J.M., Strazzulla, G., Fulchignoni, M., Migliorini, A., 2005. Analysis of near-IR spectra of 1 Ceres and 4 Vesta, targets of the Dawn mission. *Astron. Astrophys.* 436, 1113–1121. doi:10.1051/0004-6361:20042506

Wänke, H., Dreibus, G, 1994, Water abundance and accretion history of terrestrial planets. *Conference on Deep Earth and Planetary Volatiles.* p. 46.

Zolensky, M.E., Weisberg, M.K., Buchanan, P.C., Mittlefehldt, D.W., 1996. Mineralogy of carbonaceous chondrite clasts in HED achondrites and the Moon. *Meteorit. Planet. Sci.* 31, 518–537. doi:10.1111/j.1945-5100.1996.tb02093.x

Table of Contents

Chapter 1: Predictions for impactor contamination on Ceres based on hypervelocity impact experiments…………………………………………………………………………1

Chapter 3: Contrasting meteoritic signatures at East and West Clearwater

List of Tables

Chapter 4: The impact delivery of water by carbonaceous chondrite-like impactors

List of Figures

Chapter 1: Predictions for impactor contamination on Ceres based on hypervelocity impact experiments

Chapter 2: Projectile preservation during oblique impacts

Chapter 3: Implications of the unusually high meteoritic component at East Clearwater crater and absence of a meteoritic signature at West Clearwater crater

Chapter 4: The impact delivery of water by carbonaceous chondrite-like impactors

CHAPTER 1

Predictions for impactor contamination on Ceres

based on hypervelocity impact experiments

R. Terik Daly and Peter H. Schultz

Department of Earth, Environmental and Planetary Sciences

Brown University

Providence, RI USA

Abstract

New experiments predict that Ceres should be extensively contaminated with meteoritic debris derived from the asteroid belt. All types of impactors likely contribute to the contamination. Ceres may accrete debris more efficiently if it is ice rich because of enhanced projectile survival and retention in porous ice targets. Experiments indicate that if a silicate regolith lag protects subsurface ice, then some of the projectile should be injected into the regolith during high angle impacts, thereby hiding part of the projectile component from view. If impacts excavate ice, sublimation will gradually concentrate projectile relics into a surficial lag. In contrast, if the near-surface lacks ice, then accreted meteoritic debris should be distributed throughout a vertically mixed regolith. High-resolution images may reveal pristine projectile relics lining some crater floors. Moreover, we predict that the surface of Ceres is not exclusively endogenic and may be dominated by delivered exogenic debris.

1. Introduction

Like other objects in the Solar System, Ceres has been heavily bombarded by impactors [*de Elía and di Sisto*, 2011; *Turrini et al.*, 2011; *O'Brien and Sykes*, 2011 and references therein]. These impacts have undoubtedly sculpted the surface of Ceres. However, prior work demonstrated that impactors can survive and remain in and near craters during hypervelocity collisions with porous targets [*Daly and Schultz*, 2014; *Schultz and Gault*, 1990; *Svetsov*, 2011; *Turrini and Svetsov*, 2014]. Impact-delivered dark material on Vesta [*McCord et al.,* 2012; *Reddy et al.,* 2012; *Turrini et al.,* 2014] provides additional evidence for projectile retention on small bodies. It is therefore highly plausible that projectile remnants have been retained on Ceres. If true, then the current surface composition of Ceres may not solely reflect its endogenic evolution. Instead, the surface may be a chaotic combination of endogenic products and impact-delivered debris.

Ceres' enigmatic evolution [*McCord and Sotin*, 2005] may make it difficult to recognize projectile contamination. Therefore, experimental estimates of projectile retention provide useful constraints. Most previous numerical [*Bland et al.*, 2008; *Ong et al.*, 2010; *Svetsov*, 2011; *Turrini and Svetsov*, 2014; *Bruck Syal and Schultz*, 2015; *Syal et al.*, 2015] and experimental [*Schultz and Gault*, 1990; *Daly and Schultz*, 2014] studies investigating impactor delivery explored silicate targets. However, the relatively low mean density of Ceres (~2.1 g cm^{-3}) [*Thomas et al.*, 2005] raises the possibility that Ceres may host significant ice [*Castillo-Rogez and McCord*, 2010; *Castillo-Rogez*, 2011] or be composed of highly porous silicates [*Zolotov*, 2009]. The detection of water vapor around Ceres [*Küppers et al.*, 2014] indicates near-surface ice, at least in localized regions.

In this study, we combine new experiments assessing projectile retention in icy targets with earlier work that focused on projectile retention in silicate targets. These combined datasets reveal the implications of two endmember models ("ice-rich" [*Castillo-Rogez and McCord*, 2010] and "porous silicate" [*Zolotov*, 2009]) for the meteoritic contamination of Ceres. Our findings suggest that the surface of Ceres should be heavily contaminated by exogenic meteoritic debris.

2. Methods

Hypervelocity impact experiments at the NASA Ames Vertical Gun Range (AVGR) [*Gault and Wedekind*, 1978] constrained how efficiently ice-rich targets retain projectiles (Supporting Table S1). We used targets of snow (sieved through a 2 mm sieve; bulk ρ = 0.55 g cm^{-3}; ~40% porosity) and snow covered with a thin veneer of expanded perlite (sieved through a 2 mm sieve; bulk ρ = 0.20 g cm^{-3}). Perlite-veneered targets revealed how an underdense silicate surface layer, possibly present on Ceres [*Fanale and Salvail*, 1989; *Castillo-Rogez and McCord*, 2010], affects impactor retention. A layer of sand ~5 cm deep covered the bottom of the target bucket (15 cm deep) in order to minimize potential effects of rebound (particularly at steep incidence). In all cases, the target bucket was thoroughly chilled and then filled in a freezer. The target remained in the freezer until loaded into the impact chamber. Neither snow nor veneered targets are intended to directly simulate Ceres' surface. Rather, we consider endmember cases to assess possible outcomes of cratering events on Ceres. Such a strategy proved successful for the Deep Impact mission [*Schultz et al.,* 2007].

We also varied projectile type and impact angles. Basalt (ρ = 2.8 g cm^{-3}) and aluminum (2017-T4; ρ = 2.79 g cm^{-3}) projectiles have similar impedances; using both types revealed the effect of tensile strength on experimental outcomes. Impact angle varied from 30° to 90° (with respect to horizontal). Impact angle is a key aspect of this study because prior work demonstrated that impactor retention is highly sensitive to impact angle [*Daly and Schultz*, 2014; *Bruck Syal and Schultz*, 2015].

After each experiment, the portions of the target that mixed with the projectile were excavated and melted through a series of polypropylene sieves (1950 μm, 950 μm, 500 μm, 250 μm, 105 μm mesh openings). After melting, material larger than 250 μm was sorted by hand to isolate projectile relics, which were then weighed. Isolating individual projectile relics smaller than 250 μm from other material (e.g., perlite granules) was impractical. Instead, the mass of projectile in 105 to 250 μm size fraction was indirectly determined (Supporting Text S1). Any projectile pieces smaller than 105 μm were not included when calculating the projectile mass retained. Nevertheless, high-speed imaging and post-impact photography provide insight into the fate of the finest fraction (section 3.1).

Unlike prior computational work tailored to high-speed impacts at icy satellites [*Pierazzo and Chyba*, 2002], this study used impact speeds between 4.5 and 5 km s^{-1}. This range is highly relevant to Ceres, where the average impact speed is ~4.8 km s^{-1} [*O'Brien and Sykes*, 2011]. Therefore, impact speed need not be scaled when extrapolating these experiments, although other factors (e.g., size) should be considered for larger craters (e.g., [*Schultz and Gault,* 1990]). Ejecta scaling relationships [*Housen et al*, 1983] provide a framework for extrapolating these experiments to Ceres. In the gravity regime, most ejecta

lands within a few crater radii. This regime likely dominates for impacts on Ceres. Most of the excavation phase of these experiments was also gravity-dominated. For particulate targets like these, frictional shear strength during dynamic flow (not tensile strength) determines whether an event is gravity- or strength-dominated [*Schultz et al.,* 2005]. In some cases a thin crust formed on the target in the brief time between loading and firing the gun. Nevertheless, high-speed imaging proved that loose, particulate snow is excavated from beneath this crust. A normal ejecta curtain develops, consistent with gravity-dominated excavation (Fig. S1). Hence, the fraction of the projectile retained within a few crater radii in these experiments should accurately predict the fraction of the projectile retained within the same number of crater radii on Ceres. These experiments assessed impactor retention within ~5 crater radii. Laboratory experiments have successfully predicted the outcomes of planetary-scale events, including the craters made during the LCROSS [*Schultz et al.,* 2010] and Deep Impact [*Schultz et al.,* 2007] missions. Such prior successes strengthen the case for using impact experiments to make planetary-scale predictions for impactor contamination on Ceres.

3.   Results

3.1.   *Projectile retention efficiency*

Results are reported as a "projectile retention efficiency", defined as the total mass of projectile relics (solid or melted) recovered in and near the crater, normalized to the projectile mass. A retention efficiency of 100% indicates that the entire projectile mass was

retained in and near the crater; a retention efficiency of 0% means that none of the projectile was recovered from within or near the crater. All projectile retention efficiencies were normalized to a common impact speed of 4.5 km s^{-1}.

Figure 1 shows projectile retention efficiencies for aluminum and basalt projectiles in snow and perlite-veneered targets. Uncertainties associated with error bars are detailed in Supporting Text S2. At 30°, snow and perlite-veneered targets have similar projectile retention efficiencies of ~30% for aluminum projectiles. Projectile retention efficiency in both targets increased up to 60°. However, projectile retention efficiency for snow targets was far higher than for veneered targets at 45°. At vertical incidence in snow targets, 77% of aluminum impactors remained in or near the crater. However, projectile retention efficiency *decreased* for vertical impacts into the veneered target as a result of projectile disruption and deep penetration within the veneer (Fig. 1b; section 4.1).

Experiments with basalt projectiles appear to result in anomalously low projectile retention efficiencies (Fig. 1c). These low efficiencies could indicate that the majority of basalt projectiles was not retained, escaping far beyond the crater. However, basalt projectiles catastrophically disrupted, which dispersed extremely fine fragments (<105 μm diameter) into the target. Therefore, retention efficiencies could be spuriously low due to an abundance of fine fragments that were retained but not amenable to recovery. High-speed imaging and post-impact photographs clarify this issue. High-speed imaging of crater formation revealed dark gray deposits lining craters formed by basalt projectiles, similar to what was seen for aluminum impactors into the same type of target. Imaging clearly shows that for vertical impacts most of the basalt projectile relics remain inside the

crater during excavation, with some of the projectile relics escaping the crater downrange at lower incidence angles. This result is again consistent with high-speed imaging of impacts by aluminum projectiles. Post-test photographs of the craters and dark gray deposits (section 3.2) formed by basalt and aluminum projectiles in snow targets at the same impact angles look quite similar (Fig. S2, S3). Appearance alone is suggestive, but not definitive. However, aluminum and basalt have nearly identical impedances; hence, enhanced energy partitioning into the basalt due to impedance differences cannot explain the apparent order of magnitude decrease in retention for basalt projectiles. In contrast, the differing ductile and brittle character of aluminum and basalt, respectively, naturally generates different relic size distributions, with the catastrophically disrupted basalt projectile biased to smaller pieces. Hence, projectile retention efficiencies for basalt impactors are likely artificially low due to large numbers of unsampled relics <105 μm, not due to extremely low projectile retention.

3.2. Distribution and physical state of projectile relics

Projectile relics were hosted in patchy dark gray deposits of ice. The gray deposits consisted of snow that melted and rapidly quenched, trapping projectile relics within (Fig. S4). Finely dispersed projectile pieces suspended within the ice create the gray color. Individual, large (~5 mm diameter) projectile relics were also trapped in these quenched melts (Fig. S5). Thin sections of aluminum and basalt projectile relics reveal that the interiors of relics did not melt during the experiments. However, the surfaces of some aluminum relics show striations consistent with surficial melting caused by abrasion of the

projectile during penetration. Basalt relics were much finer grained than aluminum relics (Supporting Text S3; Fig. S6).

At vertical incidence, most dark deposits (and therefore projectile relics) remained inside the crater. As impact angle decreased, increasing amounts of the projectile were found beyond the downrange crater rim; nevertheless, some gray deposits remained within the crater at all incidence angles. For a given impact angle, impacts into veneered targets distributed projectile-bearing gray deposits over a larger area than impacts into snow (Fig. S4). This difference reflected the role of projectile failure within the veneer, as well as enhanced cratering efficiency in the veneered targets.

4. Implications for Ceres

The experiments suggest that significant projectile contamination should occur on Ceres. Even with the unrealistic assumption that projectile retention decreases to zero at speeds above 4.5 km s^{-1}, nearly half of all impacts into Ceres are at speeds favoring projectile retention. Unless Ceres has been recently, globally resurfaced it is hard to reconcile these experiments with a regolith on Ceres that is not heavily contaminated by projectiles.

A simple calculation based on the cratering flux at Ceres contextualizes this hypothesis. *De Elía and Di Sisto* [2011] calculated that 4,631 asteroids > 1 km in diameter have collided with Ceres over Solar System history. Assuming each asteroid was 1 km in diameter and a projectile retention efficiency of 68% (consistent with a 45° impact of

aluminum into a snow target), the equivalent of a global layer of meteoritic debris five meters thick could be retained on Ceres. Assuming a retention efficiency of 6% (consistent with results for a 45° impact of basalt into a snow target), the global equivalent layer would be 0.4 m. The impactor flux at Ceres will be some combination of metallic and stony objects. The thickness calculated using basalt retention efficiencies is surely an underestimate because it neglects the finer fraction of basalt relics that were likely retained. These calculations are also underestimates because they assume retention efficiencies for 45° (half of all impacts will be at steeper incidence) and because the largest impactors dominate the flux of impactor material [*Turrini et al.,* 2014]. *De Elía and Di Sisto* [2011] estimate that the largest cererean impactor was 72 km in diameter. Assuming 68% retention efficiency, such an impact may have delivered the equivalent of a global layer of meteoritic debris 370 m thick. This rough estimate is consistent with both impact contamination at Vesta [*McCord et al.,* 2012; *Turrini et al.,* 2014] and with predictions of extensive projectile contamination at Ceres.

Many unknown or poorly constrained properties will affect the contamination history of Ceres. Some of these factors are discussed in the three sections that follow. First, the bulk composition of Ceres—porous or ice-rich—will affect how efficiently projectiles are retained at Ceres (section 4.1). Second, a porous, insulating silicate lag that covers putative buried ice modifies the fate of retained projectile relics (section 4.2). Finally, the porous silicate and ice-rich models for Ceres imply different evolutions of the projectile contamination on the cererean surface through time (section 4.3).

4.1.Role of the composition of Ceres

Ceres will likely be contaminated by impactors in either the ice-rich (e.g., [*Castillo-Rogez and McCord*, 2010]) or porous silicate (e.g., [*Zolotov*, 2009]) models for Ceres' composition, as well as for cases that fall between these extremes. However, the efficiency of projectile retention and the physical state of the delivered projectile fraction may be different in the porous silicate and ice-rich cases.

The lower impedance of snow and veneered targets relative to porous silicate targets leads to lower peak pressures in the projectile. This has two important implications. First, lower peak pressures favor increased projectile retention in snow and veneered targets, particularly for oblique impacts, as documented in prior experiments by *Daly and Schultz* [2014]. For example, the projectile retention efficiency for aluminum projectiles in porous silicate and snow targets is nearly identical at vertical incidence. However, at 45° projectile retention efficiency was only 37% for porous silicate targets while snow targets retained 68%. Increased porosity in the silicate target might offset these effects. But, based on these experiments, an ice-rich Ceres covered with a thin silicate veneer may retain projectiles more efficiently than a porous silicate Ceres with minimal ice content.

Second, the projectile component on icy targets is more likely to include unmelted relics due to lower post-shock temperatures. Prior experiments found that much of the projectile retained by porous silicate targets melted, although some solid fragments were preserved, encased in target-derived melt at shallow incidence [*Daly and Schultz*, 2014]. The projectile relics found here, however, were unmelted, even at vertical incidence where peak pressures are highest.

4.2. The role of the veneer in the ice-rich case

If the ice-rich model for Ceres is correct, then perlite-veneered targets may be the most relevant. As discussed in section 3.1, vertical impacts into veneered targets yielded lower projectile retention efficiencies than 60° impacts. Quarterspace impact experiments in perlite targets revealed that projectile failure within the veneer at steep incidence injects projectile fragments into the subsurface beyond the final transient crater (Fig. S6). (See also *Schultz et al.* [2005].) In contrast, projectile relics are retained on the crater floor during vertical impacts into snow. Although injected projectile fragments were retained in the veneered target, they would not be recovered because the fragments were sequestered well beyond the sampled crater floor or cavity. Depending on the properties (porosity, compressibility) of the insulating silicate layer on Ceres (if such a layer exists), substantial portions of the projectile component on Ceres might be injected deep into the regolith. This process would only be important for impactors below a certain size relative to the thickness of the silicate lag. In this study, the silicate veneer was twice the projectile diameter.

4.3. A model for Ceres' surface evolution

4.3.1. The porous case

If the upper tens of kilometers of Ceres consisted of porous silicates, then the projectile component would accumulate in a vertically mixed regolith, similar to Vesta (e.g., [*McCord et al.*, 2012; *Jaumann et al.,* 2014]). Impactors of all types—not just carbonaceous impactors—would likely be retained in the regolith (e.g., [*Daly and Schultz,*

2014; *Turrini et al.,* 2014]). Recent reports of exogenic olivine on Vesta [*Le Corre et al.,* 2015] bolster predictions for multiple types of projectile relics on Ceres. The diverse clasts and chemical traces of exogenic material in howardites [e.g., *Hewins*, 1979; *Lorenz et al.*, 2001; *Lorenz et al.,* 2007; *Warren et al.,* 2009] and the Almahata Sitta ureilite [*Goodrich et al.,* 2015] provide direct evidence for retention of both stony and metallic impactors on other bodies in the asteroid belt; the same should be true for Ceres. In the porous case, the projectile component delivered by both metallic and stony projectiles may occur primarily as breccias of melted regolith mixed with both melted and unmelted portions of the projectile. The projectile component would be initially hosted in these breccias (at least for speeds ≥ 4.5 km s^{-1}) but later be comminuted by impacts. Lower-speed impacts would favor a higher abundance of solid projectile fragments.

4.3.2. *The ice-rich case*

A critical difference between the porous silicate and ice-rich cases arises because ice is not stable over much of the surface of Ceres [*Fanale and Salvail*, 1989; *Schorghofer*, 2015]. Impacts large enough to penetrate the insulating silicate layer may expose unprotected ice. Impact-exposed ices (or excavated and mixed with projectile survivors) may sublimate rapidly, depending on latitude. For example, *Fanale and Salvail* [1989] calculate that it takes only a few million years for exposed ice to retreat below a sublimation lag a few meters deep. As a result, projectile relics, accompanied by other phases in the sublimating ice (e.g., silicates, carbonates, hydroxides), would accumulate on the surface of Ceres as a lag deposit (Fig. 2), in contrast with vertical mixing in the porous silicate

13

case. Depending on the depth to putative ice, a surface lag deposit on an ice-rich Ceres may have a higher apparent *concentration* of exogenic material than the surface of a porous silicate Ceres with a vertically-mixed regolith. Injection of projectile relics into the subsurface due to projectile failure within the putative insulating silicate veneer, however, might counter this trend.

Based on these experiments, the insulating silicate veneer on an ice-rich Ceres may host coherent larger relics (e.g., hand sample size or larger) of metallic projectiles. Relics of stony impactors might be present as finer-grained debris. Although projectile relics delivered to Ceres will be larger than relics in experiments, fragments will still be fairly small. For example, increasing the projectile size by a factor of 10 only increases fragment mass by ~1.8 assuming that fragment mass scales as $\dot{\varepsilon}^{1/4}$ [*Schultz and Gault*, 1990].

4.3.3. *Clues from cratering statistics*

Multiple, unknown factors are important for assessing these hypotheses, including the ice/rock fraction in the mantle and the depth to ice (if the ice-rich model is correct). If the insulating silicate veneer is thin, then the process of excavation and sublimation of ice, which may concentrate projectile relics into a lag, may be extremely important. However, if the ice is deeply buried then this model for Ceres' surface evolution may not be correct.

In the absence of resupplied water from depth, the hypothesized lag deposit on Ceres is likely no thinner than the depth of regolith overturn. Cratering statistics are not yet available for Ceres [as of when this chapter was published], but cratering statistics from

Vesta provide a first-order constraint. *Marchi et al.* [2012] report a transition from a production slope to an equilibrium slope on Vesta for craters between 4 and 10 km in diameter, which corresponds to a saturation crater diameter, D_s, of 120 to 300 m [*Schultz et al.,* 1976]. The regolith overturn layer thickness is ~D_s/5 or 24 to 60 meters. In this case, craters 240 to 600 meters in diameter could excavate ice (assuming a 10:1 ratio of final crater diameter to excavation depth). *de Elía and di Sisto* [2011] estimate that Ceres has ~ 3×10^8 crater larger than 0.1 kilometers, with orders of magnitude more meter-scale craters. If the transition diameter on Ceres is smaller than on Vesta, then the number of impacts that excavate ice could be orders of magnitude larger based on the flux model of *de Elía and Di Sisto* [2011]. Resupply of water by diffusion might also decrease the depth to ice to as little as 0.5 m above 60° latitude [*Schorghofer*, 2015]. This could drastically increase the number of ice-excavating impacts.

4.3.4 Balance of projectile retention and target removal

Some impacts may remove more material than they deliver (e.g., [*Gault et al.*, 1963; *Svetsov*, 2011], possibly including the projectile component delivered by previous impacts. To assess the balance between projectile delivery and target removal, we combine well-established ejecta scaling relationships from *Housen et al.* [1983] with projectile retention efficiencies reported here. Comparing projectile retention efficiency to the mass of ejecta that escapes Ceres (normalized to the projectile mass) puts a first-order constraint on whether Ceres can accumulate a net projectile component (Supporting Text S4). Assuming projectile retention for aluminum projectiles, impacts between 30 and 90° at

4.5 km s^{-1} deliver more mass than they remove (Table 1). The projectile retention efficiencies measured for basalt projectiles imply that impacts between 30 and 60° could either erode slightly more than they deliver or deliver the same mass of projectile as they remove from the target (Table 1). However, when the finer fraction is considered (section 3.1; Figs. S1 and S2), the true retention efficiencies for basalt projectiles likely meet or exceed those required to balance delivery and erosion (Supporting Text S4).

By necessity, these experiments measure only the projectile retained in and near the crater. However, any portions of the projectile traveling slower than escape speed will be retained somewhere on Ceres. Hence, the global retention of impactor debris is likely higher than the amount of meteoritic debris retained in and near the crater. Computer models are needed to quantify precisely how much more of the impactor is retained globally but face their own challenges due to uncertain material properties and processes acting at small scales (below cell sizes) that nevertheless can affect retention. However, the extreme case of 100% retention provides an upper bound. In this scenario, impacts at 4.5 km s^{-1} might deliver two to twenty five times more mass than they erode (Supporting Table S2). The exact ratio depends on characteristics of the cererean surface that are poorly known at present (e.g., bulk density, strength, porosity).

Ejecta escaping Ceres will come from the upper surface (depths less than ~1/8 to 1/10 of the crater diameter). However, the upper surface is the most likely to accumulate projectile debris, particularly for an ice-rich Ceres. Removal from the upper surface could reduce the net m_{ret}/m_{esc} by removing some previously-delivered meteoritic with escaping "target-derived" ejecta. Projectile relics injected deep into the regolith would be less likely

to suffer this fate. In the ice-rich case, sublimation could progressively raise crater floors, renewing the projectile component closer to the near-surface regolith if crater floors are littered with projectile relics. The regolith likely develops a steady-state abundance of projectile relics. Increased m_{ret}/m_{esc} would increase the steady-state abundance. The values of m_{ret}/m_{esc} on Ceres may be higher than calculated because point source solutions for ejecta scaling do not account for decreased cratering efficiency with decreasing impact angle. Furthermore, compression reduces ejecta volumes in highly porous targets, [*Housen et al.*, 1999; *Schultz et al.,* 2005; *Hermalyn et al.,* 2012], which would increase m_{ret}/m_{esc}. On Vesta, a significant projectile component is well documented, even though impacts at Vesta may result in mass loss [*Turrini et al.,* 2014]. Hence, these calculations suggest that Ceres may be more extensively affected by contamination.

5. Conclusions

If predictions based on these experiments are correct, then Ceres should be heavily contaminated by impactors. Depending on the ice content of Ceres, the process of exposing ice by impacts, sublimating the ice away, and concentrating the projectile component in a lag deposit could be extremely important. In this case, some of the meteoritic debris delivered to Ceres may have been injected into the silicate veneer. This could hide part of the projectile component from the view of instruments that sense the surface. In contrast, if Ceres is ice-poor, then exogenic debris would accumulate in a vertically-mixed regolith. In either case, if an asteroid breakup event (e.g., [*Nesvorný et al.*, 2008; *Korochantseva et al.,* 2007]) occurred near Ceres, the exogenic material on Ceres could be heavily biased

toward material found in the particular asteroid that broke up. Ejecta from more recent craters can bury part of the projectile component in both the icy and silicate cases [*Turrini et al.,* 2014].

Extensive impactor contamination on Ceres may seem at odds with pre-*Dawn* observations of a homogeneous surface (e.g., [*Carry et al.*, 2008; *Ehlmann and Brown*, 2015]) and a spectrum unlike anything in the meteorite collection (e.g., [*Milliken and Rivkin,* 2009]). Multiple authors (e.g., [*Milliken and Rivkin*, 2009; *Rivkin and Volquardsen*, 2010]) interpret these observations as evidence for a widespread, perhaps global, alteration event on Ceres. Nevertheless, telescopic data may have not had sufficient spatial resolution to isolate areas with distinct spectral signatures associated with projectile contamination (e.g., 50 km pxl^{-1} for *Carry et al.* [2008]). At higher spatial resolution, *Dawn* may observe pockets of retained impactor material on crater floors and reveal signatures associated with different types of impactors. Projectile-rich deposits may crop out on crater walls that cut through deposits of injected projectile relics, if the surface of Ceres permits projectile injection. Dawn observed projectile-delivered dark material on the walls of some craters on Vesta [*McCord et al.,* 2012; *Reddy et al.,* 2012; *Turrini et al.,* 2014], though the source of those subsurface units was burial by later ejecta. Based on these impact experiments, endogenic alteration cannot be the whole story. The fact that impactor contamination at Vesta is a natural consequence of its impact history [*McCord et al.*, 2012; *Turrini et al.,* 2014; *Daly and Schultz,* 2014] lends strong support to this claim. Some, and possibly much, of the surface of Ceres may represent impactor material delivered to Ceres, rather than endogenic alteration assemblages (e.g., [*Milliken and Rivkin*, 2009; *Zolotov*, 2009]) or syn- and post-impact alteration products (e.g., [*Zolotov*, 2014]).

These experiments suggest that many other bodies in the asteroid belt likely host large amounts of meteoritic debris. Because projectile contamination is driven by the impact process, which has dramatically modified all the asteroids, projectile contamination should be ubiquitous among bodies in the main belt. The exogenic material in ureilites (e.g., Almahata Sitta) [*Goodrich et al.,* 2015] and howardites supports this experimentally-driven hypothesis of ubiquitous exogenic debris on asteroids. The OSIRIS-REx mission, which will return samples from the asteroid Bennu, may return material delivered to Bennu by impacts, in addition to samples of Bennu itself.

6. Acknowledgements

7.   References

Bland, P. A., N. A. Artemieva, G. S. Collins, W. F. Bottke, D. B. J. Bussey and K. H. Joy (2008), Asteroids on the Moon: Projectile Survival During Low Velocity Impact, *Lunar and Planetary Science Conference XXXIX,* abstract no. 2045.

Bruck Syal, M. and P. H. Schultz (2015), Impact Delivery of Water at the Moon and Mercury, *Lunar and Planetary Science Conference XXXXVI,* abstract no. 1680.

Bruck Syal, M., P. H. Schultz, and M. A. Riner (2015), Darkening of Mercury's surface by cometary carbon, *Nat. Geosci.*, *8*(5), 352–356, doi:10.1038/ngeo2397.

Carry, B., C. Dumas, M. Fulchignoni, W. J. Merline, J. Berthier, D. Hestroffer, T. Fusco and P. Tamblyn (2008), Near-infrared mapping and physical properties of the dwarf-planet Ceres, *Astron. Astrophys., 478,* 235–244, doi:10.1051/0004-6361:20078166.

Castillo-Rogez, J. C. (2011), Ceres – Neither a porous nor salty ball, *Icarus, 215*(2), 599–602, doi:10.1016/j.icarus.2011.08.007.

Castillo-Rogez, J. C. and T. B. McCord (2010), Ceres' evolution and present state constrained by shape data, *Icarus, 205*(2), 443–459, doi:10.1016/j.icarus.2009.04.008.

Daly, R. T. and P. H. Schultz (2014), How much of the impactor (and its water) ends up in Vesta's regolith?, *Lunar and Planetary Science Conference XXXXV,* abstract no. 2070.

De Elía, G. C. and R. P. di Sisto (2011), Impactor flux and cratering on Ceres and Vesta: Implications for the early solar system, *Astron. Astrophys., 534,* A129, doi:10.1051/0004-6361/201117543.

Ehlmann, B. L. and M. E. Brown (2015), First Keck adaptive optics global infrared (2.2-4.1 μm) spectral map of Ceres: Results and a review of key questions in advance of Dawn's exploration, *Lunar and Planetary Science Conference XXXXVI,* abstract no. 2807.

Fanale, F. P. and J. R. Salvail (1989), The water regime of asteroid (1) Ceres, *Icarus, 82,* 97–110, doi:10.1016/0019-1035(89)90026-2.

Gault, D. E., E. M. Shoemaker, and H. J. Moore (1963), Spray ejected from the lunar surface by meteoroid impact, *NASA Technical Note D-1767,* 42 p.

Gault, D. E. and J. A. Wedekind (1978), Experimental studies of oblique impact, *Proceedings of the 9th Lunar and Planetary Science Conference,* pp. 374–376.

Goodrich, C. A., W. K. Hartmann, D. P. O'Brien, S. J. Weidenschilling, L. Wilson, P. Michel and M. Jutzi (2015), Origin and history of ureilitic material in the solar system: The view from asteroid 2008 TC_3 and the Almahatta Sitta meteorite, *Met. Planet. Sci., 50(4),* 782–809, doi:10.1111/maps.12401.

Hermalyn, B., P. H. Schultz, M. Shirley, K. Ennico and A. Colaprete (2012), Scouring the surface: Ejecta dynamics and the LCROSS impact event, *Icarus, 218*(1), 654–665, doi:10.1016/j.icarus.2011.12.025.

Hewins, R. H. (1979), Composition and origin of metal in howardites, *Geo. Cosmo. Act, 43,* 1663–1673, doi:10.1016/0016-7037(79)90185-6.

Housen, K. R., K. A. Holsapple and M. E. Voss (1999), Compaction as the origin of the unusual craters on the asteroid Mathilde, *Nature, 402,* 155–157, doi:10.1038/45985.

Housen, K. R., R. M. Schmidt and K. A. Holsapple (1983), Crater ejecta scaling laws: Fundamental forms based on dimensional analysis, *J. Geophys. Res., 88(B3),* 2485–2499, doi:10.1029/JB088iB03p02485.

Holsapple, K. A. and K. R. Housen (2007), A crater and its ejecta: An interpretation of Deep Impact, *Icarus, 187*(1), 345–356, doi:10.1016/j.icarus.2006.08.029.

Jaumann, R. et al. (2014), The geological nature of dark material on Vesta and implications for the subsurface structure, *Icarus, 240,* 3–19, doi:10.1016/j.icarus.2014.04.035.

Korochantseva, E.V et al. (2007), L-chondrite asteroid breakup tied to Ordovician meteorite shower by multiple isochron ^{40}Ar- ^{39}Ar dating, *Met. Planet. Sci., 42*(1), 113–130, doi:10.1111/j.1945-5100.2007.tb00221.x.

Küppers, M. et al. (2014), Localized sources of water vapour on the dwarf planet (1) Ceres, *Nature, 505*(7484), 525–527, doi:10.1038/nature12918.

Le Corre, L. et al. (2015), Exploring exogenic sources for the olivine on asteroid (4) Vesta, *Icarus, 285,* 483–499, doi: 10.1016/j.icarus.2015.01.018.

Lorenz, C., M. Nazarov, G. Kurat, F. Brandstaetter and Th. Ntaflos (2001), Clast population and chemical bulk composition of the Dhofar 018 howardite, *Lunar and Planetary Science Conference XXXII,* abstract no. 1778.

Lorenz, K. A., M. A. Nazarov, G. Kurat, F. Brandstaetter and Th. Ntaflos (2007), Foreign meteoritic material of howardites and polymict eucrites, *Petrology, 15(2),* 109–125, doi:10.1134/S0869591107020014.

Marchi, S. et al. (2012), The Violent Collisional History of Asteroid 4 Vesta, *Science, 336*(6082), 690–694, doi:10.1126/science.1218757.

McCord, T. B. and C. Sotin (2005), Ceres: Evolution and current state, *J. Geophys. Res. Planets, 110*(E5), E05009, doi:10.1029/2004JE002244.

McCord, T. B. et al. (2012), Dark material on Vesta from the infall of carbonaceous volatile-rich material, *Nature, 491,* 83–86, doi:10.1038/nature11561.

Milliken, R. E. and A. S. Rivkin (2009), Brucite and carbonate assemblages from altered olivine-rich materials on Ceres, *Nat. Geosci., 2*(4), 258–261, doi:10.1038/ngeo478.

Nesvorný, D. et al. (2008), Origin of the near-ecliptic circumsolar dust band, *Astro. J., 679,* L143–L146, doi:10.1086/588841.

O'Brien, D. P. and M. V. Sykes (2011), The origin and evolution of the asteroid belt—Implications for Vesta and Ceres, *Space Sci. Rev., 163,* 41–61, doi:10.1007/s11214-011-9808-6.

Ong, L., E. I. Asphaug, D. Korycansky and R. F. Coker (2010), Volatile retention from cometary impacts on the Moon, *Icarus, 207,* 578–589, doi:10.1016/j.icarus.2009.12.012.

Pierazzo, E. and C. F. Chyba (2002), Cometary delivery of biogenic elements to Europa, *Icarus,* 157, 120–127, doi:10.1016/j.icarus.2001.6812.

Reddy, V. et al. (2012), Delivery of dark material to Vesta via carbonaceous chondritic impacts, *Icarus, 221*(2), 544–559, doi:10.1016/j.icarus.2012.08.011.

Rivkin, A. S. and E. L. Volquardsen (2010), Rotationally-resolved spectra of Ceres in the 3-μm region, *Icarus, 206*(1), 327–333, doi:10.1016/j.icarus.2009.08.026.

Schorghofer, N. (2015), Predictions of depth to ice on asteroid Ceres, *Lunar and Planetary Science Conference XXXXVI,* abstract no.1091.

Schultz, P. H. and D. E. Gault (1990), Prolonged global catastrophes from oblique impacts, in *Geological Society of America Special Papers,* vol. 247, 239–262, doi:10.1130/SPE247-p239.

Schultz, P. H., R. Greeley and D. E. Gault (1976), Degradation of small mare surface features, *Proceedings of the 7th Lunar and Planetary Science Conference,* pp. 985–1003.

Schultz, P. H., C. M. Ernst and J. L. B. Anderson (2005), Expectations for Crater Size and Photometric Evolution from the Deep Impact Collision, *Space Sci. Rev., 117,* 207–239, doi:10.1007/s11214-005-3383-7.

Schultz, P. H., C. A. Eberhardy, C. M. Ernst, M. F. A'Hearn, J. M. Sunshine and C. M. Lisse (2007), The Deep Impact oblique impact cratering experiment, *Icarus, 190*(2), 295–333, doi:10.1016/j.icarus.2007.06.006.

Schultz, P. H., B. Hermalyn, A. Colaprete, K. Ennico, M. Shirley and W. S. Marshall (2010), The LCROSS cratering experiment, *Science, 330*(6003), 468–472, doi:10.1126/science.1187454.

Svetsov, V. (2011), Cratering erosion of planetary embryos, *Icarus, 214,* 316–326, doi:10.1016/j.icarus.2011.04.026.

Thomas, P. C., J. W. Parker, L. A. McFadden, C. T. Russell, S. A. Stern, M. V. Sykes and E. F. Young (2005), Differentiation of the asteroid Ceres as revealed by its shape, *Nature, 437*(7056), 224–226, doi:10.1038/nature03938.

Turrini, D. and V. Svetsov (2014), The formation of Jupiter, the Jovian Early Bombardment and the delivery of water to the asteroid belt: The case of (4) Vesta, *Life, 4,* 4–34, doi:10.3390/life4010004.

Turrini, D., G. Magni and A. Coradini (2011), Probing the history of Solar system through the cratering records on Vesta and Ceres, *Mon. Not. R. Astron. Soc., 413,* 2439–2466, doi:10.1111/j.1365-2966.2011.18316.x.

Turrini, D. et al. (2014), The contamination of the surface of Vesta by impacts and the delivery of the dark material, *Icarus, 240,* 86–102, doi:10.1016/j.icarus.2014.02.021.

Warren, P. H., G. W. Kallemeyn, H. Huber, F. Ulff-Moller and W. Choe (2009), Siderophile and other geochemical constraints on mixing relationships among HED-meteoritic breccias, *Geo. Cosmo. Act., 73(19),* 5918–5943 doi:10.1016/j.gca.2009.06.030.

Zolotov, M. Y. (2009), On the composition and differentiation of Ceres, *Icarus, 204,* 183–193, doi:10.1016/j.icarus.2009.06.011.

Zolotov, M. Y. (2014), Formation of brucite and cronstedtite-bearing mineral assemblages on Ceres, *Icarus, 228,* 13–26, doi:10.1016/j.icarus.2013.09.020.

Tables

Table 1. Balance between target removal and projectile delivery.

Impact Angle (°)	$V_{imp} \sin(\theta)$ (km s^{-1})	m_{ret}/m_p	$(m_{esc}/m_p)_S$*	$(m_{esc}/m_p)_{HP}$†	$(m_{ret}/m_{esc})_S$	$(m_{ret}/m_{esc})_{HP}$
Aluminum projectiles into snow						
90	4.5	0.77	0.36	0.09	2.1	8.3
60	3.9	0.74	0.30	0.08	2.5	9.4
45	3.2	0.68	0.23	0.06	2.9	11.1
30	2.3	0.33	0.15	0.04	2.2	8.1
Aluminum projectiles into perlite						
90	4.5	0.51	0.44	0.11	1.2	4.5
60	3.9	0.73	0.37	0.10	2.0	7.6
45	3.2	0.38	0.29	0.08	1.3	5.0
30	2.3	0.31	0.19	0.05	1.7	6.2
Basalt projectiles into snow						
60	3.9	0.07	0.30	0.08	0.2	0.9
45	3.2	0.06	0.23	0.06	0.3	1.0
30	2.3	0.04	0.15	0.04	0.3	1.0

*Calculated using constants appropriate for dry sand/cohesive soil ($\mu = 0.41$, $v = 0.4$, $C_2 = 0.018$) from *Holsapple and Housen* [2007].

†Calculated using constants appropriate for highly porous materials ($\mu = 0.4$, $v = 0.4$, $C_2 = 0.005$) from *Holsapple and Housen* [2007]. *Holsapple and Housen* [2007] note that ejecta scaling relationships for highly porous materials are still poorly understood.

Figures

(a) Al into Snow Target

(b) Al into Veneer Target

(c) Basalt into Snow Target
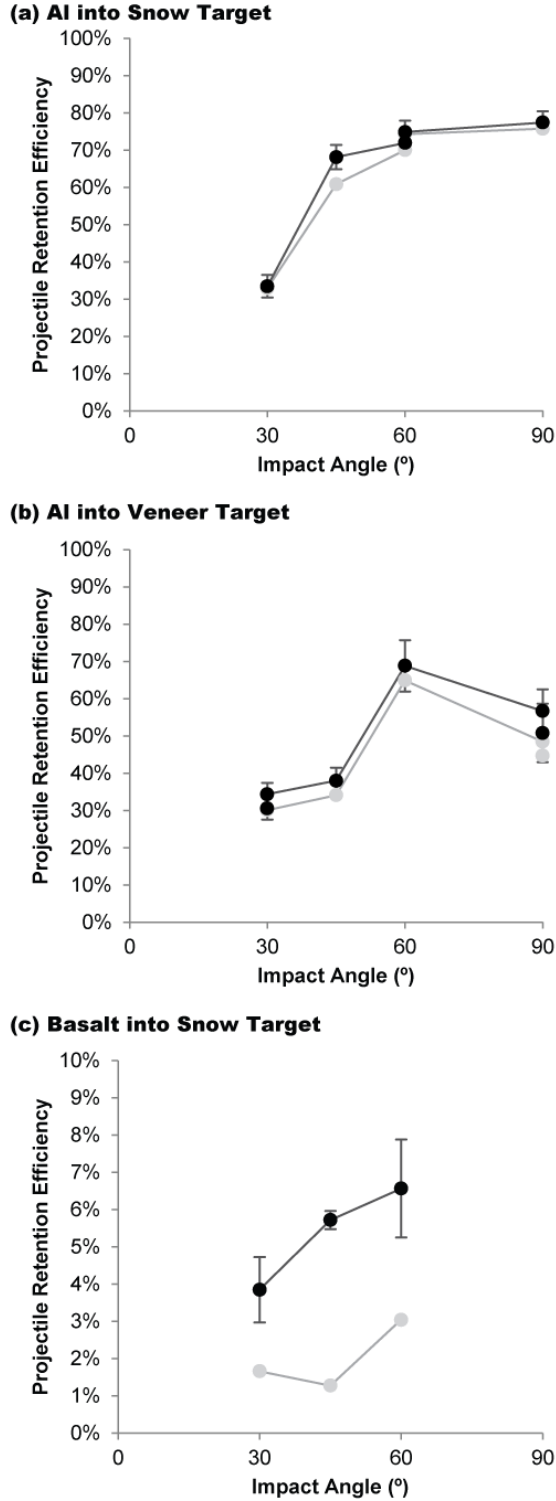
Figure 1. Projectile retention efficiencies for aluminum and basalt projectiles as a function

of target type and impact angle. Black data points include all recovered projectile

29

fragments. Gray data points only include projectile relics larger than 250 μm. (a) Projectile retention efficiency in snow targets increases with impact angle. (b) Retention efficiency in veneered targets decreases at vertical incidence. (c) Only a few percent of basalt projectiles is delivered in fragments larger than 105 μm; see text for discussion. Note that the *y*-axis scale is different in part (c).
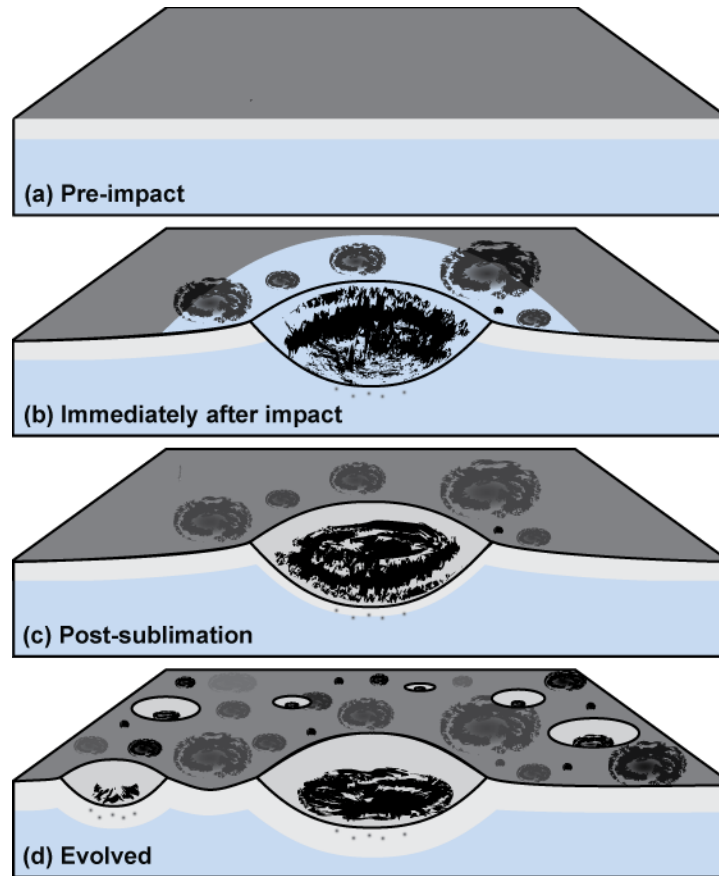
Figure 2. Possible surface evolution of an ice-rich Ceres. (a) The pre-impact surface is a silicate, hydroxide, carbonate veneer (gray) atop an ice-rich layer (blue). The veneer could include endogenic and exogenic materials. (b) Following impacts that excavate ice, projectile relics mixed with ice line the crater, with a fraction scattered beyond the rim (dark gray splotches). Depending on veneer thickness, portions of the projectile may be injected below the bottom of the crater. (c) Exposed ice may quickly sublimate, particularly near the equator. In this case, projectile relics and other refractory phases will be left behind as a lag deposit. (d) Subsequent impacts will deposit additional projectile debris regardless of whether they penetrate through the veneer and reach ice. However, when impacts do excavate ice, the sublimation of exposed ice may leave behind a lag of projectile relics,

accompanied by any nonvolatile endogenic material already present in the ice. As the surface evolves, mass wasting could cover impactor debris retained on crater walls. The rims of craters may shallow as sublimation progresses, which effectively brings the projectile component retained on the crater floor closer to the surface.

Supplementary Material

Introduction

This document includes text that clarifies our methods for determining projectile retention efficiencies and quantifying uncertainties. It provides additional observations that support our assertion that projectile relics did not melt during impact. It also explicitly describes the calculations carried out to assess the balance between projectile retention and target removal. The supplement includes figures that document the impact craters and impact products generated by the experiments used in this study. Finally, this supplement includes tables that list the impact experiments included in this study and the results of calculations.

Text S1. Estimating the mass of projectile in the 105 to 250 μm sieve fraction.

We determined the mass of projectile relics in the 105 to 250 μm sieve fraction as follows: for each experiment, material in the 105 to 250 μm sieve fraction was spread into a single layer. After inspecting the entire layer, micrographs were taken of three representative areas. The main criterion was that the areas contained projectile relics and non-projectile pieces in proportions consistent with what was seen in the entire layer. The cross sectional area of all pieces (e.g., projectile relics, perlite pieces, etc.) in each field of view was measured. Projectile relics are easily identified because they are pieces of either basalt or aluminum, as opposed to translucent to transparent light-toned granules or flat

flakes of paint from the AVGR impact chamber. The ratio of the cross sectional areas of projectile relics to the cross sectional areas of all pieces in the field of view is an estimate for the volume fraction of relics in that field of view, f_p. The mass of projectile relics in the 105 to 250 μm sieve fraction, M_{est}, is

$$M_{est} = m_{sieve} \left(\frac{f_{p,1} + f_{p,2} + f_{p,3}}{3} \right) \left(\frac{\rho_p}{\rho_t} \right) \qquad (1)$$

where m_{sieve} is the total mass of material in the 105 to 250 μm sieve fraction from an experiment, $f_{p,1}$, $f_{p,2}$, and $f_{p,3}$, are the estimated volume fraction of projectile in each of the three fields of view, ρ_p is the grain density of the projectile, and ρ_t is the grain density of the non-projectile pieces, which were primarily grains of quartz sand or perlite. The grain density of the sand used in these experiments sand is 2.65 g cm^{-3}; the grain density of perlite is 0.61 g cm^{-3}. The density of aluminum and basalt projectiles were 2.79 g cm^{-3} and 2.77 g cm^{-3}, respectively, with the exact value calculated for each projectile. In experiments with snow targets, quartz sand grains dominated the non-projectile pieces. Hence, the grain density of sand was used in those calculations. In experiments with veneered targets, perlite granules accounted for nearly all the non-projectile pieces. Hence, the grain density of perlite was used in calculations for these experiments.

Text S2. Error analysis.

Projectile retention efficiency, R, is the sum of the mass of projectile relics measured directly, M_{direct}, and the estimated mass of projectile relics in the 105 to 250 μm fraction, M_{est}. Therefore, the standard deviation of the projectile retention efficiency, σ_R, is

$$\sigma_R = \sqrt{\sigma_{M_{direct}}{}^2 + \sigma_{M_{est}}{}^2} \qquad (2)$$

where $\sigma_{M_{direct}}$ is the standard deviation of the mass of projectile relics measured directly and $\sigma_{M_{est}}$ is the standard deviation of the mass of projectile relics measured indirectly. However, M_{est} is

$$M_{est} = (m_{sieve})f_p\left(\frac{\rho_p}{\rho_t}\right) \qquad (3)$$

with variables as defined in Text S1 and the average volume fraction of projectile pieces denoted as f_p for simplicity. Treating ρ_p and ρ_t as exact values,

$$\sigma_{M_{est}} = M_{est}\frac{\rho_p}{\rho_t}\sqrt{\left(\frac{\sigma_{m_{sieve}}}{m_{sieve}}\right)^2 + \left(\frac{\sigma_{f_p}}{f_p}\right)^2} \qquad (4)$$

where $\sigma_{m_{sieve}}$ is the standard deviation of the mass in the 105 to 250 μm fraction, with all other variables are previously defined. We use replicate experiments at a single impact angle (60° aluminum projectiles into snow targets at 4.21 and 4.22 km s^{-1}, respectively) to calculate $\sigma_{M_{direct}}$ and $\sigma_{m_{sieve}}$. We assume that these two values are typical of all experiments with aluminum projectiles. In contrast, we calculate σ_{f_p} for individual

experiments using the f_p calculated from each field of view (methods section in main text). Therefore,

$$\sigma_R = \sqrt{\sigma_{M_{direct}}^2 + \left(M_{est} \frac{\rho_p}{\rho_t} \sqrt{\left(\frac{\sigma_{m_{sieve}}}{m_{sieve}} \right)^2 + \left(\frac{\sigma_{f_p}}{f_p} \right)^2} \right)^2} \qquad (5)$$

For experiments with aluminum projectiles, $\sigma_{M_{direct}}$ is the largest source of error ($\pm \sim 3\%$).

The error bars on panels (a) and (b) of Fig. 1 in the main paper are $\pm 1 \ \sigma_R$. The error bars on panel (c) are $\pm 1 \ \sigma_{M_{est}}$ because the largest uncertainty for basalt experiments comes from projectile relics <105 μm in size, not from variability in the directly measured mass of projectile relics >250 μm (see Figs. S2 and S3).

Text S3. Physical state of relics.

Larger aluminum relics were typically bowl-shaped (Fig. S5). The convex side faced the target during penetration, as evidenced by the striated texture of this face of aluminum relics. Striations typically radiated from the apex of the relic, with frothy aluminum oxide coating the striations. The opposite, concave side of the projectile relics was most clearly revealed in cross section (Fig. S6a). Frothy aluminum oxide was also present on this side of the relic. Incipient spallation on the concave side of the aluminum relic demonstrated that the interior of the aluminum relic never completely melted. Other aluminum relics showed incipient spallation and deformation patterns consistent with the interiors of relics remaining solid throughout the entire impact process. The surfaces of

36

aluminum relics, however, show evidence of melting: striated, ablation-like textures on the convex sides of aluminum relics and lobate, vesicular zones around margins of some incipient spall fragments on the concave sides of relics. This surficial melt resulted from abrasion during projectile penetration and is not associated with shock melting.

Basalt relics, in contrast, catastrophically disrupted. Like aluminum relics, basalt fragments did not melt during impact (Fig. S6b). Although the recovered basalt fragments were glass rich, the basaltic projectiles consisted of feldspar lathes set in a glassy, mafic matrix. Thin sections of recovered basalt fragments revealed the same texture as was present in the original projectiles. Finally, even the largest basalt fragments were far smaller than most of the aluminum relics. The basalt piece shown in Fig. S6b was among the largest recovered from an experiment, while Fig. S6a shows only part of one aluminum relic.

Text S4. Balance between target removal and projectile retention.

Widely-used scaling laws for impact ejecta [*Housen et al.,* 1983; *Holsapple and Housen,* 2007] can be used to estimate the mass of ejecta lost from Ceres. From these laws, the mass of ejecta ejected faster than the escape speed of Ceres is (see Table 1 of *Holsapple and Housen* [2007]):

$$\frac{m_{esc}}{m_p} = C_2 \left(\frac{v_{esc}}{v_{imp} \sin \theta} \right)^{-3\mu} \left(\frac{\delta}{\rho} \right)^{3\nu - 1} \tag{6}$$

where m_{esc} is the mass of ejecta traveling faster than the escape speed of Ceres, m_p is the mass of the projectile, C_2 is a constant, v_{esc} is the escape speed of Ceres (0.515 km s^{-1}),

v_{imp} is the impact speed (4.5 km s^{-1}), θ is the impact angle (with respect to horizontal), δ is the density of the impactor (2.79 g cm^{-3} for aluminum; 2.77 g cm^{-3} for basalt), ρ is the bulk density of the target (0.55 g cm^{-3} for snow; 0.20 g cm^{-3} for perlite), and μ and ν are scaling exponents.

We use constants for dry sand/cohesive soil ($C_2 = 0.018$, $\mu = 0.41$, $\nu = 0.4$) and for highly porous materials ($C_2 = 0.005$, $\mu = 0.4$, $\nu = 0.4$) [*Holsapple and Housen* [2007]. Although sand is a poor analog for planetary regoliths [*Hermalyn et al.*, 2012], the ejecta scaling for sand is well characterized. The values for m_{esc}/m_p calculated using dry sand scaling may overestimate m_{esc}/m_p for planetary regoliths. The ejecta scaling relationships for highly porous materials are poorly known [*Holsapple and Housen*, 2007]. Nevertheless, these two cases provide useful points of reference. In contrast, "wet soil/rock" scaling is likely not relevant to Ceres. These coefficients were derived from experiments in strength-controlled pieces of basalt that had no porosity [*Holsapple and Housen*, 2007; *Gault et al.*, 1963]. The surface of Ceres has up to 50% porosity based on pre-Dawn observations [*Mitchell et al.*, 1996; *Webster et al.*, 1988]. Porosity likely extends to depth, a consequence of the pervasive role of impacts on Ceres. In addition, many, if not most, craters on Ceres likely formed in the near gravity-dominated regime. Hence, wet soil/rock scaling is not appropriate for Ceres.

Dividing projectile retention efficiency (m_{ret}/m_p) by the left side of equation (6) (m_{esc}/m_p) reveals whether impacts deliver more mass from the projectile than they remove from the target. For conditions relevant to Ceres and projectile retention efficiencies for aluminum projectiles, impacts deliver 1.2 to 7.6 times more projectile mass than they

remove from the target. The ratio m_{ret}/m_{esc} depends on impact angle, target type, and the assumed values for C_2, μ, and ν. Using the measured projectile retention efficiencies for basalt projectiles, m_{ret}/m_{esc} ranges from 0.2 to 1.0, depending on impact angle, target type, and the assumed values for C_2, μ, and ν (see Table 1 in the main paper). Calculations based on wet soil/rock scaling indicate that impacts remove more material than they deliver (m_{ret}/m_{esc} ranges from 0.2 to 0.5 for aluminum impactors and 0.03 to 0.05 for basalt impactors). Nevertheless, calculations using the far more relevant dry sand and highly porous scaling coefficients demonstrate that impacts at these speeds deliver more material to Ceres than they erode.

As discussed in section 3.1 of the main paper, our experiments underestimate the projectile retention efficiencies of basalt projectiles. These scaling calculations can be inverted to solve for the basalt projectile retention efficiency needed to balance projectile retention with target removal. Assuming highly porous scaling, retention efficiency need only be 8% at 60°, 6% at 45°, and 4% at 30° for the mass of basalt projectile retained to balance the mass of target lost. These required levels of projectile retention are comparable to the levels measured in our experiments. Assuming dry sand scaling, the required retention efficiencies are 30% at 60°, 23% and 45°, and 25% at 30°. These values are lower than what were measured for aluminum projectiles in the same target. Given these values and the evidence in section 3.1 (see also Figs S1 and S2), the true projectile retention efficiencies for basalt projectiles are almost certainly high enough to balance projectile delivery and target erosion and quite likely high enough to deliver more mass than is removed from the Ceres by impact.

Supplementary Tables

Table S1. Summary of experiments.

Projectile	Target	Impact angle (°)	Speed (km s^{-1})	Projectile retention efficiency (wt. %)*
Basalt	Snow	60	4.89	7 ± 1†
		45	4.41	6 ± 0.2
		30	4.64	4 ± 0.9
Aluminum	Snow	90	4.67	77 ± 3
		60	4.22	75 ± 3
		60	4.21	72 ± 3
		45	4.42	68 ± 3
		30	4.80	33 ± 3
Aluminum	Veneered	90	4.49	51 ± 8
		90	4.88	57 ± 6
		60	4.47	69 ± 7
		45	4.83	38 ± 4
		30	4.99	34 ± 3
		30	4.47	31 ± 3

*Normalized to a common impact speed of 4.5 km s^{-1}.
†One sigma standard deviations; see Supporting Text S2 for details.

Table S1. Summary of hypervelocity impact experiments used in this study. All experiments were conducted at the NASA Ames Vertical Gun Range.

Table S2. Balance between target erosion and projectile delivery assuming 100% projectile retention at Ceres.

Impact Angle (°)	$(m_{ret}/m_{esc})_S$*	$(m_{ret}/m_{esc})_{HP}$†
Aluminum projectiles into snow		
90	2.8	10.7
60	3.3	12.7
45	4.3	16.3
30	6.5	24.6
Aluminum projectiles into perlite		
90	2.3	8.8
60	2.7	10.4
45	3.5	13.3
30	5.3	20.1
Basalt projectiles into snow		
60	3.3	12.8
45	4.3	16.3
30	6.6	24.7

*Calculated using constants appropriate for dry sand/cohesive soil ($\mu = 0.41$, $v = 0.4$, $C_2 = 0.018$) from *Holsapple and Housen* [2007].
†Calculated using constants appropriate for highly porous materials ($\mu = 0.4$, $v = 0.4$, $C_2 = 0.005$) from *Holsapple and Housen* [2007]. *Holsapple and Housen* [2007] note that ejecta scaling relationships for highly porous materials are still poorly understood.

Table S2. For the calculations summarized in this table, we have assumed a projectile retention efficiency of 1 (i.e., all the projectile remains on Ceres). This contrasts with the calculations summarized in Table 1 of the main text, which used the projectile retention efficiencies we measured in lab experiments. If the entire projectile remains on Ceres, then impacts could deliver as much as two to twenty five times more material than they erode.

Supplementary Figures

Figure S1. Ejecta curtain produced by the impact of an aluminum projectile into snow at 45°. The ejecta curtain is as expected for gravity-dominated excavation of a particulate target. The target bucket is 59 cm across.
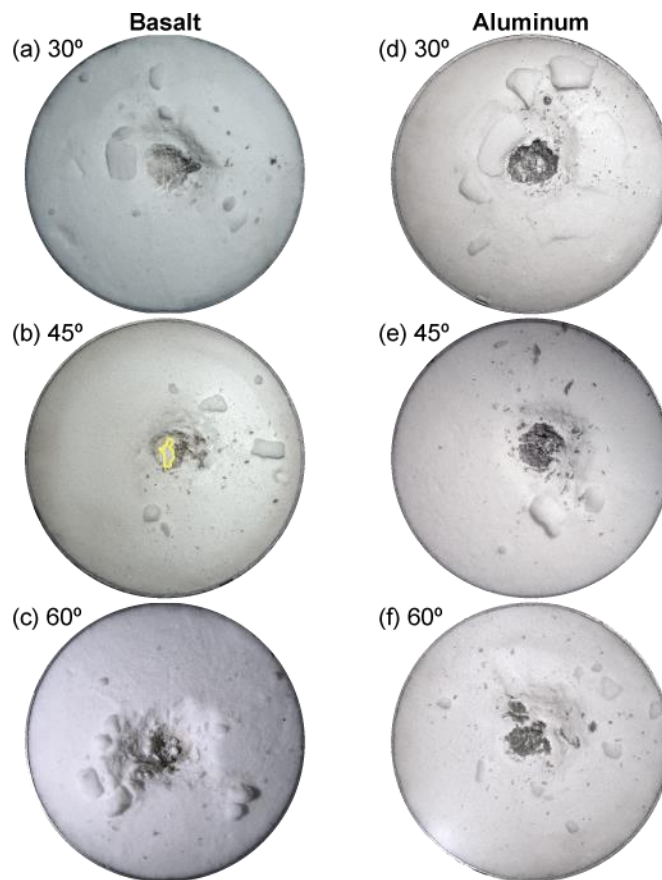
Figure S2. Post-impact images of craters formed by basalt (a–c) and aluminum (d–f) projectiles in snow targets at various impact angles. The dark areas on crater floors and walls are rich in projectile relics. For a given impact angle, craters formed by basalt and aluminum projectiles show similar distributions of projectile-laden snow. This is consistent with the interpretation that significant fractions of basalt projectiles were retained as extremely fine-grained fragments that were recovered from these experiments. The yellow outline in (b) marks an area where the crater wall collapsed, burying part of the projectile-laden snow from view.

Figure S3. Side-by-side comparisons of dark gray deposits recovered from the floors of craters formed by (a) basalt and (b) aluminum projectiles. The samples look quite similar at a given impact angle, despite being created by two different types of projectiles. Their coloration, in particular, is extremely similar, which indicates that fragments of both basalt and aluminum impactors remained on the crater floor within snow that melted and quenched. This further supports retention of large amounts of extremely fine-grained basalt fragments.
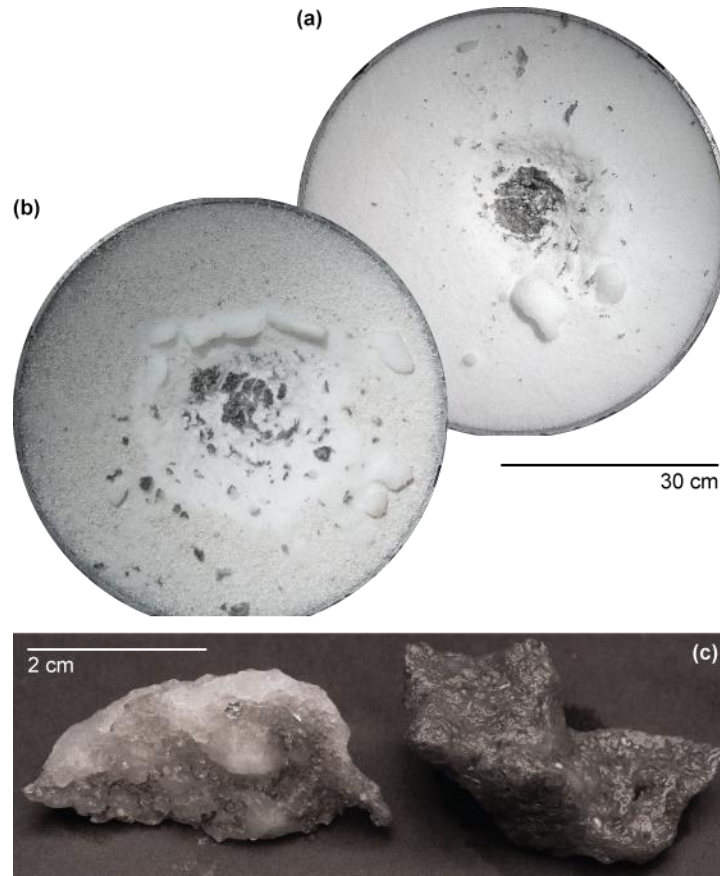
Figure S4. Craters and impact products generated by the ~4.5 km s^{-1} impact of aluminum projectiles in (a) snow and (b) perlite-veneered targets at an angle of 45°. The projectile component is distributed throughout the dark gray deposits visible inside and near the craters. (b) Samples of the dark gray deposits shown in (a). Such pieces consist of ice that melted and rapidly refroze, trapping the dispersed projectile relics. The piece on the left clearly shows a sharp contact between projectile-free white and projectile-laden dark gray ices.

Figure S5. Projectile relics recovered from the 90° impact of a 1/4" aluminum projectile into snow at 5.1 km s^{-1}.
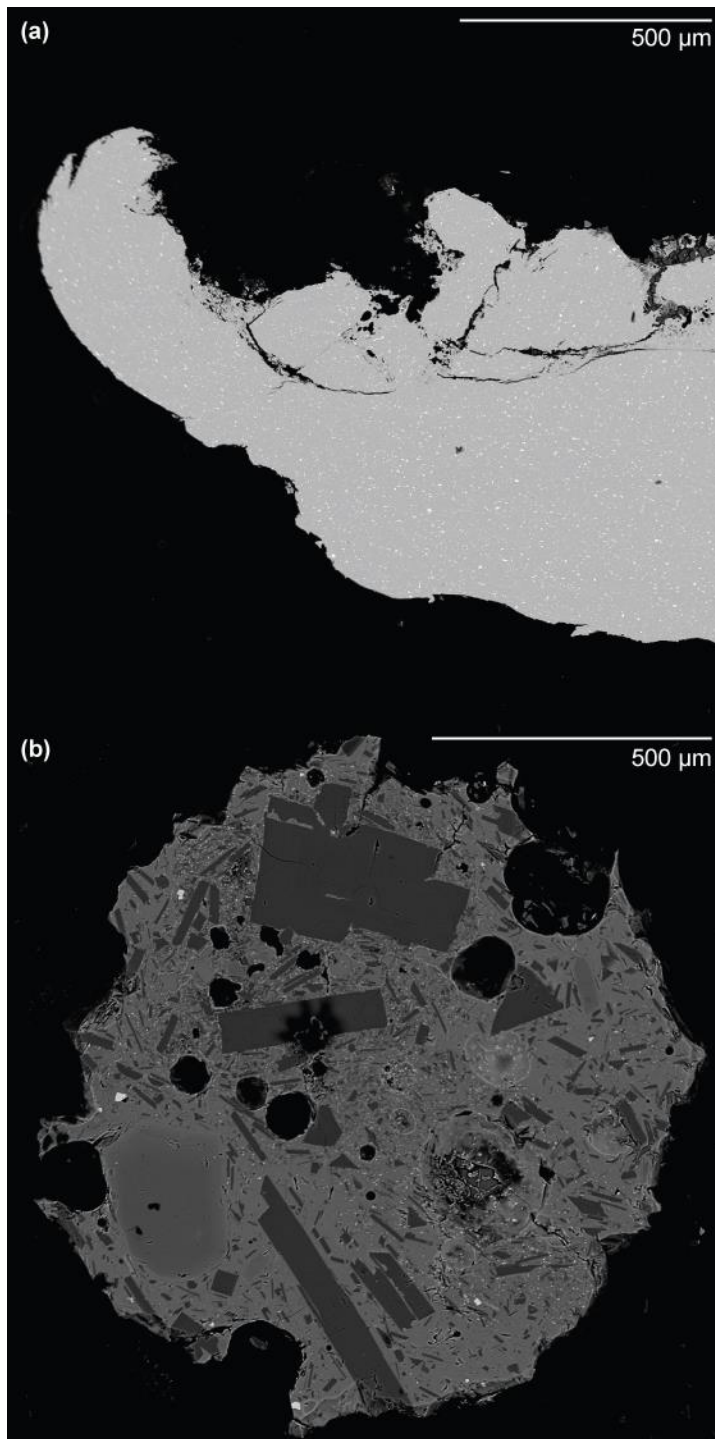
Figure S6. Projectile relics recovered from the impact of (a) aluminum and (b) basalt projectiles into snow targets. Both images are backscattered electron micrographs. The

interiors of the projectile relics did not melt. Bright spots in (a) are copper-rich regions within the aluminum alloy.
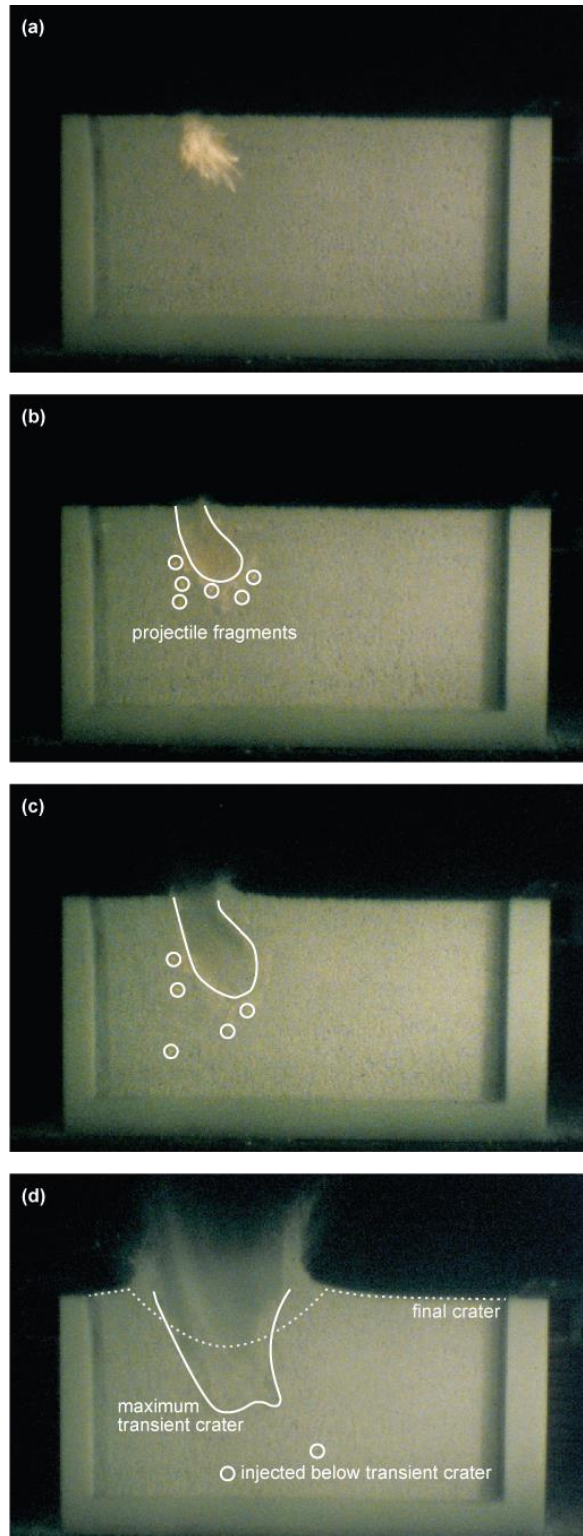
Figure S7. Quarterspace experiments reveal the dispersal of projectile fragments in perlite

targets. Panels (a) through (d) show the crater's evolution through time. (a) The projectile

fails very near the surface, injecting fragments of the projectile into the target. In panels (b) and (c), projectile fragments move ahead of the growing transient cavity. They are not involved in excavation flow. The transient crater reaches its maximum size in panel (d), with the final crater shown as a dashed line. By the time the transient crater reaches its maximum depth, several projectile fragments are already deep below the bottom of the transient crater. Although these fragments of the projectile were delivered to the target, they would not be expressed on the surface and could not have been recovered from the crater floor. In this experiment, a 0.318 cm diameter Pyrex projectile impacted a perlite target at a speed of 5.6 km s^{-1} and an angle of 60° with respect to horizontal.

References

Gault, D. E., E. M. Shoemaker and H. J. Moore (1963), Spray ejected from the lunar surface by meteoroid impact, *NASA technical note D-1767. 42 p.*

Hermalyn, B., P. H. Schultz, M. Shirley, K. Ennico and A. Colaprete (2012), Scouring the surface: Ejecta dynamics and the LCROSS impact event, *Icarus, 218(1)*, 654–665, doi:10.1016/j.icarus.2011.12.025.

Housen, K. R., R. M. Schmidt and K. A. Holsapple (1983), Crater ejecta scaling laws: Fundamental forms based on dimensional analysis, *J. Geophys. Res., 88(B3)*, 2485–2499, doi:10.1029/JB088iB03p02485.

Housen, K. R. and K. A. Holsapple (2011), Ejecta from impact craters, *Icarus, 211,* 856–875, doi:10.1016/j.icarus.2010.09.017.

Mitchell, D. L., S. J. Ostro, R. S. Hudson, K. D. Rosema, D. B. Campbell, R. Velez, J. F. Chandler, I. I. Shapiro, J. D. Giorgini and D. K. Yeomans (1996), Radar observations of asteroids 1 Ceres, 2 Pallas, and 4 Vesta, *Icarus, 124*, 113–133, doi:10.1006/icar.1996.0193.

Webster, W. J. Jr., K. J. Johnston, R. W. Harris, E. S. Lamphear, C. M. Wade, P. D. Lowman, Jr., G. H. Kaplan and P. K. Seidelmann (1988) The microwave spectrum of asteroid Ceres, *Astron. J., 95(4),* 1263–1268, doi: 10.1086/114722.

CHAPTER 2

Projectile preservation during oblique hypervelocity impacts

R. Terik Daly and Peter H. Schultz

Department of Earth, Environmental and Planetary Sciences

Brown University

Providence, RI USA

Abstract

Impact angle plays a significant role in determining the fate of the projectile. In this study, we use a suite of hypervelocity impact experiments to reveal how impact angle affects the preservation, distribution, and physical state of projectile residues in impact craters. Crater interiors preserve projectile residues in all cases, including conditions relevant to the asteroid and Kuiper belts. These residues consist of projectile fragments or projectile-rich glasses, depending on impact conditions. During oblique impacts at 30° and 45°, the uprange crater wall preserves crystalline fragments of the projectile. The fragments of water-rich projectiles such as serpentine remain hydrated. Enhanced preservation on the uprange wall results from many factors, including a weaker shock uprange, uprange acceleration as the shock reflects off the back of the projectile, and rapid quenching of melts along the projectile-target interface. These findings have three implications. First, the results suggest a new collection strategy for fly-by sample return missions. Second, these results predict that the M-type asteroid Psyche should bear exogenic impactor-derived debris. Third, these results constrain the likely impact conditions that led to the preservation of putative interstellar dust particles on the aluminum foil collectors of the Stardust spacecraft.

1. Introduction

NASA's Long Duration Exposure Facility (LDEF) spent 69 months orbiting Earth. During that time panels on the LDEF spacecraft acted as witness plates and recorded the near-Earth impact flux of micrometeorites and space debris. Over the course of the mission, the spacecraft accumulated thousands of micron- to millimeter-sized craters. Subsequent analyses revealed that a significant fraction of these craters preserved residues of the projectile: ~30% contained projectile-rich glasses [*Berthoud et al.*, 1995]. A few percent hosted intact projectile fragments [*Bunch et al.*, 1991]. Since the time of LDEF, impactor residues have also been observed in craters formed by micrometeoroids hitting the solar panels of the Hubble Space Telescope [*Kearsley et al.*, 2007].

In light of these findings, a number of studies used impact experiments to investigate how projectile residues can be preserved in these tiny craters (Table 1). Of these studies, only *Hill et al.* [1995] examined the effect of impact angle. However, results from both experiments [*Schultz and Gault*, 1990; *Schultz and Sugita*, 1997; *Daly and Schultz*, 2015, 2016] and shock physics code calculations [*Pierazzo and Melosh*, 2000; *Potter and Collins*, 2013; *Daly et al.*, 2015; *Syal et al.*, 2015] demonstrate that changes in impact angle can radically alter projectile fate. For example, *Schultz* [2012] noticed that relatively unaltered portions of the impactor were attached to the uprange wall following oblique impacts into metals and basalt, even at high angles. Most of the prior, detailed studies listed in Table 1 focused on only one or two impact variables (e.g., projectile type for *Burchell et al.,* 2008). This approach readily isolates the effects of individual impact variables.

However, it makes it difficult to assess how interactions between impact variables influence projectile preservation.

In this contribution, a new suite of hypervelocity impact experiments is reported that focuses on the effect of impact angle on the preservation of projectile residues within impact craters as a function of impact speed, projectile type, and target type. The emphasis is on characterizing the physical state of projectile residues (glassy vs. fragmental) and the distribution of projectile residues within the crater.

This study differs from previous experimental efforts in two key ways. First, the projectiles used here are significantly larger than those used in the studies listed in Table 1 and up to 300 times larger than those used by *Hill et al.* [1995]. Consequently, the craters are also much larger. This increased size makes it possible to accurately map the distribution of projectile residues within craters. In addition, the larger scale of these experiments tests how well the results from micron- to mm-scale craters can be applied to craters roughly an order of magnitude larger. Second, this study focuses on the interplay among four impact variables—impact angle, impact speed, projectile type, and target type—rather than focusing on only one or two of these variables. Under the conditions studied in these experiments, projectile preservation within craters is ubiquitous during oblique impacts.

2. Methods

Hypervelocity impact experiments at the NASA Ames Vertical Gun Range (AVGR) revealed how impact variables influence the preservation of projectile residues. Subsequent analyses with various analytical techniques revealed the nature of these residues. The next two sections detail both the impact experiments and subsequent analyses.

2.1. Hypervelocity impact experiments at the NASA Ames Vertical Gun Range

The AVGR consists of a large impact chamber and an A-frame on which two-stage light gas and powder guns can be mounted. The A-frame pivots about the impact chamber, which makes it possible to conduct experiments over a range of impact angles while keeping the target surface horizontal [*Gault and Wedekind*, 1978]. We systematically explored the effects of four impact variables: impact angle, impact speed, projectile type, and target type by (a) changing impact angle while keeping target type, projectile type and impact speed constant; (b) changing target type while keeping impact angle, projectile type, and impact speed constant; (c) changing target type while keeping impact angle, projectile type, and impact speed constant; and (d) changing impact speed while keeping impact angle, target type, and projectile type constant.

Table 2 provides the details for each experiment. Impact speeds ranged from 1.9 to 5.7 km s^{-1}, impact angle varied from 15° to 90° (with respect to horizontal), and a variety of materials were used as targets and projectiles. At speeds below 3.2 km s^{-1}, the projectiles were 12.7 mm in diameter. Experiments done at higher speeds used 6.35 mm

diameter projectiles. Both projectile sizes give comparable results for experiments done at the same speeds (Supplementary Figure S1). The targets and projectiles were selected to reveal how material properties, such as impedance, ductility, and crystallinity, influence projectile preservation. Table 3 highlights the range of impact conditions considered. The impact chamber was filled with ~1 torr of helium gas prior to each experiment. This slight atmosphere helped to prevent gases from the launch tube entering the impact chamber. An electronically-triggered flap covered the entry port immediately after the projectile entered the impact chamber, further reducing potential contamination from combustion products generated during launch.

2.2. Post-impact analysis

Three types of analyses were conducted. First, the morphology of the impact craters and projectile residues was documented by photographing the craters from a variety of perspectives over a range of magnifications. Second, chemical mixing between the target and projectile was investigated using electron microscopy. Third, crater interiors were searched for crystalline projectile fragments using visible to near-infrared spectroscopy.

Selected craters were cross-sectioned perpendicular to the projectile's trajectory in order to expose the uprange crater wall. The wall was then mapped using a LEO 1530 variable pressure scanning electron microscope (SEM) equipped with a Robinson backscatter detector and Oxford instruments electron dispersive spectroscopy (EDS) system. Other craters were cross-sectioned parallel to the projectile's trajectory. These cut

faces revealed the details of mixing along the projectile-target interface. The cut faces were polished, carbon-coated, and then studied with the Cameca SX 100 electron microprobe at Brown University. Qualitative EDS spectra were collected during analysis.

An ASD FieldSpec 3 spectroradiometer was used to acquire spectral data at visible-near infrared (VIS-NIR) wavelengths between 0.3 and 2.5 μm with 2 nm native spectral sampling that is resampled to 1 nm. Samples were illuminated with a QTH light source and a fiber optic bundle with a ~25° field of view; reflected radiance was collected with a similar fiber optic bundle. Sample spectra were converted to reflectance by ratioing data to spectra of a Spectralon panel acquired from Labsphere. Reflectance spectra from the samples were then corrected by multiplying the reflectance of the sample by the reflectance of the Spectralon panel at each wavelength. The size of the analyzed area was controlled by moving the end of the fiber optic toward or away from the sample (crater). All spectra reported here were collected while the area of interest was being illuminated from the opposite direction (e.g., spectra acquired from the uprange crater wall were illuminated by a light source positioned downrange of the crater).

3. Results

3.1. Projectile preservation

The following sections describe how impact speed, impact angle, projectile type, and target type influence projectile preservation. The results demonstrate that the craters

formed during these experiments preserve both solid, shocked fragments of the projectile and projectile-rich glasses.

3.1.1. Impact speed effects

The spatial distribution and physical state of projectile residues evolve with impact speed (Figure 1). This evolution involves three facies: a white fragmental facies, a dusty reddish-brown facies, and a red vitreous facies. The white fragmental facies and red vitreous facies are both remnants of the projectile. Each facies will be discussed in turn.

3.1.1.1. Spatial distribution of facies as a function of impact speed

The white fragmental facies appears at all impact speeds. At 1.9 and 2.3 km s^{-1}, the white fragmental facies coats substantial portions of the uprange crater wall and crater floor (Fig. 1A and 1B). In some regions this white material is fixed firmly to the crater wall. In other locations, the white fragmental material falls off easily. As impact speed increases to 3.1 and then 4.0 km s^{-1}, the white fragmental unit becomes less extensive and moves farther up the uprange crater wall (Fig. 1C and 1D). At 4.0 km s^{-1}, a patch of the dusty reddish-brown facies divides the white fragmental facies into two arcuate areas. The curvature of these areas mirrors the shape of the uprange rim (visible in the top of panel 1D). As impact speed increases to 5.0 and then 5.7 km s^{-1}, the extent of the white fragmental facies continues to shrink (Figs. 1E and 1F). However, a small, arcuate patch of the white

fragmental facies persists on the uprange crater wall. This facies is comprised of shocked, comminuted fragments of the Pyrex projectile (see section 3.1.1.2).

The dusty reddish-brown facies appears only at speeds below 5.7 km s^{-1}. At 1.9 and 2.3 km s^{-1}, the dusty reddish-brown facies appears as patches high on the uprange crater wall. These patches extend to the uprange crater rim (Figs. 1A and 1B). At 3.1 km s^{-1}, the reddish-brown facies terminates just short of the uprange crater rim (Fig. 1C). The extent of this dusty reddish-brown facies decreases beginning at 4.0 km s^{-1} (Fig. 1D and 1E). At 4.0 km s^{-1} a lobe of the dusty reddish-brown facies extends down onto the crater floor. The dusty reddish-brown facies is entirely absent at 5.7 km s^{-1} (Fig. 1F). This facies is likely composed of copper oxide. The reddish color is more consistent with Cu_2O than with CuO; the former is red while the latter is black.

The red vitreous facies first appears at 4.0 km s^{-1}, and its extent increases with impact speed (Figs 1D – 1F). In contrast with the dull luster and powdery texture of the reddish-brown facies, the red vitreous facies has a high shine and ropy texture. At 5.7 km s^{-1} this facies surrounds the white fragmental facies preserved on the uprange crater wall. The red vitreous facies coats the entire crater floor, lateral walls, and extends partially onto the downrange wall. The ropy texture of this material indicates that this bright red unit was molten when emplaced. This facies is composed of projectile-rich glass (see section 3.1.1.2).

3.1.1.2.Physical state of projectile residues

Both the white fragmental facies and the red vitreous facies represent projectile residues. The white fragmental facies is made up of solid, unmelted fragments of the projectile. In contrast, the red vitreous facies formed when the projectile melted, mixed with the copper target, and then quenched. Below 4.0 km s^{-1}, projectile residues consist almost entirely of unmelted, comminuted fragments of the projectile. Above 4.0 km s^{-1}, projectile-rich glasses account for increasing amounts of the preserved projectile residues.

Optical and scanning electron microscopy provide additional insights into the nature of the white fragmental material. Figure 2 shows optical and backscattered electron micrographs of white fragmental material scraped from the uprange walls of the craters shown in Figures 1A and 1C. These pieces have two sides. The side facing into the crater is white and fragmental, while the side closest to the crater wall is coated with a veneer of red glass. Hence, a thin layer of red glass lies between the copper crater wall and the white fragmental facies. EDS data confirm that the white material is Pyrex; the bright fleck at the bottom left of Figure 2C is a piece of the copper target. The SEM image shows that the white fragmental material has a clastic texture, which provides further evidence that this material did not melt.

In addition, both optical and scanning electron microscopy confirm that the red vitreous facies is composed of projectile-rich glasses. Figure 3 shows optical and backscattered electron micrographs of red vitreous material scraped from the uprange wall of the craters in Figures 1D and 1F. The textures are consistent with material that melted and quenched, in contrast to the fragmental textures seen in Figure 2. The glasses are

heterogeneous, as evidenced by the color variations in Figure 3B. SEM/EDS data show that glasses are primarily silicate, with varying amounts of copper. Copper is present in two forms: as copper dissolved in the silicate glass and as copper metal. Blebs of copper metal up to ~10 μm across pervade the glass. Hence, the impact-generated glasses are mixtures of the copper target and Pyrex projectile. Red bands contain more copper than clear and colorless zones. The glass is vesiculated down to the scale of a few microns. Unmelted, fragmental Pyrex is not observed in any of these impact-generated glasses.

3.1.2. *Impact angle effects*

The location and physical state of projectile residues evolves with impact angle (Fig. 4). These residues can be grouped into three facies: a white fragmental facies, a red vitreous facies, and a clear vitreous facies. Figure 4 maps the locations of these facies. Section 3.1.1 described the white fragmental and red vitreous facies. In summary, these facies are composed of unmelted fragments of the projectile and impact-generated, projectile-rich glasses, respectively. The clear vitreous facies consists of impact-generated glasses that are almost pure projectile, in contrast to the glasses of the red vitreous facies that incorporated significant amounts of copper.

The white fragmental facies occurs only at 30° and 45° (Fig. 4B and 4C). Hence, at 5 km s^{-1}, solid, unmelted fragments of Pyrex projectiles are preserved only at 30° and 45°. At both angles, the facies occurs on the uprange crater wall. However, at 45° the fragments are finer and thinner than at 30°. Hence, the area outlined in white in Fig. 4B

appears whiter than the area in Fig. 4C. Although difficult to see in this top-down view of the craters, the white fragmental facies extends farther down the uprange crater wall at 45° than at 30°.

The red vitreous facies occurs at 75° and below (Fig. 4A – 4E). Both the extent and distribution of this facies change with image angle. At 15° the red vitreous facies lines the uprange wall, side-walls, and much of the crater floor. The red vitreous facies coats irregular pits on the uprange and central portions of the crater floor. However, as the crater floor slopes upward downrange, this red glassy lining disappears. At 30° the red vitreous facies is nearly contiguous on the uprange crater wall, but becomes patchy on the crater floor and downrange. At 45° this facies is nearly absent from the uprange crater wall. Instead, it is most extensive on the floor and downrange crater wall. At 60° the red vitreous facies covers much of the crater floor, side-walls, and downrange wall, although patches of bare copper (outlined in black) exist on the crater floor. At 75°, the red vitreous facies forms an annulus just below the crater rim.

The clear vitreous facies occurs only at 75° and 90° (Fig. 4E and 4F). At 75° the clear vitreous facies covers the crater floor and lower portion of the crater walls. In general, the facies terminates below an annulus of the red vitreous facies near the top of the crater walls. However, a narrow tongue of the clear vitreous facies extends downrange beyond the red vitreous annulus. At 90° the clear vitreous facies extends up the crater wall in all directions. No other facies are present within the crater at 90°.

3.1.3. Projectile type effects

All types of projectiles were preserved within craters. The residues are a combination of surviving projectile fragments and projectile-rich glasses. The uprange wall preserved unmelted fragments, in addition to projectile-rich, impact generated glasses. The crater floor and side-walls also preserve projectile residues, but to a lesser degree than the uprange wall. The downrange wall is least likely to preserve portions of the projectile. In this section, we present results from experiments with aluminum, quartz, basalt, and serpentine projectiles.

Residues of the aluminum projectile coated the crater with a thin aluminum liner (Figure 5). The liner is only a few to several tens of microns thick where it terminates on the crater rim. Lineations within the aluminum align with the excavation flow field, particularly downrange. In addition, radial wisps of aluminum extend beyond the contact between aluminum and copper on the crater rim (Fig. 5B). These textures indicate that the aluminum that reached the crater rim was molten when emplaced.

Residues left by quartz projectiles share many similarities with those left by Pyrex (Fig. 6). A white, fragmental facies composed of unmelted quartz fragments lies on the uprange wall (Fig. 6A). Compared to Pyrex projectiles at the same angle and speed (Fig. 1E), this fragmental facies is more widespread for quartz. Such observation may indicate that quartz projectiles preserve more of their mass as fragments compared to the Pyrex projectiles. Melting quartz requires far more energy than bringing Pyrex to its working point (1999 J g^{-1} vs. 924 J g^{-1}); this difference may explain the apparent enhancement in fragmental residues from quartz projectiles. Three other facies exist

elsewhere in craters formed by quartz projectiles (Fig. 6B). These include a red vitreous facies, a dark brown facies, and a white vitreous facies. These share many similarities with the red vitreous facies, dusty reddish-brown facies, and clear vitreous facies discussed in sections 3.1.1 and 3.1.2. The red vitreous and white vitreous facies intermingle and usually lie directly on bare copper, although in some places they sit atop the dark brown facies. Given the similarity of these two facies to the red vitreous and clear vitreous facies seen in craters formed by Pyrex, these two facies are inferred to be projectile-rich, impact-generated glasses that incorporated varying amounts of copper. These glasses occasionally trap quartz fragments.

Basalt projectiles also left residues. The crater formed by basalt contained three facies: a frothy greenish-gray facies, a dusty reddish-brown facies, and an orange vitreous facies. The frothy greenish-gray facies is abundant on the uprange wall (Fig. 7A). Microscopy reveals that this facies is a mixture of basalt fragments and vesicular glass. The lower impact speed (see Table 2) of this experiment partially explains why this fragment-rich facies is so abundant. The dusty reddish-brown facies fills in much of the area between the frothy greenish-gray facies. The orange vitreous facies is visible only at higher magnification (Fig. 7B). Except for color (orange vs. red), this facies is similar to the red vitreous facies described in other craters. Hence, this facies likely represents projectile-rich, impact-generated glass. Images at higher magnification further clarify the relationships among these facies. The dusty reddish-brown facies rests on top of bare copper. The vitreous orange facies lies on top of the dusty reddish-brown facies, and the frothy greenish-gray facies rests on top of that (Fig. 7C).

The residues left by serpentine projectiles share many similarities with those left by basalt projectiles (Fig. 8), with a powdery light gray facies at the top and base of the uprange wall. This facies resembles the frothy greenish-gray facies left by the basalt projectile. Close inspection reveals that the powdery light gray facies is a mixture of fragmental and glassy material (Fig. 8B). A dusty reddish-brown facies is also present. On the uprange wall the dusty reddish-brown facies lies on top of bare copper. The light gray facies lies on top of the dusty reddish-brown facies (Fig. 8C).

3.1.4.   Target effects

Projectile residues remained in both aluminum and copper targets but were more abundant in copper targets. Craters formed in aluminum targets exhibit only two facies, in contrast to the three facies seen in copper. The first and most widespread facies in aluminum targets consists of web-like arrays of a translucent, vesicular, vitreous material that drapes crater interiors (Figure 9). These cobweb-like stringers trap a second facies of dark-colored fragmental and glassy materials. This second facies is outlined in white in Figure 9. This facies is most common on the uprange crater wall. In the crater formed by basalt, concentric web-like stringers of translucent glass surround a central zone of the dark facies on the uprange wall (Figure 9B). In addition, a second set of stringers (traced with blue) spokes radially outward from the central zone. Additional deposits of the light-colored, translucent glass are spread patchily across the floors and downrange walls of both craters.

SEM/EDS analyses reveal the nature of the dark facies (Figure 10). Ropy, stringer-like textures occur within the aluminum-rich zone (blue in the Fig. 10B) and are attached to a substrate of unmelted aluminum. The image contains two other facies: frothy, angular, fragmental material and smooth, bulbous material. The yellow color of the pixels associated with these facies indicates that these materials are high in silicon and oxygen. The two facies are therefore likely projectile fragments and projectile-rich melts, respectively. They overlap and intermingle, which provides further evidence that quenched melts cement fragments of the projectile to the uprange wall. Some pixels in the fragmental material have a light magenta hue, thereby indicating that some of the frothy fragmental material contains aluminum oxide, in addition to basalt fragments. Taken together, these observations indicate that the dark facies is a combination of projectile fragments, projectile-rich glasses, and aluminum oxide.

3.2. Visible to near-infrared spectra

Optical micrographs and SEM/EDS data indicate that the uprange wall preserves solid, unmelted fragments of the projectile. Reflectance spectra confirm this inference: relics on the uprange wall retain spectral features that are diagnostic of the different projectile materials.

Spectra were collected from multiple locations in craters formed by basalt and serpentine projectiles. In basalt pyroxene is the dominant spectrally-active mineral at VIS-NIR wavelengths. Reflectance spectra of pyroxene exhibit broad crystal field (*d-d* transition) absorptions centered near 1 and 2 μm caused by Fe^{2+} in octahedral coordination

[*Burns,* 1993; *Clark*, 1999]. In contrast, spectra of serpentine exhibit diagnostic narrow vibrational absorptions near ~1.4, ~2.1, and ~2.32 μm caused by combination and overtone vibrations of OH and Mg-OH bonds [*Calvin and King,* 1997 and references therein]. In this wavelength range copper is spectrally bland and its spectrum does not contain diagnostic absorption features. The aluminum targets, however, present challenges. Their surfaces are lightly grooved; the crater floors are rough and scalloped. Both attributes introduce strong specular and multiple scattering effects; spectra corresponding to the grooved surfaces exhibit a very strong negative spectral slope.

The spectra confirm the presence of relic serpentine on the uprange wall of craters formed in both copper and aluminum (Fig. 11). Spectral features consistent with basalt were detected in copper crater but not in the aluminum target. However, aluminum targets have an absorption feature centered at ~0.85 μm that partially overlaps the 1 μm pyroxene feature seen in spectra of the basalt projectile material (see Fig. 11). This might mask the presence of small amounts of relic basalt on the uprange wall. However, evidence for the presence of the broad ~2 µm features is also absent in the uprange spectrum. Spectra were also acquired from other locations within the craters to assess distribution of potential projectile material and melt products. Figure 12 summarizes detections of projectile fragments from VNIR reflectance data. Supplementary Figures S2 – S6 present the spectra that form the basis for Figure 12.

3.3. Projectile-target interface

Cross sections through craters cut parallel to the projectile trajectory revealed clear differences between the projectile-target interface on the uprange and downrange crater walls (Fig. 13). Prior to sectioning, the crater looked very similar to the example in Figure 1F. The copper target appears bright in these backscattered electron micrographs, whereas the Pyrex-rich glass lining the crater wall is darker. In cross-section, the silicate liner is contiguous along the uprange wall. The downrange wall exhibits only occasional patches of silicates (note the difference in scale in the insets of Figures 13A and 13B).

In cross-section, the red vitreous facies on the uprange wall consists of a matrix of impact-generated glass with inclusions of copper that range from tens of microns to possibly submicron in size, an observation consistent with the SEM micrograph in Figure 3C. The liner is only a few tens of microns thick with copper inclusions having a variety of forms. Round forms indicate that they were likely molten, whereas angular forms indicate unmelted fragments. Some of the copper inclusions (e.g., the largest inclusion in Figure 13A) may have rolled during crater formation, indicative of rapidly quenched shear.

The uprange wall highlights the importance of rapidly quenched, impact-generated melts (Figure 14). In Figs. 14A and 14D, the silicate liner contains a "mitten" and "flake" of copper, respectively, on the uprange crater wall. If the melt had quenched more slowly, then the mitten and flake would likely have been removed by flow during formation. The silicate glass between the crater wall and mitten and between the crater wall and flake is extremely heterogeneous. However, Figure 14B contains pieces of glass with sharp, angular margins. EDS spectra indicate that these pieces are pure Pyrex glass (Fig. 14C).

69

Based on composition and morphology, these are likely unmelted fragments of the Pyrex projectile embedded within the interaction zone along the projectile-target interface. Hence, unmelted projectile survivors are likely buried within the red vitreous facies on the uprange wall. These fragments, though invisible on the surface of the red vitreous facies, represent additional Pyrex fragments beyond those exposed in the arcuate, white areas on the uprange wall (e.g., Fig. 1F). In contrast, EDS data from other locations in the interaction zone contain a strong copper peak (Fig. 14F). Hence, the impact-generated glass in this region can contain copper dissolved in the silicate glass, tiny blebs of metallic copper, or a mixture of both types.

4. Discussion

4.1. Differences between projectile types

Projectile residues were observed in all craters. With the possible exception of the aluminum projectile, craters preserved both unmelted projectile fragments and impact-generated, projectile-rich glasses. Identification of these residues across a broad range of speeds, impact energies, and density ratios (Tables 2 and 3) emphasizes that preservation of all projectile types is the norm, rather than the exception, under these conditions. This finding echoes that of *Daly and Schultz* [2015, 2016], who showed that basalt and aluminum projectiles are both preserved in porous granular targets at impact speeds between 4.5 and 5 km s^{-1}.

4.2. Differences between copper and aluminum targets

Aluminum targets retain fewer projectile residues than do copper targets under identical conditions. The impedance (density times the sound speed) of aluminum is less than half that of copper (Table 5) and comparable to the impedance of basalt [*Schultz and Gault,* 1990]. Hence, all other impact variables equal, less energy is partitioned into the projectile during impacts into aluminum because of the reduced projectile-target impedance contrast. This should favor projectile survival. If impedance contrast were the only controlling variable, then aluminum targets should preserve more abundant residues—the opposite to observations.

Prior experiments for vertical impacts yielded results that would be expected given the difference in impedance contrast: *Berthoud et al.* [1995] and *Hörz et al.* [1983] launched soda lime glass spheres at ~5.5 to 6 km s^{-1} at 90º into 6061-T6 aluminum and copper, respectively. As expected given the impedance difference, *Berthoud et al.* [1995] observed fragments of the projectile within their craters, whereas *Hörz et al.* [1983] reported only projectile-derived, impact-generated glasses. In vertical impact experiments such as these, projectile residues are driven downward and stay within the crater [e.g., *Schultz and Gault*, 1990; *Daly and Schultz*, 2015]. Such experiments also demonstrate that during oblique impacts the residual projectile momentum carries projectile fragments and other residues downrange. Thus, trapping those residues becomes crucial.

Interpreting the dearth of projectile residues in aluminum craters during oblique impacts requires an understanding of the trapping process. Textures indicate that melting followed by rapid quenching plays a key role in retaining projectile fragments (Figs. 2, 3,

71

9, 10, 13, and 14). Therefore, differences in melt production may control projectile preservation. Aluminum has a higher heat capacity than copper (Table 5). It takes an additional 129 J g^{-1} to raise a gram of 6061 aluminum to its *solidus* temperature than it takes to raise a gram of copper to its *melting* point. Furthermore, the enthalpy of fusion for 6061 aluminum is nearly twice that of copper (see Table 5). Hence, it takes significantly less energy to melt a gram of copper than it does to melt a gram of aluminum. In addition, 6061 aluminum has a lower fracture toughness than copper (Table 5). Fragmentation likely therefore consumes more of the energy budget in during crater formation in aluminum targets than in the copper ones. Therefore, impacts into copper should generate a greater mass of target-derived melt. The higher impedance of the copper targets also enhances projectile melting. As the melt rapidly quenches, it traps surviving projectile fragments along the crater wall. At larger spatial scales, cold clasts may assist rapid quenching.

4.3. Significance of the uprange wall

Solid, unmelted fragments are more likely to be found on the uprange crater wall than anywhere else. Furthermore at 30 and 45° solid fragments of the projectile consistently remained on the uprange crater wall.

Multiple factors contribute to enhanced projectile preservation on the uprange wall. These include a weaker shock directed uprange [*Dahl and Schultz,* 2001] and reduced peak pressures in the back of the projectile [*Schultz and Gault,* 1990; *Pierazzo and Melosh,* 2000; *Potter and Collins,* 2013]. Such conditions favor survival of fragments derived from

this region, provided that they can be captured [*Schultz and Gault*, 1990; *Schultz and Sugita,* 1997; *Pierazzo and Melosh*, 2000; *Schultz and Eberhardy,* 2015]. Once the shock reflects off the back of the projectile, it decelerates during penetration, thereby increasing the chance of capture. The arcuate distribution of many fragmental facies on the uprange wall appear to reflect the curvature of the projectile and may represent part of the back of the projectile, glued in-place by rapidly quenched melts. Recent shock physics code calculations by *Schultz and Crawford* [2014] and *Canup et al.* [2017] indicate that the uprange portion of the projectile is more likely to survive intact. Consequently, asymmetries in projectile preservation observed in experiments may extend to much larger scales as well.

5. Implications

The findings presented here have three broader implications. First, they provide a basis for a new sample capture strategy for fly-by missions. Second, the results predict impactor contamination on M-type asteroids such as Psyche, the target of a recently-selected Discovery-class mission of the same name. Third, the results help to constrain the impact conditions that led to the preservation of putative interstellar dust particle residues [*Westphal et al.,* 2014] on aluminum foil collectors during the Stardust mission.

5.1. Sample return missions

The cometary samples returned by Stardust provide a treasure trove of information [*Brownlee et al.*, 2006; *Sandford et al.*, 2006; *Zolensky et al.*, 2006]. However, the particles were thermally altered during capture, and this alteration reduced the scientific information that can be extracted from them [*Roskosz et al.*, 2008; *Leroux et al.,* 2012]. Sample return missions have recently been proposed that rely on a similar flyby sample collection strategy. One example is the LIFE mission, which plans to return samples from Enceladus by flying through the moon's plumes [*Tsou et al.*, 2012]. The scientific value of these samples will be maximized by preserving as much of their pristine character as possible.

The experiments reported here suggest that devices designed to encounter particles at 30° could have a significant advantage compared to head-on capture geometries. In a head-on (90°) impact, the impacting particles are more likely to melt. At 30°, however, lightly-shocked, relatively pristine material would be preserved on the uprange crater wall at impact speeds less than 6 km s^{-1}. Such an approach may reduce the shock metamorphic and thermal effects associated with sample collection, thereby increasing the science return from such a mission.

5.2. Impactor components on M-type asteroids such as Psyche

The Dawn spacecraft detected deposits of dark material on Vesta that have been interpreted to be the remnants of dark, carbonaceous chondrite-like impactors [*Prettyman et al.,* 2012; *McCord et al.,* 2012; *Reddy et al.,* 2012; *De Sanctis et al.,* 2012]. Experiments

74

[*Daly et al.,* 2016] and numerical models [*Turrini et al.,* 2014; *Daly et al.,* 2015] support this hypothesis. Impactor contamination should be common among main-belt asteroids because of the modest impact speeds in the main belt [*Daly and Schultz,* 2015, 2016]. The meteorite collection supports this argument: several parent bodies accumulated exogenic debris that likely represents pieces of surviving impactors [*Goodrich et al.,* 2015; *Rubin and Bottke,* 2009].

Target properties, however, strongly influence projectile delivery, retention, and preservation [*Daly and Schultz,* 2015, 2016]. M-type asteroids, like Psyche, are very different from Vesta: metal dominates them rather than rock. Psyche is composed of nickel-iron metal, with limited deposits of orthopyroxene [*Hardersen et al.,* 2005]. Hence, the ductile metal targets examined in this study are highly relevant to Psyche. The impact speeds used here are comparable to typical main belt impact speeds [*Obrien and Sykes,* 2011]. Hence, impacts at Psyche should deposit significant quantities of exogenic debris. Depending on the degree of projectile preservation, the silicates present on the surface of Psyche today [*Hardersen et al.,* 2005] could have been delivered to Psyche, rather than inherited from the remnants of the lower mantle of Psyche's parent body. Furthermore, these experiments, which show that serpentine impactors retain OH-related near-infrared absorptions, support the hypothesis that the OH detected on Psyche by *Takir et al.* [2017] may be exogenic.

5.3. Impact conditions of interstellar dust particle candidates

Westphal et al. [2014] reported the discovery of seven unusual dust particle impacts on the Stardust Interstellar Dust Collector (SIDC). Four of these particles impacted into aluminum. The diameters of these four craters ranged from 0.28 to 0.46 μm [*Westphal et al.,* 2014]. Figures 4 and S6 of *Westphal et al.* [2014] show the distribution of Mg, Si, Fe, O, and S in the craters. *Westphal et al.* [2014] infer that areas rich in these elements are particle residues left by magnesium-rich silicates, iron-rich sulfides, and possibly iron metal. The compositions of particle residues and inferred particle trajectories implicate an interstellar origin [*Westphal et al.,* 2014].

The craters formed by these particles are much smaller than the cm-scale craters examined in the present study. However, asymmetries in projectile from oblique impacts should persist at smaller scales because of the fundamental asymmetries of oblique impacts. Although *Westphal et al.* [2014] did not discuss asymmetries in particle residues, Figures 4 and S6 indicate that elements are distributed asymmetrically. Such an observation is consistent with an oblique impact. Unfortunately, there is no way to know *a priori* whether these craters were sectioned parallel to the projectile trajectory (which would reveal uprange-downrange asymmetries), perpendicular to the trajectory, or at some other angle relative to the trajectory. The random direction of impact, however, would have resulted in a distribution of impact angles represented in the collector plate. If the craters happened to be sectioned sub-parallel to the trajectory, then the distribution of elements indicates that the particle that formed crater 1061N,3 might have consisted of a Mg-rich

silicate core surrounded by a Fe-S rim. The particle that formed 1044N,3 may have been composed of zoned Mg-rich silicates.

Westphal et al. [2014] noted: "the residues of the particles captured in the Al foil appear to be amorphous, but whether this is an original feature or an effect of hypervelocity capture alteration is unclear." In experiments, unmelted projectile fragments remained on the uprange wall at all impact speeds studied (up to 5.7 km s^{-1}). Models of the particle flux indicate that the speed of particles impacting the SIDC was likely <10 km s^{-1} [*Sterken et al.,* 2014; *Westphal et al.,* 2014]. Hence, the impact speeds of these four particles could have been comparable to the speed of experiments reported here. If impact speeds were less than ~6 km s^{-1} and the impacts were oblique, then the amorphous nature of these four particles would be likely primary, rather than a consequence of impact. If correct, this interpretation would imply that interstellar dust similar to the size of the particles that formed these craters (~0.2 to 0.3 μm [*Westphal et al.,* 2014]) is largely amorphous, consistent with models for the interstellar medium by *Kemper et al.* [2004, 2005].

6. Acknowledgements

7. References

Ashby, M. (2005), *Materials Selection in Mechanical Design*, Elsevier Butterworth-Heinemann.

Berthoud, L., J.-C. Mandeville, C. Durin, and J. Borg (1995), Debris and meteoroid proportions deduced from impact crater residue analysis, *LDEF: 69 Months in Space. Third Post-Retrieval Symposium, Part 1,* 431–444.

Brownlee, D. et al. (2006), Comet 81P/Wild 2 Under a Microscope, *Science*, 314, 1711, doi:10.1126/science.1135840.

Bunch, T. E., F. Radicati di Brozolo, R. H. Fleming, D. W. Harris, D. Brownlee, and T. W. Reilly (1991), *LDEF: 69 Months in Space. First Post-Retrieval Symposium, Part 1,* 549–564.

Bunch, T. E., L. Becker, J. Bada, J. Macklin, F. Radicati di Brozolo, R. H. Fleming, and J. Erlichman (1993), Hypervelocity impact survivability experiments for carbonaceous impactors, *LDEF: 69 Months in Space. Second Post-Retrieval Symposium, Part 2,* 453–477.

Burchell, M. J., N. J. Foster, A. T. Kearsley, and J. A. Creighton (2008), Identification of mineral impactors in hypervelocity impact craters in aluminum by Raman spectroscopy of residues, *Meteorit. Planet. Sci.,* 43, 135–142, doi:10.1111/j.1945-5100.2008.tb00614.x.

Burns, R.G. (1993), *Mineralogical Applications of Crystal Field Theory,* Cambridge University Press, 551 p.

Calvin, W. M. and T.V. King (1997), Spectral characteristics of iron-bearing phyllosilicates: Comparison to Orgueil (CI1), Murchison, and Murray (CM2), *Meteorit. Planet. Sci.,* 32, 693–701, doi:10.1111/j.1945-5100.1997.tb01554.x.

Canup, R. M., S. Marchi, and R. J. Walker (2017), The fate of impactor cores in large terrestrial collisions, *Lunar and Planetary Science Conference XLVIII,* abstract no. 1640.

Clark, R. N. (1999) *Spectroscopy of rocks and minerals, and principles of spectroscopy,* USGS.

Dahl, J. M., and P. H. Schultz (2001), Measurement of stress wave asymmetries in hypervelocity projectile impact experiments, *Int. J. Imp. Eng., 26,* 145-155.

Daly, R. T., and P. H. Schultz (2015), Predictions for impactor contamination on Ceres based on hypervelocity impact experiments, *Geophys. Res. Lett.,* 42, 7890–7898, doi:10.1002/2015GL065601.

Daly, R. T., and P. H. Schultz (2016), Delivering a projectile component to the vestan regolith, *Icarus,* 264, 9–19, doi:10.1016/j.icarus.2015.08.034.

Daly, R. T., M. Bruck Syal, and P. H. Schultz (2015), Experiments and Numerical Models Provide Complementary Information about Projectile Survival and Delivery,

Bridging the Gap III: Impact cratering in nature, experiments, and modeling, abstract no. 1080.

De Sanctis, M. C., et al. (2012), Detection of Widespread Hydrated Materials on Vesta by the VIR Imaging Spectrometer on board the Dawn Mission, *Astrophys. J. Lett.,* 758, L36, 5 pp.

Gault, D. E., and J. A. Wedekind (1978), Experimental studies of oblique impact, *Proceedings of the 9th Lunar and Planetary Science Conference,* 374–376.

Goodrich, C. A., W. K. Hartmann, D. P. O'Brien, S. J. Weidenschilling, L. Wilson, P. Michel and M. Jutzi (2015), Origin and history of ureilitic material in the solar system: The view from asteroid 2008 TC$_3$ and the Almahatta Sitta meteorite, *Met. Planet. Sci., 50(4),* 782–809, doi:10.1111/maps.12401.

Hardersen, P.S., M. J. Gaffey, P. A. Abell (2005), Near-IR spectral evidence for the presence of iron-poor orthopyroxenes on the surfaces of six M-type asteroids, *Icarus,* 175, 141–158.

Hill, D. C., M. F. Rose, S. R. Best, M. S. Crumpler, G. D. Crawford, R. H.-C. Zee, and M. J. Bozack (1995), The effect of impact angle on craters formed by hypervelocity particles, *LDEF: 69 Months in Space. Third Post-Retrieval Symposium, Part 1,* 483–498.

Hörz, F., H. Fechtig, J. Janicke, and E. Schneider (1983), Morphology and chemistry of projectile residue in small experimental impact craters, *J. Geophys. Res., 88,* S01, B353–B363, doi:10.1029/JB088iS01p0B353.

Kearsley, A. T., G. A. Graham, J. A. M. McDonnell, E. A. Taylor, G. Drolshagen, R. J. Chater, D. McPhail, and M. J. Burchell (2007), The chemical composition of micrometeoroids impacting upon the solar arrays of the Hubble Space Telescope, *Adv. Space Res.,* 39, 590–604, doi:10.1016/j.asr.2006.05.011.

Kemper, F., W.J. Vriend, and A.G.G.M. Tielens (2004), The Absence of Crystalline Silicates in the Diffuse Interstellar Medium, *Astrophys. J.,* 609, 826–837.

Kemper, F., W.J. Vriend, and A.G.G.M. Tielens (2005), Erratum: The Absence of Crystalline Silicates in the Diffuse Interstellar Medium, *Astrophys. J.,* 633, 534.

Kubaschewski, O., C. B. Alcock, and P. J. Spencer (1993), *Materials thermochemistry,* 6th ed., Pergamon, Oxford.

Leroux, H. (2012), Fine-grained material of 81P/Wild 2 in interaction with the Stardust aerogel, *Meteorit. Planet. Sci.,* 27, 612–622, doi:10.1111/j.1945-5100.2011.01309.x.

McCord, T. B. et al. (2012), Dark material on Vesta from the infall of carbonaceous volatile-rich material, *Nature, 491,* 83–86, doi:10.1038/nature11561.

O'Brien, D. P. and M. V. Sykes (2011), The origin and evolution of the asteroid belt—Implications for Vesta and Ceres, *Space Sci. Rev., 163,* 41–61, doi:10.1007/s11214-011-9808-6.

Pierazzo, E., and H. J. Melosh (2000), Hydrocode modeling of oblique impacts: The fate of the projectile, *Meteorit. Planet. Sci.,* 35, 117–130, doi:10.1111/j.1945-5100.2000.tb01979.x.

Potter, R. W. K., and G. S. Collins (2013), Numerical modeling of asteroid survivability and possible scenarios for the Morokweng crater-forming impact, *Meteorit. Planet. Sci.,* 48(5), 744–757, doi:10.1111/maps.12098.

Prettyman, T. H. et al. (2012), Elemental Mapping by Dawn Reveals Exogenic H in Vesta's Regolith, *Science,* 338, 242 – 246.

Reddy, V. et al. (2012), Delivery of dark material to Vesta via carbonaceous chondritic impacts, *Icarus,* 221, 544–559.

Roskosz, M., H. Leroux, and H. C. Watson (2008), Thermal history, partial preservation and sampling bias recorded by Stardust cometary grains during their capture, *Earth Planet. Sci. Lett.,* 273, 195–202, doi:10.1016/j.epsl.2008.06.033.

Rubin, A. E. and W. F. Bottke (2009), On the origin of shocked and unshocked CM clasts in H-chondrite regolith breccias, *Meteorit. Planet. Sci.,* 44, 701–724, doi:10.1111/j.1945-5100.2009.tb00764.x.

Sandford, S. A. et al. (2006), Organics Captured from Comet 81P/Wild 2 by the Stardust Spacecraft, *Science,* 314, 1720, doi:10.1126/science.1135841.

Schultz, P. H., and D. E. Gault (1990), Prolonged global catastrophes from oblique impacts, *Geol. Soc. Am. Spec. Pap.,* 247, 239–262, doi:10.1130/SPE247-p239.

Schultz, P. H., and S. Sugita (1997), Fate of the Chicxulub Impactor, *Lunar and Planetary Science Conference XXVIII,* abstract no. 1261.

Schultz, P. H. (2012), Surviving Impact in Experiments and on Planets, *Amer. Geophys. Union Fall Meeting*, San Francisco, abstract no. 1504366.

Sterken, V.J., et al. (2014) Stardust Interstellar Preliminary Examination X: Impact speeds and directions of interstellar grains on the Stardust dust collector, *Met. Planet. Sci.,* 49, 1680–1697.

Valencia, J.J. and P.N. Quested (2008) Thermophysical properties, in *ASM Handbook, volume 15: Casting*, 468 – 481, doi:10.1361/asmhba0005240.

Westphal, A.J., et al. (2014) Evidence for interstellar origin of seven dust particles collected by the Stardust spacecraft, *Science,* 345, 786 – 791.

Tables

Table 1. Summary of prior experimental work assessing projectile residues.

Reference	Projectile type	Target type	Impact angle (°)	v_{imp} (km/s)
Bunch et al. [1993]	200 μm Murchison 300 to 400 μm diamond	Al plates	90	4.8 – 5.9
Berthoud et al. [1995]	150 μm soda lime glass	6061-T6 Al	90*	1 – 14
Hill et al. [1995]	20 to 100 μm olivine	Cu	15 – 60	8 – 13.5
Hörz et al. [1983]	2 mm soda lime glass 1.5 mm basaltic glass	Au, Cu	90*	4.4 – 6.4
Kearsley et al. [2007]	4 to 250 μm grains of C chondrite, olivine, enstatite, diopside, albite, anorthite, spinel, corundum, magnetite, pyrrhotite, kamacite, nepheline, serpentine, or calcite	Solar cells	90*	5.5 – 6.3
Burchell et al. [2008]	38 to 350 μm grains of olivine, rhodonite, enstatite, diopside, wollastonite, or lizardite	1100 Al foil	90	6

*Reference does not explicitly define impact angle; 90° is assumed. All angles reported with respect to horizontal.

Table 2. Summary of experiments*.

Effect of impact angle

Angle (°)	Target	Projectile	Projectile diameter (mm)	Impact speed (km s^{-1})
15	Copper[†]	Pyrex	6.35	5.05
30	Copper	Pyrex	6.35	5.02
30	Copper	Pyrex	12.7	3.13
45	Copper	Pyrex	6.35	5.02
45	Copper	Pyrex	12.7	3.01
60	Copper	Pyrex	6.35	4.89
75	Copper	Pyrex	6.35	5.32
90	Copper	Pyrex	6.35	5.32

Effect of impact speed

Angle (°)	Target	Projectile	Projectile diameter (mm)	Impact speed (km s^{-1})
30	Copper	Pyrex	12.7	1.91
30	Copper	Pyrex	12.7	2.25
30	Copper	Pyrex	12.7	3.13
30	Copper	Pyrex	6.35	3.48
30	Copper	Pyrex	6.35	4.00
30	Copper	Pyrex	6.35	5.02
30	Copper	Pyrex	6.35	5.57
30	Copper	Pyrex	6.35	5.69

Effect of projectile type

Angle (°)	Target	Projectile	Projectile diameter (mm)	Impact speed (km s^{-1})
30	Copper	2024 Al	6.35	5.02
30	Copper	Pyrex	6.35	5.02
30	Copper	Quartz	6.35	5.11
30	Copper	Serpentine[§]	6.35	4.31
30	Copper	Basalt[§]	6.35	4.36
30	Copper	Quartz	6.35	3.01
30	Copper	Basalt[§]	6.35	3.07
30	Copper	Agate	12.7	2.94

Table 2 (cont.). Summary of experiments*.

Angle (°)	Target	Projectile	Projectile diameter (mm)	Impact speed (km s^{-1})
Effect of target type				
30	Aluminum[‡]	Pyrex	6.35	4.50
30	Copper	Pyrex	6.35	5.02
30	Copper	Pyrex	6.35	3.13
30	Aluminum	Pyrex	6.35	3.14
30	Copper	Serpentine[§]	6.35	4.13
30	Aluminum	Serpentine[§]	6.35	4.31
30	Copper	Quartz	6.35	5.11
30	Aluminum	Quartz	6.35	5.24
30	Copper	Basalt[§]	6.35	3.07
30	Aluminum	Basalt[§]	6.35	3.12
30	Copper	Agate	12.7	2.94
30	Aluminum	Agate	12.7	3.10

*Some experiments are listed under multiple subheadings.

[†]Blocks of 110-H00 copper. Blocks came in two sizes, depending on the projectile diameter. For experiments using 6.35 mm projectiles, the blocks were 2.5 cm by 5 cm by 7.6 cm. For experiments using 12.7 mm projectiles, the blocks were 3.8 cm by 10.2 cm by 10.2 cm.

[‡]Blocks of 6061-T6511 aluminum. Blocks came in two sizes, depending on the projectile diameter. For experiments using 6.35 mm projectiles, the blocks were 2.5 cm by 7.6 cm by 7.6 cm. For experiments using 12.7 mm projectiles, the blocks were 5 cm by 10.2 cm by 10.2 cm.

[§]Instead of spheres, these projectiles were 6.35 mm diameter slugs due to machining constraints.

Table 3. Range of impact conditions explored in this study.

	ρ_{target} (g cm^{-3})	$\rho_{projectile}$ (g cm^{-3})	$\rho_{projectile}/\rho_{target}$	Range of impact speeds (km s^{-1})	Range of impact energies (kJ)
Pyrex into Al	2.70	2.23	0.83	3.1 to 4.5	3.0 to 11.7
Pyrex into Cu	8.89	2.23	0.25	1.9 to 5.7	1.8 to 11.7
Serpentine into Al	2.70	2.52	0.93	4.1	4.7
Serpentine into Cu	8.89	2.52	0.28	4.3	4.9
Quartz into Al	2.70	2.65	0.98	5.2	4.1
Quartz into Cu	8.89	2.65	0.30	3.0 to 5.1	1.3 to 3.9
Basalt into Al	2.70	2.8	1.04	3.1	2.7
Basalt into Cu	8.89	2.8	0.31	3.1 to 4.4	2.6 to 3.5
Agate into Al	2.70	2.6	0.96	3.1	13.3
Agate into Cu	8.89	2.6	0.29	2.9	12.0
Al into Cu	8.89	2.79	0.31	4.9 to 5.0	4.4 to 4.8

Table 4. Mechanical properties of targets.

Target	6061-T6 Al	110 ETP Cu H00
Density (g cm^{-3})	2.70	8.89
Sound speed (km s^{-1})	6.3	4.7
Impedance (kg m^{-2} s^{-1} x 10^{-6})	17	42
Tensile yield strength (MPa)	276	195
Ultimate tensile strength (MPa)	310	250
Shear strength (MPa)	207	170
K_{IC} (MPa m$^{1/2}$)	22 – 35[*]	30 – 90[*]

Unless otherwise noted, all data come from the Matweb material property database.
[*]*Ashby* [2005]

Table 5. Thermodynamic properties of targets.

Target	6061-T6 Al	110 ETP Cu H00[*]
Heat capacity	$0.7067+6 \times 10^{-4}T -1 \times 10^{-7}T^2$ J g^{-1} K^{-1}	$5.41+1.4e\text{-}3T$ J mol^{-1} K^{-1}
Enthalpy of fusion (J g^{-1})	380	208.7
Solidus temperature (K)	873	N/A
Liquidus temperature (K)	915	N/A
Melting point (K)	N/A	1356
ΔH to incipient melting (J g^{-1})[†]	587	458

[*]This alloy is >99.9% Cu; hence, the data listed here are for pure Cu. [†]Calculated from 298 K to the solidus temperature (Al) or from 298 K to the melting point (Cu). All data from *Valencia and Quested* [2008].

Figures
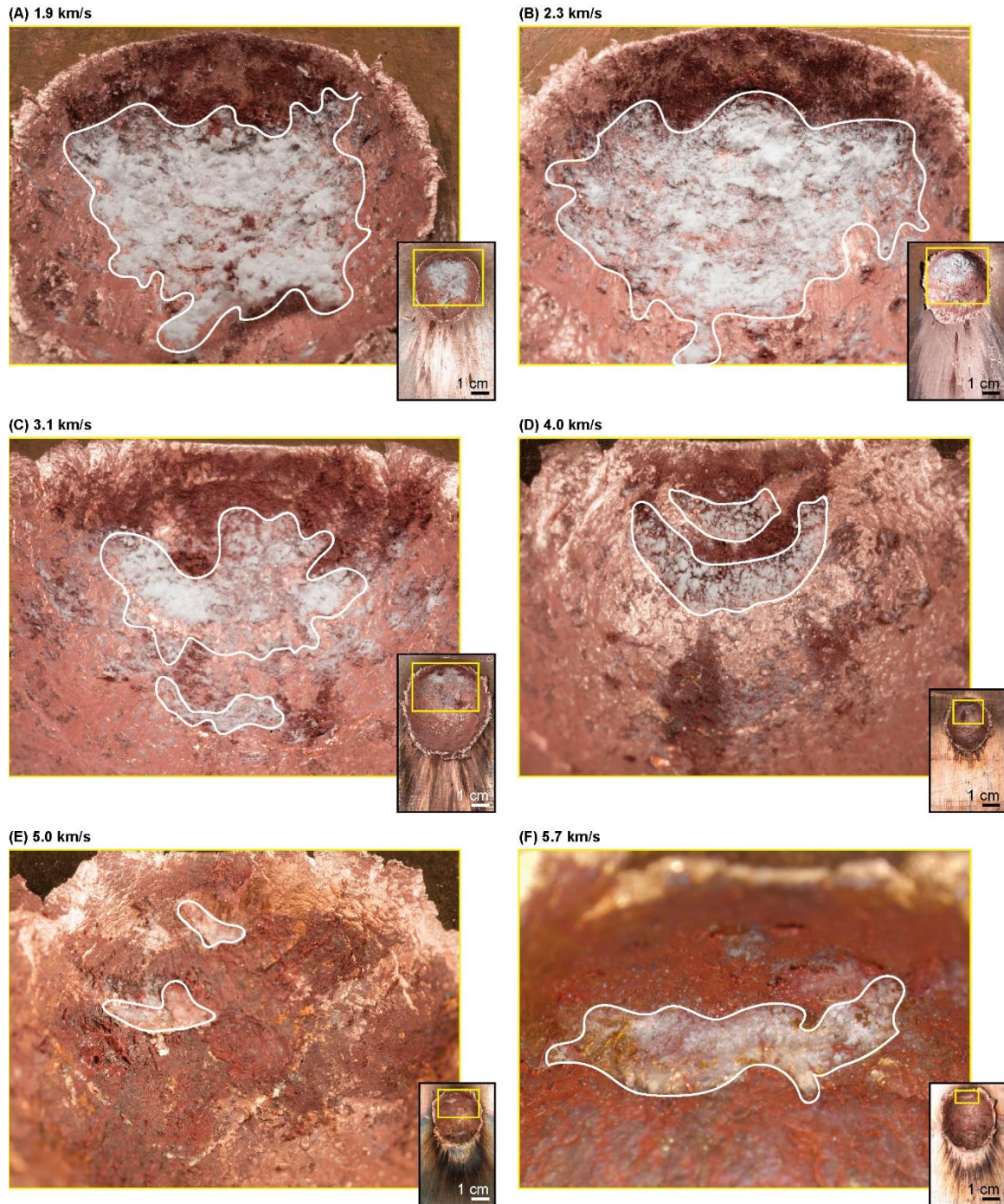
Figure 1. Evolution of projectile residues with impact speed between (A) 1.9 and (F) 5.7 km s^{-1}. Crater interiors contain three facies: a dusty reddish-brown facies, a vitreous

red facies, and a white fragmental facies, in addition to bare copper. The white fragmental facies is made of comminuted, but unmelted, portions of the projectile. The extent of the white fragmental facies is outlined in white. Yellow boxes in the smaller thumbnails mark the field of view shown in the larger image. Craters shown here formed when 6.35 mm diameter Pyrex projectiles impacted copper targets at 30°.
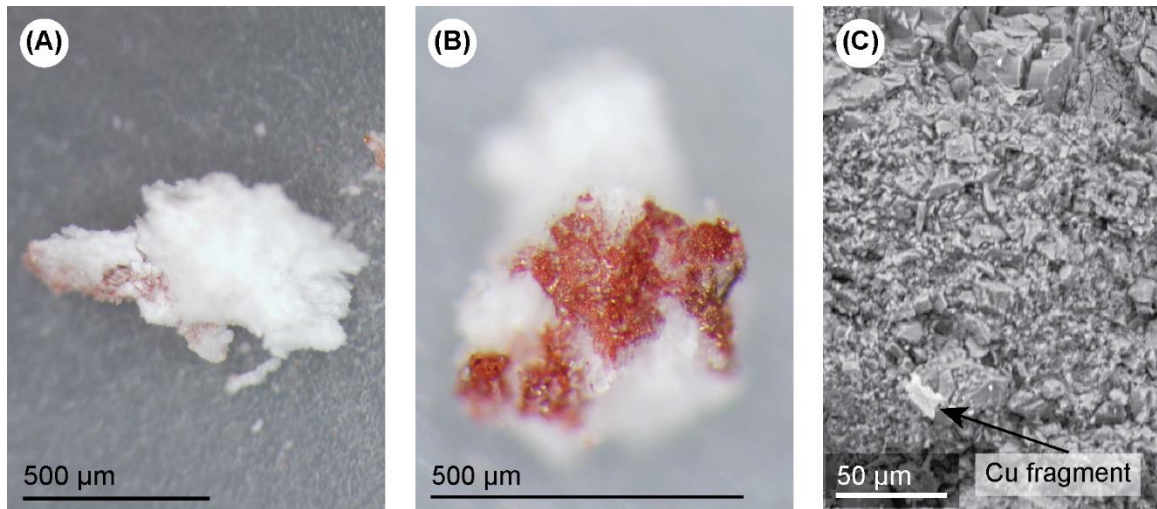
Figure 2. The white fragmental facies. The pieces have two sides. (A) The side facing into the crater consists of unmelted fragments of the projectile. (B) The back side is coated with red glass. This glass liner attaches the fragmental facies to the crater wall. (A) and (B) are optical micrographs. (C) Backscattered electron micrograph of the white fragmental material.
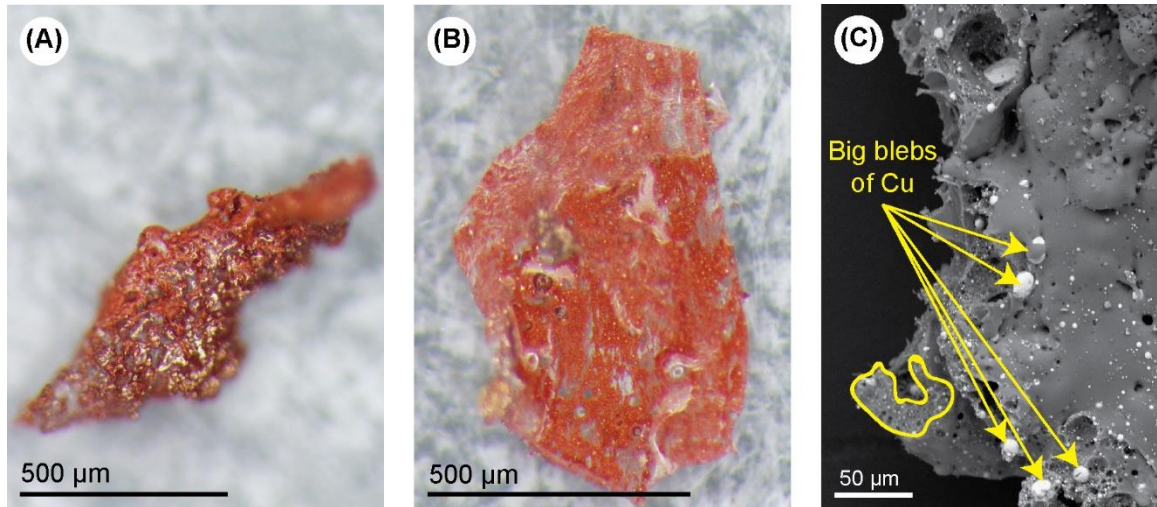
Figure 3. The red vitreous facies. (A) The red glasses are vesicular with a glassy luster and ropy texture. (B) The glass is heterogeneous. Some areas are deeply red, while other areas are clear and colorless. Glass in (A) and (B) contains bright, copper-colored blebs. (A) and (B) are optical micrographs. (C) Backscattered electron micrograph of the red vitreous material. Big, rounded blebs of copper rest within a silicate glass matrix. Fine-scale vesiculation and smaller copper blebs pervade the glass (see area circled in yellow).
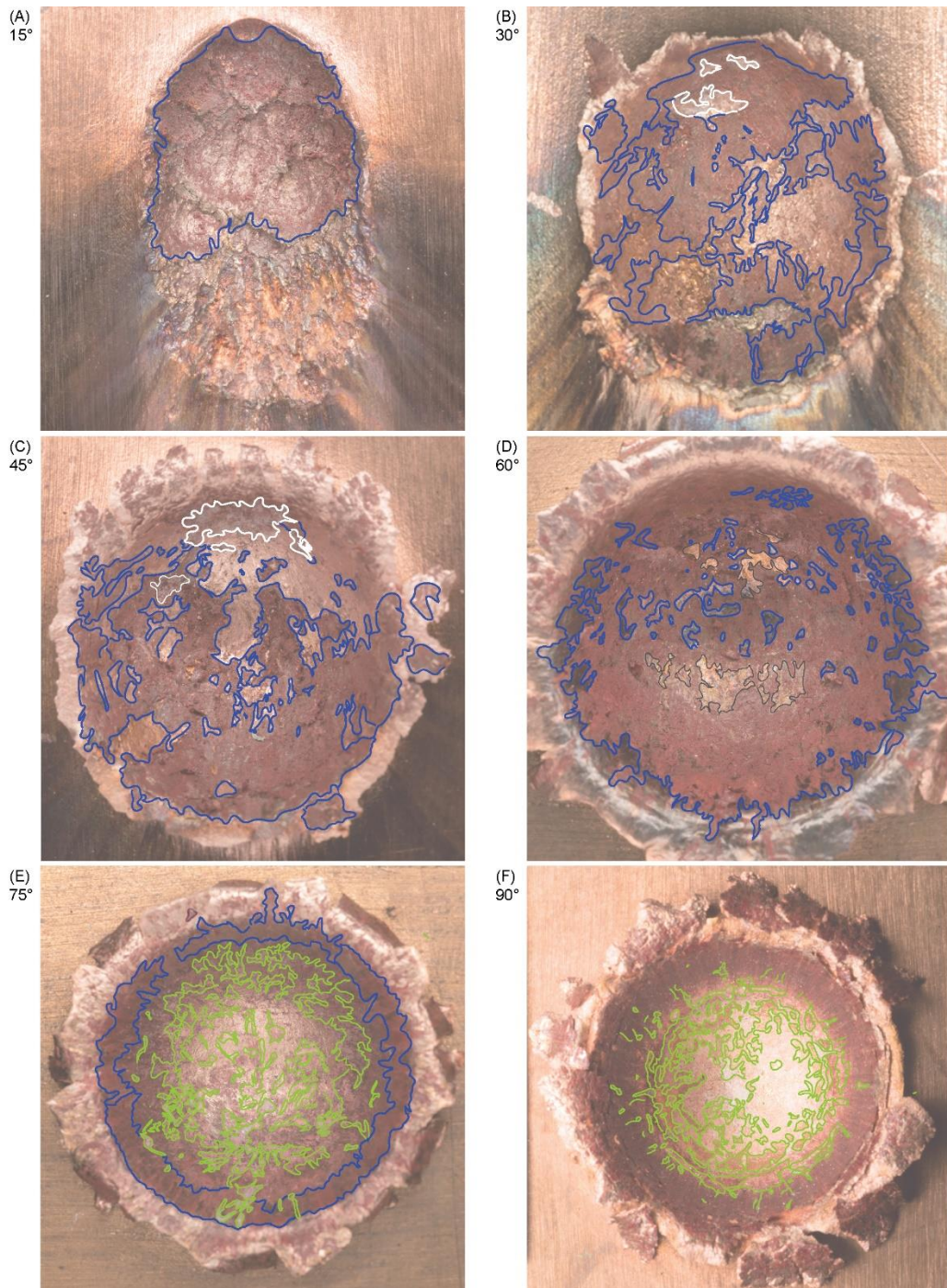
Figure 4. Distribution of projectile residues as a function of impact angle. Three facies of residues exist: a white, fragmental facies outlined in white, a red vitreous facies outlined in blue, and a clear vitreous facies outlined in green. The white fragmental facies consists

of unmelted projectile relics. The red and clear vitreous facies are projectile-rich, impact-generated glasses that incorporated different amounts of copper. These craters formed when 6.35 mm diameter Pyrex projectiles impacted copper targets at ~5 km s^{-1}. The projectile entered from the top of each image. All images have been scaled to the size of the crater.
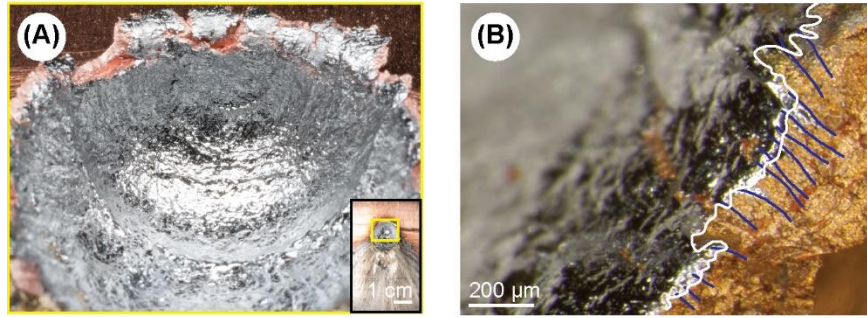
Figure 5. Projectile residues left by an aluminum projectile impacting a copper target at 30° and 5.0 km s^{-1}. (A) A thin liner of aluminum coats the entire crater interior. (B) The contact between the aluminum projectile and copper target on the crater rim. The white line maps the contact between the two materials. Blue lines show where wisps of aluminum radiate outward from the crater rim. This texture indicates that the aluminum in this location was molten when emplaced.
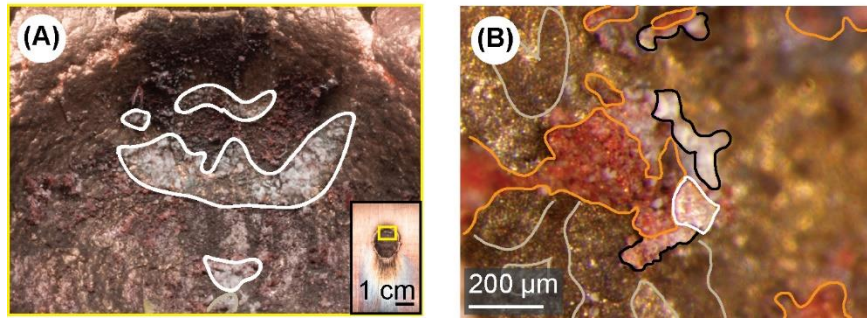
Figure 6. Projectile residues left by a quartz projectile impacting a copper target at 30° and 5.1 km s^{-1}. (A) The uprange wall retains unmelted fragments of quartz, outlined in white. (B) Multiple facies exist elsewhere. A dusty reddish-brown facies (outlined in tan) lies on top of bare copper. A red vitreous facies (outlined in orange) rests on top of the dusty reddish-brown facies. A white vitreous facies (outlined in black) intermingles with the red vitreous facies. Finally, quartz fragments (such as the one outlined in white) are occasionally trapped within the white vitreous facies.
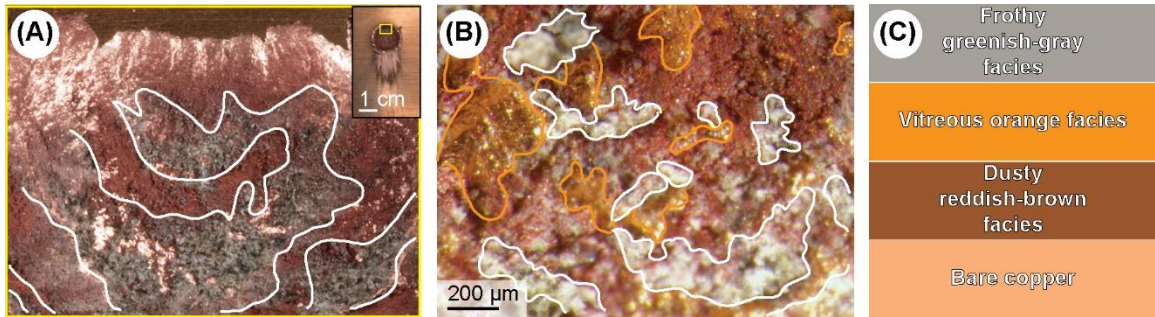
Figure 7. Projectile residues left by a basalt projectile impacting a copper target at 30° and 3.1 km s^{-1}. (A) Fragments of basalt are preserved within the frothy greenish-gray facies outlined in white on the uprange wall. (B) Multiple facies are present on the uprange wall. These include an orange vitreous facies (outlined in orange), the frothy greenish-gray facies (outlined in white), and the dusty reddish-brown facies. (C) Inferred stratigraphy of the three facies.
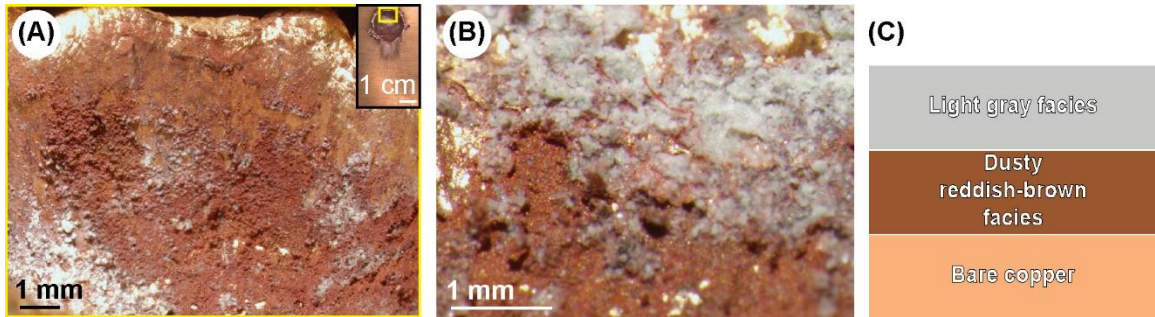
Figure 8. Projectile residues left by a serpentine projectile impacting a copper target at 30° and 4.3 km s^{-1}. (A) Fragments of serpentine are preserved on the uprange crater wall within a light gray facies; however, the bulk of the uprange wall is either bare copper or coated with the dusty reddish-brown facies. (B) The light gray facies lies on top of the dusty reddish-brown facies, which sits on top of the copper crater wall. (C) Inferred stratigraphy of facies.
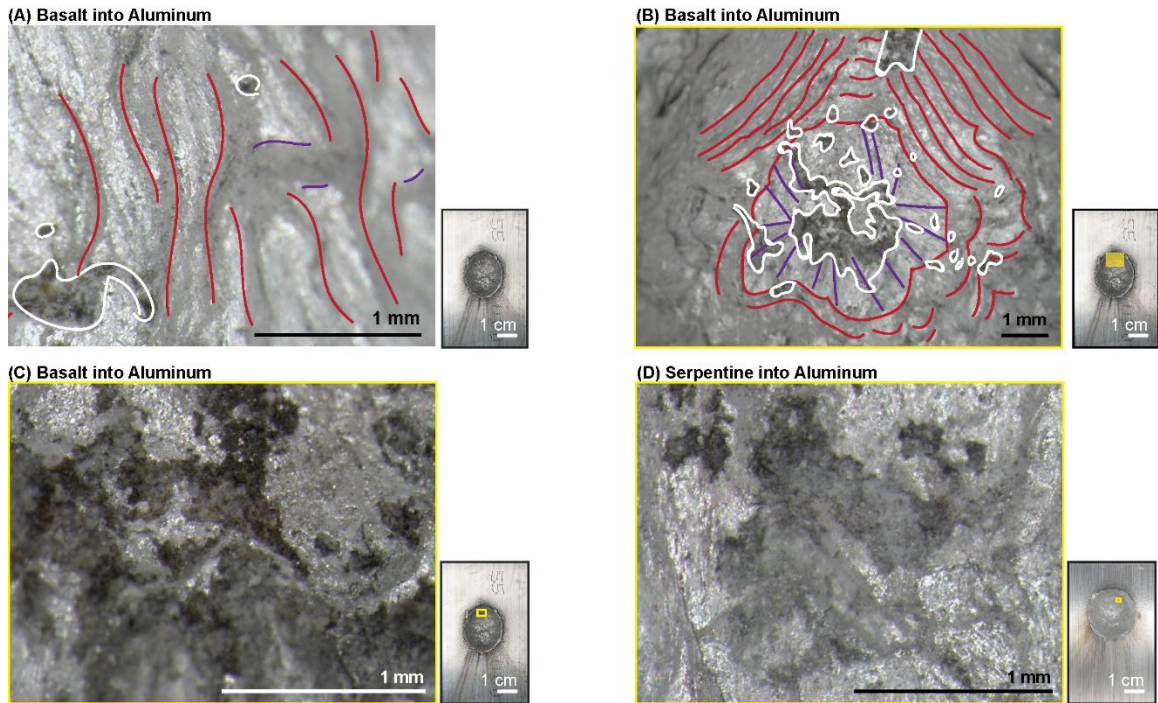
Figure 9. Projectile residues left when basalt and serpentine projectiles impacted aluminum targets. Other than target type, the impact conditions were the same as those for the craters in Figures 7 and 8. (A) Wispy, web-like, translucent glasses drape the crater interiors. (B) These webs, outlined in red, radiate out from a point partway down the uprange wall. This central zone, outlined in white, is rich in basalt relics and aluminum oxide. Blue lines trace stringers of glass that spoke outward from the central zone. (C) Magnified view of the central zone. (D) Craters formed by serpentine also have similar distributions of fragments and glasses.
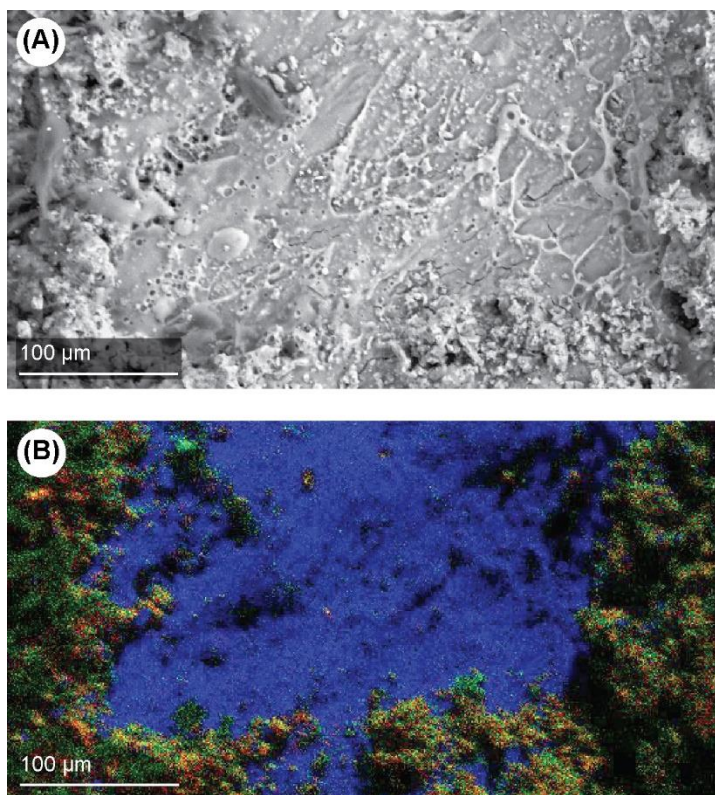
Figure 10. The uprange wall of a crater formed by a basalt projectile impacting an aluminum target at 30° and 3.1 km s^{-1}. (A) Backscattered electron image of the uprange wall. Variations in brightness correspond to variations in average atomic number. (B) Element map of the region in (A). Red is oxygen, green is silicon, and blue is aluminum. Green and yellow pixels (e.g., left and right borders of the map) are consistent with silicates; magenta pixels likely represent aluminum oxide. Shadowing prevented x-rays from some parts of the crater wall from reaching the EDS detector. Consequently, some pixels are black.
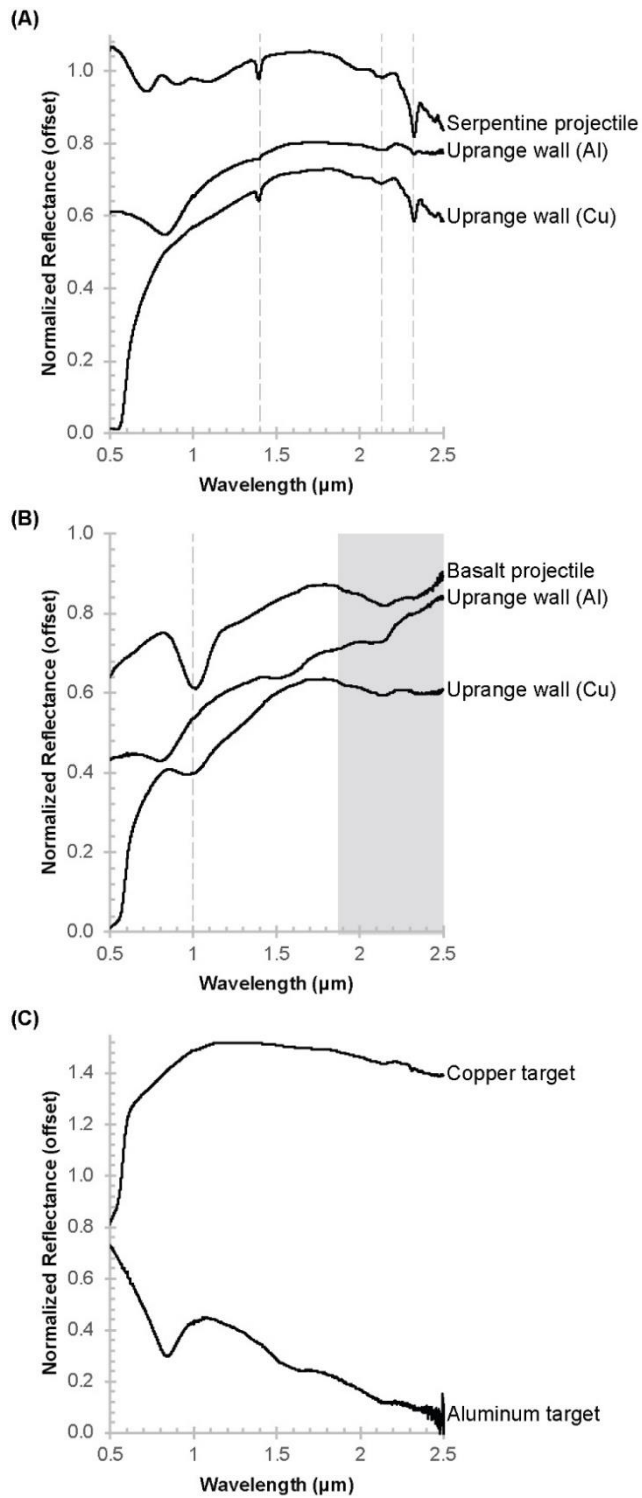
Figure 11. Reflectance spectra from the uprange walls of craters formed in copper and aluminum. (A) The uprange walls of both craters preserve solid, unmelted, lightly-shocked

serpentine, as indicated by diagnostic absorptions at 1.9, 2.1, and 2.3 μm. The absorptions are stronger in the copper crater. (B) Only spectra of the crater formed in copper show the 1 and 2 μm absorption features of the basalt projectile. The spectrum from the crater formed in aluminum does not show these diagnostic features. Vertical lines in (A) mark the diagnostic 1.4 μm, 2.1 μm, and 2.3 μm absorptions for serpentine. In (B) a dashed line marks the center of the 1 μm absorption. A gray rectangle marks the approximate extent of the 2 μm absorption.
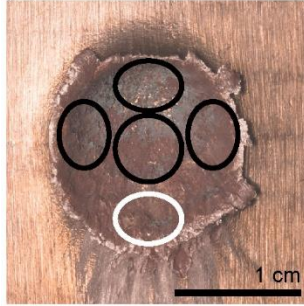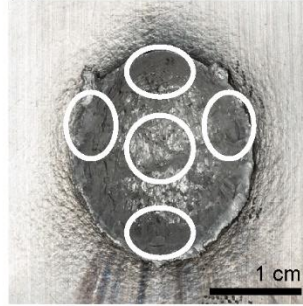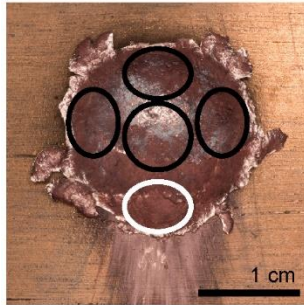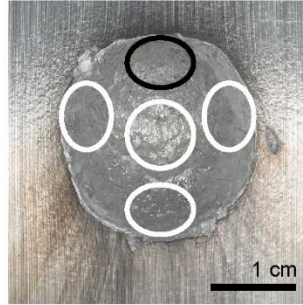
Figure 12. Summary of detections of crystalline projectile relics. Black ovals mark areas that showed the diagnostic absorptions of the basalt or serpentine projectiles. White ovals mark locations that did not contain these diagnostic absorptions. See Figs. S2 – S6.
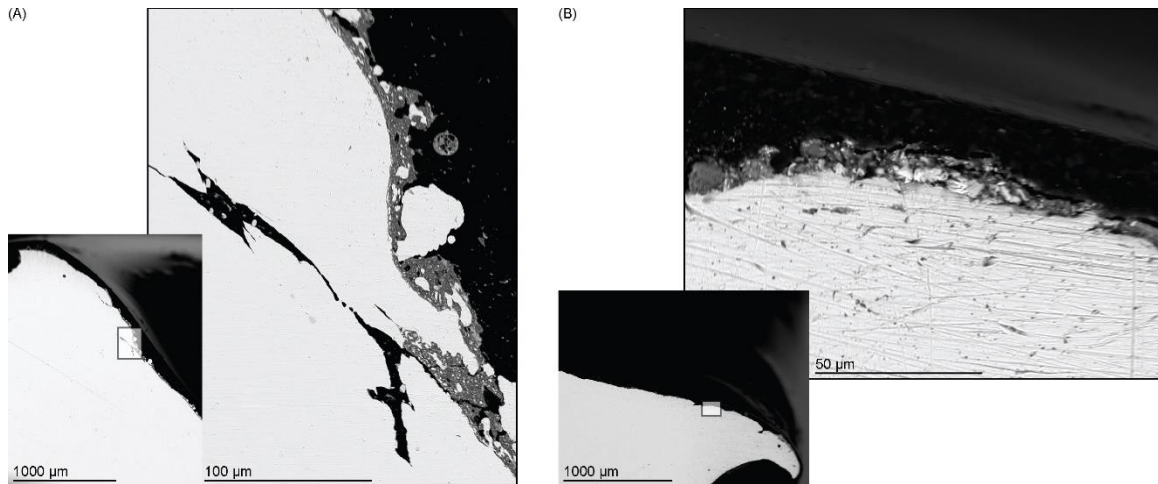
Figure 13. Backscattered electron images of a crater cross sectioned parallel to the projectile trajectory. The images reveal the profile of the projectile-target interface on the (A) uprange wall and (B) downrange wall. In this experiment a 6.35 mm diameter Pyrex projectile impacted a copper target at 30° and 5.6 km s^{-1}. In both images the projectile entered from the left.
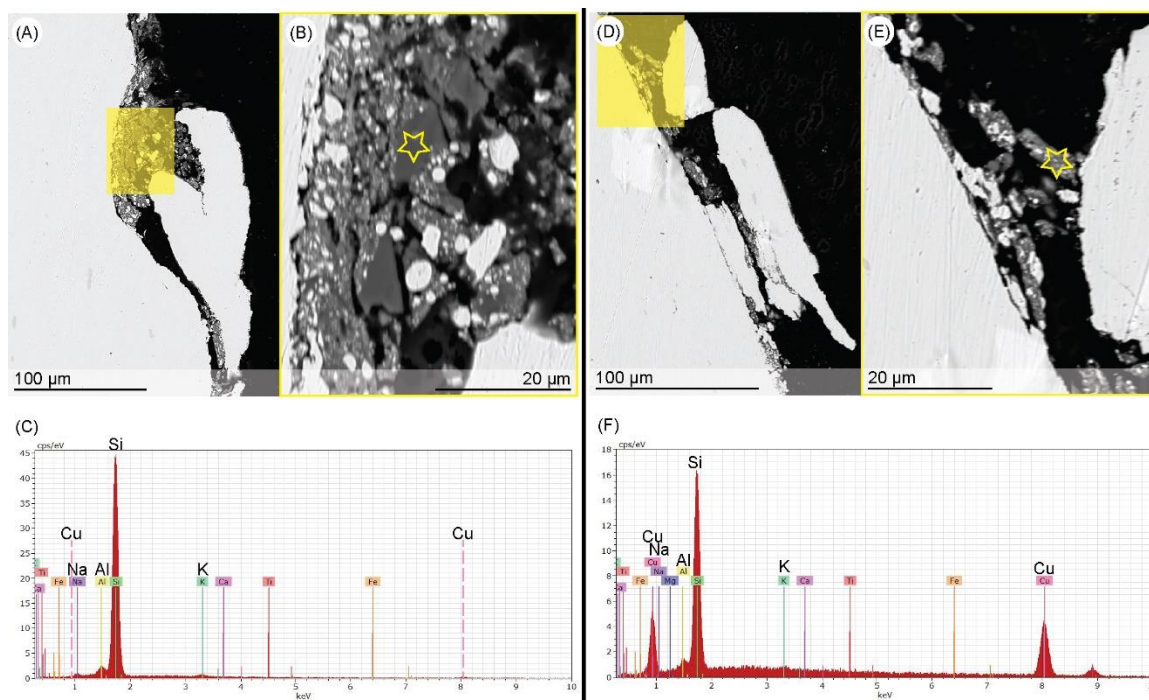
Figure 14. The projectile-target interface. (A) Cross section through the projectile-target interface showing a mitten of copper and a silicate-rich liner. (B) Silicate-rich regions include angular pieces. (C) EDS spectra from the location in (B) outlined with a yellow star demonstrate that the compositions of these areas are consistent with pure Pyrex. (D) A flake of copper frozen in place by rapid quenching of impact-generated glass. (E) Angular pieces like those in (B) are lacking in this region. (F) EDS spectra from the location in (E) outlined with a yellow star revealed significant copper. The projectile entered from the left of each micrograph.

Supplementary Figures

(A) 6.35 mm diameter Pyrex projectile at 3.5 km/s

1 cm
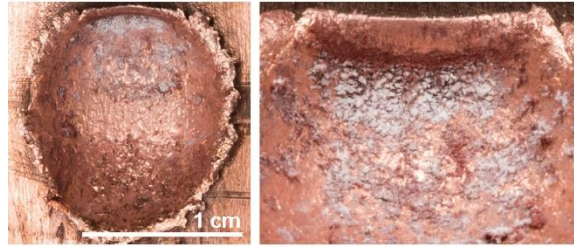
(B) 12.7 mm Pyrex projectile at 3.1 km/s

1 cm
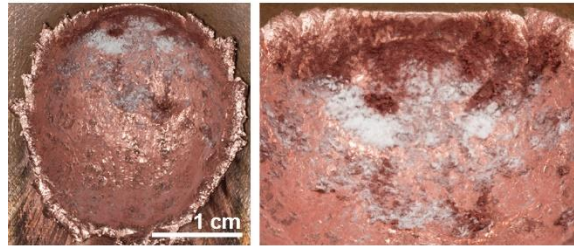
Figure S1. The residues left by 6.35 mm and 12.7 mm diameter Pyrex spheres are extremely similar at similar impact speeds (panels A and B, respectively). Based on these similarities, projectile size has a negligible effect on the spatial distribution and character of projectile residues discussed in section 3.1.1.
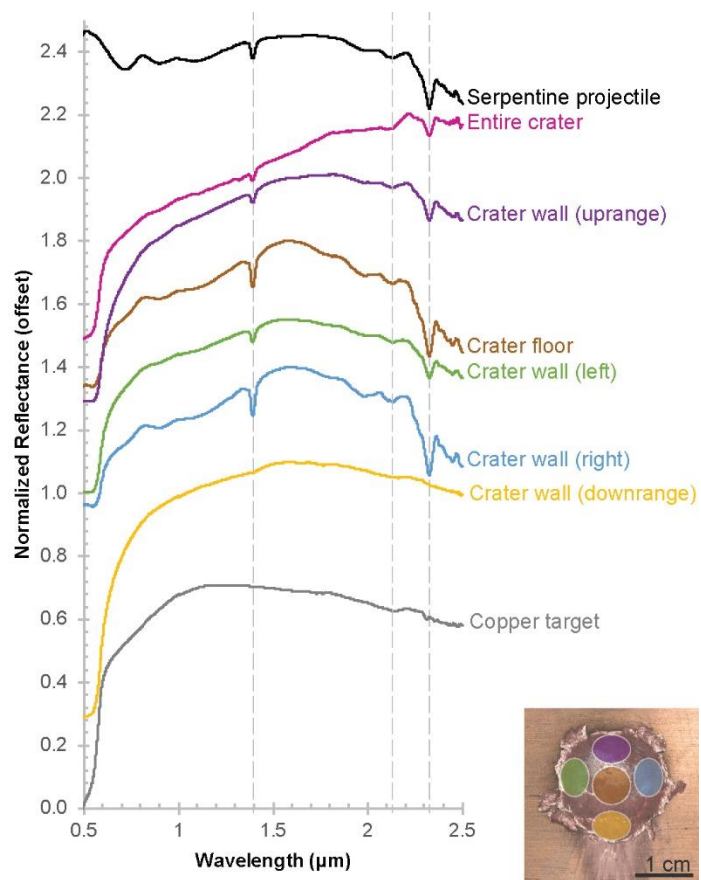
Figure S2. Visible to near-infrared spectra of the copper target, serpentine projectile, and multiple locations inside the crater. Crystalline serpentine is present everywhere except the downrange crater wall. The thumbnail at lower right shows the location of each spectrum. The color of each circle in the thumbnail matches the color of the corresponding spectrum. Vertical lines mark the diagnostic 1.4 μm, 2.1 μm, and 2.3 μm absorptions. Absorption strengths (band depths) vary between locations. Several factors, including particle size, can affect band depth, but if variations in band depth reflect variations in abundance, then serpentine is most abundant on the crater floor, right wall, and uprange wall. Serpentine appears absent in spectra corresponding to the downrange wall.
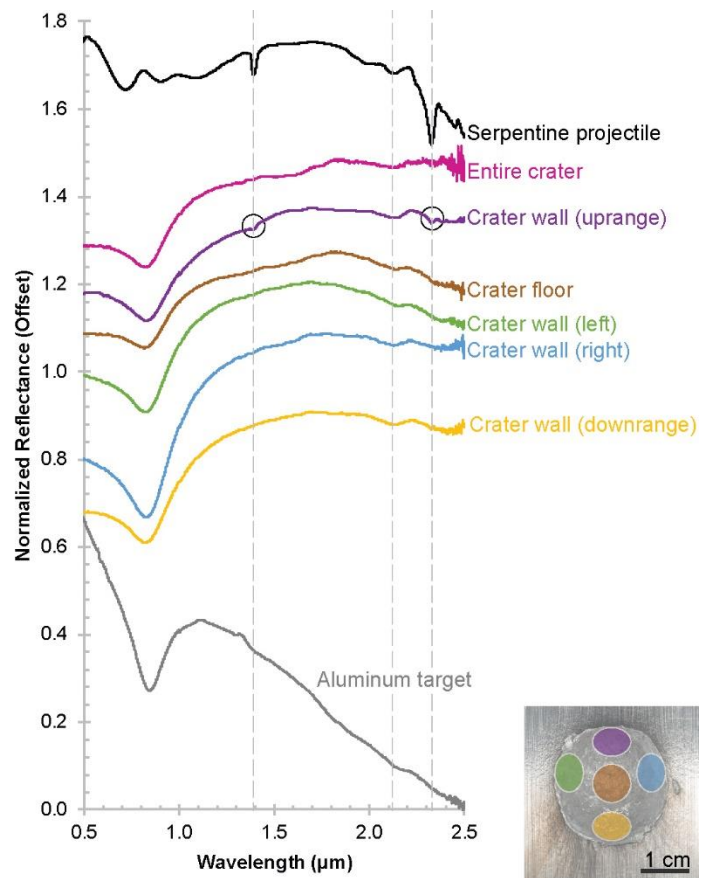
Figure S3. Visible to near-infrared spectra of the aluminum target, serpentine projectile, and multiple locations inside the crater. Crystalline serpentine is only present on the uprange crater wall. The thumbnail at lower right shows the location of each spectrum. The color of each circle in the thumbnail matches the color of the corresponding spectrum. Vertical lines mark the diagnostic 1.4 μm, 2.1 μm, and 2.3 μm absorptions.
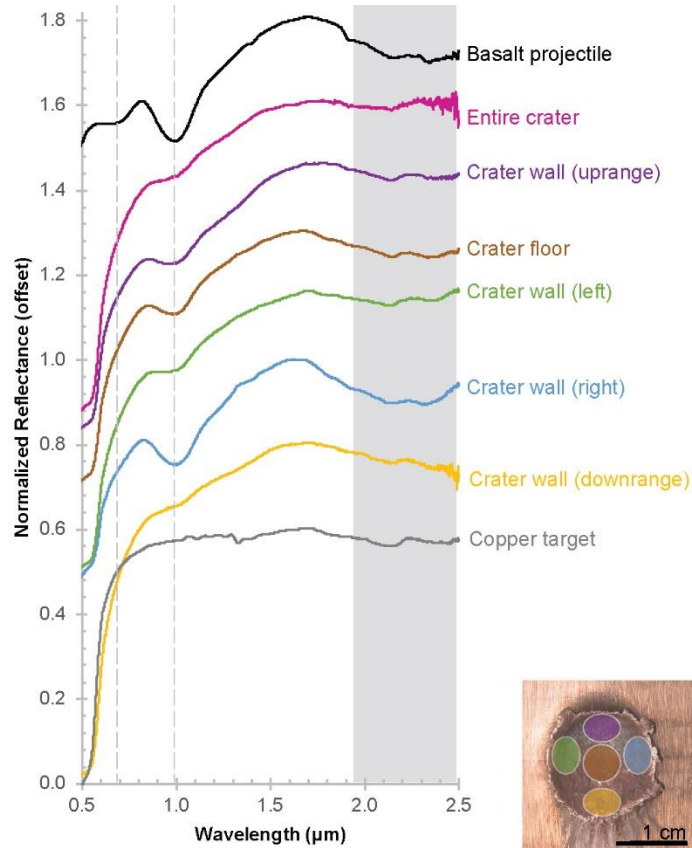
Figure S4. Visible to near-infrared spectra of the copper target, basalt projectile, and multiple locations inside the crater. Crystalline basalt is present everywhere except the downrange crater wall. The thumbnail at lower right shows where each spectrum was taken. The color of each circle in the thumbnail matches the color of the corresponding spectrum. A dashed vertical line marks the center of the 1 μm absorption. A gray rectangle marks the approximate extent of the 2 μm absorption. Together these two features are diagnostic of pyroxene, which is the spectrally dominant mineral in the basalt projectile. Band depth varies across these locations, and the 1 μm band is stronger than the 2 μm absorption. Several factors, including particle size, can affect band depth. However, if variations in band depth reflect variations in abundance, then basalt is most abundant on the right wall, crater floor, and uprange wall.

111
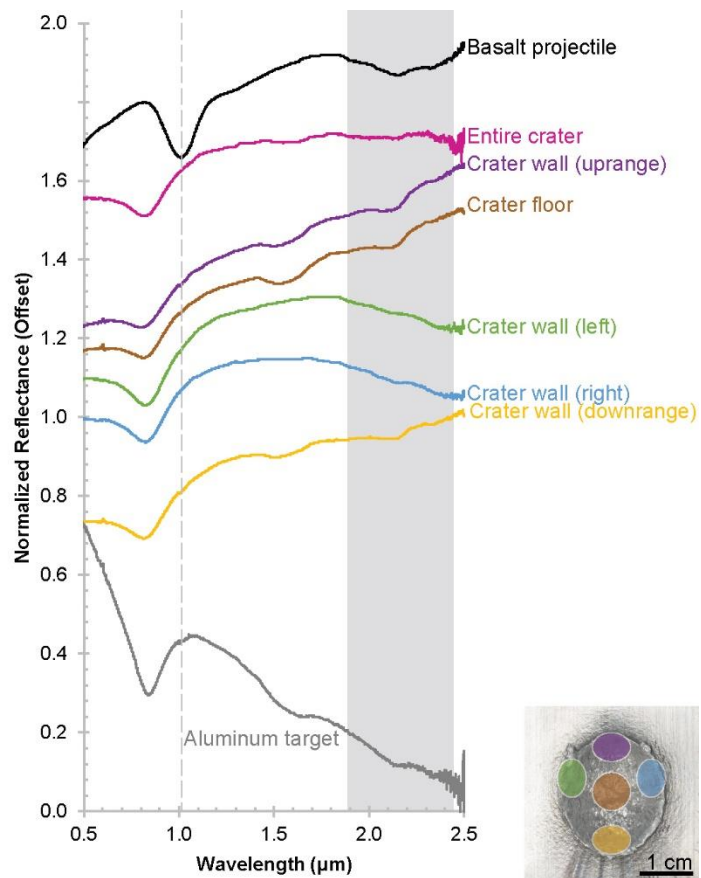
Figure S5. Visible to near-infrared spectra of the aluminum target, basalt projectile, and multiple locations inside the crater. The spectra do not clearly show the 1 and 2 µm absorptions seen in the projectile. The thumbnail at lower right shows where each spectrum was taken. The color of each circle in the thumbnail matches the color of the corresponding spectrum. A dashed vertical line marks the center of the 1 µm absorption. A gray rectangle marks the approximate extent of the 2 µm absorption.
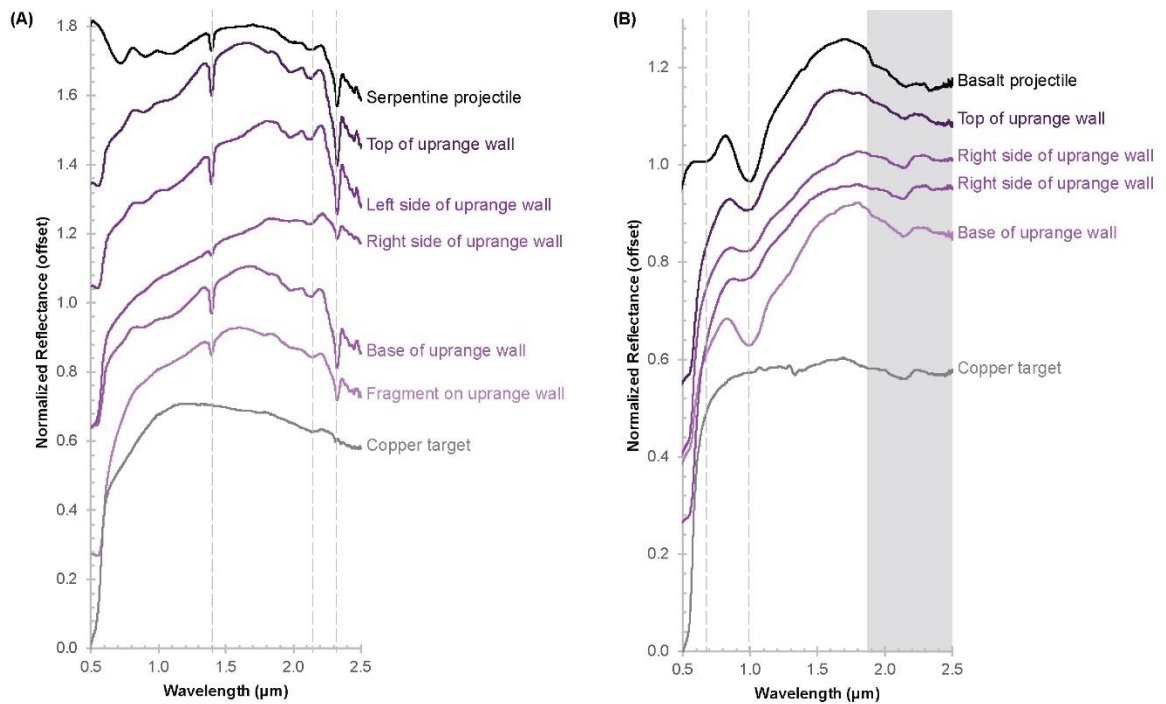
Figure S6. Spectra of one to two mm diameter spots on the uprange crater wall. This higher spatial resolution accentuates the diagnostic spectral features on the uprange wall. Crystalline relics of both serpentine (A) and basalt (B) are pervasive across the uprange walls of these craters. Dashed lines denote diagnostic absorption features; the gray box in panel (B) highlights the extent of the 2 μm pyroxene absorption.

CHAPTER 3

Contrasting meteoritic signatures at East and West Clearwater Craters

R. Terik Daly[a], Peter H. Schultz[a], Staci W. Loewy[b], John C. Lassiter[b], Lucy Thompson[c], and John G. Spray[c]

[a]Department of Earth, Environmental and Planetary Sciences, Brown University,

324 Brook St., Box 1846, Providence, RI 02912

[b]Department of Geological Sciences, Jackson School of Geosciences, The University of

Texas at Austin, 1 University Station C1100, Austin, TX 78712

[c]Department of Earth Sciences, University of New Brunswick, Fredericton,

New Brunswick, Canada, E3B 5A3

Abstract

Osmium isotopes provide a powerful tool for identifying meteoritic signatures in impactites. We apply the osmium isotope method to impact melts from the East and West Clearwater craters located in Quebec, Canada. Impact melts from East Clearwater have $^{187}Os/^{188}Os$ ratios of 0.1281 to 0.1285. These values indicate a significant meteoritic component: the level of meteoritic contamination in impact melts at East is higher than that of all terrestrial craters studied to date except Morokweng. Such finding aligns with earlier results from chromium isotopes and platinum-group elements. In contrast, impact melts from West Clearwater are highly radiogenic, with $^{187}Os/^{188}Os$ ratios between 6.604 and 59.12. These ratios are indistinguishable from $^{187}Os/^{188}Os$ ratios in country rocks and provide no evidence for a meteoritic component in impact melts at West Clearwater. East and West Clearwater formed in almost identical targets. Hence, target effects cannot readily explain the differences in these craters' meteoritic signatures. If melt sheet heterogeneity is similar at the two craters, the probability that melts at West Clearwater host an undetected chondritic component is <1%. While multiple scenarios could explain the non-detection of a meteoritic signature at West, a differentiated achondrite impactor is one possibility that could be readily tested. At East, an unusually low impact speed may best explain the unusually strong meteoritic signature. Nevertheless, the signature (or its nondetection) at both craters still could be related to an asymmetric distribution or preservation of the impactor component due to impact angle or the impact process.

1. Introduction

About fifty of Earth's impact craters have been searched for geochemical traces of the projectile. Once confirmed, projectile signatures can provide insights into asteroid belt dynamics, impactor populations, and flux rates. Moreover, the geochemical signatures of impact have the potential to enhance our understanding of impact processes or to reveal aspects of the process that remain poorly understood. Craters with unusual geochemical signatures are some of the most likely to provide new insights into impact processes.

A handful of craters that have been searched for meteoritic signatures are notable for one of two reasons: either a meteoritic signature has not been detected or the signature is unusually strong. East and West Clearwater craters fall into these two contrasting categories. *Palme et al.* [1978] reported up to 8 wt.% CI chondrite in impact melts from East Clearwater but failed to detect any meteoritic signature in melts from West Clearwater. In the nearly forty years since Palme's pioneering work, nearly sixty craters across the globe have been searched for meteoritic signatures [*Goderis et al.*, 2013; *Koeberl*, 2014]. Meteoritic signatures are present at the vast majority of them. Thus, the non-detection of an impactor signature at West Clearwater is unusual. Furthermore, the 8 wt.% impactor component at East Clearwater continues to be the highest reported at a terrestrial crater (e.g., *Goderis et al.* [2013] and references therein).

The last four decades have yielded significant improvements in analytical geochemistry and the advent of new methods for detecting meteoritic signatures in impactites [e.g., *Goderis et al.,* 2013 and references therein]. These new methods may uncover subtle signatures at West Clearwater that *Palme et al.* [1978] missed. Additionally,

subsequent studies revealed that East Clearwater was formed by an ordinary chondrite [*McDonald*, 2002; *Koeberl et al.*, 2007]. This knowledge enables a more nuanced assessment of the meteoritic signature at East Clearwater. The Clearwaters have yet another valuable trait: they formed in nearly identical targets. Such an occurrence makes the Clearwaters a natural laboratory for exploring how impact processes influence the geochemical signatures in impactites.

1.1. Geologic context

The Clearwater craters are located in Quebec, Canada [*Dence et al.*, 1965]. West Clearwater is larger, with a present-day rim-to-rim diameter of about 32 km. Most of the crater is filled by a lake. The lake itself is only about 25 km across [*Grieve,* 2006]. West Clearwater contains a ring of islands ~16 km in diameter. A few small islands exist in the center of the lake [*Grieve,* 2006]. Due to its heavily eroded state, however, West Clearwater may have originally been much larger [e.g., *Grieve,* 2006]. The present-day rim-to-rim diameter of East Clearwater is about 26 km [*Biren et al.,* 2016]. Radar images show that a "fracture halo" [*Smith et al.,* 1999] surrounds both craters. The halo is ~65 km across at West Clearwater and ~35 km across at East Clearwater. This halo has been interpreted as the expression of impact-related fractures in the target rock [*Grieve,* 2006]. The target rocks were primarily Archean granitic gneisses, along with granodiorites, diorites, and tonalites. Occasional mafic intrusions also occur in the area [*Rosa and Martin*, 2010; *Rosa*, 2011].

Despite their geographic proximity, multiple isotopic systems indicate that the craters formed separately. For example, (U,Th)/He dates West Clearwater crater to 280 ±

27 Ma and East Clearwater crater to 450 ± 56 Ma [*Biren et al.*, 2016]. Argon-argon worked yielded more precise dates: 286.2 ± 2.2 Ma for West Clearwater and between 460 and 470 Ma for East Clearwater [*Schmieder et al.,* 2015].

1.2. Detecting meteoritic signatures

Meteoritic signatures in impactites can be discerned in one of three ways: platinum-group element abundances and ratios, osmium isotopes, and chromium isotopes [*Tagle and Hecht*, 2006; *Koeberl et al.,* 2012; *Goderis et al.,* 2013; *Koeberl,* 2014]. The osmium isotope technique is the most sensitive [*Koeberl et al.*, 2012]. Hence, the osmium isotope method is the most likely to uncover a hitherto undetected meteoritic signature. The method is predicated on the radioactive decay of ^{187}Re to ^{187}Os, with a half-life of 42.3 ± 1.3 billion years. The higher the Re/Os ratio of a closed system, the more quickly the system grows radiogenic ^{187}Os. Most meteorites have Re/Os ratios less than about 0.1, and therefore have present-day ^{187}Os/^{188}Os ratios of about 0.11 to 0.18. (As is customary, the abundance of radiogenic ^{187}Os is normalized to stable, nonradiogenic ^{188}Os.) In contrast, the Re/Os ratio of rocks in Earth's crust is usually >10. Hence, old crustal rocks have ^{187}Os/^{188}Os ratios ≥ 1. Furthermore, most meteorites contain orders of magnitude more osmium than do terrestrial crustal rocks. Hence, a tiny amount of meteoritic osmium significantly lowers the ^{187}Os/^{188}Os ratio in impactites. See *Koeberl and Shirey* [1997] and *Koeberl* [2014].

2. Methods

2.1. Sample acquisition

In the mid-1960s and 1970s the Dominion Observatory acquired drill cores and surface samples from East and West Clearwater craters [*Dence et al.*, 1965; *Dence*, 1968]. The samples analyzed in this study were collected during these early expeditions. A total of ten samples have been analyzed: five from East Clearwater and five from West Clearwater. See Table 1.

Samples from East Clearwater come from drill cores DCW 2-63 and DCW 1-64 (Fig. 1). Hole 2-63 was drilled about 2.9 km southeast of the crater center and avoided the central uplift [*Dence et al.*, 1965; *Palme et al.*, 1979]. After passing through water, fluvio-glacial deposits, post-crater sediment fill, and breccias, the drill hole entered and ended in the impact melt sheet [*Dence et al.*, 1965; *Dence*, 1968; *Palme et al.*, 1979]. Hole 1-64 was drilled into the central uplift of East Clearwater [*Dence,* 1968], about 2 km west-northwest of the crater center [*Palme et al.,* 1979]. After passing through water and sediments, DCW 1-64 intersected shocked gneisses [*Dence,* 1968]. The rocks from drill hole 1-64 are heavily fractured and faulted, with zones of crushing and shearing up to several meters thick. Some of the materials in this drill core have been partially altered since emplacement: chlorite, sericite, hematite, and calcite are common secondary phases [*Dence,* 1968]. In this study, samples of impact melt rock came from core DCW 2-63, and samples of shocked country rocks came from core DCW 1-64.

The samples from West Clearwater come from both the surface and from drill core DCW 5-63 (Fig. 1). The core was drilled near the inner edge of the ring of islands [*Dence*

et al., 1965]. The drill hole passed through breccias before entering shattered basement rock [*Dence et al.,* 1965]. Within the shattered basement section of core 5-63, textures consistent with cataclastic flow and shearing, as well as melt veins that cut across the gneissic foliation of the basement rock, are pervasive (core log archived at the University of New Brunswick). The sample analyzed from DCW 5-63 comes from a melt vein near the bottom of the drill core.

2.2. Sample preparation

All samples were thoroughly sanded with 220-grit SiC in order to remove saw marks and then washed with Nanopure water. Samples were wrapped in thick plastic and coarse crushed. Chips were washed with Nanopure water and dried. Samples were then ground by hand in an alumina mortar and pestle. Both mortar and pestle were thoroughly cleaned with Nanopure water between samples. Each sample was ground in two steps. First, a small portion was powdered, then removed. Without rinsing the mortar or pestle, the remainder of the sample was then powdered. This two-step process helped to further mitigate contamination. The second "clean" split was used for all chemical and isotopic analyses.

2.3. Major and minor element analyses

Major and minor element compositions were determined using inductively coupled plasma atomic emission spectroscopy (ICP-AES). Rock powders were prepared using a

LiBO$_2$ flux fusion technique; see [*Murray et al.*, 2000] for full details. In brief, 0.04 g aliquots of each homogenized rock powder were mixed with flux and fused at 1050° C for ten minutes. The molten beads were then digested in 10% HNO$_3$, with the resulting solutions filtered and then diluted. In addition to the Clearwater samples, ten USGS rock standards and five blanks were processed during the same run. Diluted solutions were analyzed on a JY 2000 ICP-AES instrument in the Environmental Chemistry Facility at Brown University. After correcting for instrumental drift and blank intensities, raw intensities were converted to elemental concentrations using the measured intensities and known concentrations of elements in the USGS standards [see *Murray et al.,* 2000]. Two of the Clearwater samples were run in triplicate to assess the potential effects of sample heterogeneity. Analyses were reproducible to within 3% for Al, Ca, K, Mg, Mn, and Na, to within 4% for Fe and Si, and to within 5% for Ti. P concentrations were only reproducible to within 6%, but the samples had less than 0.4 wt.% P$_2$O$_5$.

2.4. Os isotope measurements

Whole-rock osmium isotope measurements were performed at the University of Texas at Austin. 800 mg of whole-rock powder were mixed with reverse aqua regia (4 mL concentrated HCl and 6 mL concentrated HNO$_3$) and a mixed ^{190}Os – ^{185}Re spike. These mixtures were digested in quartz tubes for 12 hours at 260 °C and 100 bars in an Anton Paar high-pressure asher. Osmium was extracted from the resulting solutions using CCl$_4$ followed by HBr. Osmium was further purified by microdistillation. Osmium isotopic compositions were measured on a Triton thermal ionization mass spectrometer in negative

mode by ion counter and a peak hopping routine. Osmium was run on Pt filaments as OsO_3^-. See the supplementary material of [*Byerly and Lassiter*, 2012] for additional details on sample digestion, osmium extraction, and instrument settings.

Average Os analytical blanks were ~0.2 pg g^{-1}. This represents less than 0.001% of the total Os in impact melt samples from East Clearwater. Due to their much lower Os concentrations, impact melts from West Clearwater have blank corrections between 0.8 and 6.4%. Country rocks have blank corrections between 0.6 and 13%. However, the country rocks and impact melt samples from West have such high $^{187}Os/^{188}Os$ ratios that these blank corrections do not affect interpretation of the data. The long-term average $^{187}Os/^{188}Os$ of the UMD standard analyzed in the Lassiter lab is 0.11379, consistent with published values [*Chatterjee and Lassiter*, 2016].

2.5. Electron microprobe work

Two thin sections were mapped using the Cameca SX 100 electron microprobe at Brown University. Maps were generated using a 15 kV accelerating voltage, 10 nA beam current, and 10 μm beam diameter.

3. Results

Tables 2 – 4 show the results of geochemical and isotopic analyses. Country rocks are highly radiogenic with low osmium abundances ($^{187}Os/^{188}Os$: 1.723 to 65.93; 2 to 46

ppt Os). Impact melts at East Clearwater are unradiogenic and have much more osmium (^{187}Os/^{188}Os: 0.1281 to 0.1285; 23,320 to 26,580 ppt Os). The four impact melts from West look like country rocks (^{187}Os/^{188}Os: 6.604 to 59.12; 6 to 48 ppt Os). See Figure 2.

3.1. East Clearwater

The high Os concentrations and low ^{187}Os/^{188}Os ratios implicate a meteoritic component at East Clearwater, consistent with prior work done using platinum group elements [*Palme et al.*, 1978, 1979, 1981; *Evans et al.*, 1993; *Schmidt*, 1997; *McDonald*, 2002] and chromium isotopes [*Koeberl et al.*, 2007]. The meteoritic signature at East Clearwater has a present-day ^{187}Os/^{188}Os ratio of ~0.128, consistent with an ordinary or enstatite chondrite impactor [*Day et al.*, 2016]. Hence, platinum-group element ratios [*McDonald*, 2002], chromium isotopes [*Koeberl et al.*, 2007], and osmium isotopes each point to an ordinary chondrite impactor at East Clearwater.

Data for impact melts from East Clearwater lay along two-component mixing curves between the country rocks and ordinary chondrites (Fig. 2). Mixing the impact melt samples with a bulk mantle reservoir cannot account for the observed osmium abundances and ^{187}Os/^{188}Os (Fig. 2). The major element data further rule out a significant mantle contribution. Based on osmium concentrations, DCW 2-63-1100 is 4.2 wt.% ordinary chondrite, whereas DCW 2-63-1120 is 3.7 wt.% ordinary chondrite. Such values are lower than the 7.4 wt.% meteoritic component at East reported by *Palme et al.* [1978]. However, *Palme et al.* [1978] assumed a CI chondrite impactor. CI chondrites have lower osmium concentrations than ordinary chondrites (460.5 ppb vs. 634 ppb Os) [*Day et al.,* 2016].

123

Hence, a larger amount of CI chondrite would be needed to produce the same Os abundance. Based on the osmium abundances for ordinary chondrites, the samples in *Palme et al.* [1978] contained 5.6 wt.% and 6.5 wt.% ordinary chondrite, respectively.

3.2. West Clearwater

The four impact melts from West Clearwater have no detectable meteoritic component. Given our detection limits, if a chondritic component is present, it must be <0.002 wt.%. This result is consistent with *Palme et al.* [1978], despite the superior sensitivity of the osmium isotope method and increased number of samples analyzed. Relationships between major elements and osmium further evince that impact melts analyzed from West Clearwater do not carry a chondritic component (Fig. 3).

4. Discussion

4.1. The non-detection of a meteoritic signature at West Clearwater

For nearly four decades, the claim of the absence of a meteoritic signature at West Clearwater has been based on two rocks analyzed by *Palme et al.* [1978]. The two samples came from "the middle and inside rim of the island ring". The rocks were "moderately altered, with sheet silicates (chlorite, montmorillonite) replacing interstitial glass". The present study tripled the number of samples from West searched for a meteoritic signature and analyzed a mixture of both surface and drill core samples. Moreover, the samples were

analyzed using the most sensitive tool available for the detection of meteoritic signatures. Nevertheless, a meteoritic signature remains undetected.

Three broad categories of possibilities could account for the non-detection. First, melts at West Clearwater may not have ever incorporated a meteoritic component. Second, melts at West Clearwater might carry a meteoritic signature that remains undetected. Third, melts at West Clearwater may have contained a meteoritic component that has subsequently been removed. Table 5 lists a variety of scenarios that fall into each category. Subsequent sections discuss each scenario in turn.

4.1.1. *Possibility #1: An impactor signature was never present*

The average impact on Earth (17 km s^{-1} and 45°) seems conducive to contributing a detectable meteoritic component in impact melts because most terrestrial craters searched to date have a meteoritic signature [e.g., *Goderis et al.,* 2013 and references therein]. If conditions were sufficiently extreme, however, an impact might not impart a meteoritic signature.

4.1.1.1. *Extremely high-speed impact*

Sufficiently high impact velocities enhance vaporization such that the projectile component might be dispersed without leaving a trace in the impact melt. However, even at 20 km s^{-1} and 45° only 10% of a rocky projectile vaporizes upon impact [*Pierazzo and*

Melosh, 2000]. The mass of melt and vapor scales with impact energy, to first order [e.g., *Pierazzo et al.,* 1997]. Hence, doubling the speed could quadruple the mass of vaporized projectile.

Dynamical models for asteroids predict that impact speeds at Earth do not exceed 50 km s^{-1} [*Le Feuvre and Wieczorek,* 2011]. Even if an asteroidal impactor were entirely vaporized, the vapor would be temporarily contained within the growing crater and interact with the melt. Low-angle impacts are an exception as much of the vapor may remain above the crater and comes primarily from the uppermost surface layer [e.g., *Eberhardy and Schultz,* 2015]. Hence, even an unusually high-velocity asteroidal impact may not fully account for the absence of even a trace of the impactor.

Comets, however, collide with Earth at higher velocities than asteroids do, but come have a much lower probability: the most likely impact velocity for long-period comets is 54 km s^{-1}. Jupiter-family comets typically have impact velocities of 17 km s^{-1} [*Weissman,* 2006]. The high encounter speeds of long-period comets would enhance vaporization of cometary material. A rare cometary impact cannot be ruled out and Section 4.1.2.4 explores this possibility in greater detail.

4.1.1.2. *Highly-oblique impact*

Both projectile fate and crater morphology evolve with impact angle. If the impact that formed West Clearwater were highly oblique (<15° with respect to horizontal), then the projectile (and its vapor) would have decoupled [*Schultz and Gault*, 1990], possibly leaving little to no impactor signature in the intra-crater impact melt. If the impact that

formed West were <15°, then the final crater would have remained circular due to circularization during collapse at large scales, if the impact angle was greater than 8° [*Schultz,* 1992]. Therefore, a highly oblique impact might explain the non-detection of an impactor signature in impact melts at West Clearwater if the impact angle were between 8 and 15°. Given the ~sin(2θ)dθ distribution of impact angles [*Gilbert,* 1893; *Shoemaker,* 1962], the probability of such an event is ~5%.

4.1.1.3.   Target layering

Low-impedance sedimentary layers, such as limestone, can affect crater morphology, as well as shock intensity and asymmetry [*Schultz,* 2007; *Collins et al.,* 2008; *Stickle and Schultz,* 2012, 2013]. Such effects can influence crater scaling: for impacts between 15 and 30°, a relatively thin low-impedance sedimentary layer (~ 25% of a projectile diameter) can effectively decouple the projectile from the underlying substrate with respect to crater size [*Schultz et al.,* 2013]. Experiments demonstrate that impactor decoupling also affects vaporization. At 15° even a very thin ($<$ 5% of a projectile diameter) low-impedance surface layer can prevent significant vaporization in strength-dominated targets [Schultz, 2006].

A 32 km diameter final crater would require a 2 km to 4 km diameter projectile. Therefore, a sediment layer would have needed to be 0.5 to 1 km thick to significantly affect crater size. If the original, pre-erosion diameter of West Clearwater had been larger, then the projectile needed to form the crater may have also been larger. In this situation, an even thicker sediment layer would have been needed. The presence of limestone blocks in

the melt at West Clearwater [*Rosa and Martin,* 2010] indicates that the pre-impact surface may have been covered with up to 130 meters of limestone at the time of impact [*Schmieder et al.,* 2015]. This layer would not have been thick enough to affect the crater's final size. However, whether a layer of such thickness would have affected projectile fate is unclear. Therefore, whether target layering can account for the absence of an impactor signature at West Clearwater deserves further study.

4.1.2. *Possibility #2: An impactor signature is present but undetected*

4.1.2.1. *Masking by an indigenous component*

In areas with high PGE abundances or unradiogenic $^{187}Os/^{188}Os$ ratios, high "background levels" of these elements can mask a meteoritic signature. This complication cannot explain the non-detection at West Clearwater. The four country rocks analyzed have highly radiogenic $^{187}Os/^{188}Os$ ratios and extremely low osmium concentrations.

4.1.2.2. *Inadequate sampling*

Although this study tripled the number of impact melts analyzed from West Clearwater, the total number of samples analyzed remains small: six. At several other Canadian craters, however, six or fewer samples were enough to reveal a meteoritic signature using PGEs (Tables 6 and 7). However, fifteen samples of impact melt from Mistastin have been analyzed without a detection of a signature. Hence, it is unusual, but

not unprecedented, to have analyzed six samples and not found an impactor signature. Of the four craters in Table 7, only West Clearwater has been searched using osmium isotopes, which is the most sensitive method for detecting meteoritic signatures [e.g., *Tagle and Hecht*, 2006; *Koeberl,* 2014; *Goderis et al.,* 2013]. Consequently, Mistastin would be a logical target for more detailed studies using osmium isotopes.

4.1.2.3.   Differences in sulfide mineralogy

Tiny sulfide grains carry the bulk of the meteoritic component at East Clearwater [*Palme et al.,* 1979]. Given the preferential partitioning of PGEs into sulfides over silicates [*Fleet et al.*, 1996], differences in sulfide mineralogy could potentially contribute to differences in the meteoritic signatures at East and West Clearwater. In order to assess this possibility, thin sections from two samples were examined: DCW 2-63-1100 from East and DCW 77-13 from West. Although the samples have very similar bulk compositions (see Table 2), they exhibit very different sulfide abundances (Fig. 4). In the thin section from East Clearwater, accessory sulfides up to several hundred microns across are present. In the thin section from West Clearwater (DCW 77-13), the few sulfides are extremely small (<5 μm across) and contained entirely within apatite grains. Only three grains of apatite were present in the mapped portion of the thin section from West.

Given the much lower abundance and significantly smaller sizes of sulfides in the impact melt at West Clearwater, one possible explanation for the absence of a meteoritic signature in melts at West relates to fewer available sulfides to host PGEs. More detailed work on a larger number of samples of melt from the two craters will be needed to explore

this possibility. However, a comparison with the Morokweng crater in South Africa suggests that differences in sulfides are likely insufficient. Both the sulfide-poor and sulfide-rich portions of the impact melt at Morokweng carry a clear meteoritic signature. The data clearly revealed a meteoritic component in the sulfide-poor melt, even though the PGE abundances in the sulfide-poor region are five to ten times lower [*McDonald et al.*, 2001]. Hence, differences in the sulfides at East and West may not easily account for the non-detection of meteoritic material at West.

4.1.2.4. Differentiated achondrite or cometary impactor

Differentiated achondrites have lower PGE abundances than chondrites, stony-iron meteorites, or iron meteorites. For example, the median $^{187}Os/^{188}Os$ ratio in eucrites is 0.13278, with an average osmium concentration of 0.025 ppb [*Dale et al.*, 2012]. Given that some Clearwater country rocks contain more osmium than the average eucrite does, a eucrite signature in the impact melts at West Clearwater could not be distinguished from the target rock. In general, basaltic achondrites typically cannot be detected by osmium isotopes [*Koeberl and Shirey*, 1997]. This does not mean that impact melts formed by basaltic achondrite-like impactors do not carry a meteoritic component. Rather, the meteoritic component cannot be easily detected due to the similarities Earth's crust and the basaltic impactor. Hence, the impact melts at West Clearwater could carry an as-of-yet undetected meteoritic signature of a differentiated achondrite.

Although osmium isotopes would not be able to detect a differentiated achondrite impactor, chromium isotopes might. A two-component mixing model can constrain the

amount of meteoritic material that would be needed to leave a detectable ε^{53}Cr signature in impact melts at West. Chromium concentration and ε^{53}Cr varies among meteorite types [e.g., *Lugmair and Shukolyukov,* 1998]. These calculations assumed a eucrite impactor, for the sake of example. *Lugmair and Shukolyukov* [1998] measured chromium in eight noncumulate eucrites and found a median total-rock chromium concentration of 1990 ppm. The median total rock ε^{53}Cr of these samples was 1.15 [*Lugmair and Shukolyukov,* 1998]. (These ε^{53}Cr values include a second-order correction that more recent studies omit.) Based on data from the literature (Tables S5 and S6) and the new data reported here, target rocks at the Clearwater craters have a median chromium concentration of 118 ppm. The ε^{53}Cr of terrestrial rocks is 0 [e.g., *Lugmair and Shukolyukov,* 1998; *Koeberl et al.,* 2014 and references therein].

Figure 5 shows the results of a mixing model that used these values for chromium concentration and ε^{53}Cr. *Koeberl et al.* [2007] successfully detected meteoritic components in samples with a ε^{53}Cr as low as 0.17. Hence, a eucritic component, if present, could likely be detected if the eucritic component were to exceed 1 wt.%. Although a 1 wt.% meteoritic component is larger than that at many terrestrial craters [e.g., *Goderis et al.,* 2013], 1 wt.% is not unreasonably high. Hence, follow-up studies using chromium isotopes could provide an effective way to evaluate the possibility of a differentiated achondrite impactor at West Clearwater crater.

Another possibility is that a cometary impact formed West. Cometary impacts should account for only a few percent of impact on the Earth [*Weissman,* 2006] and therefore might account for the few terrestrial craters without a meteoritic signature.

Although cometary dust would likely have chondritic PGE abundances, the volatiles in the nucleus would vaporize. Expanding vaporized ices could entrain cometary silicates and deposit them far afield. Having been transported, the silicates might not be incorporated into the impact melt and impart a chondritic signature.

In the event of a cometary impact a light element isotope signature (e.g., ^{3}He) may be preserved in distal sediments of the same age. A search for a spike in extraterrestrial helium at ~280 Ma could be done using a nearby ocean sediment core. A ^{3}He signature, however is not definitive. An enrichment in ^{3}He near the time of the Chesapeake Bay and Popigai impacts was originally attributed to a comet shower [*Farley et al.,*1998]. However, chromium isotopes implicate an asteroidal, rather than cometary, source for the ^{3}He enrichment [*Kyte et al.,* 2011].

4.1.2.5.Melt sheet heterogeneity

If the meteoritic component at West Clearwater were heterogeneously distributed in the melt, then the six samples from West might have "missed" the meteoritic component. Heterogeneity of the meteoritic component could occur in one of two modes. First, the meteoritic component might be concentrated in projectile-rich nuggets distributed evenly throughout the melt sheet. We term this "raisin-bread" heterogeneity. The projectile-rich nuggets are akin to the raisins: localized, but evenly distributed. Second, the meteoritic component might be localized in specific parts of the crater. Such large-scale asymmetries might occur if the impact that formed West Clearwater were oblique. Impact experiments [*Daly and Schultz,* 2017] and shock physics code calculations [e.g., *Schultz and Crawford,*

2014] indicate that oblique impacts preferentially deposit the impactor component in specific locations within the crater. In this section, we consider raisin-bread heterogeneity. Large-scale asymmetrical heterogeneity is discussed further in section 4.3.

One possibility is that the impact melt at West Clearwater is more heterogenous than the melt at East: the "raisins" of meteoritic contamination might be fewer or farther between at West than at East. Harker diagrams reveal, however, that comparable degrees of major element heterogeneity occur in the melt sheets at East and West Clearwater (Fig. 6). This pattern is consistent with the "relative homogeneity" of major elements at many other terrestrial craters [*Grieve et al.*, 1977; *Dressler and Reimold*, 2001; *Goderis et al.*, 2013]. Although the two melt sheets do have slightly different average compositions, such differences likely reflect minor differences in the proportions of country rocks incorporated into the melts.

Notwithstanding the relative homogeneity of major elements, trace elements could be more heterogeneous. PGEs, including Os, are often hosted in minor phases, which makes analyses prone to nugget effects [e.g., *Koeberl*, 2014; *Goderis et al.*, 2013]. The chondritic component at East Clearwater places constraints on the potential for such an effect at West Clearwater. Including the results published previously (see supplementary tables S1 – S6), twelve samples of impact melt from East Clearwater have been analyzed for osmium abundances. Ten of these twelve samples carry a meteoritic component, even though tiny nickel-iron sulfide grains carry the meteoritic signature [*Palme et al.,* 1979].

Figure 7 shows depth profiles of impact melt samples from drill core 2-63. Only samples with both major and trace element data are shown in order to facilitate direct

comparisons. No systematic depth trends are seen for most major element oxides. MgO and TiO_2 may decrease slightly with depth. Trace elements are more variable; however, the five trace elements shown here are all affected by the impactor signature. Copper varies most strongly with depth: below about 300 meters, copper is more abundant, except in the sample where the meteoritic signature is absent. Nickel and cobalt, however, become somewhat less abundant in the drill core below 300 meters. Osmium, the most sensitive tracer of meteoritic contamination of the elements shown here, varies among the samples, but does not systematically increase or decrease with depth in the portion of the melt sheet sampled here.

The ordinary chondrite component in the ten samples with a clear chondritic signature ranges from about 3 to 9 wt.%. So, the signature is indeed slightly heterogeneous, as reported by *Palme et al.* [1979]. Nevertheless, the salient point is that most (83%) samples from East carry a clear meteoritic signature. If this detection frequency is relevant to West and treating samples from West as independent, there is only a $(2/12)^4 = 0.08\%$ chance that a meteoritic signature is present at West but not detected. These assumptions are not strictly valid because of differences in sampling: samples from East come from a single drill core, whereas samples from West come from multiple locations across the melt-capped islands and from a drill core.

Alternatively, the potential heterogeneity of a meteoritic signature at West can be constrained by comparing the variability of trace elements in melts from East and West Clearwater. The data in tables S1 – S6 enable such a comparison, with certain caveats. Many samples from East Clearwater have not been analyzed for the same minor elements

as impact melts from West Clearwater (see tables S1 – S6). At least four samples of impact melt from East and West, respectively, have been analyzed for Os, Ni, Co, and Cr. It would be preferable to use other elements (e.g., REEs) in order to compare minor element variability because the impactor component has less effect on the rare-earth elements. But, given existing data, assessment of relative variations in Os, Ni, Co, and Cr in the two melts is the best that can be done for this contribution.

Table 8 includes the basic statistics for Os, Ni, Co, and Cr concentrations in impact melts from East and West. These data are depicted as histograms in Figure 8. Except for osmium, far fewer analyses are available for samples of impact melt from East Clearwater. The elements Os, Ni, Co, and Cr have different concentration ranges at East and West because of the meteoritic signature at East. Nevertheless, the relative standard deviation of each element (the standard deviation divided by the mean) provides an additional constraint on heterogeneity at East and West Clearwater. Based on relative standard deviations in Os, Ni, Co, and Cr, the melt at West may be slightly more heterogeneous in trace elements than the melt at East. But, the differences are not large enough to readily attribute the complete apparent absence of an impactor signature at West to a more heterogeneous melt sheet.

One additional approach could yield insight into the likelihood that an impactor signature at West has eluded detection because of raisin-bread-style heterogeneity. While the best approach is to analyze more samples, PGE analyses are costly and time-consuming. Many more samples from West have been analyzed for Cu, Ni, Co, and Cr than for PGEs. Of these elements, Ni has been the most often analyzed in samples from West Clearwater. A much higher meteoritic component would be needed in order to

noticeably perturb Ni abundances (due to higher background levels in crustal rocks). However, this loss in sensitivity is offset by the larger set of samples for which data is available.

None of the nickel abundances in about seventy-five samples of impact melt from West Clearwater hint at a meteoritic signature (Fig. 9). Osmium isotopes or PGEs might yield a subtler meteoritic signature in some of these samples. Nevertheless, in both osmium versus major element oxides (Fig. 3) and nickel versus major element oxides (with much more data; Fig. 9), impact melts from West Clearwater exhibit the same systematics as the country rocks: nickel decreases with silicon, aluminum, sodium, and potassium and increases with magnesium, iron, calcium, and manganese. If an impactor signature were present (but undetected due to heterogeneity), then none of these seventy five samples would have enough meteoritic material to noticeably perturb Ni abundances.

Although the data cannot definitively rule out a meteoritic signature that is undetected due to raisin-bread heterogeneity in the melt, the evidence to date makes this explanation unlikely. Melts at East and West are relatively homogeneous in major element compositions. The possible slight enhancement of minor element variability at West is insufficient to explain the significant differences between melts at the two craters. The vast majority (83%) of impact melts analyzed at East carry a meteoritic signature. Hence, it is unlikely that all four impact melts analyzed from West would fail to show a meteoritic signature, if melts at West carried a chondritic component distributed heterogeneously in a raisin-bread manner. Furthermore, fewer than six samples have been enough to reveal a meteoritic component at several other Canadian craters (see Table 7). It is therefore not

136

straightforward to attribute the non-detection of a meteoritic component at West to raisin-bread-style melt sheet heterogeneity.

4.1.3. Possibility #3: An impactor signature used to be present

4.1.3.1. Weathering or remobilization

Another possibility is that the chondritic signature at West Clearwater may have been present but later weathered away. *Palme et al.* [1979] showed that some of the PGEs in impact melts from East have been fractionated relative to one another, which may indicate limited remobilization. There is also evidence for some hydrothermal activity at both Clearwaters shortly after impact [*Dence et al.*, 1965; *Osinski et al.*, 2013]. Aqueous alteration, however, was more intense at East than at West [*Dence et al.*, 1965; *Schmieder et al.*, 2015]. Furthermore, work by *Lambert* [1982] at Rochechouart indicates that weathering can fractionate, but not entirely erase, the impactor signature. Studies at other terrestrial craters reached similar conclusions [*Koeberl*, 1998; *Tagle and Hecht*, 2006; *Goderis et al.*, 2013]. Hence, it is unlikely that impact melts at West Clearwater had a chondritic signature that was later removed by weathering or aqueous alteration.

4.1.3.2. Erosion

The final possibility considered here is that the impactor signature at West Clearwater was concentrated in only part of the melt sheet, which has since been eroded

away. *Rae et al.* [2017] modeled the formation of West Clearwater using the iSALE shock physics code. Based on their models, *Rae et al.* [2017] inferred that West Clearwater has experienced ~2 km of erosion. However, this value depends on the parameters chosen for acoustic fluidization in the iSALE models. Nevertheless, West must have been heavily eroded based on its current appearance.

East Clearwater presumably experienced further erosion during the 180 million years that elapsed between the formation of East and West. The absence of a topographic rim at East Clearwater, in contrast to the ~425 m tall topographic rim at West Clearwater [*Grieve,* 2006] indicates that erosion at East was quite significant. The topographic rim at West, however, is inconsistent with a structurally uplifted crater rim of only 34 km since *Grieve* [2006] suggests that the crater may have been much larger. Regardless, the impact melts from East Clearwater that survived erosion contain clear meteoritic signatures. Hence, it is difficult to envision a scenario in which melts that bear a meteoritic component would have been eroded from West but not East, unless the meteoritic component at East were preferentially near the bottom of the melt sheet and all but this lowest portion of the melt sheet has been eroded from East.

4.1.4. Summary

Table 9 summarizes the viability of the explanations proposed for the non-detection of a meteoritic signature at West Clearwater.

4.2. The signature at East Clearwater

Although the non-detection of an impactor signature at West Clearwater is unusual, the meteoritic component at East Clearwater is also unusual. It is significantly higher than the <1 wt.% seen at most terrestrial craters [*Koeberl*, 1998; *Tagle and Hecht,* 2006; *Koeberl et al.*, 2012; *Goderis et al.*, 2013; *Koeberl*, 2014]. The new data reported here, combined with the literature data in Supplementary Table S2, reveals an average ordinary chondrite component of 5.1 ± 1.7 wt.% in impact melts at East. Only Morokweng, which has up to 5.7 wt.% ordinary chondrite in its melt, has a comparable amount of meteoritic material in its impact melt [*McDonald et al.*, 2001; *Goderis et al.*, 2013].

The unusually high meteoritic component at East is best explained by a low-velocity impact. Models of Earth's impact flux predict speeds as low as ~10 km s^{-1} [*Le Feuvre and Wieczorek,* 2011]. These relatively "gentle" speeds favor projectile delivery. A lower velocity impact increases the fraction of the impactor that melts rather than vaporizes [*O'Keefe and Ahrens,* 1977; *Pierazzo et al.,* 1977]. This enhancement could increase the level of meteoritic material incorporated into impact melts. Such a scenario has a low probability, but the number of craters with meteoritic components comparable to East Clearwater is also low.

4.3. Large-scale asymmetries in meteoritic signatures

In oblique hypervelocity impact experiments, the projectile component is preserved asymmetrically [*Daly and Schultz,* 2015, 2016, 2017]. These asymmetries develop at

impact angles at high as 60° and become increasingly acute as impact angle decreases to 15° [*Daly and Schultz,* 2017]. In metal targets, the uprange crater wall preserves enhanced levels of projectile material [*Daly and Schultz,* 2017]. Recent shock physics code calculations by *Crawford and Schultz* [2014] showed enhanced preservation uprange at larger scales (i.e., the scale of the Moscoviense basin on the moon). Both experiments and shock physics codes show that area downrange of the crater can be peppered with projectile-rich debris. If East and West Clearwater were oblique impacts, then the impactor component may, at large scales, be distributed asymmetrically in the melt sheets. Some areas near the uprange wall might be highly enriched in a meteoritic component, whereas other areas might have a paucity of meteoritic material. If East were an oblique (<45°) impact from the southeast, then such an asymmetry might explain the unusually high meteoritic component in drill core DCW 2-63. Multiple cores in the melt sheet at various azimuths could address such a possibility. A similar approach would also be valuable at West in areas where the melt sheet may be accessible by drilling.

5. Conclusions

The search for meteoritic signatures in the impact melt of West Clearwater crater again yielded no detection. Such a null result persisted despite tripling the number of samples searched and using osmium isotopes, the most sensitive tool available for detecting meteoritic signatures in impactites [*Koeberl and Shirey*, 1997; *Koeberl*, 1998; *Tagle and Hecht*, 2006; *Koeberl et al.*, 2012; *Goderis et al.*, 2013; *Koeberl*, 2014]. At East Clearwater, in contrast, osmium isotope analyses revealed extremely strong meteoritic signatures,

consistent with earlier work by *Palme et al.* [1978, 1979] and others [*Evans et al.*, 1993; *Schmidt*, 1997; *McDonald*, 2002]. The starkly different levels of impactor contamination at East and West Clearwater provide further evidence that the two craters formed under different conditions and, therefore, at two separate times.

The impactor signatures (or its absence) at East and West Clearwater may be due to low-probability impact scenarios. East may have formed during an unusually low-speed impact, whereas West may have formed during the impact of a basaltic achondrite-like object, such as a V-type asteroid. Such a scenario could be tested using chromium isotopes. Basaltic achondrites are not particularly common. However, dynamical models indicate that V-type asteroids large enough to form craters like the Clearwaters impact Earth occasionally [*Galiazzo et al.,* 2017]. Alternatively, the character of the signature at East and West may reflect large-scale asymmetries in the meteoritic component in the melt sheets of these two craters. Impact experiments [*Daly and Schultz,* 2017] and models [*Schultz and Crawford,* 2014] both reveal such asymmetries. New drilling campaigns could evaluate whether large-scale asymmetries in the impactor component exist in the two melt sheets.

6. Acknowledgements

7. References

Biren, M. B., M. C. van Soest, J.-A. Wartho, K. V. Hodges, and J. G. Spray (2016), Diachroneity of the Clearwater West and Clearwater East impact structures indicated by the (U–Th)/He dating method, *Earth Planet. Sci. Lett.*, *453*, 56–66, doi:10.1016/j.epsl.2016.07.053.

Bostock, H. H. (1969), *The Clearwater Complex, New Quebec*, Geological Survey of Canada.

Byerly, B. L., and J. C. Lassiter (2012), Evidence from mantle xenoliths for lithosphere removal beneath the central Rio Grande Rift, *Earth Planet. Sci. Lett.*, *355–356*, 82–93, doi:10.1016/j.epsl.2012.08.034.

Chatterjee, R., and J. C. Lassiter (2016), ^{186}Os/^{188}Os variations in upper mantle peridotites: Constraints on the Pt/Os ratio of primitive upper mantle, and implications for late veneer accretion and mantle mixing timescales, *Chem. Geol.*, *442*, 11–22, doi:10.1016/j.chemgeo.2016.08.033.

Collins, G. S., T. Kenkmann, G. R. Osinski, and K. Wünnemann (2008), Mid-sized complex crater formation in mixed crystalline-sedimentary targets: Insight from modeling and observation, *Meteorit. Planet. Sci.*, *43*(12), 1955–1977, doi:10.1111/j.1945-5100.2008.tb00655.x.

Dale, C. W., K. W. Burton, R. C. Greenwood, A. Gannoun, J. Wade, B. J. Wood, and D. G. Pearson (2012), Late Accretion on the Earliest Planetesimals Revealed by the Highly Siderophile Elements, *Science*, *336*(6077), 72–75, doi:10.1126/science.1214967.

Daly, R.T., and P.H. Schultz (2015), Predictions for impactor contamination on Ceres based on hypervelocity impact experiments, *Geophys. Res. Lett.,* 42, 7890 – 7898.

Daly, R. T., and P. H. Schultz (2016), Delivering a projectile component to the vestan regolith, *Icarus*, *264*, 9–19, doi:10.1016/j.icarus.2015.08.034.

Daly, R. T., and P. H. Schultz (2017), Projectile Preservation During Oblique Hypervelocity Impacts, *Lunar and Planetary Science Conference XXXXVIII*, abstract no. 1573.

Day, J. M. D., A. D. Brandon, and R. J. Walker (2016), Highly Siderophile Elements in Earth, Mars, the Moon, and Asteroids, *Rev. Mineral. Geochem.*, *81*(1), 161–238, doi:10.2138/rmg.2016.81.04.

Dence, M. R. (1968), Shock zoning at Canadian craters: Petrography and structural implications, in *Shock metamorphism of natural materials*, pp. 169–184, Mono Book Corp.

Dence, M. R., M. J. S. Innes, and C. S. Beals (1965), On the Probable Meteorite Origin of the Clearwater Lakes, Quebec, *J. R. Astron. Soc. Can.*, *59*, 13–22.

Dressler, B. O., and W. U. Reimold (2001), Terrestrial impact melt rocks and glasses, *Earth-Sci. Rev.*, *56*(1–4), 205–284, doi:10.1016/S0012-8252(01)00064-2.

Evans, N. J., D. C. Gregoire, R. A. F. Grieve, W. D. Goodfellow, and J. Veizer (1993), Use of platinum-group elements for impactor identification - Terrestrial impact craters and Cretaceous-Tertiary boundary, *Geochim. Cosmochim. Acta*, *57*, 3737–3748, doi:10.1016/0016-7037(93)90152-M.

Farley, K.A., A. Montanari, E.M. Shoemaker, C.S. Shoemaker (1998), Geochemical evidence for a comet shower in the late Eocene, *Science,* 280, 1250–1253.

Fleet, M. E., J. H. Crocket, and W. E. Stone (1996), Partitioning of platinum-group elements (Os, Ir, Ru, Pt, Pd) and gold between sulfide liquid and basalt melt, *Geochim. Cosmochim. Acta*, *60*(13), 2397–2412, doi:10.1016/0016-7037(96)00100-7.

Galiazzo, M. A., E. A. Silber, and D. Bancelin (2017), V-type near-Earth asteroids: Dynamics, close encounters and impacts with terrestrial planets, *Astron. Nachrichten*, doi:10.1002/asna.201613273.

Gault, D. E., and J. A. Wedekind (1978), Experimental studies of oblique impact, *Proceedings of the 9th Lunar and Planetary Science Conference,* 374–376.

Goderis, S., F. S. Paquay, and P. Claeys (2013), Projectile identification in terrestrial impact structures and ejecta materials, in *Impact cratering: Processes and products*, pp. 223–239, Wiley-Blackwell.

Goebel, E., H. Baddenhausen, H. Palme, and U. Reimold (1980), The projectile of the Lappajarvi impact crater, *Z. Naturforschung Teil A*, *35*, 197–203, doi:10.1515/zna-1980-0205.

Grieve, R.A.F. (2006) Clearwater, in *Impact structures in Canada,* Geological Association of Canada, p. 51 – 62.

Grieve, R. A. F., M. R. Dence, and P. B. Robertson (1977), Cratering processes - As interpreted from the occurrence of impact melts, in *Impact and explosion cratering: planetary and terrestrial implications,* pp. 791–814.

Grieve, R. A. F., R. B. Bottomley, M. A. Bouchard, P. B. Robertson, C. J. Orth, and M. Attrep Jr. (1991), Impact melt rocks from New Quebec Crater, Quebec, Canada, *Meteoritics*, *26*, 31–39.

Kelley, S. P., and S. C. Sherlock (2013), The geochronology of impact craters, in *Impact cratering: Processes and products*, pp. 240–253, Wiley-Blackwell.

Koeberl, C. (1998), Identification of meteoritic components in impactites, *Geol. Soc. Lond. Spec. Publ.*, *140*(1), 133–153, doi:10.1144/GSL.SP.1998.140.01.11.

Koeberl, C. (2014), 2.5 - The Geochemistry and Cosmochemistry of Impacts, in *Treatise on Geochemistry (Second Edition)*, edited by H. D. Holland and K. K. Turekian, pp. 73–118, Elsevier, Oxford.

Koeberl, C., A. Shukolyukov, and G. W. Lugmair (2007), Chromium isotopic studies of terrestrial impact craters: Identification of meteoritic components at Bosumtwi,

Clearwater East, Lappajärvi, and Rochechouart, *Earth Planet. Sci. Lett.*, *256*, 534–546, doi:10.1016/j.epsl.2007.02.008.

Koeberl, C., and S. B. Shirey (1997), Re–Os isotope systematics as a diagnostic tool for the study of impact craters and distal ejecta, *Palaeogeogr. Palaeoclimatol. Palaeoecol.*, *132*(1–4), 25–46, doi:10.1016/S0031-0182(97)00045-X.

Koeberl, C., P. Claeys, L. Hecht, and I. McDonald (2012), Geochemistry of impactites, *Elements*, *8*, 37–42.

Kyte, F.T., A. Shukolykov, A.R. Hildebrand, G.W. Lugmair, and J. Hanova, Chromium-isotopes in Late Eocene impact spherules indicate a likely asteroid belt provenance, *Earth Planet. Sci. Lett.,* 302, 279 – 286, doi:10.1016/j.epsl.2010.12.006

Lambert, P. (1982), Anomalies within the system: Rochechouart target rock meteorite, *Geol. Soc. Am. Spec. Pap.*, *190*, 57–68, doi:10.1130/SPE190-p57.

Le Feuvre, M., and M. A. Wieczorek (2011), Nonuniform cratering of the Moon and a revised crater chronology of the inner Solar System, *Icarus,* 214(1), 1–20, doi:10.1016/j.icarus.2011.03.010.

Lugmair, G.W. and A. Shukolyukov (1998), Early solar system timescales according to ^{53}Mn-^{53}Cr systematics, *Geochem. Cosmochim. Acta,* 62, 2863–2886.

McDonald, I., K. Bartosova, C. Koeberl (2009), Search for a meteoritic component in impact breccia from the Eyreville core, Chesapeake Bay impact structure:

Considerations from platinum-group element contents, *GSA Spec Pap.,* 458, 469–479.

McDonald, I. (2002), Clearwater East impact structure: A re-interpretation of the projectile type using new platinum-group element data from meteorites, *Meteorit. Planet. Sci.*, *37*, 459–464, doi:10.1111/j.1945-5100.2002.tb00828.x.

McDonald, I., M. A. G. Andreoli, R. J. Hart, and M. Tredoux (2001), Platinum-group elements in the Morokweng impact structure, South Africa: Evidence for the impact of a large ordinary chondrite projectile at the Jurassic-Cretaceous boundary, *Geochim. Cosmochim. Acta*, *65*(2), 299–309, doi:10.1016/S0016-7037(00)00527-5.

Morgan, J. W., H. Higuchi, R. Ganapathy, and E. Anders (1975), Meteoritic material in four terrestrial meteorite craters, *Proceedings of the 6th Lunar and Planetary Science Conference*, 1609–1623.

Murray, R. W., D. J. Miller, and K. A. Kryc (2000), Analysis of major and trace elements in rocks, sediments, and interstitial waters by inductively-coupled plasma-atomic emission spectrometry (ICP-AES), *ODP Tech. Note 29*.

O'Keefe, J.D. and Ahrens, T.J. (1977), Impact-induced energy partitioning, melting, and vaporization on terrestrial planets, *Proc. 8th Lunar Planet. Sci. Conf.,* 3357–3374.

Osinski, G. R. et al. (2013), Impact-generated hydrothermal systems on Earth and Mars, *Icarus*, *224*(2), 347–363, doi:10.1016/j.icarus.2012.08.030.

Palme, H., E. Goebel, and R. A. F. Grieve (1979), The distribution of volatile and siderophile elements in the impact melt of East Clearwater, Quebec, *Proceedings of the 10th Lunar and Planetary Science Conference*, 2465–2492.

Palme, H., M. J. Janssens, H. Takahashi, E. Anders, and J. Hertogen (1978), Meteoritic material at five large impact craters, *Geochim. Cosmochim. Acta*, *42*, 313–323, doi:10.1016/0016-7037(78)90184-9.

Palme, H., R. A. F. Grieve, and R. Wolf (1981), Identification of the projectile at the Brent crater, and further considerations of projectile types at terrestrial craters, *Geochim. Cosmochim. Acta*, *45*, 2417–2424, doi:10.1016/0016-7037(81)90095-8.

Pierazzo, E., A. M. Vickery, and H. J. Melosh (1997), A Reevaluation of Impact Melt Production, *Icarus*, *127*, 408–423, doi:10.1006/icar.1997.5713.

Pierazzo, E., and H. J. Melosh (2000), Hydrocode modeling of oblique impacts: The fate of the projectile, *Meteorit. Planet. Sci.*, *35*, 117–130, doi:10.1111/j.1945-5100.2000.tb01979.x.

Rae, A. S. P., G. S. Collins, R. a. F. Grieve, G. R. Osinski, and J. V. Morgan (2017), Complex crater formation: Insights from combining observations of shock pressure distribution with numerical models at the West Clearwater Lake impact structure, *Meteorit. Planet. Sci.*, doi:10.1111/maps.12825.

Rosa, D. F. (2011), The Sheet of Impact Melt at West Clearwater Lake, Northern Quebec, PhD dissertation, The McGill University.

Rosa, D. F., and R. F. Martin (2010), A Spurrite-, Merwinite- and Srebrodolskite-Bearing Skarn Assemblage, West Clearwater Lake Impact Crater, Northern Quebec, *Can. Mineral.*, *48*(6), 1519–1532, doi:10.3749/canmin.48.5.1519.

Schmidt, G. (1997), Clues to the nature of the impacting bodies from platinum-group elements (PGEs, RE and Au) in borehole samples from the Clearwater East crater (Canada) and the Boltysh impact crater (Ukraine), *Meteorit. Planet. Sci.*, *32*, 761–767, doi:10.1111/j.1945-5100.1997.tb01566.x.

Schmieder, M., W. H. Schwarz, M. Trieloff, E. Tohver, E. Buchner, J. Hopp, and G. R. Osinski (2015), New 40Ar/39Ar dating of the Clearwater Lake impact structures (Québec, Canada) – Not the binary asteroid impact it seems?, *Geochim. Cosmochim. Acta*, *148*, 304–324, doi:10.1016/j.gca.2014.09.037.

Schultz, P. H., and D. E. Gault (1990), Prolonged global catastrophes from oblique impacts, *Geol. Soc. Am. Spec. Pap.*, *247*, 239–262, doi:10.1130/SPE247-p239.

Schultz, P.H. (1992), Atmospheric Effects on Ejecta Emplacement and Crater Formation on Venus from Magellan, *J. Geophys. Res.,* 97, 16183–16248.

Schultz, P.H., Sugita, S., Eberhardy, C.A., Ernst, C.M. (2006), The role of ricochet on impact vaporization, *Int. J. Impact Eng*. 33, 771–780.

Schultz, P. H., B. Hermalyn, and J. Veverka (2013), The Deep Impact crater on 9P/Tempel 1 from Stardust-NExT, *Icarus,* 222, 202–515.

Schultz, P. H. (2007), Impact cratering in soft sediment layers, *Bridging the Gap II: Effect of Target Properties on the Impact Cratering Process,* abstract no. 8033.

Smith, S.K., R.A.F. Grieve, J.R. Harris, and V. Singhroy (1999), The Utilization of RADARSAT-1 Imagery for the Characterization of Terrestrial Impact Landforms, *Canadian J. Remote Sens.,* 25, 218–228.

Stickle, A. M., and P. H. Schultz (2013), Investigating pressure magnitudes at depth for oblique impacts into layered targets: Applications to terrestrial impacts in sedimentary targets, *Met. Planet. Sci.*, 48, 1638–1650, doi: 10.1111/maps.12152.

Stickle, A. M., and P. H. Schultz (2012), Subsurface damage from oblique impacts into low-impedance layers, *J. Geophys. Res. Planets*, *117*(E7), E07006, doi:10.1029/2011JE004043.

Tagle, R., and L. Hecht (2006), Geochemical identification of projectiles in impact rocks, *Meteorit. Planet. Sci.*, *41*, 1721–1735, doi:10.1111/j.1945-5100.2006.tb00448.x.

Tagle, R., J. G. Spray, and R. T. Schmitt (2008), Search for Projectile Traces in Melt Rocks of the Charlevoix and Dellen Impact Structures, *Lunar and Planetary Science Conference XXXIX*, abstract 1787.

Tagle, R., P. Claeys, R. A. F. Grieve, R. T. Schmitt, and J. Erzinger (2006), Evidence for a Second L Chondrite Impact in the Late Eocene: Preliminary Results from the Wanapitei Crater, Canada, *Lunar and Planetary Science Conference XXXVII*, abstract 1278.

Weissman, P.R. (2006), The cometary impactor flux at Earth, in *Near Earth Objects, Our Celestial Neighbors: Opportunities and Risk,* Proceedings IAU Symposium No. 236.

Wolf, R., A. B. Woodrow, and R. A. F. Grieve (1980), Meteoritic material at four Canadian impact craters, *Geochim. Cosmochim. Acta*, *44*(7), 1015–1022, doi:10.1016/0016-7037(80)90289-6.

Tables

Table 1. Samples analyzed in this study.

	Sample ID	Sample mass (g)	Depth (m)	Sample description*	Description of corresponding core section[†]
Clearwater East	DCW 2-63-1100	5.4	311.5[‡]	Dark, clast-free impact melt.	Medium-grained melt; grain size up to 0.6 mm. Few obvious inclusions.
	DCW 2-63-1120	4.6	316.8[‡]	Dark, clast-free impact melt.	Not logged.
	DCW 1-64-568	2.8	173.1[‡]	Pink, granitic gneiss with vein (cataclastic?). Country rock.	Medium- to fine-grained dark gray gneiss with hornblende, biotite, and chlorite. Some brecciation.
	DCW 1-64-1770	2.7	539.5[‡]	Granitic with shatter cones. Country rock.	Gneiss. Brecciated.
	DCW 1-64-3270	3.8	996.7[‡]	Granitic material. Country rock.	Medium-grained gray gneiss with dark green inclusions (chlorite?). Breccia.
Clearwater West	DCW 5-63-686	2.9	209.1	Large melt area.	- [§]
	DCW 21-62	13.3	-	Impact melt with mesocratic-looking grains.	N/A (surface sample)
	DCW 77-13	5.5	-	Gray, medium- to fine-grained impact melt.	N/A (surface sample)
	DCW 77-36	4.3	-	Fresh, crystalline impact melt.	N/A (surface sample)
	DCW 20-62B	3.3	-	Gabbroic country rock from central island.	N/A (surface sample)

*Lucy Thompson (Personal communication).
[†]Descriptions for DCW 2-63 from the 1978 log of R. A. F. Grieve. Descriptions for DCW 1-64 come from the 1991 log of Ralf Hische, translated by Lucy Thompson. Copies of these logs are available at the Planetary and Space Science Centre at the University of New Brunswick.
[‡]Drill hole 2-63 slanted with depth. The depths given are "true depths" that have been corrected for this slant using Fig. 2 of *Palme et al.* [1979].
[§]Dence described surrounding samples as sheared/disrupted granitic and mafic gneisses cut by red-toned melt veins. Copies of these logs are available at the Planetary and Space Science Centre at the University of New Brunswick.

Table 2. Results of major element geochemical analyses.

Sample ID	Al$_2$O$_3$ (wt.%)	CaO (wt.%)	FeO$_T$ (wt.%)	K$_2$O (wt.%)	MgO (wt.%)	MnO (wt.%)	Na$_2$O (wt.%)	P$_2$O$_5$ (wt.%)	SiO$_2$ (wt.%)	TiO$_2$ (wt.%)
East Clearwater										
DCW 2-63-1100 avg.*	14.24	3.43	4.88	3.43	3.57	0.07	3.32	0.19	62.68	0.46
DCW 2-63-1100 no.1*	14.50	3.47	4.95	3.51	3.70	0.07	3.41	0.19	64.29	0.48
DCW 2-63-1100 no.2*	14.44	3.48	5.00	3.41	3.60	0.07	3.32	0.20	63.65	0.47
DCW 2-63-1100 no.3*	13.78	3.35	4.69	3.38	3.43	0.07	3.21	0.19	60.09	0.44
DCW 2-63-1120*	14.15	3.21	5.00	3.47	3.09	0.06	3.39	0.20	62.68	0.50
DCW 1-64-568†	13.46	1.70	1.19	5.57	0.35	0.02	3.06	0.06	74.88	0.14
DCW 1-64-1770†	13.61	1.95	1.34	4.00	0.54	0.02	3.52	0.07	76.08	0.16
DCW 1-64-3270†	17.21	6.97	7.77	1.03	4.16	0.13	5.65	0.38	52.86	0.72
West Clearwater										
DCW 5-63-686*	13.30	6.43	13.44	0.10	5.46	0.14	5.34	0.38	49.97	2.26
DCW 21-62 avg.*	10.60	11.58	8.09	1.55	10.33	0.19	2.19	0.13	50.87	0.74
DCW 21-62 no. 1*	10.71	11.64	8.13	1.54	10.34	0.19	2.22	0.12	51.34	0.75
DCW 21-62 no. 2*	10.14	11.17	7.77	1.48	10.02	0.19	2.11	0.12	48.31	0.70
DCW 21-62 no. 3*	10.95	11.94	8.38	1.62	10.63	0.20	2.24	0.14	52.96	0.77
DCW 77-13*	15.67	4.13	4.57	3.40	2.43	0.03	3.59	0.25	62.84	0.62
DCW 77-36*	15.80	4.79	5.10	3.79	2.89	0.05	3.69	0.32	61.26	0.74
DCW 20-62B†	15.06	10.80	7.48	0.32	10.33	0.15	3.16	0.06	51.29	0.30

*Impact melt
†Country rock

Table 3. Results of minor element geochemical analyses.

Sample ID	Co (ppm)	Cr (ppm)	Cu (ppm)	Ni (ppm)
East Clearwater				
DCW 2-63-1100 avg.*	46	296	20	816
DCW 2-63-1100 no.1*	45	295	21	837
DCW 2-63-1100 no.2*	47	306	20	887
DCW 2-63-1100 no.3*	47	287	19	724
DCW 2-63-1120*	44	261	22	736
DCW 1-64-568[†]	3	2	1	1
DCW 1-64-1770[†]	3	1	2	2
DCW 1-64-3270[†]	32	66	65	22
West Clearwater				
DCW 5-63-686*	64	36	38	39
DCW 21-62 avg.*	40	373	28	111
DCW 21-62 no. 1*	41	385	37	137
DCW 21-62 no. 2*	39	350	21	89
DCW 21-62 no. 3*	42	384	25	107
DCW 77-13*	16	45	11	19
DCW 77-36*	20	32	23	12
DCW 20-62B[†]	42	218	141	191

*Impact melt
[†]Country rock

Table 4. Results of osmium isotope analyses.

Sample ID	Os (ppt)	187Os/188Os
East Clearwater		
DCW 2-63-1100*	26,580	0.1285 ± 0.00003
DCW 2-63-1120*	23,320	0.1281 ± 0.00001
DCW 1-64-568[†]	3	1.723 ± 0.032
DCW 1-64-1770[†]	2	7.500 ± 0.018
DCW 1-64-3270[†]	30	65.93 ± 0.06
West Clearwater		
DCW 5-63-686*	48	59.12 ± 0.18
DCW 21-62*	22	7.831 ± 0.017
DCW 77-13*	12	6.604 ± 0.009
DCW 77-36*	6	10.15 ± 0.02
DCW 20-62B[†]	46	8.489 ± 0.004

Table 5. Possible explanations for the non-detection of a meteoritic signature at West Clearwater.

Case 1: An impactor signature was never present.	Case 2: An impactor signature is present but undetected.	Case 3: An impactor signature used to be present but has been lost.
Possible reasons:	Possible reasons:	Possible reasons:
High-speed impact	Masking by an indigenous component	Weathering or remobilization
Highly oblique (<15°)	Inadequate sampling	Erosion
Target layering	Differentiated achondrite or cometary impactor	
Differences in sulfide mineralogy	Melt sheet heterogeneity (raisin bread)	
	Melt sheet heterogeneity (large-scale asymmetries)	

Table 6. Canadian craters whose impact melts have *not* revealed a meteoritic signature.

Crater name	Age (Ma)*	Diameter (km)†	Method	# of samples analyzed	Reference
Mistastin	36 ± 4	28	Platinum-group element abundances or ratios	15 total 5 surface samples in *Morgan et al.* [1975], 2 surface samples in *Wolf et al.* [1980], 4 surface samples in *Palme et al.* [1978]; 4 samples, presumably from the surface, in *Palme et al.* [1981]	*Morgan et al.* [1975]; *Palme et al.* [1978]; *Palme et al.* [1981]; *Wolf et al.* [1980]
West Clearwater	286.2 ± 2.2	36	Platinum-group element abundances or ratios (Palme et al., 1978); Os isotopes (this study)	6 total 2 surface samples in *Palme et al.* [1978]; 4 surface samples in this study	*Palme et al.* [1978]; this study
Saint Martin	220 ± 32	40	Platinum-group element abundances or ratios	1 surface sample	*Goebel et al.* [1980]
Manicouagan	214± 1	85	Platinum-group element abundances or ratios	4 total 2 surface samples in *Palme et al.* [1978]; 2 surface samples in *Palme et al.* [1981]	*Palme et al.* [1978]; *Palme et al.* [1981]

*All ages except West Clearwater from *Kelley and Sherlock* [2013]. West Clearwater from *Schmieder et al.* [2015].

†From the Earth Impact Database, http://www.passc.net/EarthImpactDatabase/

Table 7. Canadian craters whose impact melts have revealed a meteoritic signature.

Crater name	Age (Ma)*	Diameter (km)[†]	Method	# of samples analyzed	Reference
New Quebec	1.4 ± 0.1	3.44	Platinum-group element abundances or ratios	<u>6 total</u> 3 surface samples [*Grieve et al.,* 1991]; 3 surface samples [*Evans et al.,* 1993]	*Grieve et al.* [1991]; *Evans et al.* [1993]
Brent	>453	3.8	Platinum-group element abundances or ratios	<u>6 total</u> 4 drill core samples [*Palme et al.,* 1981]; 2 drill core samples [*Evans et al.,* 1993]	*Palme et al.* [1981; *Evans et al.* [1993]
Gow	< 250	5	Platinum-group element abundances or ratios	<u>3 surface samples</u>	*Wolf et al.* [1980]
Wanapitei	37.2 ± 1.2	7.5	Platinum-group element abundances or ratios	<u>16 total</u> 3 surface samples [*Wolf,* 1980]; 3 surface samples [*Evans et al.,* 1993]; 10 samples [*Tagle et al.,* 2006]	*Wolf et al.* [1980]; *Evans et al.* [1993]; *Tagle et al.* [2006]
Nicholson	< 400	12.5	Platinum-group element abundances or ratios	<u>3 surface samples</u>	*Wolf et al.* [1980]

Table 7 (cont.) Canadian craters whose impact melts have revealed a meteoritic signature.

Crater name	Age (Ma)*	Diameter (km)†	Method	# of samples analyzed	Reference
East Clearwater	460 – 470	26	Platinum-group element abundances or ratios; osmium isotopes (this study); chromium isotopes (Koeberl et al., 2007)	<u>24 total‡</u> 3 drill core samples [*Palme et al.,* 1978]; 13 drill core samples [*Palme et al.,* 1979]; 2 drill core samples [*Evans et al.,* 1993]; 5 drill core samples [*Schmidt,* 1997]; 1 drill core sample [*Koeberl et al.,* 2007]	*Evans et al.* [1993]; *Koeberl et al.* [2007]; *Palme et al.* [1978], *Palme et al.* [1979]; *Schmidt* [1997]
Charlevoix	342 ± 15	54	Platinum-group element abundances or ratios	<u>22 surface samples</u>	*Tagle et al.* [2008]

*All ages except East Clearwater from the Earth Impact Database, www.passc.net/EarthImpactDatabase. East Clearwater from *Schmieder et al.* [2015].

†From the Earth Impact Database, www.passc.net/EarthImpactDatabase

‡24 separate analyses are reported; however, several studies report data for samples with identical IDs. For instance, the two samples reported by *Palme et al.* [1978] are also reported by *Palme et al.* [1979], although the studies report data for different elements. One of the *Evans et al.* [1993] samples has the same ID as a sample in *Palme et al.* [1979]. The five samples in *Schmidt* [1997] have the same IDs as five of the samples in *Palme et al.* [1979]. *Koeberl et al.* [2007] report data for a sample with the same ID as a sample in *Palme et al.* [1979].

Table 8. Minor element variability in impact melts at East and West Clearwater.

Location		Os (ppb)	Ni (ppm)	Co (ppm)	Cr (ppm)
East Clearwater	Number of analyses	12	6	4	4
	Mean	29.7	700	39	246
	Maximum	55.5	946	50	296
	Minimum	0.038	80	16	140
	Range	55.5	866	34	156
	Standard deviation	13.7	315	15	72
	Relative standard deviation	46%	45%	40%	29%
West Clearwater	Number of analyses	7	59	48	64
	Mean	0.018	32	16	172
	Maximum	0.048	111	64	373
	Minimum	0.006	9	10	26
	Range	0.04	102	54	347
	Standard deviation	0.01	14	9	74
	Relative standard deviation	79%	42%	56%	43%

161

Table 9. Viability of possible explanations for the non-detection of a meteoritic signature at West Clearwater.

Case 1: An impactor signature was never present.	Case 2: An impactor signature is present but undetected.	Case 3: An impactor signature used to be present but has been lost.
Possible reasons:	Possible reasons:	Possible reasons:
High-speed impact: *inconsistent*	Masking by an indigenous component: *inconsistent*	Weathering or remobilization: *insufficient*
Highly oblique (<15°): *cannot be ruled out*	Inadequate sampling: *unlikely given results from other craters*	Erosion: *cannot be ruled out*
Target layering: *needs further study*	Differentiated achondrite or cometary impactor: *cannot be ruled out*	
Differences in sulfide mineralogy: *unlikely, but needs further study*	Melt sheet heterogeneity (raisin bread): *cannot be ruled out, but somewhat unlikely*	
	Melt sheet heterogeneity (large-scale asymmetries): *cannot be ruled out, but plausible given results from impact experiments*	

Figures
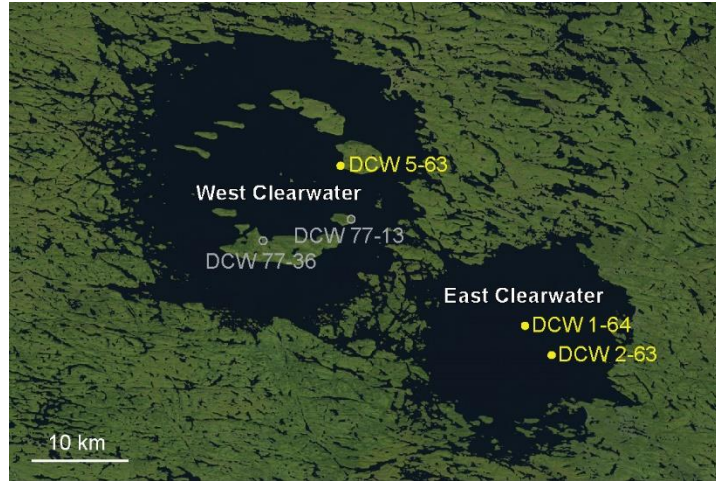
Figure 1. Locations of drill cores and surface samples from East and West Clearwater craters. Drill core DCW 1-64 penetrated shocked country rock in the central uplift at East. DCW 2-63 encountered the melt sheet. DCW 5-63 at West Clearwater tapped melt-rich breccias and shocked country rocks. Gray circles on islands inside West Clearwater mark the locations of two surface samples of impact melt. The locations of DCW 2-63 and DCW 5-63 come from Figure 2 of *Dence et al.* [1965]. The location of DCW 1-64 is estimated from Figure 2 of *Dence* [1968] and Figure 1 of *Palme et al*. [1979]. Locations of surface samples come from *Rosa* [2011]. Basemap: Landsat image LC80180212015250LGN00.
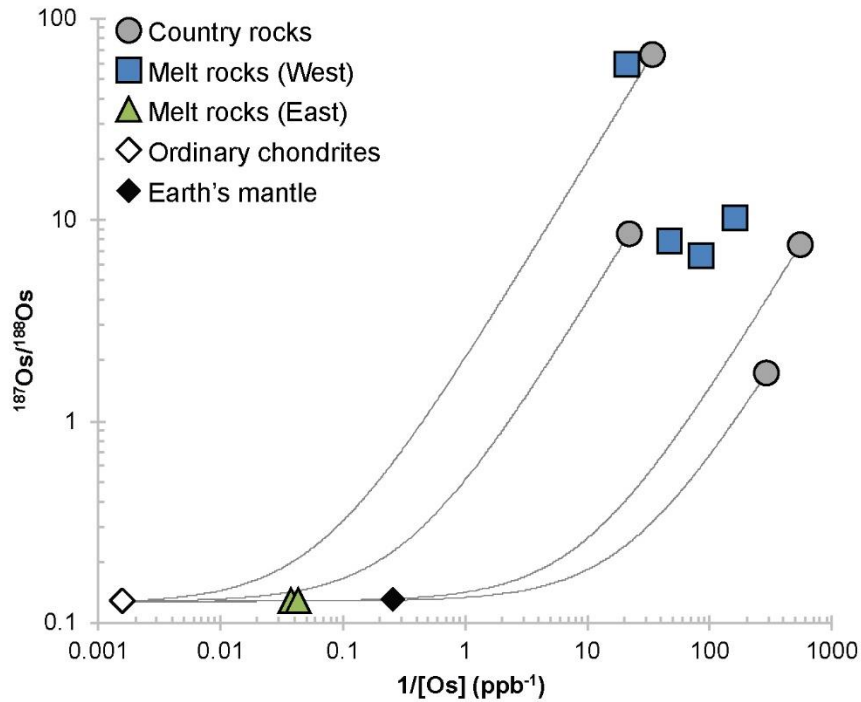
Figure 2. Osmium isotope ratios and osmium concentrations in samples of impact melt from East and West Clearwater craters, as well as nearby country rocks. Gray curves define two-component mixing between ordinary chondrites and each country rock analyzed. Samples from East Clearwater plot along these mixing curves, consistent with a meteoritic component at East Clearwater. The osmium data from East Clearwater rule out a significant mantle contribution. Impact melt samples from West Clearwater look like country rocks, with no signs of a meteoritic component. The data for Earth's mantle and ordinary chondrites come from *Day et al.* [2016].
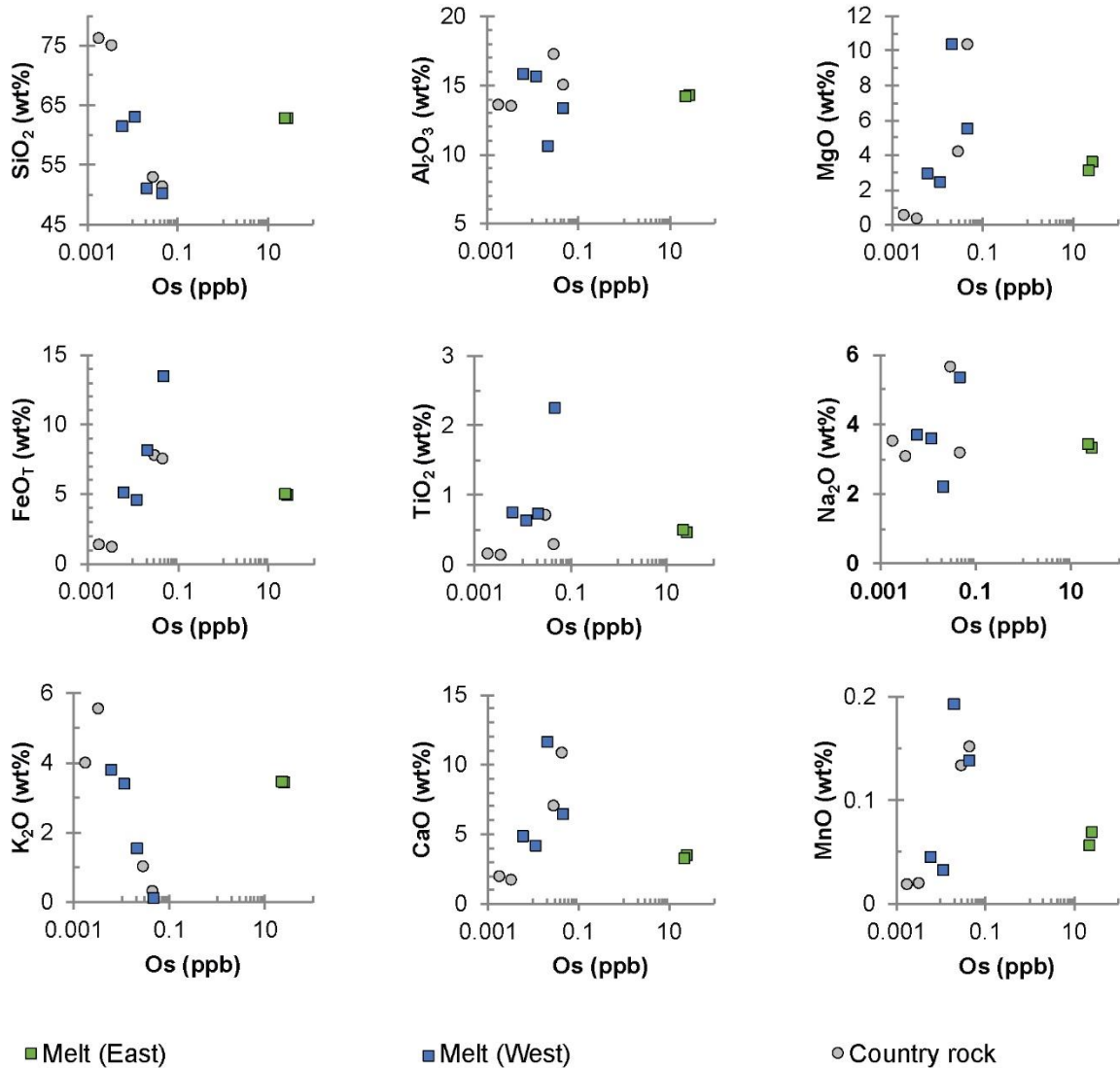
Figure 3. Relationships between osmium concentrations and major element oxides in country rocks and impact melts from East and West Clearwater. Impact melts from West Clearwater (blue squares) exhibit the same systematics as country rocks (gray circles), especially for SiO_2, MgO, FeO_T, K_2O, CaO, and MnO. This similarity provides additional evidence that impact melts from West Clearwater do not carry a meteoritic component. In contrast, the samples from East Clearwater (green squares) that carry a meteoritic component plot separately from the other samples.
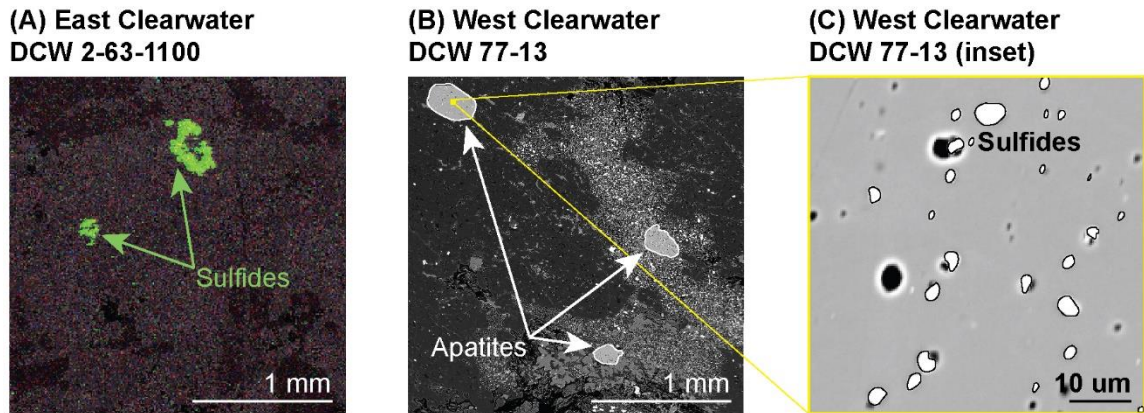
Figure 4. Differences between sulfides in impact melts at East and West Clearwater. (A) An element map of sulfur (green) draped over a back-scattered electron micrograph of a thin section of sample DCW 2-63-1100, an impact melt from East Clearwater. (B) and (C) show parts of a thin section of sample DCW 77-13, an impact melt from West Clearwater. Both (B) and (C) are back-scattered electron micrographs. Large sulfides like those seen in (A) are absent in the sample from West. (B) shows the only apatite grains in the thin section. (C) shows a small area of the largest apatite grain in (B). The area shown in (C) corresponds to the small yellow square in (B). The apatite grain hosts many tiny sulfide grains, outlined with black in (C). These grains contrast sharply with the much larger sulfides seen in (A).
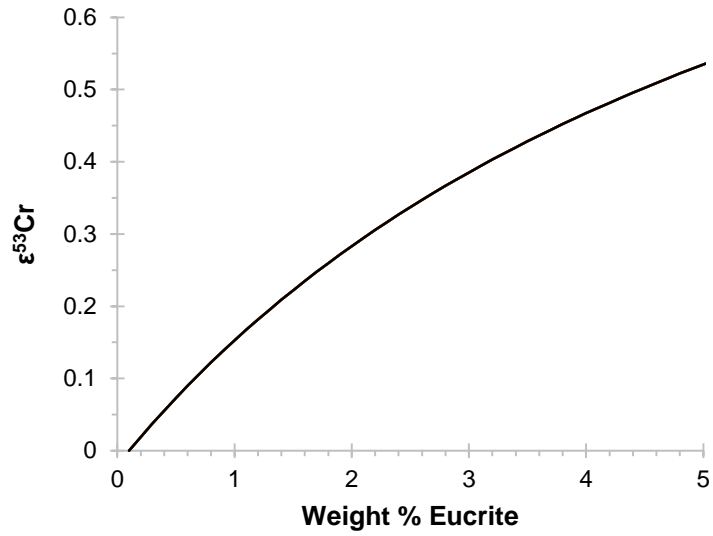
Figure 5. Results of a two-component mixing model between a eucrite impactor and country rocks at the Clearwater craters. The ε^{53}Cr of the impact melt is a function of the amount of eucrite added to the country rocks. A eucritic component in excess of 1 wt.% should be detectable.
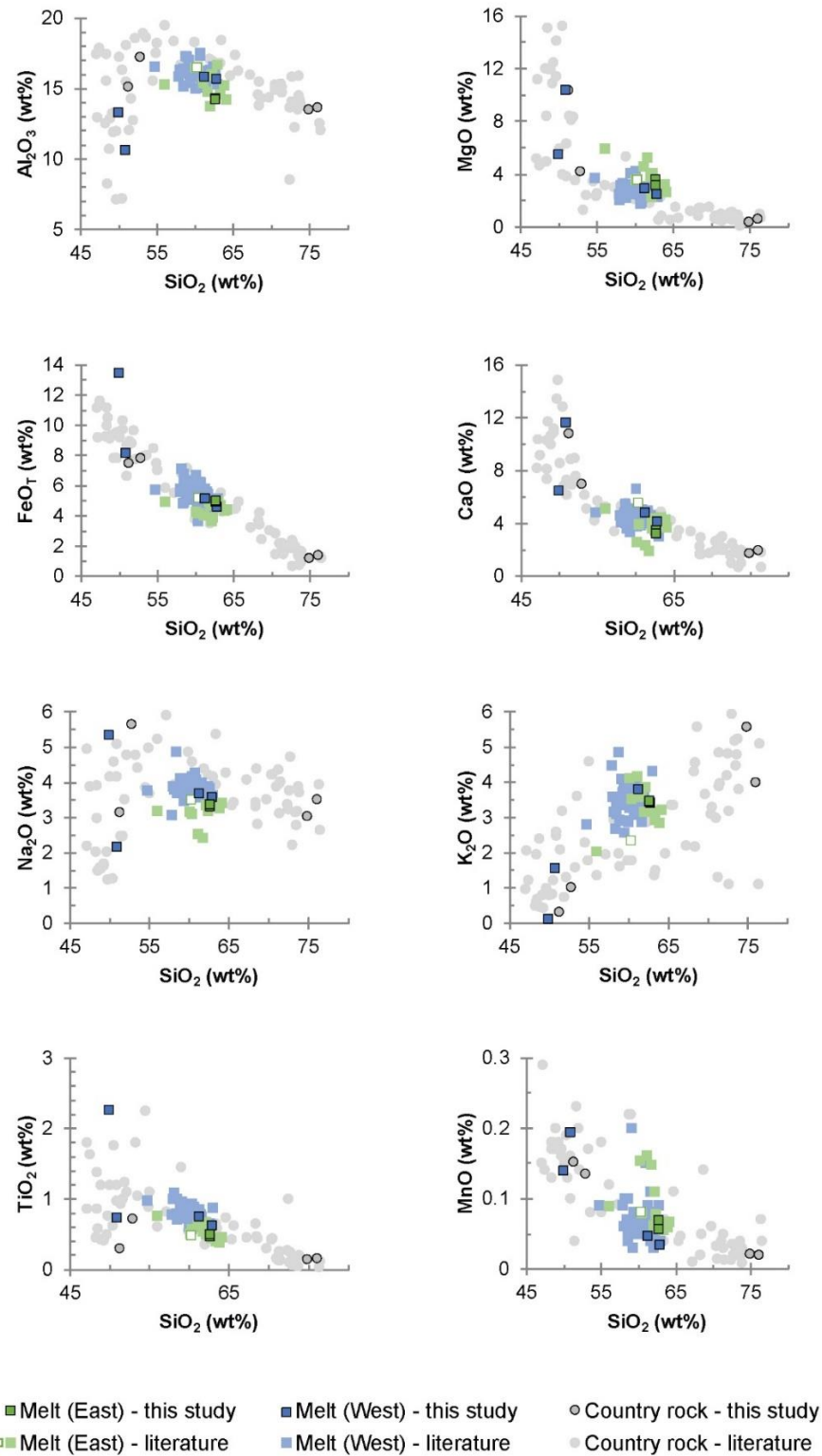
Figure 6. Harker diagrams for country rocks and impact melts from the Clearwaters. Impact melts from East and West are slightly offset in composition; however, the spread

of compositions in the melts at East and West appear similar. Blue squares denote impact melt rocks from West Clearwater. Green squares denote melts from East. Gray circles denote country rocks. Points outlined in black are from this study. Symbols with no outlines come from tables S1 – S3. A sample from East Clearwater that does not carry a meteoritic component is shown as a white square outlined with green to facilitate comparisons between this sample and samples from East Clearwater that carry a meteoritic signature.
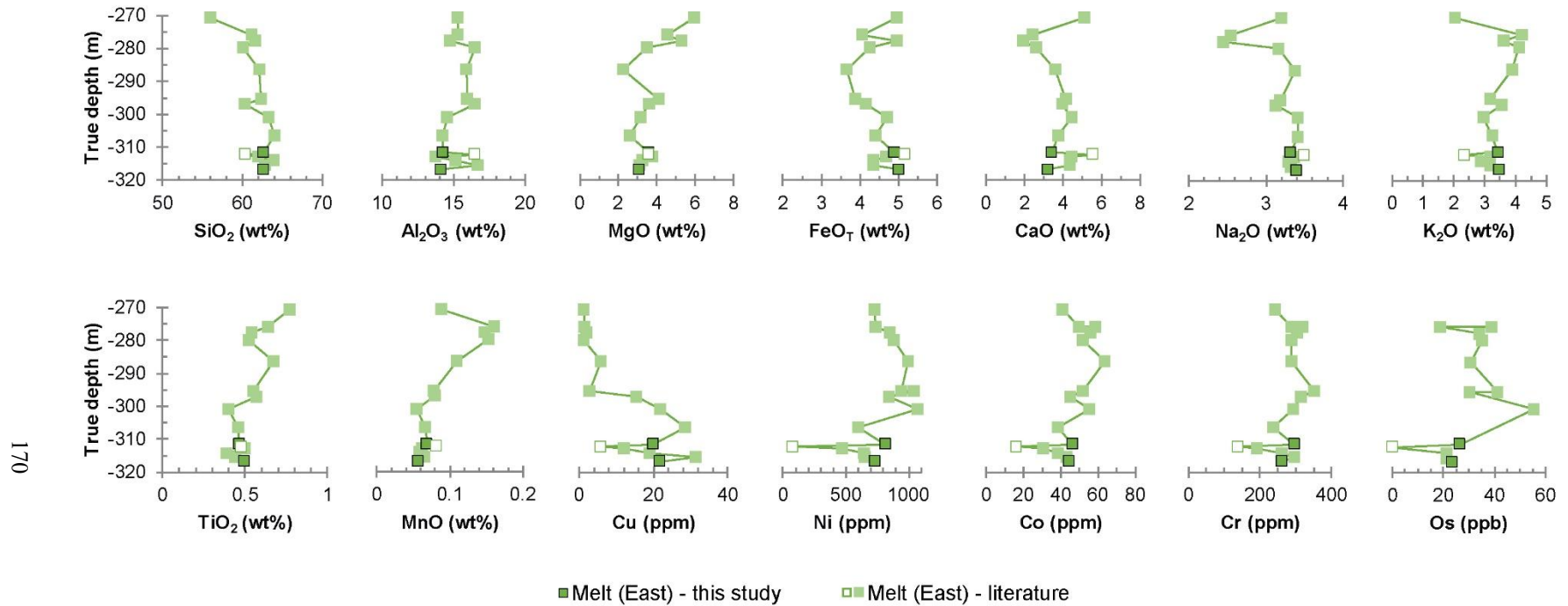
Figure 7. Depth profiles for major element oxides and select trace elements in drill core 2-63. Data in dark green were collected in this study. The remaining data come from the literature. All but one sample carry a meteoritic signature; the sample that does not carry this signature is shown as a white square outlined in green. Drill core 2-63 slanted with depth; the y-axis gives the samples' true depths, corrected using the data in *Palme et al.* [1979].
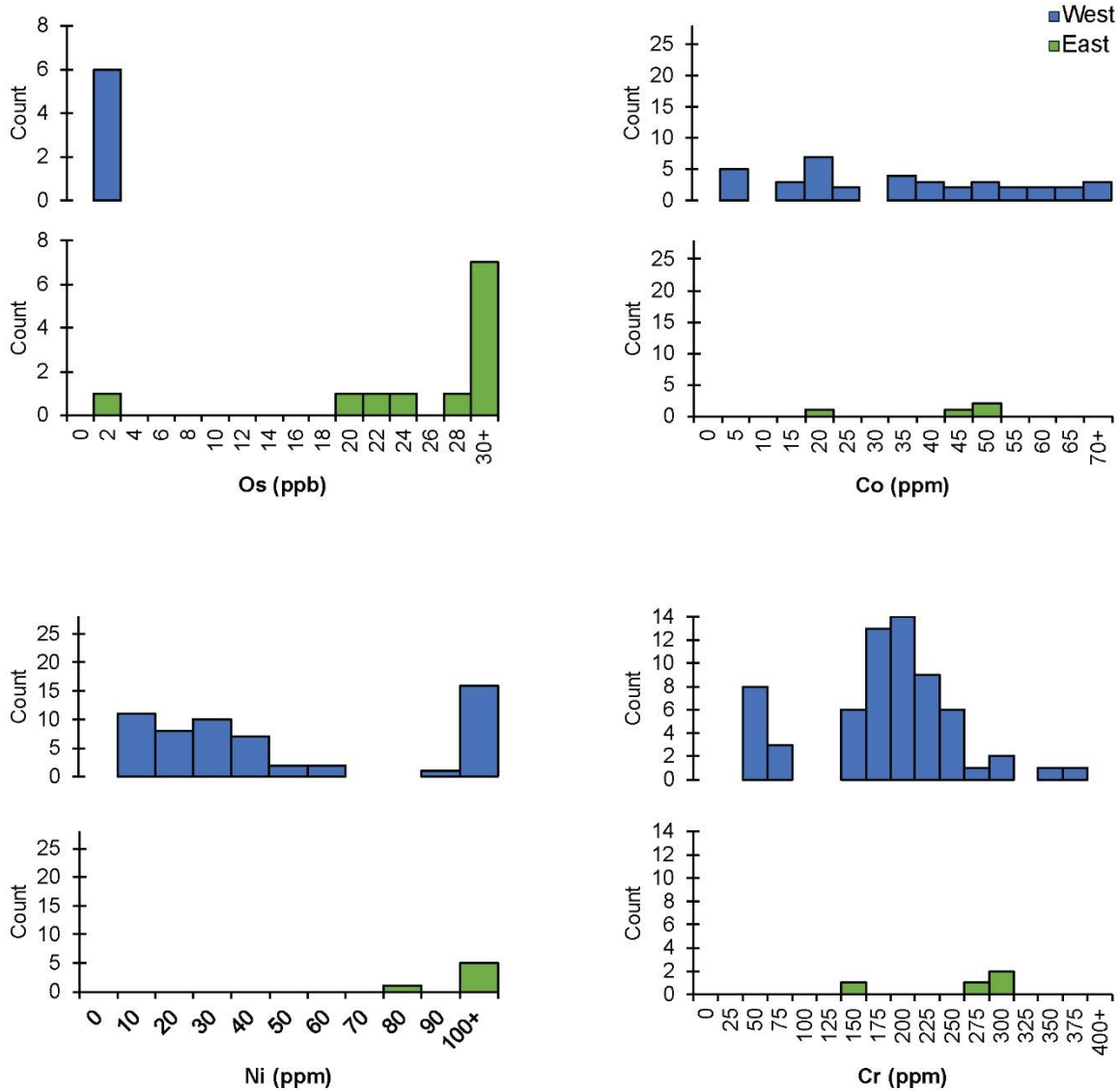
Figure 8. Histograms of Os, Co, Ni, and Cr in impact melts from East and West Clearwater (colored green and blue, respectively). Apart from osmium, more data is available at West. The concentration ranges of each element at the two craters are very different due to the meteoritic component at East. However, relative standard deviations indicate that these elements may be slightly more heterogeneously distributed at West.
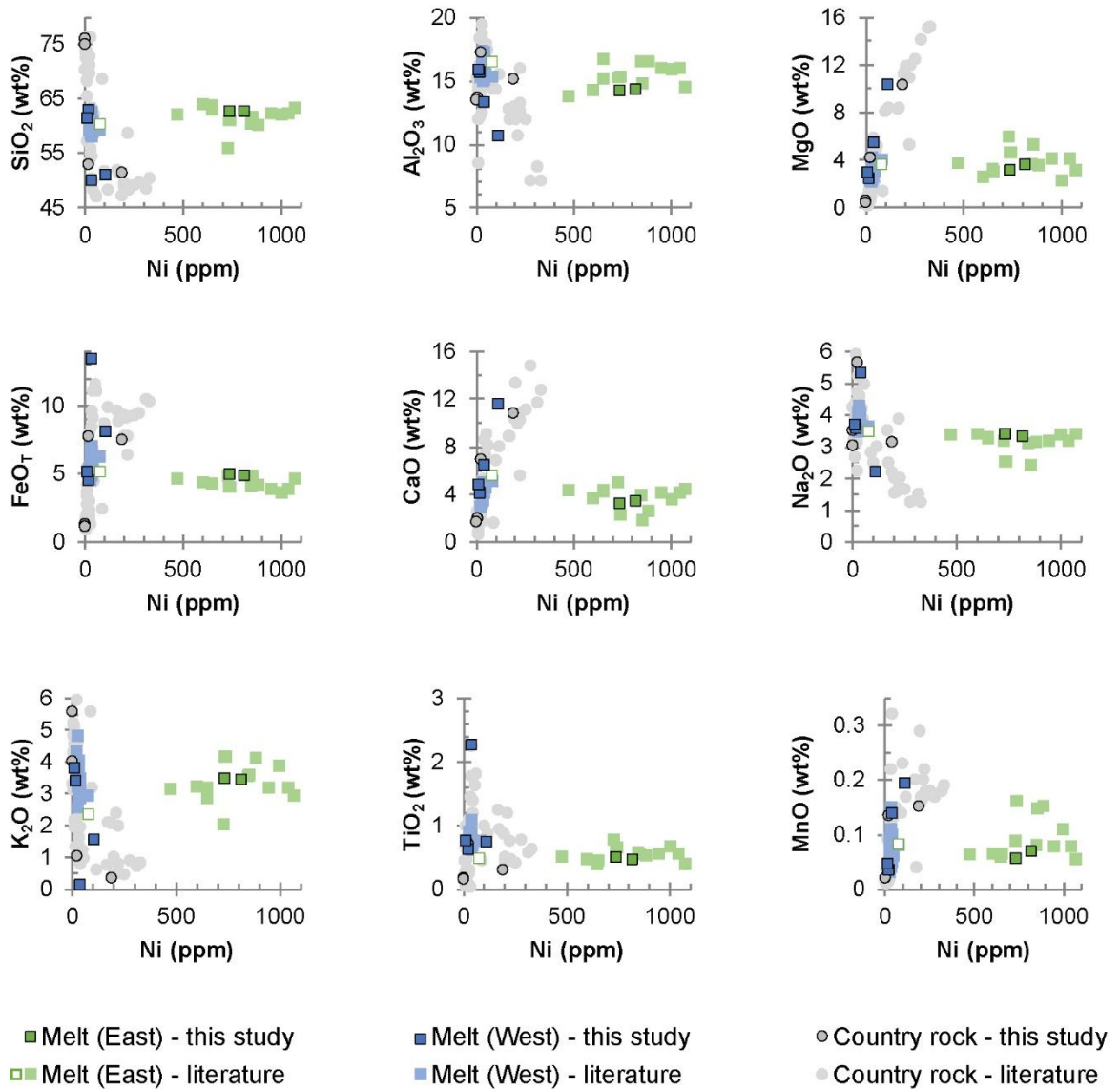
Figure 9. Correlations between Ni and major element oxides in country rocks and impact melts from East and West Clearwater. No melts from West have Ni abundances that suggest a meteoritic signature. Blue squares denote impact melt rocks from West Clearwater. Green squares denote impact melt rocks from East Clearwater. Gray circles denote country rocks. Points outlined in black are from this study. Symbols with no outlines come from tables S1 – S3. A sample from East Clearwater that does not carry a meteoritic

component is shown as a white square outlined with green to facilitate comparisons between this sample and samples from East Clearwater that carry a meteoritic signature.

Supplementary Tables

Table S1. Literature data for impact melts from East Clearwater crater (major elements).

Sample ID	SiO_2 (wt.%)	TiO_2 (wt.%)	Al_2O_3 (wt.%)	FeO_T* (wt.%)	MnO (wt.%)	MgO (wt.%)	CaO (wt.%)	Na_2O (wt.%)	K_2O (wt.%)	Ref
DCW 2-63-947	56.02	0.77	15.28	4.95	0.089	5.95	5.09	3.2	2.04	1
DCW 2-63-965	61.12	0.64	15.3	4.05	0.161	4.56	2.37	2.55	4.19	1
DCW 2-63-972	61.67	0.54	14.79	4.95	0.148	5.29	1.89	2.45	3.6	1
DCW 2-63-980.5	60.1	0.52	16.49	4.26	0.153	3.5	2.59	3.17	4.12	1
DCW 2-63-1005	62.13	0.67	15.89	3.66	0.11	2.24	3.6	3.38	3.88	1
DCW 2-63-1039	62.3	0.55	15.98	3.87	0.078	4.09	4.14	3.19	3.18	1
DCW 2-63-1045	60.35	0.57	16.47	4.16	0.079	3.6	3.96	3.13	3.54	1
DCW 2-63-1060	63.3	0.4	14.55	4.7	0.055	3.17	4.43	3.42	2.95	1
DCW 2-63-1082	64.07	0.46	14.22	4.4	0.066	2.6	3.72	3.42	3.23	1
DCW 2-63-1103	60.3	0.48	16.47	5.17	0.081	3.58	5.54	3.49	2.34	1
DCW 2-63-1105	62.03	0.5	13.75	4.67	0.062	3.76	4.41	3.37	3.16	1
DCW 2-63-1110	63.86	0.39	15.19	4.34	0.059	3.24	4.31	3.29	2.85	1
DCW 2-63-1115	62.87	0.44	16.7	5.02	0.065	3.1	4.34	3.33	3.18	1

*Data have been recalculated, if needed, to express all iron as FeO.

References: [1] *Palme et al.* [1979]

174

Table S2. Literature data for impact melts from East Clearwater crater (minor elements).

Sample ID	Os (ppb)	Re (ppb)	Ir (ppb)	Ru (ppb)	Rh (ppb)	Pt (ppb)	Pd (ppb)	Cu (ppm)	Ni (ppm)	Co (ppm)	Cr (ppm)	Ref
DCW 2-63-947								1.37	727	41.2	242	1
DCW 2-63-965								1.55	735	58.6	318	1
DCW 2-63-965	39.0	2.31	38.9				58.1		739	49.7	287	2
DCW 2-63-965	18.6	0.55	16.96	25.4	7.11		27.1					3
DCW 2-63-972	39.00		37.50					1.93	853	55.8	304	1
DCW 2-63-972	34.0	0.68	32.12	46.7	12.33		42.2					3
DCW 2-63-980.5								1.13	893	52.0	286	1
DCW 2-63-980.5	35.3	2.14	32.1				39.4		883			4
DCW 2-63-1005								5.80	998	63.6	352	1
DCW 2-63-1005	30.6	0.21	28.69	44.3	9.24		29.7					3
DCW 2-63-1039								2.74	1039	52.1	315	1
DCW 2-63-1039	41.4	2.43	40.1				48.5		946			4
DCW 2-63-1039	30.3	0.91	28.39	43.7	11.23		33.8					3
DCW 2-63-1045								15.40	845	45.2	269	1
DCW 2-63-1060	55.50		41.20			146.5		15.70	1370	55.7	292	1
DCW 2-63-1082								28.60	598	38.5	236	1
DCW 2-63-1103								5.69	97	15.3	140	1
DCW 2-63-1103	0.038	0.308	<0.02				<1.4		80	16.1	140	2
DCW 2-63-1105								12.10	470	30.7	190	1
DCW 2-63-1110								19.10	648	38.3	259	1
DCW 2-63-1110	21.2	0.53	19.80	30.5	8.01		28.2					3
DCW 2-63-1115			24.7			68.10		31.40	650	43.0	295	1

References: [1] *Palme et al.* [1979]   [2] *Palme et al.* [1981]   [3] *Schmidt* [1997]   [4] *Palme et al.* [1978]
[5] *Evans et al.* [1993]

Table S3. Literature data for impact melts from West Clearwater crater (major elements).

Sample ID	SiO$_2$ (wt.%)	TiO$_2$ (wt.%)	Al$_2$O$_3$ (wt.%)	FeO$_T$* (wt.%)	MnO (wt.%)	MgO (wt.%)	CaO (wt.%)	Na$_2$O (wt.%)	K$_2$O (wt.%)	Ref.
LP-122	61.23	0.85	15.84	5.78	0.09	2.83	4.60	3.91	3.24	2
LP-125	59.38	0.75	15.37	6.30	0.08	4.04	5.12	3.64	2.92	2
LP-130	59.47	0.78	16.32	5.70	0.08	3.26	4.32	4.13	2.57	2
LP-133	59.38	0.88	16.16	6.05	0.05	3.21	4.91	3.69	3.35	2
LP-21	58.93	0.72	17.26	5.78	0.07	2.80	4.98	4.09	2.94	2
LP-94	58.80	0.90	17.30	5.07	0.06	2.22	3.65	4.12	4.84	2
DCW-77-1	60.93	0.79	15.71	5.63	0.15	2.81	4.88	3.67	3.63	2
DCW-77-15	60.89	0.69	15.54	5.47	0.06	3.01	4.56	3.68	3.19	2
DCW-77-16	61.47	0.79	15.43	5.61	0.07	2.50	4.12	3.69	3.67	2
DCW-77-17	60.80	0.70	15.99	5.31	0.05	2.89	5.03	3.66	3.21	2
DCW-77-18	61.10	0.72	15.76	5.32	0.05	2.68	4.61	3.71	3.30	2
DCW-77-28	61.37	0.75	15.08	5.52	0.05	2.55	4.28	3.62	3.49	2
DCW-77-29	61.64	0.75	15.72	5.44	0.04	2.33	4.28	3.80	3.51	2
DCW-77-30	61.12	0.75	15.74	5.36	0.05	2.81	4.70	3.77	3.39	2
DCW-77-31	60.84	0.82	15.63	5.52	0.05	2.72	4.53	3.64	3.86	2
DCW-77-32	60.67	0.80	15.84	5.79	0.05	2.75	4.54	3.69	3.61	2
DCW-77-33	60.21	0.71	15.86	5.79	0.06	3.12	4.84	3.77	3.27	2
DCW-77-34	61.23	0.79	15.59	5.53	0.05	2.65	4.54	3.68	3.56	2
DCW-77-35	61.29	0.79	15.59	5.59	0.06	2.59	4.40	3.76	3.67	2
DCW-77-36	61.13	0.81	15.73	5.40	0.05	2.75	4.54	3.71	3.71	2
DCW-77-37-4	60.69	0.80	15.87	5.44	0.05	2.62	4.68	3.78	3.67	2
DCW-77-49	61.01	0.84	15.93	5.78	0.05	2.43	4.04	3.74	4.02	2
DCW-77-5	61.22	0.78	15.86	5.55	0.06	2.71	4.70	3.73	3.41	2
DCW-77-50	61.39	0.80	15.87	5.60	0.07	2.55	4.60	3.80	3.68	2
DCW-77-51	61.11	0.82	16.23	5.57	0.08	2.51	4.44	3.72	3.81	2
DCW-77-52	61.32	0.80	15.80	5.61	0.07	2.53	4.45	3.79	3.74	2
DCW-77-53	60.71	0.76	15.87	5.61	0.06	2.85	4.85	3.77	3.57	2
DCW-77-54	60.74	0.76	15.93	5.56	0.08	2.91	4.88	3.78	3.54	2
DCW-77-61	60.45	0.85	15.88	5.46	0.06	2.76	4.11	3.69	3.84	2
DCW-77-7	61.26	0.74	15.63	5.43	0.05	2.80	4.49	3.74	3.55	2
DCW-77-8	60.96	0.72	15.91	5.36	0.05	2.86	4.90	3.72	3.28	2
DR-010	60.98	0.75	15.80	5.33	0.06	2.57	4.41	3.76	3.47	2
LP-2	61.05	0.71	15.81	5.45	0.05	2.81	4.81	3.73	3.33	2
LP-23	61.41	0.66	15.87	5.04	0.06	3.00	4.80	3.80	3.11	2

Table S3 (cont.). Literature data for impact melts from West Clearwater crater (major elements).

Sample ID	SiO$_2$ (wt.%)	TiO$_2$ (wt.%)	Al$_2$O$_3$ (wt.%)	FeO$_T$* (wt.%)	MnO (wt.%)	MgO (wt.%)	CaO (wt.%)	Na$_2$O (wt.%)	K$_2$O (wt.%)	Ref.
LP-23-B	60.63	0.76	15.95	6.19	0.05	2.90	3.82	3.92	3.31	2
LP-23-D	61.58	0.75	15.69	5.39	0.11	2.82	4.96	3.66	3.37	2
LP-47	61.04	0.79	15.53	5.72	0.06	2.92	4.54	3.74	3.46	2
LP-89	59.96	0.84	16.07	6.05	0.06	2.61	4.59	3.60	3.81	2
LP-95-4	59.33	0.84	15.96	5.29	0.05	3.14	4.81	3.49	3.99	2
DCW-77-11F	58.53	0.77	16.37	6.79	0.04	2.86	4.01	3.70	3.34	2
DCW-77-13	62.07	0.65	15.83	4.96	0.05	2.66	4.18	3.71	3.30	2
DCW-77-22	61.59	0.64	15.82	5.17	0.08	2.59	4.64	4.02	2.88	2
DCW-77-55	58.09	1.09	16.26	7.08	0.10	3.13	4.56	3.83	3.17	2
DCW-77-58	60.92	0.79	15.96	5.50	0.07	3.08	4.54	3.90	3.32	2
DCW-77-59	59.99	0.61	14.95	5.08	0.08	4.20	6.61	3.70	2.89	2
DCW-77-62	59.19	0.80	16.99	5.48	0.03	2.88	3.31	3.79	3.74	2
DCW-77-66	62.40	0.65	16.55	4.58	0.06	2.42	3.51	3.91	3.35	2
DCW-77-67	60.75	0.67	17.27	4.93	0.05	2.60	4.01	4.30	3.08	2
DCW-77-9	62.62	0.66	16.13	4.98	0.09	2.41	3.96	3.84	3.48	2
LP-34	60.56	0.89	15.94	6.24	0.06	2.39	4.11	3.95	3.72	2
LP-45	60.10	0.88	16.03	6.70	0.07	2.46	3.78	3.93	3.29	2
LP-45-3	62.96	0.88	15.23	5.16	0.04	2.28	3.02	3.66	4.31	2
315	58.00	1.00	16.30	5.79	0.06	2.00	4.10	3.90	3.60	3
322	54.70	0.98	16.50	5.71	0.09	3.70	4.80	3.80	2.80	3
201	57.90	0.78	15.80	5.58	0.09	2.50	4.60	3.10	4.50	3
78	58.40	0.80	16.10	4.82	0.07	3.30	4.80	4.90	2.70	3
86	58.50	1.00	15.20	6.25	0.10	2.30	5.50	3.90	3.10	3
144	60.30	0.93	15.90	3.62	0.06	2.70	3.90	4.20	3.70	3
208	60.70	0.70	17.50	4.12	0.06	1.70	4.20	4.10	3.10	3
236	60.20	0.83	16.10	4.53	0.05	2.60	4.40	3.90	3.50	3
A934	62.00	0.63	16.30	4.51	0.03	2.90	4.60	3.70	3.70	3
A935	60.80	0.60	15.70	4.84	0.06	1.90	4.30	3.60	3.60	3
57	60.90	0.82	15.90	5.02	0.07	3.00	4.50	4.10	3.70	3
192	61.00	0.85	16.10	4.81	0.06	2.20	4.70	3.90	3.70	3
264	58.50	0.71	15.10	4.86	0.05	3.20	4.60	3.70	3.30	3
82	59.00	0.79	16.30	5.29	0.05	2.80	4.20	3.70	3.60	3

*If the source reported Fe$_2$O$_3$ or FeO and Fe$_2$O$_3$ separately, then the data has been recalculated to express all iron as FeO. References: [1] *Palme et al.* [1978]   [2] *Rosa* [2011]   [3] *Bostock* [1969]

Table S4. Literature data for impact melts from West Clearwater crater (minor elements).

Sample ID	Os (ppb)	Re (ppb)	Ir (ppb)	Pd (ppb)	Cu (ppm)	Ni (ppm)	Co (ppm)	Cr (ppm)	Ref.
DCW 150-63	<0.012	-	0.012	<1.1		25			1
DCW 146 63	<0.01		0.013	<1		10			1
DCW 1-63-428	0.015	-	<0.16	5.5		<9			1
LP-122					38	27	12	144	2
LP-125					23	78	30	330	2
LP-130					19	27	10	174	2
LP-133					23	34	12	216	2
LP-21					32	39	15	244	2
LP-94					36	26	19	170	2
DCW-77-1					35	31	11	150	2
DCW-77-15					23	41	15	300	2
DCW-77-16					28	26	13	160	2
DCW-77-17					24	34	10	214	2
DCW-77-18					22	34	17	210	2
DCW-77-28					14	36	14	208	2
DCW-77-29					25	27	n.d.	168	2
DCW-77-30					30	29	14	172	2
DCW-77-31					23	30	11	188	2
DCW-77-32					21	28	17	150	2
DCW-77-33					34	39	12	250	2
DCW-77-34					29	29	12	148	2
DCW-77-35					78	33	18	186	2
DCW-77-36					23	28	10	182	2
DCW-77-37-4					41	35	12	196	2
DCW-77-49					36	31	13	178	2
DCW-77-5					33	29	n.d.	154	2
DCW-77-50					35	32	16	198	2
DCW-77-51					29	27	n.d.	168	2
DCW-77-52					25	33	18	192	2
DCW-77-53					33	33	n.d.	212	2
DCW-77-54					67	29	17	168	2
DCW-77-61					38	30	16	176	2
DCW-77-7					35	32	n.d.	192	2
DCW-77-8					25	38	n.d.	282	2
DR-010					30	30	12	168	2

Table S4 (cont.). Literature data for impact melts from West Clearwater crater (minor elements).

Sample ID	Os (ppb)	Re (ppb)	Ir (ppb)	Pd (ppb)	Cu (ppm)	Ni (ppm)	Co (ppm)	Cr (ppm)	Ref.
LP-2					25	29	11	178	2
LP-23					59	37	14	230	2
LP-23-B					29	26	14	160	2
LP-23-D					24	30	11	162	2
LP-47					37	37	11	178	2
LP-89					36	30	13	160	2
LP-95-4					45	25	n.d.	148	2
DCW-77-11F					31	31	16	248	2
DCW-77-13					26	36	16	230	2
DCW-77-22					40	37	16	260	2
DCW-77-55					45	36	12	228	2
DCW-77-58					35	36	11	190	2
DCW-77-59					21	34	12	202	2
DCW-77-62					36	24	11	160	2
DCW-77-66					21	31	11	220	2
DCW-77-67					31	32	n.d.	220	2
DCW-77-9					50	33	13	200	2
LP-34					37	30	12	182	2
LP-45					31	32	n.d.	210	2
LP-45-3					24	22	13	142	2
315						n.d.	n.d.	54	3
322						n.d.	n.d.	54	3
201						n.d.	n.d.	<30	3
78						n.d.	n.d.	<0	3
86						n.d.	<20	n.d.	3
144						n.d.	n.d.	n.d.	3
208						n.d.	n.d.	n.d.	3
236						n.d.	n.d.	n.d.	3
A934						n.d.	n.d.	26	3
A935						n.d.	n.d.	42	3
57						n.d.	n.d.	n.d.	3
192						n.d.	n.d.	n.d.	3
264						n.d.	n.d.	64	3
82						n.d.	n.d.	36	3

References: [1] *Palme et al.* [1978]   [2] *Rosa* [2011]   [3] *Bostock* [1969]

Table S5. Literature data for country rocks near the Clearwater craters (major elements).

Sample ID	SiO$_2$ (wt.%)	TiO$_2$ (wt.%)	Al$_2$O$_3$ (wt.%)	FeO$_T$* (wt.%)	MnO (wt.%)	MgO (wt.%)	CaO (wt.%)	Na$_2$O (wt.%)	K$_2$O (wt.%)	Ref.
DCW-1-64-465	54.49	2.25	15.53	8.49	0.32	3.43	4.20	3.88	2.30	1
DCW-1-64-478	57.15	0.82	18.38	5.53	0.09	3.03	3.43	5.93	1.96	1
DCW-1-64-472	72.45	1.00	8.54	1.85	0.04	1.03	0.97	3.25	4.82	1
DCW-1-64-1442	70.44	0.45	15.27	1.44	0.01	0.58	2.65	4.25	3.31	1
1-63-113	50.45	1.77	16.31	9.70	0.13	4.01	6.85	4.62	1.23	4
1-63-1163	49.65	0.50	11.96	7.83	0.16	11.43	13.43	2.05	0.99	4
1-63-1303	50.37	0.63	7.17	10.33	0.19	15.21	12.81	1.28	0.84	4
1-63-281	56.00	0.61	19.47	5.84	0.12	3.19	5.24	5.26	1.37	4
1-63-434	51.89	1.25	12.76	9.66	0.20	8.32	8.98	3.53	0.74	4
1-63-593	47.16	0.86	12.93	9.22	0.29	11.17	10.37	2.22	2.07	4
1-63-910	49.70	0.77	7.10	9.51	0.17	14.11	14.85	1.27	0.91	4
3-63-1217	73.79	0.20	13.96	1.66	0.03	0.38	1.96	3.74	3.82	4
3-63-65	63.28	0.65	16.79	5.52	0.04	2.25	4.88	3.97	1.38	4
3-63-832	48.35	0.87	15.53	9.98	0.17	8.38	8.11	3.02	0.62	4
3-63-977	69.65	0.30	14.37	3.06	0.06	1.54	1.78	3.55	3.68	4
4-63-290	58.91	1.45	15.94	7.18	0.22	2.28	5.06	4.03	1.62	4
4-63-322	73.00	0.07	12.27	1.96	0.03	0.52	2.03	2.25	5.96	4
5-63-174	71.23	0.14	15.35	2.06	0.05	0.97	3.06	4.37	1.32	4
5-63-514	68.31	0.65	13.80	4.22	0.05	1.44	1.70	3.33	4.56	4
DCW-77-10	62.32	0.68	16.94	4.53	0.06	2.18	4.70	4.23	2.88	4
DCW-77-11	71.29	0.24	14.72	1.65	0.03	0.76	2.01	3.16	4.86	4
DCW-77-12	70.38	0.43	14.89	2.82	0.03	0.86	2.01	4.24	3.10	4
DCW-77-14	65.58	0.62	16.25	4.96	0.05	0.69	3.44	3.46	3.36	4
DCW-77-19	53.51	1.05	18.66	8.05	0.08	2.39	5.16	4.45	3.61	4
DCW-77-20	71.41	0.13	15.15	1.48	0.01	0.43	2.09	4.04	3.98	4
DCW-77-21	73.75	0.05	14.20	0.94	0.01	0.10	0.97	3.90	5.24	4
DCW-77-27	72.36	0.28	13.67	2.14	0.01	0.59	1.64	3.39	4.21	4
DCW-77-2A	58.06	1.07	16.23	7.02	0.06	3.01	5.34	3.81	2.94	4
DCW-77-2B	61.09	0.82	15.50	5.57	0.05	2.54	4.57	3.70	3.76	4
DCW-77-3	58.08	1.00	16.68	6.85	0.06	2.87	5.19	3.95	2.93	4
DCW-77-39	48.86	0.43	12.87	9.34	0.17	11.92	10.70	1.58	0.46	4
DCW-77-39-2	49.23	0.42	11.92	9.37	0.18	12.48	11.18	1.66	0.44	4
DCW-77-4	47.45	1.64	17.87	11.62	0.14	4.66	9.15	3.90	1.24	4
DCW-77-40	48.46	0.58	8.25	10.51	0.18	15.09	11.73	1.53	0.70	4

Table S5 (cont.). Literature data for country rocks near the Clearwater craters (major elements).

Sample ID	SiO$_2$ (wt.%)	TiO$_2$ (wt.%)	Al$_2$O$_3$ (wt.%)	FeO$_T$* (wt.%)	MnO (wt.%)	MgO (wt.%)	CaO (wt.%)	Na$_2$O (wt.%)	K$_2$O (wt.%)	Ref.
DCW-77-41	48.28	0.46	12.56	9.29	0.18	11.98	10.28	2.05	0.51	4
DCW-77-42	68.63	0.44	14.30	2.46	0.14	1.42	1.65	2.85	5.59	4
DCW-77-43	55.01	1.11	18.20	7.01	0.08	2.55	4.98	3.70	4.60	4
DCW-77-45-1	48.35	1.39	17.46	11.15	0.13	4.92	7.39	3.92	1.96	4
DCW-77-46-2	76.34	0.03	12.53	1.34	0.07	1.00	1.85	3.97	1.11	4
DCW-77-47	47.06	1.81	17.42	11.16	0.15	5.18	8.19	4.98	0.97	4
DCW-77-60	68.41	0.47	15.49	3.43	0.05	1.39	2.94	4.41	2.18	4
DCW-77-63-2	73.38	0.15	13.50	1.41	0.02	0.89	0.70	3.18	5.19	4
DCW-77-63-3	72.64	0.25	14.07	2.37	0.02	1.10	2.40	4.74	1.11	4
DR-006	68.28	0.66	14.55	3.71	0.02	0.86	2.27	3.45	4.32	4
DR-011	76.42	0.12	12.00	1.21	0.04	0.66	0.71	2.68	5.11	4
A1	63.00	0.66	16.70	5.10	0.07	<0.5	3.70	4.20	3.20	5
B1	63.40	0.59	18.40	4.31	0.07	0.80	4.40	5.40	1.50	5
C1	53.20	1.80	18.90	7.96	0.17	1.30	6.20	4.80	1.60	5
D1	71.00	0.16	15.20	2.21	0.04	<0.5	2.90	3.90	3.00	5
D2	58.70	0.75	16.00	6.49	0.22	5.30	5.60	3.90	2.00	5
E1	71.30	0.26	14.80	2.18	0.03	<0.5	2.00	4.00	3.90	5
F1	50.90	1.20	18.10	6.64	0.10	3.80	6.20	5.10	2.50	5
G1	50.90	0.98	15.50	8.70	0.16	6.30	7.30	4.20	2.60	5
H1	50.00	1.20	17.20	9.18	0.15	5.90	8.60	4.20	0.80	5
I1	61.90	0.36	17.10	3.47	0.05	1.80	4.20	4.40	3.10	5
I2	51.60	1.00	14.30	8.78	0.23	8.10	6.90	2.50	3.20	5
J1	72.60	0.11	15.80	0.69	0.02	<0.5	2.50	3.80	3.20	5
K1	67.20	0.46	16.00	3.23	0.01	1.20	3.40	4.10	2.20	5
K2	51.40	0.94	12.00	8.94	0.04	8.40	8.90	2.50	2.10	5
L1	59.90	0.55	18.30	3.79	0.07	2.10	5.00	4.90	1.80	5
M1	73.50	0.18	14.50	1.27	0.04	0.60	1.70	2.80	4.50	5
M2	52.10	1.10	18.60	7.78	0.14	3.50	7.60	4.80	1.30	5
N1	64.60	0.74	15.90	4.42	0.11	<0.5	4.20	4.30	2.00	5
N2	73.60	0.05	15.90	0.76	0.02	<0.5	1.60	3.20	4.80	5
O1	60.40	0.73	17.10	4.65	0.08	3.00	4.40	4.60	1.80	5
P1	54.90	0.90	17.50	7.48	0.18	2.30	5.70	5.00	1.80	5

Table S5 (cont.). Literature data for country rocks near the Clearwater craters (major elements).

Sample ID	SiO$_2$ (wt.%)	TiO$_2$ (wt.%)	Al$_2$O$_3$ (wt.%)	FeO$_T$* (wt.%)	MnO (wt.%)	MgO (wt.%)	CaO (wt.%)	Na$_2$O (wt.%)	K$_2$O (wt.%)	Ref.
163	49.20	0.44	13.20	7.80	0.17	10.90	10.90	1.70	0.80	5
50	48.80	1.20	10.70	9.16	0.20	11.90	10.00	1.60	2.40	5

*Data have been recalculated, if needed, to express all iron as FeO.
References: [1] *Palme et al.* [1979]   [2] *Schmidt* [1997]   [3] *Palme et al.* [1978]   [4] *Rosa* [2011]   [5] *Bostock* [1969]

Table S6. Literature data for country rocks near the Clearwater craters (minor elements).

Sample ID	Os (ppb)	Re (ppb)	Ir (ppb)	Ru (ppb)	Rh (ppb)	Pd (ppb)	Cu (ppm)	Ni (ppm)	Co (ppm)	Cr (ppm)	Ref.
DCW-1-64-465			<1				2	34	21.5	80	1
DCW-1-64-478			<1				3.1	12.4	18.3	9	1
DCW-1-64-472			<1				1.1	3.8	3.7	10.4	1
DCW 1 64 472	0.03	0.16	0.03	<0.1	1.71	1.6					2
DCW 64- 472	0.029	0.4	<0.008		7.4		6			3	3
DCW-1-64-1442			<1				1	0.5	2.6	2.4	1
1-63-113							28	33	22	152	4
1-63-1163							122	198	41	1866	4
1-63-1303							230	329	63	2046	4
1-63-281							23	28	n.d.	162	4
1-63-434							118	164	39	802	4
1-63-593							32	190	46	1404	4
1-63-910							149	277	54	2788	4
3-63-1217							7	11	n.d.	60	4
3-63-65							35	32	n.d.	224	4
3-63-832							274	116	36	662	4
3-63-977							22	24	n.d.	186	4
4-63-290							27	32	n.d.	194	4
4-63-322							10	22	n.d.	124	4
5-63-174							33	14	n.d.	56	4
5-63-514							15	12	n.d.	92	4
DCW-77-10							29	44	n.d.	248	4
DCW-77-11							24	22	n.d.	72	4
DCW-77-12							37	8	n.d.	68	4
DCW-77-14							23	11	13	74	4
DCW-77-19							467	24	19	82	4
DCW-77-20							8	16	n.d.	96	4
DCW-77-21							6	7	n.d.	48	4
DCW-77-27							5	10	n.d.	54	4
DCW-77-2A							47	32	17	138	4
DCW-77-2B							27	26	12	144	4
DCW-77-3							30	38	17	200	4
DCW-77-39							235	201	58	926	4

Table S6 (cont.). Literature data for country rocks near the Clearwater craters (minor elements).

Sample ID	Os (ppb)	Re (ppb)	Ir (ppb)	Ru (ppb)	Rh (ppb)	Pd (ppb)	Cu (ppm)	Ni (ppm)	Co (ppm)	Cr (ppm)	Ref.
DCW-77-39-2							228	251	62	1050	4
DCW-77-4							36	51	35	256	4
DCW-77-40							290	313	74	1560	4
DCW-77-41							206	224	58	940	4
DCW-77-42							334	86	16	132	4
DCW-77-43							83	27	13	112	4
DCW-77-45-1							94	41	33	148	4
DCW-77-46-2							56	28	n.d.	110	4
DCW-77-47							97	56	34	246	4
DCW-77-60							6	13	n.d.	118	4
DCW-77-63-2							16	7	n.d.	60	4
DCW-77-63-3							19	21	n.d.	190	4
DR-006							14	8	n.d.	86	4
DR-011							59	10	n.d.	40	4
A1								n.d.	<20	n.d.	5
B1								n.d.	n.d.	n.d.	5
C1								n.d.	n.d.	42	5
D1								n.d.	n.d.	n.d.	5
D2								220	n.d.	410	5
E1								n.d.	n.d.	n.d.	5
F1								n.d.	40	54	5
G1								n.d.	n.d.	170	5
H1								39	47	<30	5
I1								n.d.	n.d.	n.d.	5
I2								97	52	75	5
J1								n.d.	n.d.	n.d.	5
K1								n.d.	n.d.	<30	5
K2								170	48	820	5
L1								n.d.	n.d.	<30	5
M1								n.d.	n.d.	n.d.	5
M2								n.d.	280	30	5
N1								n.d.	n.d.	<30	5
N2								n.d.	n.d.	n.d.	5

Table S6 (cont.). Literature data for country rocks near the Clearwater craters (minor elements).

Sample ID	Os (ppb)	Re (ppb)	Ir (ppb)	Ru (ppb)	Rh (ppb)	Pd (ppb)	Cu (ppm)	Ni (ppm)	Co (ppm)	Cr (ppm)	Ref.
O1								n.d.	n.d.	n.d.	5
P1								n.d.	<20	71	5
163								220	n.d.	270	5
50								210	73	720	5

References: [1] *Palme et al.* [1979]   [2] *Schmidt* [1997]   [3] *Palme et al.* [1978]   [4] *Rosa* [2011]   [5] *Bostock* [1969]

CHAPTER 4

The impact delivery of water by carbonaceous chondrite-like impactors

R. Terik Daly and Peter H. Schultz

Department of Earth, Environmental and Planetary Sciences

Brown University

Providence, RI USA

Abstract

Water plays a critical role in the evolution of planets, moons, and small bodies. Multiple lines of evidence indicate that impacts deliver water to a range of objects. However, the efficiency of water delivery and the nature of the materials that host impact-delivered water remain unclear. New experiments at the NASA Ames Vertical Gun Range reveal that impacts deliver 25 to 36% of the water in the impactor ($OH + H_2O$) under impact conditions typical among main-belt asteroids. Delivered water resides in lightly-shocked impactor relics, melt-bearing impact breccias, and impact glasses. Impact glasses trap both OH and H_2O; this trapping is a critical step of the water delivery process under these conditions. H_2O is the dominant species in impact glasses. This work demonstrates that significant amounts of water in the impactor could be delivered during typical impacts by main-belt objects. These findings strengthen the hypothesis that hydrated dark material on Vesta represents the remnants of dark, carbonaceous chondrite-like impactors without requiring low-probability, low-velocity impacts. Moreover, the hydroxyl recently detected on Psyche may represent hydrated, impactor-rich materials.

1. Introduction

Bodies in the inner solar system likely acquired their water from volatile-rich impactors from the outer asteroid belt, giant planet region, and Kuiper belt [*Morbidelli et al.*, 2000]. Although the impact flux may have been higher earlier in solar system history, water-delivering impacts have continued to affect a number of objects in the solar system, including the Moon [*Colaprete et al.*, 2010; *Schultz et al.*, 2010] and Mercury [*Neumann et al.*, 2013; *Bruck Syal and Schultz*, 2015]. Both cometary and asteroidal impactors can deliver water [*Bruck Syal and Schultz*, 2015; *Sekine et al.*, 2015; *Svetsov and Shuvalov*, 2015]. While comets carry water in the form of water ice [*Bruck Syal and Schultz*, 2015], many asteroids carry their water as OH bound in hydrous minerals [*Tyburczy et al.*, 1986, 1991; *Sekine et al.*, 2012, 2015].

1.1. *Evidence for water delivering impacts among asteroids*

Both the meteorite collection and spacecraft data provide evidence that impacts deliver water to meteorite parent bodies and large asteroids. Several meteorite types contain clasts of hydrated, exogenic material that were most likely delivered by impacts. These meteorites include H chondrite regolith breccias [*Rubin and Bottke,* 2009 and references therein; *Briani et al.,* 2012 and references therein; *Krzesińska and Fritz,* 2014 and references therein], R chondrites [*Greshake*, 2014], howardites [*Zolensky et al.,* 1996; *Lorenz et al.,* 2007; *Krzesińska and Fritz,* 2014 and references therein], polymict eucrites

188

[*Zolensky et al.*, 1996; *Lorenz et al.*, 2007], a diogenite [*Zolensky et al.*, 1996], and polymict ureilites [*Goodrich et al.*, 2015].

Spacecraft observations made by *Dawn* at asteroid (4) Vesta provide further evidence that impacts have ferried water to asteroids. Dawn discovered deposits of dark material peppering Vesta's near-surface layers. Dark material likely represents the remnants of dark, carbonaceous chondrite-like impactors [*McCord et al.*, 2012; *Prettyman et al.*, 2012; *Reddy et al.*, 2012; *de Sanctis et al.*, 2012; *Daly and Schultz*, 2016]. Significantly, most dark material deposits are associated with excess hydrogen [*Prettyman et al.*, 2012] and a near-infrared hydroxyl absorption feature [*de Sanctis et al.*, 2012]. This correlation indicates that in many cases some, if not all, of the hydroxyl in impacting carbonaceous chondrite-like objects is preserved on Vesta.

In addition to evidence from the meteorite collection and *Dawn* mission, multiple shock physics codes indicate that impacts could deliver water across a range of plausible conditions [*Ong et al.*, 2010; *Turrini and Svetsov*, 2014; *Bruck Syal and Schultz*, 2015; *Svetsov and Shuvalov*, 2015]. Nevertheless, shock physics codes cannot yet fully represent material behavior. In the main asteroid belt, where average impact speeds are ~5 km s^{-1} [*O'Brien and Sykes*, 2011], these limitations can become particularly acute [e.g., *Quintana et al.*, 2015].

1.2. *Unanswered questions about water-delivering impacts on asteroids*

The evidence outlined in the preceding section demonstrates that OH-rich impactors can deliver water to asteroids and meteorite parent bodies. However, in some cases the hydrated clasts in meteorites appear partially devolatilized [*Zolensky et al.*, 1996; *Rubin and Bottke*, 2009; *Krzesińska and Fritz*, 2014]. This devolatilization probably occurred during the initial impact. Later impacts are not very efficient at devolatilizing hydrated material, unless that material is very close to the impact point [*Rivkin and Pierazzo*, 2005]. Previous shock experiments also indicate that volatile loss largely occurs during the initial impact: the equation of state for carbonaceous chondrites suggests that they completely devolatize above $\sim$3.1 km s^{-1} (30 GPa), with the assumption of a carbonaceous chondrite into carbonaceous chondrite impact at vertical incidence [*Tyburczy et al.,* 1986]. Eighty percent of impacts in the main asteroid belt exceed this speed [*O'Brien and Sykes*, 2011]. Although peak pressures decay with distance from the impact point, devolatilization can be further enhanced by porosity and frictional shear [*Schultz*, 1996]. Hence, an even larger fraction of main belt impacts could trigger impactor devolatilization.

Regardless of the exact conditions needed for devolatilization, the fate of water liberated from OH-rich impactors is unclear. The decomposition of OH-rich minerals such as serpentine liberates structurally bound hydroxyl as molecular water [*Lange and Ahrens,* 1982; *Tyburczy et al.*, 1986; *Tomioka et al.*, 2007]. Given the low surface gravity of even large asteroids, molecular water may rapidly escape. However, *Harris and Schultz* [2011] reported that impact glasses can trap water derived from the projectile. In this scenario, impact glasses may trap water vapor liberated by the devolatilization of carbonaceous

190

chondrite-like impactors, water that would otherwise be lost to space. This process would increase the efficiency of water delivery during impacts of carbonaceous chondrite-like objects. However, the efficiency of this trapping process remains unclear.

1.3. *Goals of this study*

This study focuses on two major questions. First, how efficiently do carbonaceous chondrite-like impactors deliver water ($OH + H_2O$) under the impact conditions that prevail in the main asteroid belt? Second, how is delivered water stored on asteroids: in surviving fragments of the projectile? In impact breccias? Or in impact glasses? We focus on carbonaceous chondrite-like impactors because dynamical models [*Morbidelli et al.*, 2000] and, for the Earth and Moon, isotopic markers [*Saal et al.*, 2013] indicate that water-delivering impactors in the early inner solar system were akin to carbonaceous chondrites. To examine these two questions, we use hypervelocity impact experiments. These experiments measure the amount of water ($OH + H_2O$) delivered by impact, interrogate how that water is stored (e.g., hydrous melts vs. projectile relics), and assess the speciation of delivered water (OH vs. H_2O). The results show that for a typical impact in the main asteroid belt, up to 36% of the structural water in the impactor is trapped within impactor relics, impact-generated glasses, and melt-bearing breccias.

2.   Methods

2.1.   *Hypervelocity impact experiments at the NASA Ames Vertical Gun Range*

Experiments were performed at the NASA Ames Vertical Gun Range (AVGR). The light-gas guns at the AVGR launch projectiles at speeds up to ~6 km s^{-1}. The AVGR can easily vary impact angle while keeping the target surface perpendicular to the gravity vector. In addition, the AVGR features a large~2.5 meter diameter impact chamber [*Gault and Wedekind*, 1978]. Hence, any volatiles liberated during impact can expand freely. This capacity sets the AVGR apart from facilities that generate planar shock experiments such as those reported by *Tyburczy et al.* [1986, 1991]. Although planar shock experiments are necessary to deduce equations of state, shock devolatilization during planar impact experiments can be highly sensitive to capsule design [*Kraus et al.,* 2013].

Impact experiments isolate a specific process, in this case water delivery, and assess how impact variables affect the outcomes of the cratering process. In this study, impacts were done at 30° and 45° (with respect to horizontal) and a speed of ~5 km s^{-1}, conditions comparable to the average impact speed among main-belt asteroids [*O'Brien and Sykes*, 2011]. The target material was airfall pumice. Airfall pumice is a useful analog for silicate regoliths [*Schultz et al.*, 2005] like those on asteroids. The pumice was sieved to <106 μm and then heat-treated to drive off volatiles (see Supplementary Text S1). Serpentine slugs served as projectiles. These projectiles should give similar results to carbonaceous chondrite projectiles because the shock responses of the two materials are similar [*Tyburczy et al.*, 1986] and the two have similar OH contents (12 and 10 wt.%, respectively). However, serpentine is readily available and easier to launch. See Table 1.

192

The experimental setup differed from the half-space targets used in other studies that assessed projectile delivery at the AVGR [*Daly and Schultz*, 2015, 2016]. A Mylar tray about 12 cm long, 7 cm wide, and 2 cm deep was filled with heat-treated pumice. The pumice-filled tray was suspended over a well inside the impact chamber (Fig. 1). The tray was slightly deeper than three times the projectile diameter. Thus, the projectile should fully couple to the pumice. However, the Mylar ruptures when the shock reflects from the free surfaces of the tray. This rupture allows much of the molten impact products to travel into the well, rather than upward and outward. This approach captures projectile-rich melts and breccias that would otherwise be lost downrange due to the residual projectile momentum and cratering flow field. The well was lined with a thick plastic sheet to facilitate sample recovery. Such tray experiments ensure that the projectile experiences the full range of temperatures and pressures that it would undergo during a half-space experiment, while enabling the capture and analysis of impact products that would otherwise be lost.

After each experiment impact products were recovered from the plastic-lined well. After an additional step of hand sorting (to remove any extraneous debris, such as bits of Mylar), recovered impact products were weighed and characterized using optical microscopy.

2.2.   Analytical methods

Impact products were analyzed using a variety of techniques, including inductively coupled plasma atomic emission spectroscopy (ICP-AES), x-ray diffraction (XRD), thermogravimetric (TG) analysis, Fourier transform infrared (FTIR) spectroscopy, and electron microprobe (EMP) analysis. See Table 2. Several methods provide similar—but not identical—information. These differences allow answering the two questions raised in section 1.3, a synergy elaborated on throughout the rest of this paper. The details of each method are described here in turn.

2.3.1. Inductively coupled plasma atomic emission spectroscopy (ICP-AES)

Major element compositions were determined using inductively coupled plasma atomic emission spectroscopy (ICP-AES). Samples of recovered impact materials, the heat-treated pumice target, and serpentine projectile were powdered to <45 μm in an agate mortar. Aliquots of homogenized powders were digested using flux fusion and nitric acid digestion [*Murray et al.*, 2000]. In addition to the samples, USGS rock standards and blanks were processed during the same run. Solutions were analyzed on a JY2000 Ultratrace ICP atomic emission spectrometer at Brown University. After correcting for instrumental drift and blanks, raw intensities were converted to elemental concentrations using the measured intensities and known concentrations of elements in the USGS standards [*Murray et al.,* 2000].

2.3.2. Thermogravimetric analysis/differential scanning calorimetry

The volatile contents of impact materials, heat-treated pumice target, and serpentine projectile were investigated using thermogravimetry (TG) and differential scanning calorimetry (DSC). Aliquots of homogenized powders (<45 μm) of each sample (21.5 mg, on average) were loosely packed into 70 μL alumina crucibles and analyzed on a Mettler Toledo TGA/DSC-1 STARe system. The instrument simultaneously measured sample temperature, mass, and heat flow. Under an N_2 purge, sample temperature was increased from 50 to 850 °C at a rate of 20 K min^{-1}. Heating samples to 850 °C ensured that serpentine in the samples completely dehydroxylated [*Viti*, 2010; *Gualtieri et al.*, 2012]. TG profiles were corrected for buoyancy and convection effects by subtracting the profile of the empty crucible. The Mettler-Toledo instrument accurately measures mass changes as small as 4 μg. The mass losses in even the most volatile-poor samples exceed this limit by a factor of ~15. Thus, all mass changes reported here are meaningful.

2.3.4. X-ray diffraction (XRD)

X-ray diffraction data constrain the mineralogy and amorphous content of impact materials, the heat-treated pumice target, and serpentine projectile. Samples were analyzed using a Bruker D2 PHASER x-ray diffractometer at Brown University. Due to the small volumes of impact materials available, powders were analyzed on a zero-diffraction plate.

Two sets of data were gathered. Samples were initially measured from 8 to 60° 2θ using a coupled two theta/theta scan type, an increment of 0.02024 2θ, Cu-α radiation, and

a count time of 2 seconds per step. These scans were used to characterize the mineralogy and amorphous content of each sample. Afterward, powders were mixed with high-purity corundum in a 4:1 ratio (by mass) and analyzed from 5 to 70° 2θ using a coupled two theta/theta scan type, an increment of 0.01826 2θ, Cu-α radiation, and a count time of 15 seconds per step. The scans from this second set of data were resampled to increments of 0.02° 2θ modeled using FULLPAT [*Chipera and Bish*, 2002]. This program quantitatively models abundances of crystalline and amorphous phases in a material using a user-generated library of standards. FULLPAT models can optimize one of several functions. The models reported here minimized the quantity $\Sigma\left|\text{Delta}\right|^{1/2}$, where delta is the difference between the observed intensity and the modeled intensity at each 2θ point. *Chipera and Bish* [2002] report that minimizing $\Sigma\left|\text{Delta}\right|^{1/2}$ yields the best results for samples with a high amorphous component, such as those analyzed here.

2.3.5. Electron microprobe (EMP) analyses

Samples were embedded in epoxy, polished, carbon coated, and then analyzed on the Cameca SX 100 electron microprobe at Brown University (15 kV, 10 nA current, 10 µm beam diameter). Wavelength dispersive spectroscopy was used for all quantitative analyses. A sodium loss routine [*Devine et al.*, 1995] corrected for any sodium devolatilized during analysis.

196

2.3.6. Fourier-transform (FTIR) infrared spectroscopy

Transmission-mode FTIR data can be used to estimate the speciation and abundance of OH and H_2O in impact products. Samples of impact glass were impregnated with orthodontic resin and sectioned using a low-speed saw. The resulting slabs were mounted on glass slides with additional orthodontic resin and then polished. The final polish was with 1 µm diamond paste. After polishing, the orthodontic resin was dissolved using acetone. The polished side of the sample was placed against the glass slide, and the sample was again embedded in orthodontic resin. Once the second side of the sample was polished, the sample and slide were soaked in acetone to dissolve the orthodontic resin. This step was repeated to ensure removal of all resin; however, the highly vesicular nature of the samples complicated removal.

Spectra were acquired on a Bruker LUMOS FTIR microscope at Brown University. Data were acquired over 600 to 6000 cm^{-1} at 4 cm^{-1} for a total of 500 scans for each spectrum. The detector was cooled with liquid nitrogen for one hour prior to start of analyses and was maintained cold throughout the entire analytical run.

The Beer-Lambert law was used to quantify the amount of hydroxyl and molecular water present in the regions of the glasses where spectra were collected:

$$C = \frac{MW * Abs}{\rho * d * \varepsilon} \qquad (1)$$

where *C* is the concentration of the species being measured, *MW* is the molecular weight of the species, *Abs* is the height of the absorbance peak above background, ρ is the density in g L^{-1}, *d* is the sample thickness in cm, and ε is the linear molar absorptivity coefficient

in L mol^{-1} cm^{-1}. Table 3 lists the linear molar absorptivities used in this study. These values are for rhyolitic glasses, which is appropriate given the high silica contents of the impact-generated glasses (Table 5). Sample thickness was measured using a Mitutoyo micrometer with a resolution of ±1 μm. Densities were estimated from the bulk composition of the samples using the Gladstone-Dale rule [*Silver et al.*, 1990; *Mandeville et al.*, 2002].

Total dissolved water was determined using the absorbance band near 3570 cm^{-1}. Water dissolved as molecular H_2O was determined using the band near 1630 cm^{-1}. Water dissolved as OH was computed from the 4500 cm^{-1} band [e.g., *Stolper,* 1982; *Mandeville et al.,* 2002; *Okumura et al.,* 2003]. The background was approximated with tangential line segments between 2500 and 3750 cm^{-1}, 4800 and 5400 cm^{-1}, and 1550 and 1690 cm^{-1}, respectively.

3.   Results

This section is divided into six parts. The first section describes the materials recovered from these experiments. The five remaining parts address the following questions: (1) How much of the non-volatile components in the projectile were retained in the recovered impact materials? (2) How much crystalline serpentine is present in impact glasses and breccias? (3) Do impact glasses or breccias contain any water? (4) How much water is present in the recovered impact materials? (5) Where is the water in impact materials coming from? We organize the results based on these questions, rather than by

individual analytical methods, because these questions can in most cases only be answered by combining multiple sets of data.

3.1. Recovered impact materials

The impact products recovered from experiments fall into three classes: impact glasses, serpentine relics, and breccia pieces. Table 4 reports the mass of each class of materials recovered from each experiment. Breccias comprise the bulk of the material (between 53 and 57 wt.%). Impact glasses account for 42 to 43 wt.% of the mass of recovered material with serpentine relics as a minor component (1 to 4 wt.%).

The impact glasses are vesicular pieces of translucent glass with a vitreous luster (Fig. 2A). Occasionally dark flecks are trapped within the glass (e.g., upper right corner of Fig. 2A). Serpentine relics consist of small fragments of serpentine found unattached to any other impact materials (Fig. 2B). Breccia pieces are a mixture of shock-compressed pumice and serpentine fragments bound together by impact-generated glasses. These melt breccias are similar to the projectile-contaminated pieces reported by *Daly and Schultz* [2016]. In some cases the breccias are mostly impact-generated glass, with a small amount of clastic pumice and a scattering of tiny dark flecks within the glass (e.g., Fig. 2C). In other cases, thin veins of quenched melt attached larger pieces of serpentine to the breccias (e.g., Fig. 2D).

3.2. How much of the non-volatile components in the projectile were retained in the recovered impact materials?

Answering this question relies primarily on the results of ICP-AES. However, constraints from TGA data are also needed. Table 5 reports the compositions of the serpentine projectile, heat-treated pumice, impact glasses, and breccias recovered from the experiments. Several aliquots of powdered serpentine and heat-treated pumice were run to assess reproducibility. Impact glasses and breccias should be two-component mixtures of the serpentine projectile and heat-treated pumice target. Hence, two-component mixing calculations can quantify how much the projectile and target contribute to the glasses and breccias. Using notation similar to *Cantagrel et al.* [1984], the following equation describes two-component mixing:

$$(C_{serp} - C_{pum})\chi_{serp} = (C_{br} - C_{pum}) \qquad (2)$$

where C_{serp}, C_{pum}, and C_{br} are the abundances of an oxide in the serpentine projectile, heat-treated pumice, and breccias, respectively. The term X_{serp} is the mass fraction of the projectile in the impact glasses or breccia, depending on the sample in question.

Before using equation (2), ICP-AES data were normalized using the method of *Allègre et al.* [1995]. After normalizing analytical totals based on mass losses during TG analysis, the concentration of each oxide was divided by its standard deviation, multiplied by the concentration range of that oxide among all samples, divided by the analytical error for that oxide, and divided by the mean concentration of the oxide. This method gives the strongest weight to oxides with small analytical errors and large concentration ranges.

Figure 3 shows the result of one such mixing model. If impact glasses and breccias are two-component mixtures of the target and projectile, then all oxides will plot along a single line that passes through the origin. The slope of that line, calculated from least-squares regression, is X_{serp}. In all cases, the oxides plot along a line passing through the origin, consistent with the impact materials being two-component mixtures. This relationship rules out significant contamination by a third compositional endmember. Table 6 summarizes the results of these mixing calculations.

The mass fraction of the non-volatile components in the projectile that were recovered can be calculated from these mixing models. The mass of each class of impact materials is multiplied by X_{serp} and divided by the mass of the projectile. The results are added together to yield the total projectile retention efficiency for a given experiment (Table 7). The projectile retention efficiency ranges from 14% to 16% at 30°, up to 19% at 45°. Impact breccias account for most of the retained projectile. At 30° serpentine relics account for the least amount. At 45° impact glasses carry the least projectile material.

3.3.   *How much crystalline serpentine is present in impact glasses and breccias?*

X_{serp} is based solely on bulk chemistry. Hence, it provides no information about the physical state of the projectile incorporated into the impact glasses or breccias. However, it is critical to know how much of the projectile is preserved as serpentine-rich glasses and surviving crystalline serpentine, respectively. This information is needed to determine the relative importance of impact-generated glasses and serpentine survivors to

the total water budget. X-ray diffraction (XRD) can quantify the abundance of *crystalline* serpentine in impact glasses and breccias.

3.3.1. *Diffraction patterns of the target and projectile*

Figure 4 shows the XRD patterns of the heat-treated pumice target and serpentine projectile. The heat-treated pumice target contains glass, with small amounts of anorthite, tridymite, quartz, muscovite, and hematite. The serpentine projectile is almost entirely antigorite, with a small amount of calcite.

Figure 5 shows XRD patterns for impact glasses and breccias. All samples have a significant amorphous component, as indicated by the "amorphous hump" between ~15 and 35° 2θ. In addition, all patterns have peaks from the serpentine projectile and pumice target (labeled S and P, respectively). However, not all samples display all the peaks seen in the serpentine projectile or pumice target. For example, Figure 5B has a peak near 8.8° 2θ attributed to muscovite. Muscovite peaks are present in the target pumice (Fig. 4), but they are not discernable in the other impact materials. Antigorite peaks are more intense in breccias than in impact glasses. Impact glasses, but not breccias, have peaks near 32.2, 36.4, and 52.1° 2θ due to forsterite. Enstatite, if present, would have peaks near 28.1 and 31.0° 2θ. Such peaks are absent in both impact glasses and breccias.

3.3.2. FULLPAT modeling of diffraction patterns

XRD patterns can be modeled quantitatively in order to determine the abundance of crystalline antigorite. Because the impact materials have a large amorphous component, we use FULLPAT [*Chipera and Bish*, 2002] to model the abundance of antigorite in impact products. FULLPAT uses least-squares minimization to optimize the fit of selected library standards to the observed XRD pattern. Corundum-spiked patterns of the antigorite projectile, a tektite, and the heat-treated pumice target were treated as library standards. The tektite represents glass generated during the impact. It is not a perfect analog; however, none of the impact-generated glasses in these experiments were pure enough to use as a glass standard. Forsterite abundances in the impact glasses are likely ~1 wt.%, which is comparable to the uncertainty in FULLPAT model results. Therefore, forsterite can be omitted without significantly impacting the model results.

The outputs of these FULLPAT models are F_{serp}, F_{targ}, and F_{glass} which represent the abundances (in wt.%) of the antigorite projectile, heat-treated target pumice, and tektite (i.e., impact-generated glass). Table 8 provides the FULLPAT results. Impact glasses contain 0.3 to 2.7 wt.% crystalline serpentine. Breccias contain 1.4 to 7.9 wt.% crystalline serpentine. Model totals range from 92.7% to 110.8%. Some patterns are modeled quite well (e.g., impact breccias from experiment 160713), while others are not. However, the R factors are all less than 0.1, which indicates that the model results are good [*Chipera and Bish*, 2002].

Figure 6 compares the observed (blue) and modeled (red) XRD patterns. Small gray plots above each pattern show the difference between the observed and modeled patterns.

In the impact glasses from experiments 160713 and 160714, FULLPAT accurately reproduces the height of the antigorite peak near 12° 2θ. Hence, these serpentine abundances are well constrained. FULLPAT overestimates serpentine abundance in impact glasses from experiment 160715 and in breccias from experiments 160713 and 160715. These abundances are therefore upper limits. The abundance of serpentine calculated by FULLPAT is too low for breccias from experiment 160714. Hence, this value is a lower bound.

The amorphous component is difficult to model. Three factors contribute to this difficulty. First, the tektite is not strictly identical to the impact glasses produced during these experiments; the two glasses formed over different temporal scales. Second, both impact-generated glasses and the pumice contribute to the amorphous hump in the mixtures. Third, the materials in the impact glasses and breccias have been shocked to various degrees, which strains the lattice. However, the FULLPAT library standards are unshocked. Nevertheless, the goal for FULLPAT modeling is to constrain the abundance of crystalline serpentine so the serpentine-related peaks are the priority.

Given the importance of constraining F_{serp}, a second set of models was run. Instead of modeling the entire pattern between 5 and 70° 2θ, patterns were only modeled from 12 to 12.4° 2θ, a range that encompasses the strongest antigorite peak. These models yielded better fits to the amplitude of the ~12.2° 2θ peak at the expense of accuracy in modeling the background and amorphous components. Based on this second set of models, the abundance of crystalline serpentine in impact glasses is 0.3 to 0.8 wt.%, whereas the abundance of crystalline serpentine in breccias is 1.5 to 5.2 wt.%. The two sets of

FULLPAT models provide endmembers for F_{serp}. The true abundance of crystalline serpentine likely lies between the values in Tables 8 and 9.

3.4. Do impact glasses or breccias contain any water?

Absorbance features related to OH and molecular H_2O are seen in FTIR data acquired through doubly polished sections of impact glasses from all three experiments (Figs. 7–9). Hence, the glasses contain water. Table 10 lists the band assignments considered here, including the OH- and H_2O-related absorbance features near 5200 cm^{-1}, 4500 cm^{-1}, 4000 cm^{-1}, 3570 cm^{-1}, and 1630 cm^{-1}. Absorbance peaks between ~1500 and 2000 cm^{-1} are due to vibrations of the aluminosilicate glass lattice, except for the $v2$ bending mode of H_2O near ~1630 cm^{-1} [*Newman et al.*, 1986].

In order to characterize variability in the abundance and speciation of water, spectra were acquired from multiple pieces of impact glass (Figs. 8 and 9). All spectra display a strong, broad asymmetric absorbance feature near 3570 cm^{-1}. The absorbance of this band varies from location to location and from sample to sample. In addition, all the spectra show a symmetrical absorbance feature near 1630 cm^{-1}. This feature is definitive evidence of molecular water [*Stolper,* 1982; *Newman et al.,* 1986; *Mandeville et al.,* 2001].

Other parts of the spectra differ. For example, the sample from experiment 160715 shows a molecular water feature near 5200 cm^{-1}; however, this feature is absent in the sample from experiment 160713. Given the presence of a 1630 cm^{-1} band, the absence of the 5200 cm^{-1} absorption is unexpected. Perhaps the 5200 cm^{-1} feature is too weak to be

seen due to the lower absorptivity of the combination mode at 5200 cm^{-1} and an increased

level of noise in the spectra at higher wavenumbers. The X-OH feature near 4500 cm^{-1} is

subtle, but present, in the sample from experiment 160715. However, this feature is absent

in the 160713 sample. Finally, spectra from experiment 160715 have features near

3000 cm^{-1} caused by organics. These are attributed to C-H surface contamination. These

features are so small (compared to the 3570 cm^{-1} total water band) that they do not affect

the interpretation of the bands related to OH and H_2O.

The water contents of these glasses were calculated using the Beer-Lambert law

(Table 11). Total water contents (OH and H_2O) based on the band near 3570 cm^{-1} range

from 380 to 1360 ppm in experiment 160713 and 2160 to 8560 ppm in experiment 160715.

These are likely conservative lower bounds (see Supplementary Text S3). In order to assess

speciation, the abundance of molecular water was calculated using the 1630 cm^{-1} feature

and the abundance of hydroxyl using the 4500 cm^{-1} feature. Note that the 4500 cm^{-1} band

only appears in the sample from experiment 160715. Most of the "water" in the glass is

molecular water, not hydroxyl (Fig. 10; Table 11). This is surprising, as *Stolper* [1982] and

Mandeville et al. [2002] found that below ~4 wt.% H_2O most of the water in silicate glasses

is stored as hydroxyl. *Stopler* [1982] did not detect any molecular water in glasses with

<0.2 wt.% total water. However, those previous studies dealt with much larger total water

contents (e.g., up to 7 wt.% H_2O in *Stolper* [1982]) and with volcanic glasses or glasses

produced during petrologic experiments. The glasses analyzed here have much lower total

water contents and formed during impact, rather than during a volcanic eruption. Higher

quench rates may favor molecular water over hydroxyl. In addition, these impact glasses

are highly vesicular, and molecular water trapped in vesicles may be contributing to the absorbance feature at 1630 cm^{-1}.

3.5. *How much water is present in the recovered impact materials?*

Spectra reveal the speciation of water in impact glasses and constrain their total water contents. However, water contents in even single pieces of glass are quite variable (e.g., Table 11). This heterogeneity precludes using the FTIR data to determine the *bulk* water content of impact glasses. Thermogravimetric (TG) and differential scanning calorimetry (DSC) are done on bulk powders. Hence, these data are better suited to quantifying the total water content of impact glasses and breccias. Electron microprobe data indirectly constrain the OH content of serpentine relics.

3.5.1. *Description of TG/DTG/DSC profiles*

Impact glasses lose mass gradually beginning at 50 °C (Fig. 11). DTG profiles indicate a maximum rate of mass loss between 145 and 154 °C, depending on the sample. DSC curves have minima between 145 and 194 °C. Starting between 495 and 600 °C (again, depending on the sample), the gradual mass loss is overprinted by a second mass loss event, which lasts to between 730 and 750 °C (depending on the sample). In impact glasses from experiments 160714 and 160715, this second mass loss is accompanied by W-shaped DTG peaks. The two minima in experiment 160714 occur at 660 and 690 °C. In

experiment 160715 the minima occur at 530 and 700 °C. Overall, impact glasses lost between 0.75 and 0.92 wt.% from 100 to 850 °C. See Table 12.

Profiles of breccia pieces exhibit many of the same characteristics as impact glasses (Fig. 11). Breccia pieces gradually lose mass beginning at 50 °C. DTG profiles indicate a maximum rate of mass loss between 150 and 155 °C, depending on the sample. DSC curves have minima between 140 and 149 °C. However, breccias lose more of their mass during this portion of the heating routine than the impact glasses lose. In addition, mass loss events that start between 515 to 590 °C (depending on the sample) and last until 740 °C are more pronounced in the breccias. DTG profiles between ~495 and 750 °C also exhibit stronger features than those of the impact glasses. The W-shaped peak in breccias from experiments 160713 and 160714 has two DTG minima at ~645 and 690 °C. The DTG peak for breccias from experiment 160715 is highly asymmetric and very deep compared with the DTG peaks in other breccia samples. The DTG maximum in this sample occurs near 695 °C. Overall, the breccias lost between 2.03 and 2.75 wt.% from 100 to 850 °C (Table 12).

3.5.2. Interpretation of TG/DTG/DSC profiles

The TG/DTG/DSC profiles of impact glasses and breccias are consistent with loss of OH and/or H_2O from an amorphous phase, antigorite, and, in the case of the breccias, additional thermally active phase(s). In all materials, adsorbed water accounts for most of the mass losses between 50 °C and 100 °C. Mass losses are minimal in this temperature range. Between 100 and 500 °C TG and DTG profiles are similar to perlite [*Foldvari*,

2011], a hydrated volcanic glass. Hence, mass losses between 100 and ~500 °C are attributed to diffusive loss of OH and/or H_2O from the glass. The broad, endothermic DSC signal is consistent with removal of OH or H_2O.

The temperature range and TG profile shape for mass loss events between ~515 and 740 °C are consistent with antigorite dehydroxylation (i.e., the serpentine projectile) [*Viti*, 2010; *Gualtieri et al.*, 2012]. The typical dehydroxylation interval for antigorite is shaded gray in Figure 11. In impact products, this mass loss event occurs over a narrower temperature range. This difference likely reflects shock damage. The shape of the DTG peak in this temperature range provides even stronger evidence that the mass loss is due to antigorite dehydroxylation: the W-shaped or asymmetric character of DTG profiles (particularly in the impact breccias) is diagnostic and reflects the overlapping reactions that take place during antigorite dehydroxylation [*Viti*, 2010; *Gualtieri et al.*, 2012].

Small DTG peaks in the breccias between ~300 and 450 °C indicate the presence of thermally active phases that are not present in the impact glasses. These temperatures may be consistent with brucite, $Mg(OH)_2$ [*Foldvari*, 2011], a mineral that has been suggested as a decomposition product of shocked serpentine [*Tyburczy et al.*, 1991; *Sekine et al.*, 2012]. XRD patterns do not show peaks at 18.53, 32.88, 37.98; 50.79; and 58.68 °2θ that would demonstrate the presence of brucite. Given the very small mass losses associated with these DTG peaks, brucite, if present, is likely below the detection limit.

3.5.3. Summary of TGA results

The TG, DTG, and DSC data reveal mass losses caused by loss of OH and/or H_2O. Impact glasses contain 0.75 to 0.92 wt.% OH + H_2O. Breccias contain 2.03 to 2.75 wt.% OH + H_2O (Table 12; Fig. 11). Profile shapes reveal that the volatile loss is due to two major reservoirs: an amorphous component and crystalline (but presumably shocked) antigorite. The amorphous phase slowly releases its OH and H_2O between ~100 and 500 °C. Antigorite dehydroxylates and quickly releases structural hydroxyl from 515 to 850 °C.

3.5.4. Hydration state of serpentine relics

Due to their small sizes, serpentine relics (e.g., Fig. 2B) were not powdered and measured on the TGA. Instead, samples were studied with the electron microprobe. Table 13 summarizes the compositions of serpentine relics from each experiment. Figure 12 shows the specific sites analyzed. Serpentine relics have oxide abundances and analytical totals that agree well with the data for the bulk serpentine projectile (Table 5). The similar analytical totals indicate that these isolated serpentine relics have not been dehydrated by impact. Instead, the data imply that they retained their original OH inventory.

3.6. Where is the water in impact materials coming from?

Comparisons between the TG/DTG/DSC profiles of impact products, heat-treated pumice target, and the antigorite projectile constrain the source of water.

3.6.1. TG/DTG/DSC profiles of the serpentine projectile

Figure 13 shows TG, DTG, and DSC profiles of three samples of the serpentine projectile. Samples were run in triplicate in order to assess reproducibility. The TG profiles show a single mass-loss event between ~515 and ~850 °C. The total mass loss in this interval is 12.07 ± 0.12 wt.% (2σ standard deviation). All three profiles have a DTG maximum at 718 °C. DSC profiles show an endothermic reaction between 730 and 770 °C, as well as an exothermic reaction near 845 °C.

The temperature of the DTG maximum, shape of the DTG profile, and endothermic followed by exothermic DSC features are diagnostic of antigorite dehydroxylation [*Viti*, 2010; *Gualtieri et al.*, 2012]. XRD data also show that the projectile is nearly pure antigorite (see section 3.3.1). The exothermic DSC peak near 845 °C likely signals the crystallization of enstatite. The reaction occurs at slightly higher temperatures than the 820 to 826 °C reported by *Viti* [2010]. However, this difference is a consequence of the higher heating rate used here, which shifts peaks to higher temperatures.

3.6.2. TG/DTG/DSC profiles of heat-treated pumice

Two samples of heat-treated pumice were analyzed to assess reproducibility. TG profiles show a gradual mass loss between 100 and 850 °C (Fig. 14). This profile is consistent with diffusive loss of a small amount of OH. No signals in the TG, DTG, or DSC profiles suggest the presence of other thermally active phases. TG and DTG profiles of replicates are indistinguishable despite the extremely low volatile contents of these samples. The DSC profiles show similar trends, but are offset from one another. The average mass loss was 0.20 ± 0.04 wt.% (2σ standard deviation).

3.6.3. Implications for the source of water in the impact materials

Impact glasses and breccias lost more mass than the heat-treated pumice target during TGA (Fig. 11 and Table 12). Therefore, the impact products have higher water contents than the target. The water contents of impact glasses are about four times larger than the water content of the heat-treated pumice. Melt-bearing breccias contain nearly ten times more water than the target. Hence, impact glasses and breccias must have incorporated water from some other source. The water content of the projectile (12.07 wt.%) greatly exceeds the water contents of all impact products. Hence, the projectile can supply the water in the impact glasses and melt-bearing breccias. Given the quantities of water in impact products, the bulk of their water must be derived from the projectile.

4. Discussion

4.1.   *How much of the water in the projectile was delivered?*

The mass losses and TG profiles of impact glasses and breccias can be used to calculate the abundance of projectile-derived water in these impact products. This amount is termed the "serpentine equivalent". Serpentine equivalent is the amount of serpentine (by mass) that a breccia or glass must have incorporated in order to explain the water content of that breccia or glass. Prior to calculations of serpentine equivalent, mass losses of impact materials are corrected for the 0.2 wt.% water that could come from the heat-treated pumice target (Table 14).

Comparisons between serpentine equivalent and X_{serp} reveal whether the amount of water in the glasses and breccias matches expectations. Difference between X_{serp} and the serpentine equivalent indicate that impact glasses captured 76 to 100% of the water bound in the part of the projectile that was incorporated into the glasses. In impact breccias, however, serpentine equivalent exceeds X_{serp}. In fact, breccias trapped two to three times more water than would be expected if all the water associated with the serpentine that was incorporated into the breccias were trapped. The surplus water must be derived from the projectile; other sources of water are insufficient (Supplementary Text S4). In total, between 25 and 29% of the water in the projectile is delivered at 30°. At 45° water delivery increases to 36%.

4.2.   *How much do glasses and relics contribute to the water budget?*

Given F_{serp} and the known water content of the projectile, the amount of mass that impact glasses and breccias should lose during TGA due to serpentine dehydroxylation can be estimated. Comparison between the actual mass loss and this anticipated mass loss reveals how much water is stored in crystalline serpentine versus other reservoirs (Table 15). In impact glasses, only 5 to 18% of the total water ($OH + H_2O$) is stored in crystalline serpentine. The remaining water is stored in the glass itself or in vesicles. In breccias, crystalline serpentine accounts for 16 to 38% of the water budget. The remaining water is either stored in impact-generated glass, vesicles, or in some other portion of the breccia. Impact-generated glasses form at high temperatures; such temperatures enhance the solubility of water in silicate melts [*Harris et al.,* 2015; *Bureau and Keppler,* 1999; *Paillat et al.,* 1992].

The importance of these other reservoirs can be discerned from TG profiles (Fig. 11). The TG profiles, however, do not easily distinguish water lost from impact-generated glasses and water lost from pumice that trapped water from the vapor plume (see section 4.3). In the case of impact glasses, the samples are clearly made almost entirely of impact-generated glass (Fig. 2A, 8, and 9). Hence, impact-generated glasses must be the primary contributor to mass losses between 100 and ~500 °C. The breccias contain impact-generated glasses, but they also contain comminuted, shock-lithified pumice (Figs. 2C and 2D). If shocked pumice helped to trap the surplus water in the breccias (section 4.3), then both impact glasses and shocked pumice could contribute to the mass loss between 100 and ~500 °C. The contributions of impact-generated glasses and shocked pumice cannot

be separated using the TG data. It is clear, however, that surviving serpentine relics hold only a fraction of the total water in impact glasses and breccias.

4.3.   *A mechanism for trapping surplus water*

The surplus of projectile-derived water in impact breccias can be explained by the timing of serpentine devolatilization and evolution of the vapor plume. Planar shock experiments predict complete serpentine devolatilization above ~50 to 60 GPa [*Lange and Ahrens*, 1982; *Sekine et al.*, 2015]. The equation of state for serpentine [*Tyburczy et al.*, 1991] predicts that symmetric impacts at 5 km s^{-1} produce a peak pressure of 60.4 GPa in the projectile. Given that these impact experiments are oblique, however, frictional heating along the projectile-target interface further enhances vaporization, even though the peak pressures are reduced [*Schultz*, 1996; *Schultz and Eberhardy*, 2015]. Hence, near the point of impact the projectile could completely devolatilize. The forsterite in impact glasses demonstrates that part of the projectile dehydroxylated. The fate of water in the projectile during an oblique impact is complex due to the complex shock history in a sphere during penetration. Decoupling the projectile (due to spallation and shear) and entrapment before fully interacting with the target ensures preservation of impactor relics [*Schultz and Crawford*, 2016; *Daly and Schultz*, 2015, 2016]. Therefore, the recovery of serpentine relics that apparently retained all their water (section 3.5.4) does not preclude complete dehydration of serpentine near impact point. Devolatilization occurs not only after penetration and decompression but during further interactions with the target downrange from the point of impact [*Schultz et al.*, 2006; *Schultz and Eberhardy*, 2015].

Impact vapor envelopes the transient crater [*O'Keefe and Ahrens*, 1977; *Schultz and Eberhardy*, 2015]. Glasses and breccias line the interior of the transient crater [*Daly and Schultz*, 2016] and are therefore well positioned to incorporate water from the vapor plume. This provides one mechanism whereby the amount of water delivered exceeds what would be expected from X_{serp}: surplus water was released near the point of impact by projectile fragments, but the fragments themselves were later lost downrange. In spectral studies of impacts, vapor with atomic and molecular lines fills the transient cavity [*Schultz and Eberhardy,* 2015]. By implication, in a water-rich plume breccias could trap volatiles during their formation. Vapor envelopment and melt/breccia production overlap in time. High-speed imaging shows that the vapor plume is still self-luminous as glowing pieces of melt leave the growing crater. Shock comminution of the pumice likely increases the surface area of pumice grains and introduces strain into crystal lattices and pumice glass. These effects may enhance the ability of the breccias to trap water from the vapor plume. For example, if shock comminution were to increase surface area by a factor of three, then three times as many H_2O molecules could be able to hydrogen bond to surface silanol groups. In addition, *McCord et al.* [2011] suggested that increased surface area due to comminution may enhance OH production on the moon via solar wind implanation. The application of such ideas to shock-comminuted material deserves further study.

5.   Conclusions

Carbonaceous chondrite-like objects rich in serpentine deliver significant quantities of water into a regolith under impact conditions that are common in the main asteroid belt.

At 30° (with respect to horizontal), an average of 27% of the water in the projectile is delivered. In a 45° impact 36% of the water in the projectile is delivered. Water delivery is nearly double that expected based on projectile retention efficiency.

The data also indicate that impact glasses trap all or nearly all the water that is associated with the serpentine that was incorporated into the glasses. Impact breccias, however, have a surplus of water because they incorporate water from portions of the projectile that devolatilized and then escaped downrange. Recovered, lightly-shocked isolated serpentine relics retain all their structural water. These findings align with preliminary work by *Harris and Schultz* [2011] and *Harris et al.* [2015]. However, here we provide (a) the first detailed account for OH and H_2O derived from the projectile in impact glasses, (b) the first measurement of the efficiency of water delivery in oblique impact experiment, and (c) the first constraint on the distribution of impact-delivered water among projectile survivors and other reservoirs such as impact glass and breccias.

The results of this study indicate that the remnants of carbonaceous chondrite-like impactors and the impact melts created by them should trap all, if not more, of the water carried in the retained rocky fraction of the projectile. For example, if 15% of the mass of the projectile were delivered at 30° (based on these experiments), then at least 15% but up to 30% of the "water" present in the impactor also would be delivered, trapped within impact glasses, impact breccias, and projectile relics on the surface of the target.

The findings of this study provide new insights into the nature of hydrated dark material on Vesta. The experiments indicate that the delivery of the water in carbonaceous chondrite-like impactors is a natural outcome of impacts in the main belt. The delivered

217

water is hosted in a combination of impactor relics, melt breccias, and impact glasses. Crystalline serpentine relics are discernable in spectroscopic data in some regions of dark material [*Nathues et al.*, 2014]. Impact glasses are naturally dark due to xenocrysts and recrystallized minerals [*Schultz et al.*, 2006] and could also contribute to the exogenic hydration on Vesta. Although the experiments reported here are small in scale, *Harris and Schultz* [2005] reported the detection of water in terrestrial impact glasses. Such observations indicate that trapping of volatiles in impact melts also may be viable at larger scales, including those relevant to Vesta and possibly the Moon.

These experiments were done at 5 km s^{-1}. About half of the impacts at Vesta and on main-belt asteroids occur at speeds faster than 5 km s^{-1} [*O'Brien and Sykes*, 2011]. At these higher speeds, impacts are more likely to devolatilize hydrous impactors. Consequently, if volatile-rich relics of the projectile were the primary reservoir for impact-delivered water, then water delivery efficiency would be expected to decrease at these higher speeds. However, impact melt—and therefore impact glass—production increases with impact speed. If impact melt also successfully traps OH and H_2O during collisions in the main belt (as it does in experiments), then impacts at speeds >5 km s^{-1} may still deliver significant quantities of volatiles to Vesta. Impacts below 5 km s^{-1} would also deliver volatiles due to the gentler temperatures and pressures achieved during lower-speed impacts. At lower speeds, more of the delivered water would be hosted in impactor relics rather than in impact melts or impact-melt breccias.

Many other asteroids should be laden with significant meteoritic debris derived from the asteroid belt. This is a natural consequence of their impact history and the range

of impact speeds in the main belt. Hence, many asteroids—particularly the larger ones—are likely plastered with water (OH+H_2O) delivered during impacts by volatile-rich asteroids and meteoroids. Impact delivery is also a likely source for the hydration signatures seen on some metallic, M-type asteroids such as Psyche, as also suggested by *Takir et al.* [2017]. Combined with other results from hypervelocity impact experiments into metals [*Daly and Schultz,* 2017], we predict the preservation of hydrated impactor materials on Psyche. These predictions can be tested when the recently-approved Discovery-class Psyche mission [*Elkins-Tanton et al.*, 2016] reaches Psyche in 2030.

6.   Acknowledgements

7. References

Allègre, C. J., P. Schiano, and E. Lewin (1995), Differences between oceanic basalts by multitrace element ratio topology, *Earth Planet. Sci. Lett.*, *129*(1–4), 1–12, doi:10.1016/0012-821X(94)00235-Q.

Briani, G., M. Gounelle, M. Bourot-Denise, and M. E. Zolensky (2012), Xenoliths and microxenoliths in H chondrites: Sampling the zodiacal cloud in the asteroid Main Belt, *Meteorit. Planet. Sci.*, *47*(5), 880–902, doi:10.1111/j.1945-5100.2012.01367.x.

Bruck Syal, M., and P. H. Schultz (2015), Impact Delivery of Water at the Moon and Mercury, *Lunar and Planetary Science Conference XXXXVI*, abstract no. 1680.

Bureau, H. and H. Keppler (1999) Complete miscibility between silicate melts and hydrous fluids in the upper mantle: experimental evidence and geochemical implications, *Earth. Planet. Sci. Lett.,* 165, 187–196.

Cantagrel, J.-M., J. Didier, and A. Gourgaud (1984), Magma mixing: origin of intermediate rocks and "enclaves" from volcanism to plutonism, *Phys. Earth Planet. Inter.*, *35*(1–3), 63–76, doi:10.1016/0031-9201(84)90034-7.

Chipera, S. J., and D. L. Bish (2002), FULLPAT: a full-pattern quantitative analysis program for X-ray powder diffraction using measured and calculated patterns, *J. Appl. Crystallogr.*, *35*(6), 744–749, doi:10.1107/S0021889802017405.

Colaprete, A. et al. (2010), Detection of Water in the LCROSS Ejecta Plume, *Science*, *330*, 463, doi:10.1126/science.1186986.

Daly, R.T., and P.H. Schultz (2015), Predictions for impactor contamination on Ceres based on hypervelocity impact experiments, *Geophys. Res. Lett.,* 42, 7890 – 7898.

Daly, R. T., and P. H. Schultz (2016), Delivering a projectile component to the vestan regolith, *Icarus*, *264*, 9–19, doi:10.1016/j.icarus.2015.08.034.

Daly, R. T., and P. H. Schultz (2017), Projectile Preservation During Oblique Hypervelocity Impacts, *Lunar and Planetary Science Conference XXXXVIII*, abstract no. 1573.

Delmelle, P., F. Villiéras and M Pelletier (2005) Surface area, porosity and water adsorption properties of fine volcanic ash particles, *Bulletin of Volcanology,* 67, 160–169.

De Sanctis, M. C. D. et al. (2012), Detection of Widespread Hydrated Materials on Vesta by the VIR Imaging Spectrometer on board the Dawn Mission, *Astrophys. J. Lett.*, *758*(2), L36, doi:10.1088/2041-8205/758/2/L36.

Devine, J. D., J. E. Gardner, H. P. Brack, G. D. Layne, and M. J. Rutherford (1995), Comparison of microanalytical methods for estimating H_2O contents of silicic volcanic glasses, *Am. Mineral.*, *80*, 319–328.

Elkins-Tanton, L. T. et al. (2016), Asteroid (16) Psyche: The Science of Visiting a Metal World, *Lunar and Planetary Science Conference XXXXVII*, abstract 1631.

Foldvari, M. (2011), *Handbook of thermogravimetric system of minerals and its use in geological practice*, Occasional Papers of the Geological Institute of Hungary, Budapest.

Gault, D. E., and J. A. Wedekind (1978), Experimental studies of oblique impact, *Proceedings of the 9th Lunar and Planetary Science Conference,* 374–376.

Goodrich, C. A., W. K. Hartmann, D. P. O'Brien, S. J. Weidenschilling, L. Wilson, P. Michel, and M. Jutzi (2015), Origin and history of ureilitic material in the solar system: The view from asteroid 2008 TC3 and the Almahata Sitta meteorite, *Meteorit. Planet. Sci.*, *50*(4), 782–809, doi:10.1111/maps.12401.

Greshake, A. (2014), A strongly hydrated microclast in the Rumuruti chondrite NWA 6828: Implications for the distribution of hydrous material in the solar system, *Meteorit. Planet. Sci.*, *49*(5), 824–841, doi:10.1111/maps.12295.

Gualtieri, A. F., C. Giacobbe, and C. Viti (2012), The dehydroxylation of serpentine group minerals, *Am. Mineral.*, *97*(4), 666–680, doi:10.2138/am.2012.3952.

Harris, R. S., and P. H. Schultz (2011), The Potential of Impact Melts as a Lunar Water Reservoir, *A Wet Vs. Dry Moon: Exploring Volatile Reservoirs and Implications for the Evolution of the Moon and Future Exploration*, p. 22.

Harris, R. S., P. H. Schultz, and M. Bruck Syal (2015), Preservation of Cometary and Asteroidal Volatiles in Impact Melt: An Overlooked Reservoir for Hollow Formation on Mercury, *Lunar and Planetary Science Conference XXXXVI*, abstract no. 2585.

Kraus, R. G., S. T. Stewart, M. G. Newman, R. E. Milliken, and N. J. Tosca (2013), Uncertainties in the shock devolatilization of hydrated minerals: A nontronite case study, *J. Geophys. Res. Planets*, *118*(10), 2137–2145, doi:10.1002/jgre.20147.

Krzesińska, A., and J. Fritz (2014), Weakly shocked and deformed CM microxenoliths in the Pułtusk H chondrite, *Meteorit. Planet. Sci.*, *49*(4), 595–610, doi:10.1111/maps.12276.

Lange, M. A., and T. J. Ahrens (1982), Impact induced dehydration of serpentine and the evolution of planetary atmospheres, *Proceedings of the 13th Lunar and Planetary Science Conference,* A451–A456.

Lorenz, K. A., M. A. Nazarov, G. Kurat, F. Brandstaetter, and T. Ntaflos (2007), Foreign meteoritic material of howardites and polymict eucrites, *Petrology*, *15*(2), 109–125, doi:10.1134/S0869591107020014.

Mandeville, C. W., J. D. Webster, M. J. Rutherford, B. E. Taylor, A. Timbal, and K. Faure (2002), Determination of molar absorptivities for infrared absorption bands of H2O in andesitic glasses, *Am. Mineral.*, *87*(7), 813–821, doi:10.2138/am-2002-0702.

McCord, T. B., L. A. Taylor, J.-P. Combe, G. Kramer, C. M. Pieters, J. M. Sunshine, and R. N. Clark (2011), Sources and physical processes responsible for OH/H2O in the lunar soil as revealed by the Moon Mineralogy Mapper (M3), *J. Geophys. Res. Planets*, *116*(E6), E00G05, doi:10.1029/2010JE003711.

McCord, T. B. et al. (2012), Dark material on Vesta from the infall of carbonaceous volatile-rich material, *Nature*, *491*, 83–86, doi:10.1038/nature11561.

Morbidelli, A., J. Chambers, J. I. Lunine, J. M. Petit, F. Robert, G. B. Valsecchi, and K. E. Cyr (2000), Source regions and timescales for the delivery of water to the Earth, *Meteorit. Planet. Sci.*, *35*(6), 1309–1320, doi:10.1111/j.1945-5100.2000.tb01518.x.

Murray, R. W., D. J. Miller, and K. A. Kryc (2000), Analysis of major and trace elements in rocks, sediments, and interstitial waters by inductively-coupled plasma-atomic emission spectrometry (ICP-AES), *ODP Tech. Note 29*.

Nathues, A. et al. (2014), Detection of serpentine in exogenic carbonaceous chondrite material on Vesta from Dawn FC data, *Icarus*, *239*, 222–237, doi:10.1016/j.icarus.2014.06.003.

Neumann, G. A. et al. (2013), Bright and Dark Polar Deposits on Mercury: Evidence for Surface Volatiles, *Science*, *339*(6117), 296–300, doi:10.1126/science.1229764.

Newman, S., E. M. Stolper, and S. Epstein (1986), Measurement of water in rhyolitic glasses; calibration of an infrared spectroscopic technique, *Am. Mineral.*, *71*(11–12), 1527–1541.

O'Brien, D. P., and M. V. Sykes (2011), The origin and evolution of the asteroid belt—Implications for Vesta and Ceres, *Space Sci. Rev.*, *163*, 41–61, doi:10.1007/s11214-011-9808-6.

O'Keefe, J. D., and T. J. Ahrens (1977), Impact-induced energy partitioning, melting, and vaporization on terrestrial planets, *Proceedings of the 8th Lunar and Planetary Science Conference,* 3357–3374.

Okumura, S., M. Nakamura, and S. Nakashima (2003), Determination of molar absorptivity of IR fundamental OH-stretching vibration in rhyolitic glasses, *Am. Mineral.*, *88*(11–12), 1657–1662, doi:10.2138/am-2003-11-1204.

Ong, L., E. I. Asphaug, D. Korycansky, and R. F. Coker (2010), Volatile retention from cometary impacts on the Moon, *Icarus*, *207*, 578–589, doi:10.1016/j.icarus.2009.12.012.

Paillat, O., S.C. Elphick, and W.L. Brown (1992), he solubility of water in NaAlSi3O8 melts: a re-examination of Ab-H2O phase relationships and critical behaviour at high pressures, *Contrib. Min. Petro.,* 112, 490–500.

Pierazzo, E., and H. J. Melosh (2000), Hydrocode modeling of oblique impacts: The fate of the projectile, *Meteorit. Planet. Sci.*, *35*(1), 117–130, doi:10.1111/j.1945-5100.2000.tb01979.x.

Prettyman, T. H. et al. (2012), Elemental Mapping by Dawn Reveals Exogenic H in Vesta's Regolith, *Science*, *338*(6104), 242–246, doi:10.1126/science.1225354.

Quintana, S. N., P. H. Schultz, and D. A. Crawford (2015), Target Strength as an Important Consideration for Low-Speed Impacts, *Lunar and Planetary Science Conference XXXXVI*, abstract no. 2727.

Reddy, V. et al. (2012), Delivery of dark material to Vesta via carbonaceous chondritic impacts, *Icarus*, *221*, 544–559, doi:10.1016/j.icarus.2012.08.011.

Rivkin, A. S., and E. Pierazzo (2005), Investigating the Impact Evolution of Hydrated Asteroids, *Lunar and Planetary Science Conference XXXVI*, abstract no. 2014.

Rubin, A. E., and W. F. Bottke (2009), On the origin of shocked and unshocked CM clasts in H-chondrite regolith breccias., *Meteorit. Planet. Sci.*, *44*, 701–724, doi:10.1111/j.1945-5100.2009.tb00764.x.

Saal, A. E., E. H. Hauri, J. A. V. Orman, and M. J. Rutherford (2013), Hydrogen Isotopes in Lunar Volcanic Glasses and Melt Inclusions Reveal a Carbonaceous Chondrite Heritage, *Science*, *340*(6138), 1317–1320, doi:10.1126/science.1235142.

Schultz, P. H. (1996), Effect of impact angle on vaporization, *J. Geophys. Res.*, *101*, 21117–21136, doi:10.1029/96JE02266.

Schultz, P. H., and C. A. Eberhardy (2015), Spectral probing of impact-generated vapor in laboratory experiments, *Icarus*, *248*, 448–462, doi:10.1016/j.icarus.2014.10.041.

Schultz, P. H., and D. E. Gault (1990), Prolonged global catastrophes from oblique impacts, *Geol. Soc. Am. Spec. Pap.*, *247*, 239–262, doi:10.1130/SPE247-p239.

Schultz, P. H., B. Hermalyn, A. Colaprete, K. Ennico, M. Shirley, and W. S. Marshall (2010), The LCROSS Cratering Experiment, *Science*, *330*, 468, doi:10.1126/science.1187454.

Schultz, P. H., S. Sugita, C.A. Eberhardy, and C.M. Ernst (2006), The role of ricochet impacts on impact vaporization, *Int. J. Impact Eng.,* 33, 771–780.

Schultz, P. H., C. M. Ernst, and J. L. B. Anderson (2005), Expectations for Crater Size and Photometric Evolution from the Deep Impact Collision, *Space Sci. Rev.*, *117*, 207–239, doi:10.1007/s11214-005-3383-7.

Schultz, P. H., M. Zárate, W. E. Hames, R. S. Harris, T. E. Bunch, C. Koeberl, P. Renne, and J. Wittke (2006), The record of Miocene impacts in the Argentine Pampas, *Meteorit. Planet. Sci.*, *41*, 749–771, doi:10.1111/j.1945-5100.2006.tb00990.x.

Sekine, T., C. Meng, W. Zhu, and H. He (2012), Direct evidence for decomposition of antigorite under shock loading, *J. Geophys. Res. Solid Earth*, *117*(B3), B03212, doi:10.1029/2011JB008439.

Sekine, T., T. Kimura, T. Kobayashi, and T. Mashimo (2015), Dynamic water loss of antigorite by impact process, *Icarus*, *250*, 1–6, doi:10.1016/j.icarus.2014.11.008.

Silver, L. A., P. D. Ihinger, and E. Stolper (1990), The influence of bulk composition on the speciation of water in silicate glasses, *Contrib. Mineral. Petrol.*, *104*(2), 142–162, doi:10.1007/BF00306439.

Stolper, E. (1982), Water in silicate glasses: An infrared spectroscopic study, *Contrib. Mineral. Petrol.*, *81*(1), 1–17, doi:10.1007/BF00371154.

Svetsov, V. V., and V. V. Shuvalov (2015), Water delivery to the Moon by asteroidal and cometary impacts, *Planet. Space Sci.*, *117*, 444–452, doi:10.1016/j.pss.2015.09.011.

Takir, D., V. Reddy, J. A. Sanchez, M. K. Shepard, and J. P. Emery (2017), Detection of Water and/or Hydroxyl on Asteroid (16) Psyche, *Astron. J.*, *153*, 31, doi:10.3847/1538-3881/153/1/31.

Tomioka, N., K. Tomeoka, K. Nakamura-Messenger, and T. Sekine (2007), Heating effects of the matrix of experimentally shocked Murchison CM chondrite: Comparison with micrometeorites, *Meteorit. Planet. Sci.*, *42*(1), 19–30, doi:10.1111/j.1945-5100.2007.tb00214.x.

Turrini, D., and V. Svetsov (2014), The formation of Jupiter, the Jovian Early Bombardment and the delivery of water to the asteroid belt: The case of (4) Vesta, *Life*, *4*, 4–34, doi:10.3390/life4010004.

Tyburczy, J. A., B. Frisch, and T. J. Ahrens (1986), Shock-induced volatile loss from a carbonaceous chondrite: implications for planetary accretion, *Earth Planet. Sci. Lett.*, *80*(3), 201–207, doi:10.1016/0012-821X(86)90104-4.

Tyburczy, J. A., T. S. Duffy, T. J. Ahrens, and M. A. Lange (1991), Shock wave equation of state of serpentine to 150 GPa: Implications for the occurrence of water in the Earth's lower mantle, *J. Geophys. Res. Solid Earth*, *96*(B11), 18011–18027, doi:10.1029/91JB01573.

Viti, C. (2010), Serpentine minerals discrimination by thermal analysis, *Am. Mineral.*, *95*(4), 631–638, doi:10.2138/am.2010.3366.

Wetzel, D.T. (2014), *Abundance, speciation, and role of volatiles in planetary basalts,* PhD dissertation, Brown University, 187 p.

Zolensky, M. E., M. K. Weisberg, P. C. Buchanan, and D. W. Mittlefehldt (1996),
Mineralogy of carbonaceous chondrite clasts in HED achondrites and the Moon,
Meteorit. Planet. Sci., *31*, 518–537, doi:10.1111/j.1945-5100.1996.tb02093.x.

Zhuravlev, L.T. (2000), The surface chemistry of amorphous silica. Zhuravlev model,
Colloids and Surfaces A: Physicochemical and Engineering Aspects, 173, 1–38.

Tables

Table 1. Summary of experiments.

Experiment number	Angle (°)	Target	Projectile	Projectile diameter (mm)	Weight (g)	Speed (km s^{-1})	Chamber pressure (mmHg)
160713	30	Heat-treated pumice	Serpentine	6.35	0.4894	5.00	0.48
160714	30	Heat-treated pumice	Serpentine	6.35	0.5152	5.12	0.40
160715	45	Heat-treated pumice	Serpentine	6.35	0.5090	5.12	0.38

Table 2. Summary of analytical methods.

Technique	Abbreviation	Description of data	Data constrain
Inductively coupled plasma atomic emission spectroscopy	ICP-AES	Elemental abundances	How much of the non-volatile components in the projectile are present in impact glasses and breccias
X-ray diffraction	XRD	Diffraction pattern whose peaks correspond to minerals and amorphous material in impact glasses and breccias	How much crystalline serpentine exists in impact glasses and breccias
Thermogravimetric analysis/differential scanning calorimetry	TG/DTG/DSC	Mass loss, rate of mass loss, and heat flow into samples during heating	Bulk water content of impact glasses and breccias; distribution of water between impact glass and serpentine; water delivery efficiency
Fourier-transform infrared spectroscopy	FTIR	Absorbance spectrum	Total and molecular water content in field of view; speciation of OH vs. H_2O in impact glasses
Electron microprobe	EMP	In-situ compositions of serpentine relics	Hydration state of serpentine clasts

Table 3. Linear molar absorptivities used in this study.

Band (cm^{-1})	ε (L mol^{-1} cm^{-1})	Source
4500	1.73	*Newman et al.* [1986]
3750	75	*Okumura et al.* [2003]
1630	55	*Newman et al.* [1986]

Table 4. Masses of recovered impact materials.

Experiment Number	Angle (°)	Impact glasses (g)	Breccia pieces (g)	Serpentine relics (g)	Total (g)
160713	30	0.4221	0.5686	0.0117	1.0023
160714	30	0.5095	0.6501	0.0161	1.1758
160715	45	0.4717	0.5754	0.0400	1.0870

Table 5. Compositions of projectile, target, and impact products.

		Al_2O_3 (wt.%)	CaO (wt.%)	FeO_T (wt.%)	K_2O (wt.%)	MgO (wt.%)	MnO (wt.%)	Na_2O (wt.%)	SiO_2 (wt.%)	Total (wt.%)
Serpentine projectile	Replicate 1	2.99	2.78	8.30	0.00	34.16	0.12	0.01	38.68	87.05
	Replicate 2	2.99	2.70	8.17	0.03	33.91	0.12	0.02	39.31	87.25
Heat-treated pumice target	Replicate 1	12.89	0.74	1.14	4.50	0.06	0.05	3.96	78.16	101.5
	Replicate 2	12.88	0.64	1.15	4.45	0.06	0.05	4.05	77.34	100.6
	Replicate 3	12.74	0.53	1.16	4.83	0.06	0.05	3.97	77.22	100.6
	Replicate 4	12.63	0.51	1.11	4.79	0.06	0.05	4.09	78.23	101.5
Experiments										
160713 (30°)	Glasses	11.87	0.76	1.42	4.06	1.50	0.05	3.80	71.22	94.67
	Breccias	11.84	0.78	1.59	4.09	2.85	0.05	3.59	72.85	97.65
160714 (30°)	Glasses	12.43	0.70	1.40	4.36	2.01	0.05	3.87	76.26	101.1
	Breccias	11.96	0.67	1.54	4.15	3.17	0.05	3.71	74.68	99.92
160715 (45°)	Glasses	12.14	0.72	1.29	4.34	1.16	0.05	3.68	73.55	96.92
	Breccias	11.46	0.72	1.87	3.97	4.26	0.05	3.50	76.80	102.6

Table 6. Results of two-component mixing models.

Experiment Number	Angle (°)	Material	X_{Serp}	2σ*	R^2
160713	30	Impact glasses	0.071	0.013	0.993
		Breccias	0.063	0.012	0.992
160714	30	Impact glasses	0.041	0.006	0.995
		Breccias	0.052	0.017	0.977
160715	45	Impact glasses	0.034	0.012	0.975
		Breccias	0.067	0.022	0.978

*Two sigma uncertainties based on the uncertainty in regression slope.

Table 7. Projectile retention efficiencies.

Experiment number	Angle (°)	Impact product	Fraction of projectile retained		2σ*
160713	30	Impact glasses		6.2%	0.6%
		Breccias		7.3%	0.6%
		Serpentine fragments		2.4%	-
		Total retention	_16%_		_1.1%_
160714	30	Impact glasses		4.0%	0.4%
		Breccias		6.5%	0.9%
		Serpentine fragments		3.1%	-
		Total retention	_14%_		_1.1%_
160715	45	Impact glasses		3.2%	0.6%
		Breccias		7.5%	1.1%
		Serpentine fragments		7.9%	-
		Total retention	_19%_		_1.2%_

*Supplementary Text S2 outlines how these 2σ uncertainties were calculated.

Table 8. Results of FULLPAT modeling from 5 to 70° 2θ.

Material	Experiment	F_{serp} (wt.%)	F_{targ} (wt.%)	F_{glass} (wt.%)	Total (wt.%)	$\Sigma |$Delta$|^{1/2}$ *	R factor[†]
Impact glasses	160713	0.3	85.3	7.1	92.7	248.2	0.026
	160714	0.7	88.2	7.6	96.5	241.1	0.024
	160715	2.7	100.0	0.0	102.7	274.4	0.035
Breccia pieces	160713	2.4	92.8	2.5	97.7	248.6	0.022
	160714	1.4	100.0	9.5	110.8	262.3	0.026
	160715	7.9	89.0	0.4	97.3	251.4	0.022

*The values of $\Sigma |$Delta$|^{1/2}$ that remain after optimizing the fit between the summed library standards and the observed pattern.
[†]R factors assess the quality of the model fit. R < 0.1 indicates a good analysis.

Table 9. Results of FULLPAT modeling from 12 to 12.4° 2θ.

Material	Experiment	F_{serp} (wt.%)	F_{targ} (wt.%)	F_{glass} (wt.%)	Total (wt.%)	$\Sigma |$Delta$|^{1/2}$ *	R factor[†]
Impact glasses	160713	0.3	87.3	6.3	93.9	1.2	0.027
	160714	0.5	100.0	1.7	102.2	2.2	0.032
	160715	0.8	100.0	0.0	100.8	0.0	0.058
Breccia pieces	160713	1.5	100.0	3.9	105.4	2.8	0.072
	160714	3.5	100.0	14.9	118.4	2.9	0.109
	160715	5.2	100.0	15.1	120.3	4.3	0.232

*The values of $\Sigma |$Delta$|^{1/2}$ that remain after optimizing the fit between the summed library standards and the observed pattern.
[†]R factors assess the quality of the model fit. R < 0.1 indicates a good analysis.

Table 10. Assignment of absorbance features.

Band location (cm^{-1})	Attribution	Reference
5200	combination of stretching and bending modes of H_2O molecules	*Stolper* [1982]; *Newman et al.* [1986]; *Mandeville et al.* [2002]
4500	combination stretching and bending mode of X-OH groups (X = Al, Si)	*Stolper* [1982]; *Newman et al.* [1986]; *Mandeville et al.* [2002]
~3230 - ~3570 (broad)	Fundamental OH stretching mode of molecular H_2O, Si-OH, Al-OH; overtone of HOH bending	*Stolper* [1982]; *Newman et al.* [1986]; *Mandeville et al.* [2002]
1630	Fundamental bending mode of H_2O	*Stolper* [1982]; *Newman et al.* [1986]; *Mandeville et al.* [2002]

Table 11. Summary of Beer-Lambert results.

Sample	Color Code[‡]	3570 cm^{-1} band			1630 cm^{-1} band			4500 cm^{-1} band		
		Abs	Peak (cm^{-1})	H_2O_{tot} (ppm)	Abs	Peak (cm^{-1})	H_2O_m (ppm)	Abs	Peak (cm^{-1})	OH (ppm)
160713 Piece B*	Green	0.038	3585	380	0.027	1623	360	-	-	-
160713 Piece B	Blue	0.045	3585	450	0.026	1623	350	-	-	-
160713 Piece B	Black	0.135	3585	1360	0.060	1630	820	-	-	-
160715 Piece D†	Blue-gray	0.228	3585	2280	0.096	1625	1310	0.002	4516	920
160715 Piece D	Red	0.216	3585	2170	0.100	1623	1360	0.002	4456	810
160715 Piece D	Bright green	0.461	3587	4620	0.217	1627	2970	0.005	4499	1110
160715 Piece D	Purple	0.689	3618	6910	0.409	1627	5580	0.004	4516	1590
160715 Piece D	Red-orange	0.355	3585	3560	0.122	1625	1670	0.004	4458	1470
160715 Piece D	Light blue	0.215	3583	2160	0.069	1625	940	0.003	4435	1040
160715 Piece D	Gold	0.232	3585	2320	0.098	1625	1340	0.003	4458	1050
160715 Piece D	Gray	0.506	3587	5070	0.254	1625	3470	0.004	4456	1570
160715 Piece D	Green	0.854	3618	8560	0.483	1627	6610	0.004	4458	1700
160715 Piece D	Blue	0.470	3587	4710	0.232	1627	3170	0.003	4456	1320
160715 Piece D	Black	0.516	3587	5180	0.278	1627	3800	0.004	4437	1440

*Sample thickness: 0.0102 cm; density: 2,346 g L^{-1}
†Sample thickness: 0.0096 cm; density: 2,341 g L^{-1}
‡Corresponds to the color of spectra in Figs. 8 (160713) and 9 (160715)

Table 12. Results of TGA analyses.

	Impact Glasses			Breccia Pieces		
Experiment number	160713 (30°)	160714 (30°)	160715 (45°)	160713 (30°)	160714 (30°)	160715 (45°)
Mass at 50C (mg)	14.8954	25.5023	14.0491	12.0232	11.2297	26.9499
Mass at 100C (mg)	14.8844	25.4909	14.0411	12.0101	11.2157	26.9187
Mass at 850C (mg)	14.7480	25.2949	13.9360	11.7660	10.9640	26.1830
Mass Loss: 50 to 100 °C (wt.%)	0.07%	0.05%	0.06%	0.11%	0.12%	0.12%
Mass Loss: 100 to 850 °C (wt.%)	0.92%	0.77%	0.75%	2.03%	2.24%	2.73%
Onset of major mass loss event (°C)	515	600	495	590	515	570
Onset of major mass loss event (°C)	750	730	730	740	740	740
Mass loss during event (wt.%)	0.18%	0.14%	0.17%	0.47%	0.74%	1.18%
DSC minimum (°C)	178	145	194	149	147	140
	146	145	154	155	150	153
		660	700	350	340	475
Temperatures of other DTG peaks (°C)		690		430	410	640*
				645	550	695
				695	645	
					690	

*Shoulder in DTG peak.

Table 13. Composition of serpentine relics measured by electron microprobe (wt.%).

Experiment ID	Spot	MgO	FeO$_T$	CaO	Al$_2$O$_3$	SiO$_2$	Total
160713 (30°)	1	36.93	5.03	0.12	2.38	42.70	87.16
	2	36.94	5.31	0.09	2.80	42.50	87.64
	3	37.14	5.35	0.03	2.60	42.51	87.63
	4	37.25	5.33	0.00	2.77	42.73	88.08
	5	36.88	5.29	0.03	2.88	42.36	87.44
	6	36.68	5.27	0.00	2.41	42.68	87.04
	7	37.13	5.08	0.01	2.24	43.03	87.49
160714 (30°)	1	37.63	5.04	0.00	1.86	43.60	88.13
	2	37.25	5.04	0.00	2.15	43.16	87.60
	3	36.95	4.90	0.00	2.04	43.30	87.20
	4	36.85	5.21	0.00	2.36	42.99	87.41
	5	37.10	5.06	0.00	2.27	43.35	87.77
	6	36.85	5.14	0.01	2.32	42.84	87.16
160715 (45°)	1	36.43	5.27	0.02	2.69	41.95	86.36
	2	32.87	5.62	0.02	11.39	35.58	85.48
	3	33.08	5.39	0.03	12.36	35.35	86.21
	4	36.44	5.14	0.03	2.22	42.66	86.49
	5	36.07	4.97	0.02	2.71	41.84	85.61
	6	36.64	5.03	0.02	1.59	42.88	86.16

Table 14. Comparison between X_{serp} and the serpentine equivalent calculated from TGA data.

	Impact Glasses			Breccia Pieces		
Experiment number	160713 (30°)	160714 (30°)	160715 (45°)	160713 (30°)	160714 (30°)	160715 (45°)
X_{serp}*	7.1 ± 1.3%	4.1 ± 0.6%	3.4 ± 1.2%	6.3 ± 1.2%	5.2 ± 1.7%	6.7 ± 2.2%
Serpentine Equivalent†	5.9%	4.7%	4.5%	15.2%	16.9%	21.0%

*± 2σ uncertainty in X_{serp}.

†Assumes that all the mass loss between 100 and 850 °C is due to water derived from the serpentine projectile.

Table 15. Distribution of water between serpentine and impact glasses.

	Impact Glasses			Breccia Pieces		
Experiment Number	160713 (30°)	160714 (30°)	160715 (45°)	160713 (30°)	160714 (30°)	160715 (45°)
Expected TGA mass loss given F_{serp}*	0.04%	0.08%	0.10%	0.29%	0.42%	0.95%
TGA mass loss not due to serpentine[†]	0.68%	0.48%	0.45%	1.54%	1.62%	1.58%
Fraction of water not in serpentine	95%	85%	82%	84%	79%	62%

*For all samples except impact glasses from 160714, this is calculated from the upper bound of F_{serp}. This approach maximizes the amount of water attributed to serpentine. The FULLPAT model for the glasses from 160714 overestimates serpentine abundance, so the lower bound is used for that sample.

[†]After accounting for a 0.2 wt.% contribution from the heat-treated pumice target.
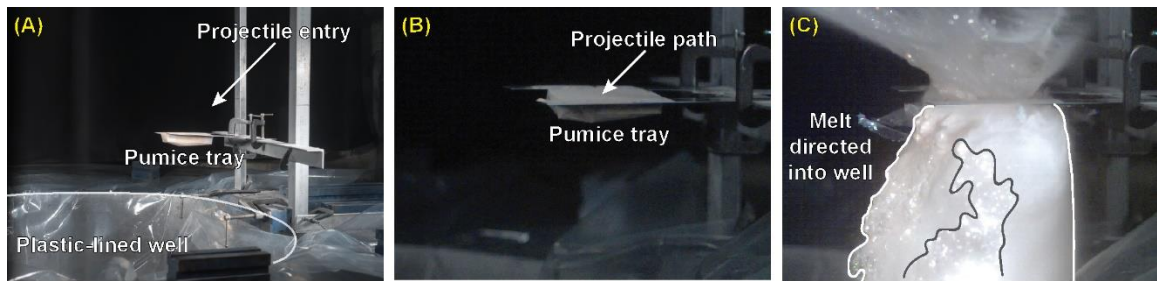
Figures

Figure 1. Experimental setup. (A) A tray of Mylar was filled with sieved, heat-treated airfall pumice. The center of the tray was beneath the impact point. A sheet of thick plastic lines the well of the impact chamber to facilitate recovery of impact products. (B) Close-up of pumice tray showing the path of the projectile for a 45° experiment. (C) The same view as (B), but 761.5 μs after impact. The Mylar has ruptured, directing most of the luminous melt downward into the well for recovery. White lines mark the extent of the glowing plume; the region outlined in gray contains an abundance of luminous melt.
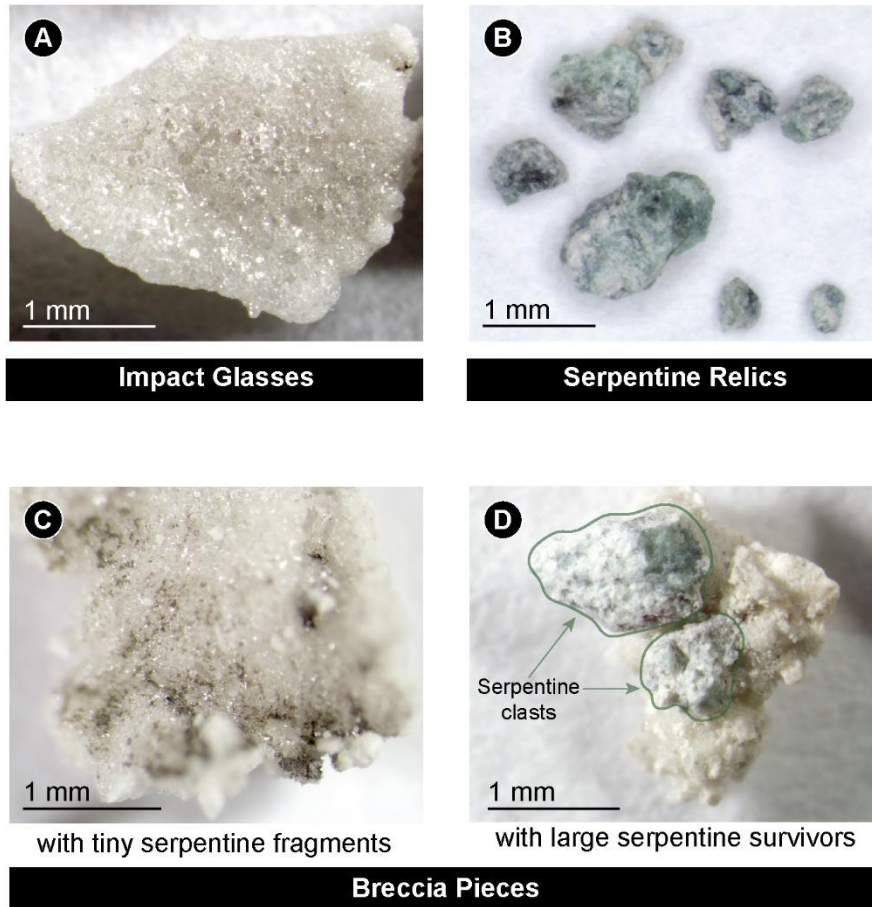
Figure 2. The materials recovered from impact experiments fall into three categories: (A) impact glasses, (B) serpentine relics, and (C, D) breccia pieces.
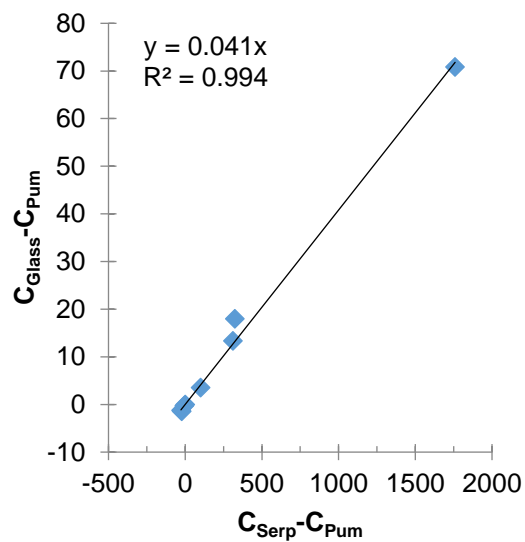
Figure 3. If impact materials are mixtures of the serpentine projectile and pumice target, then the oxides from each sample will plot along a line through the origin. The slope of that line is X_{serp}, the mass fraction of the projectile in the impact material. The data for this representative sample of impact glass from experiment 160713 are highly linear, which establishes that the glass is a two-component mixture of the target and projectile. The slope indicates that the glass is 4.1 wt.% projectile.
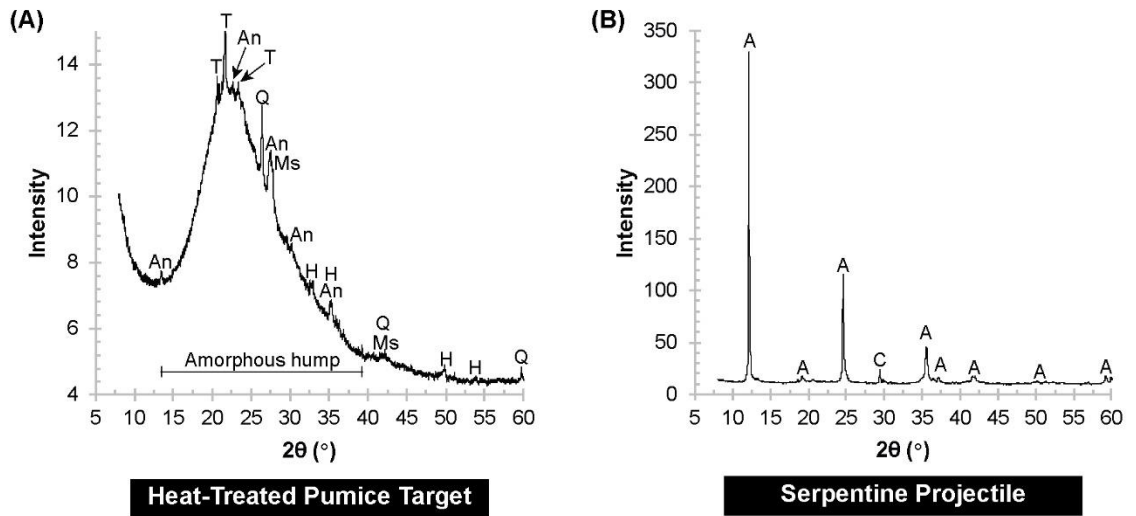
Figure 4. X-ray diffraction patterns for (A) the heat-treated pumice target and (B) the serpentine projectile. The heat-treated pumice is predominately glass, with lesser amounts of anorthite (An), tridymite (T), quartz (Q), muscovite (Ms), and hematite (H). The serpentine projectile is nearly pure antigorite (A) with only a minor amount of calcite (C).
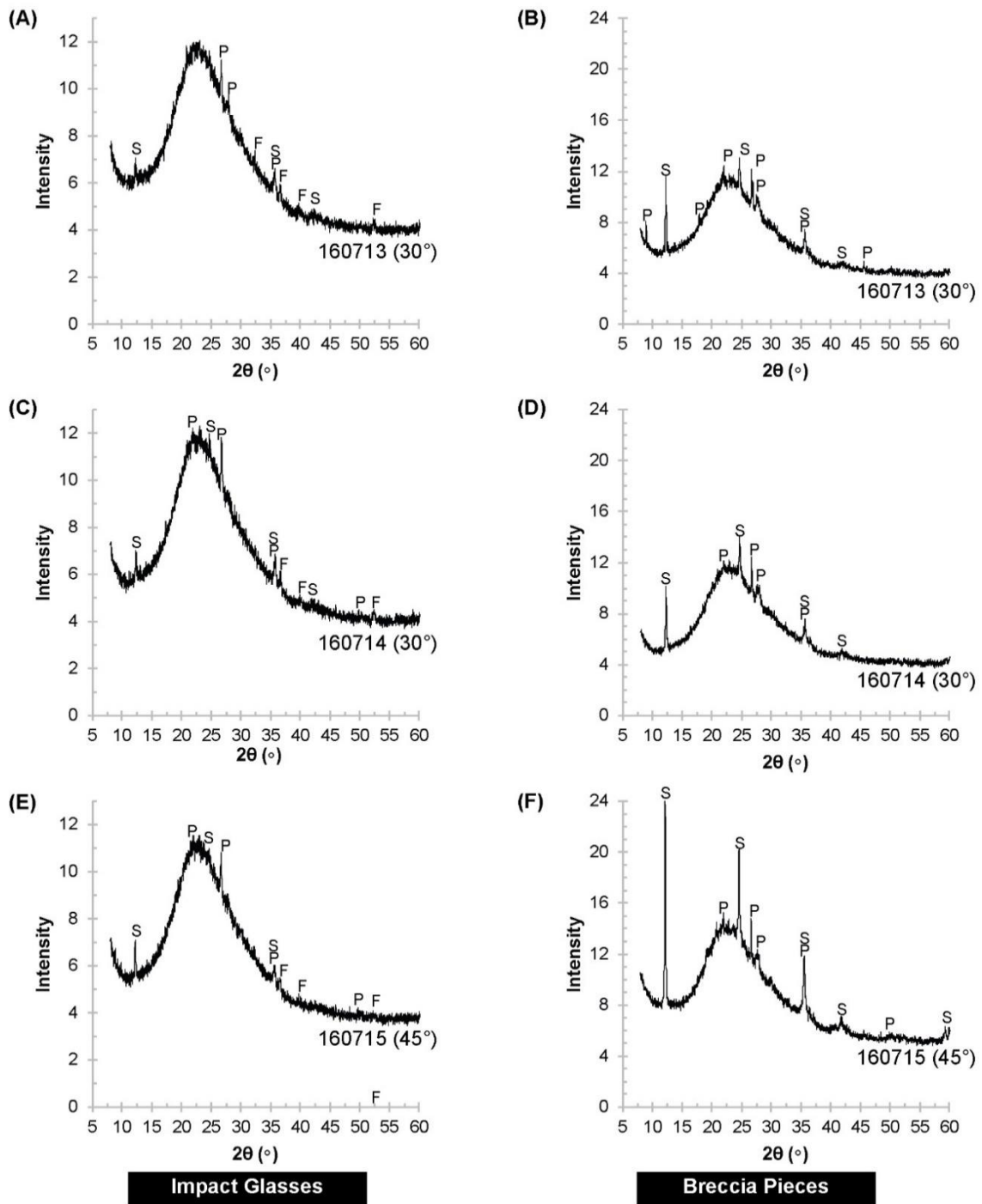
Figure 5. X-ray diffraction patterns for impact glasses and breccias from three impact experiments. Peaks labeled "S" are due to the serpentine projectile, while peaks labeled "P" are from the pumice target. Forsterite (F) is a decomposition product of antigorite.
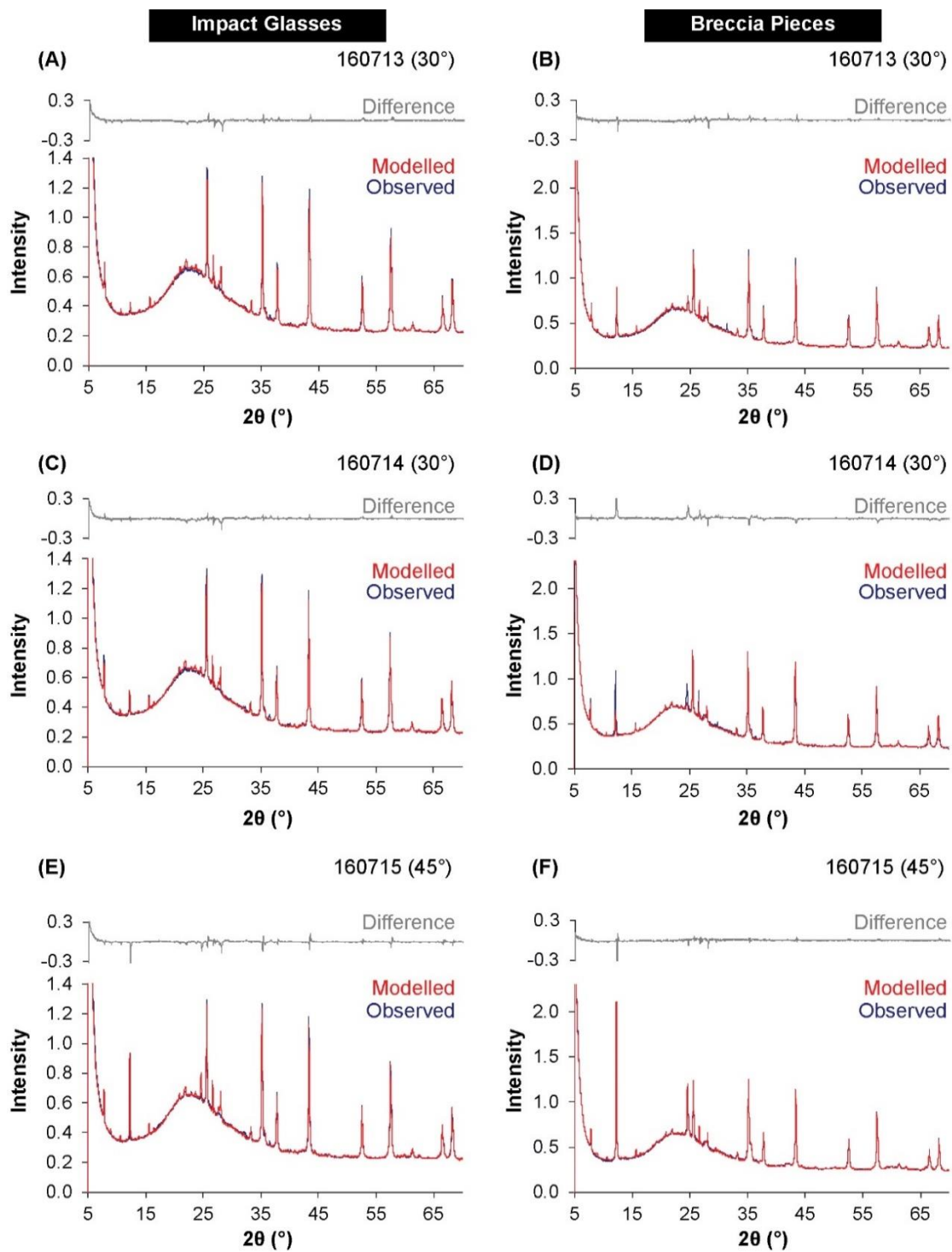
Figure 6. Comparison between observed XRD patterns (blue) and the model patterns produced by FULLPAT (red). A small graph (gray) above each diffraction pattern shows the difference between the observed and modeled patterns.
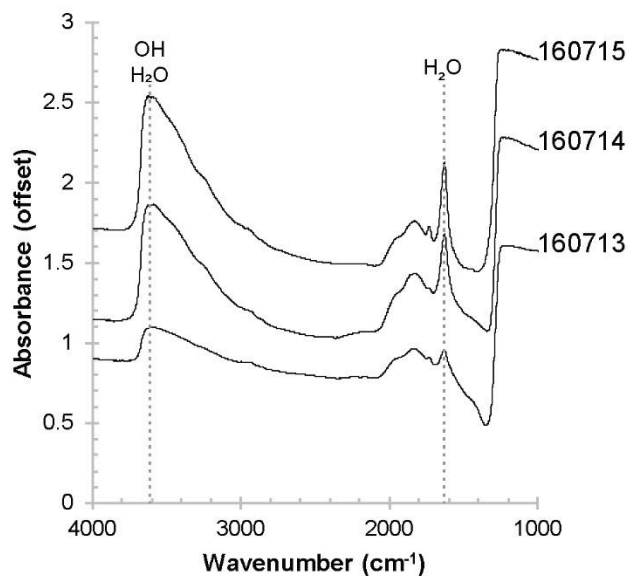
250

Figure 7. Transmission spectra of impact glasses from experiments 160713, 160714, and 160715. All three spectra have strong absorbance peaks near 3570 cm^{-1} and 1630 cm^{-1}. The asymmetric peak near 3570 cm^{-1} can be caused by both OH and/or H_2O, whereas only H_2O contributed to the more symmetric peak near 1630 cm^{-1}. Hence, spectra of all three glasses are consistent with the presence of both OH and molecular water. Spectra have been offset to better reveal their structure.
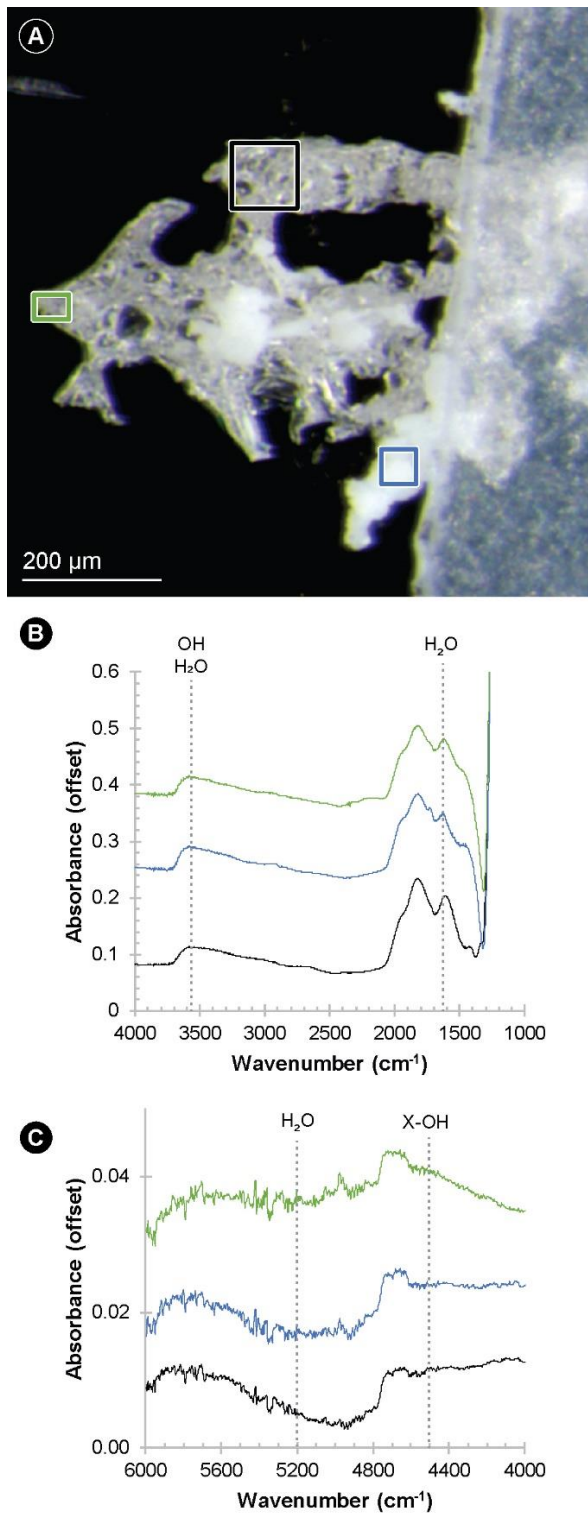
Figure 8. Transmission spectra from a piece of impact glass from experiment 160713. (A)

Optical micrograph of doubly-polished piece of impact glass. Colored squares show where

spectra were collected. The colors of the squares correspond to the colors of the spectra in panels (B) and (C). (B) Transmission spectra between 1000 and 4000 cm^{-1}. Peaks at both 3570 and 1630 cm^{-1} are present. (C) Transmission spectra between 4000 and 6000 cm^{-1}. The molecular water feature at 5200 cm^{-1} and X-OH feature at 4500 cm^{-1} both appear absent. An absorbance peak near 4700 cm^{-1} is present but unassigned.
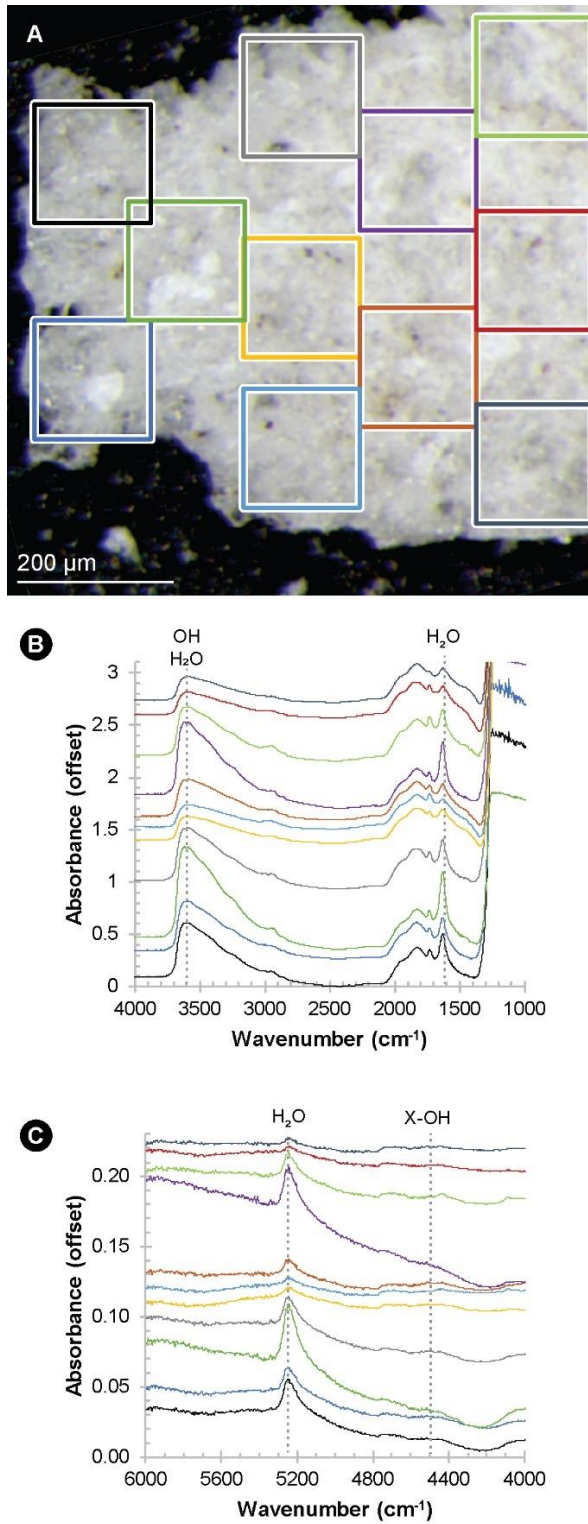
Figure 9. Transmission spectra of a piece of impact glass from experiment 160715. (A)

Optical micrograph of a doubly-polished piece of impact glass. Colored squares show

where spectra were collected. The colors of the squares correspond to the colors of the spectra in panels (B) and (C). (B) Transmission spectra between 1000 and 4000 cm^{-1}. Peaks at both 3570 and 1630 cm^{-1} are present. The small absorbance peaks near ~2850 and 3000 cm^{-1} are attributed to C-H surface contamination. (C) Transmission spectra between 4000 and 6000 cm^{-1} range. The H$_2$O feature near 5200 cm^{-1} is quite strong. The X-OH feature at 4500 cm^{-1} is small but discernable.
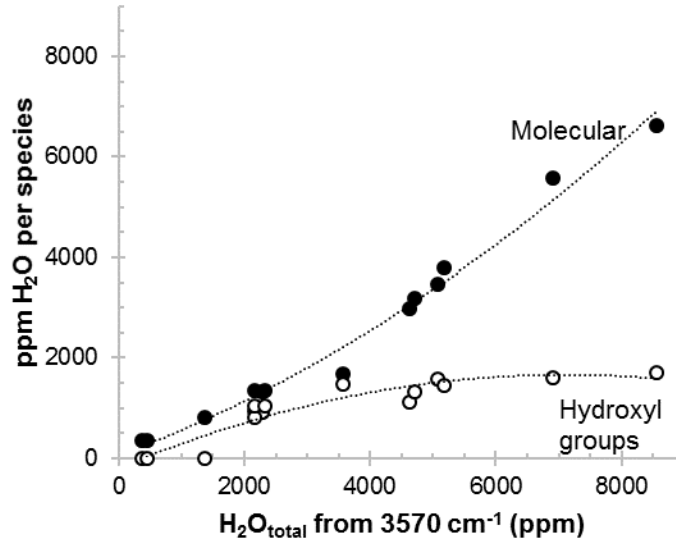
Figure 10. Speciation of water in impact glasses. Molecular water dominates the total water budget. Spectra in which a 4500 cm^{-1} feature was absent are plotted as having 0 ppm hydroxyl. As total water content increases, most the newly-added water is dissolved as molecular water rather than as hydroxyl.
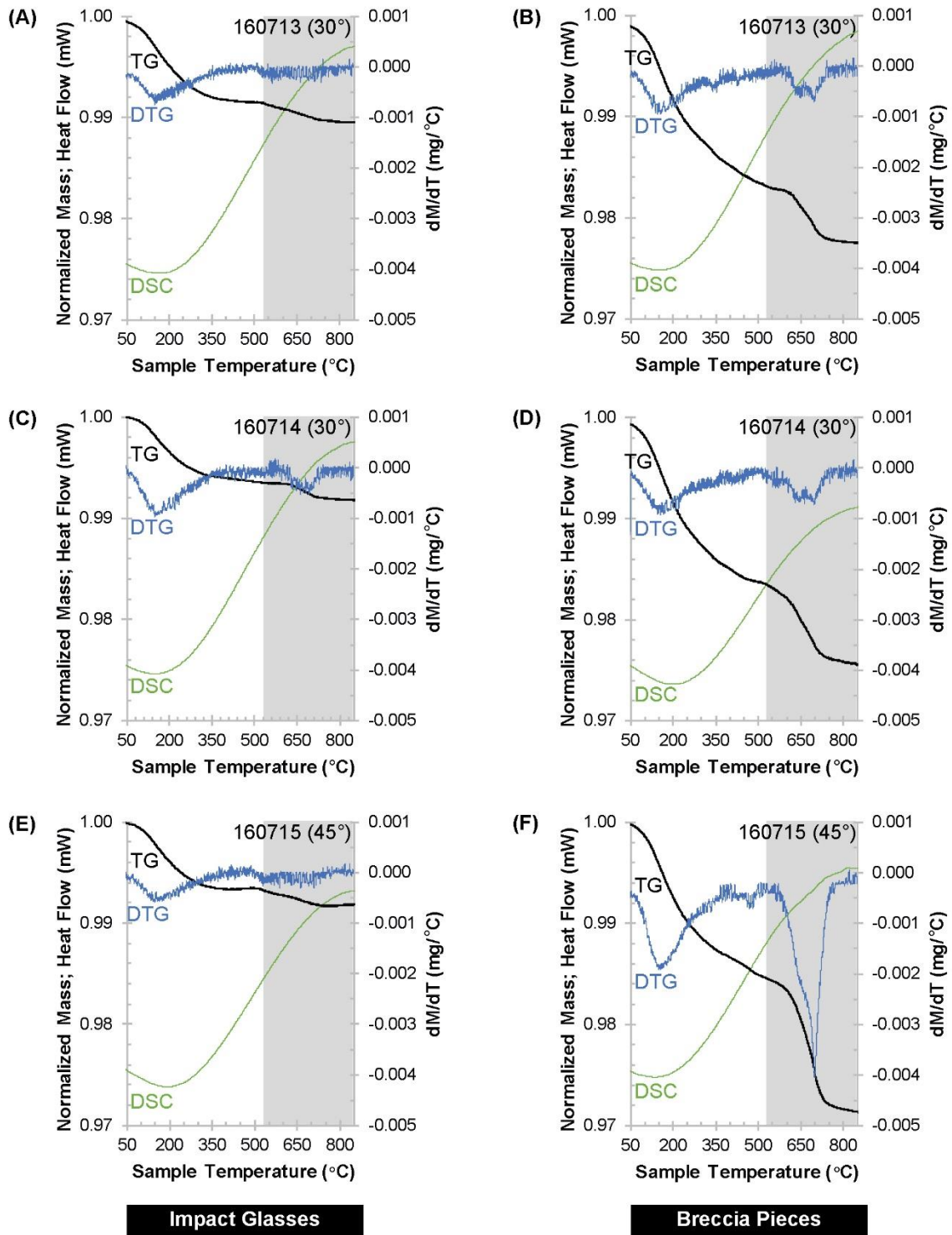
Figure 11. Thermogravimetric (TG), derivative thermogravimetric (DTG), and differential

scanning calorimetry (DSC) profiles for impact glasses (left column) and melt-bearing

breccias (right column). Each row corresponds to an experiment. For example, (A) and (B) show the profiles for impact glasses and breccia pieces recovered from experiment 160713. The y-axis at left is for both TG and DSC profiles. The DSC data have been divided by 7,000 and offset by +0.97 so they can plot on the same axis as the TG data. The y-axis at right side is for the DTG data. The gray rectangle marks the reaction interval for antigorite.
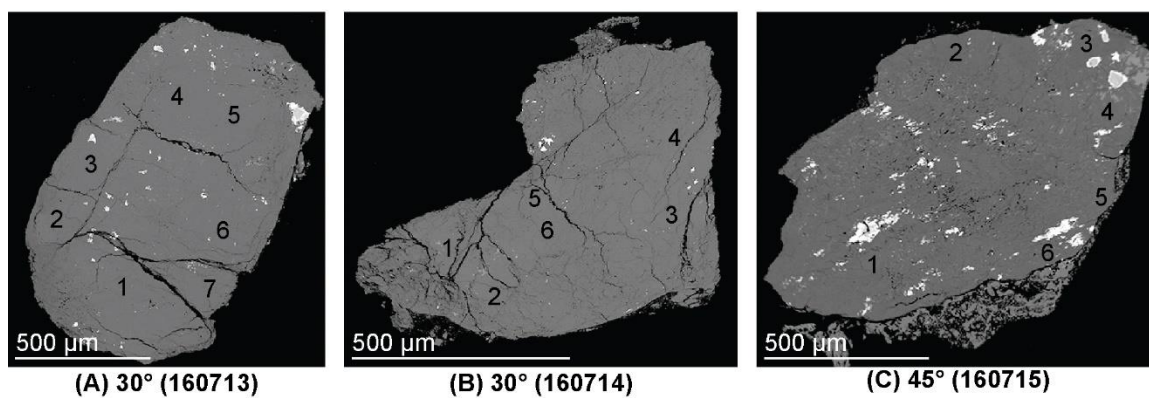
Figure 12. Backscattered electron micrographs of serpentine relics recovered from experiments (A) 160713, (B) 160714, and (C) 160715. Numbers mark the places where the data listed in Table 13 were acquired. Based on EDS spectra, the bright phases are ilmenite and chromite.
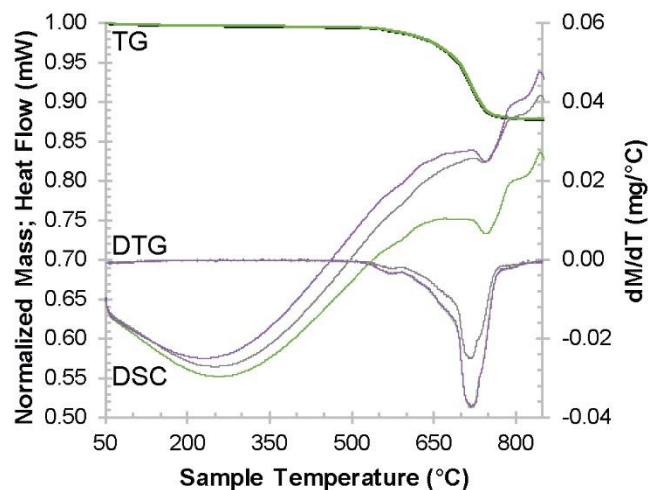
Figure 13. Thermogravimetric (TG), derivative thermogravimetric (DTG), and differential scanning calorimetry (DSC) profiles for three powders made from the serpentine projectiles. The y-axis at left is for both TG and DSC profiles. The DSC data have been divided by 300 and offset by +0.3 so they can plot on the same axis as the TG data. The y-axis at right is for the DTG data.
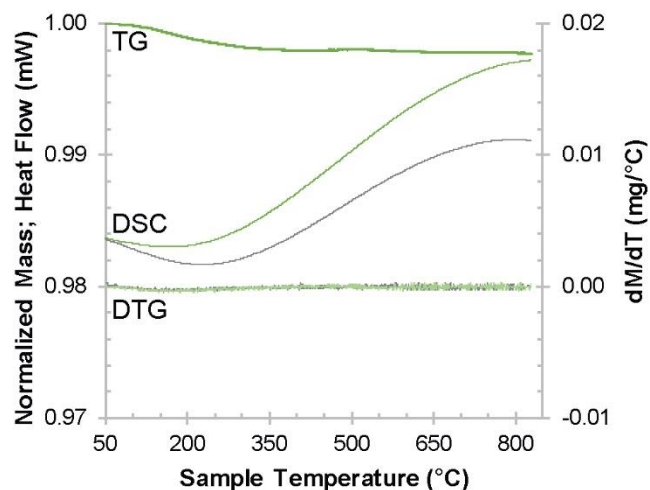
Figure 14. Thermogravimetric (TG), derivative thermogravimetric (DTG), and differential scanning calorimetry (DSC) profiles for the heat-treated pumice target. The y-axis at left is for both TG and DSC profiles. The DSC data have been divided by 10,000 and offset by +0.96 so they can plot on the same axis as the TG data. The y-axis at right is for the DTG data.

Supplementary Text S1. Heat-treatment of target pumice

Volcanic pumice often contains 1 to 2 wt.% volatiles, a relatively high volatile content that may interfere with studies of water delivery. In order to drive off volatiles, the pumice used in these experiments was heated for 90 minutes at 850 °C. After heating, the pumice cooled to room temperature in a desiccator. The pumice lost an average of 1.24 wt.% during the heat treatment. Due to the large volume of heat-treated pumice needed, heat-treated pumice was stored in sealed plastic bags for up to two weeks prior to the experiments. Aliquots of heat-treated pumice were powdered to <45 μm and run on a thermogravimetric analyzer at the completion of the AVGR experiments. The thermogravimetric data indicate that the heat-treated pumice contained 0.20 wt.% OH + H_2O.

Supplementary Text S2. Uncertainties for projectile retention efficiency

The total projectile retention efficiency, R_{tot}, is the sum of the projectile retention efficiencies of the glasses, R_{gl}, breccias, R_{br}, and serpentine relics, R_{rel}. Therefore, the error in R_{tot} reflects the errors in R_{gl}, R_{br}, and R_{rel}:

$$\sigma_{R_{tot}} = \sqrt{\sigma_{R_{gl}}{}^2 + \sigma_{R_{br}}{}^2 + \sigma_{R_{rel}}{}^2}$$

Comparisons between the masses of serpentine relics recovered during replicate experiments at 30° directly constrains σ_{Rrel}. However, the uncertainties on the other two terms are more complicated because they depend on additional parameters:

262

$$R_{gl} = \frac{\chi_{serp,gl} M_{gl}}{M_p} \qquad\qquad R_{br} = \frac{\chi_{serp,br} M_{br}}{M_p}$$

where $\chi_{serp,gl}$ is the mass fraction of serpentine in the glasses, M_{gl} is the mass of glasses recovered, and M_p is the mass of the projectile, $\chi_{serp,br}$ is the mass fraction of serpentine in the breccias, and M_{br} is the mass of breccias recovered. Therefore,

$$\sigma_{R_{gl}} = R_{gl} \sqrt{\left(\frac{\sigma_{\chi_{serp,gl}}}{\chi_{serp,gl}}\right)^2 + \left(\frac{\sigma_{M_{gl}}}{M_{gl}}\right)^2 + \left(\frac{\sigma_{M_p}}{M_p}\right)^2}$$

$$\sigma_{R_{br}} = R_{br} \sqrt{\left(\frac{\sigma_{\chi_{serp,br}}}{\chi_{serp,br}}\right)^2 + \left(\frac{\sigma_{M_{br}}}{M_{br}}\right)^2 + \left(\frac{\sigma_{M_p}}{M_p}\right)^2}$$

The uncertainty in the mass of the projectile is insignificant compared to the uncertainties associated with the other quantities. This fact reduces the equations to

$$\sigma_{R_{gl}} = \frac{R_{gl}}{M_p} \sqrt{\left(\frac{\sigma_{\chi_{serp,gl}}}{\chi_{serp,gl}}\right)^2 + \left(\frac{\sigma_{M_{gl}}}{M_{gl}}\right)^2}$$

$$\sigma_{R_{br}} = \frac{R_{br}}{M_p} \sqrt{\left(\frac{\sigma_{\chi_{serp,br}}}{\chi_{serp,br}}\right)^2 + \left(\frac{\sigma_{M_{br}}}{M_{br}}\right)^2}$$

Both $\chi_{serp,gl}$ and $\chi_{serp,br}$ are the slopes of regression lines. Hence $\sigma_{\chi_{serp,gl}}$ and $\sigma_{\chi_{serp,br}}$ are the standard deviations of the slopes of the regression lines. Comparisons between the masses of breccias and glasses recovered from duplicate experiments at 30° constrains $\sigma_{M_{gl}}$ and $\sigma_{M_{br}}$. Putting these pieces together,

263

$$\sigma_{R_{tot}} = \sqrt{\left(\frac{R_{gl}}{M_p}\sqrt{\left(\frac{\sigma_{\chi_{serp,gl}}}{\chi_{serp,gl}}\right)^2 + \left(\frac{\sigma_{M_{gl}}}{M_{gl}}\right)^2}\right)^2 + \left(\frac{R_{br}}{M_p}\sqrt{\left(\frac{\sigma_{\chi_{serp,br}}}{\chi_{serp,br}}\right)^2 + \left(\frac{\sigma_{M_{br}}}{M_{br}}\right)^2}\right)^2 + \sigma_{R_{rel}}^2}$$

$$\sigma_{R_{tot}} = \sqrt{\left(\frac{R_{gl}}{M_p}\sqrt{\left(\frac{\sigma_{\chi_{serp,gl}}}{\chi_{serp,gl}}\right)^2 + (0.13)^2}\right)^2 + \left(\frac{R_{br}}{M_p}\sqrt{\left(\frac{\sigma_{\chi_{serp,br}}}{\chi_{serp,br}}\right)^2 + (0.10)^2}\right)^2 + (0.0032)^2}$$

Supplementary Text S3. Accuracy of water content calculations

The highly vesicular nature of these impact glasses complicates water content calculations. Vesiculation introduces uncertainty into both sample thickness, *d,* and density, ρ. For the Beer-Lambert law to yield accurate results, *d* must be the path length of light through the sample. This is demonstrably not the case for these samples because of their highly vesicular nature (e.g., see Figs. 2, 5, 6). Instead, the path length is probably shorter than the measured sample thickness. Scattering, reflection, and refraction through vesicles introduce additional complexities. The highly vesicular nature of the glasses also complicates characterizing the densities of the samples. The densities of the samples reported here were estimated using the Gladstone-Dale rule [*Silver et al.*, 1990; *Mandeville et al.*, 2002]. This approach does not consider the porosity of the samples. Hence, the densities calculated from the Gladstone-Dale rule are too high. Because of these two factors, the use of the Beer-Lambert law to quantify water contents should yield conservative lower bounds.

Supplementary Text S4. Alternative sources of water

In addition to the serpentine projectile, impact materials could incorporate water from the heat-treated pumice target, from the residual atmospheric water vapor in the impact chamber, from a monolayer of water molecules adsorbed onto the pumice, or during the time that elapsed between the experiments and TG analyses.

Option 1: Target-derived water. As described in section 3.6.2 and Supplementary Text S1, the heat-treated pumice contained 0.20 wt.% OH + H_2O at the time of the experiments. To compensate for water in the heat-treated pumice, 0.20 wt.% was subtracted from the total weight loss of each sample prior to calculating the serpentine equivalent. For example, if a sample lost 1% of its mass, only 0.8% was used to calculate serpentine equivalent. Hence, the potential contribution of the target is incorporated into the serpentine equivalent calculations. The target cannot be the source for the unexpectedly high water contents of the impact breccias.

Option 2: Atmospheric water vapor in the impact chamber. During these experiments the pressure in the impact chamber was between 5.0 and 6.3 x 10^{-4} atm. Impact products may have trapped some of the residual water vapor in the chamber. On the warmest day that the experiments were conducted, the average temperature was 21.7 °C (71 °F). The maximum relative humidity was 86%. The dew point was 12.8 °C (55 °F). The atmospheric pressure was 29.98 inches of Hg (data for 13 July 2016 at the Moffett Federal Airfield; accessed via *wunderground.com*). Hence, the absolute humidity was 16 g m^{-3}. The impact chamber has a volume of about 59 m^3. Prior to pumping, the air in the impact chamber would contain 944 g of water vapor. Once the chamber was pumped

down to 5 x 10^{-4} atm, however, the chamber only contained ~19 mg of water vapor. The serpentine projectiles contained ~60 mg of OH. Furthermore, the impact products only interacted with a tiny volume (<1%) of the residual gas in the impact chamber. Thus, residual water vapor cannot significantly contribute to the water content of the breccias.

Option 3: Adsorbed monolayer of water. Another possibility is that a monolayer of adsorbed water coated pumice grains at the time of experiments. Such water might have been trapped along grain boundaries during shock lithification and contribute to the unusually high water contents of the breccias. However, simple calculations reveal that this scenario is unlikely.

In order to calculate the amount of adsorbed water, the reactive surface area of the pumice must be known. Although the reactive surface area of the sieved airfall pumice has not been directly measured, it is likely similar to that of volcanic ash. *Delmelle et al.* [2005] reported data for six samples of volcanic ash with particles <100 μm. The pumice particles used in this study are <106 μm. Hence, the measurements are relevant to the pumice particles used in the present study. The specific surface areas of the samples measured by *Delmelle et al.* [2005] ranged from 1.1 to 2.1 m^2 g^{-1}. The density of surface OH groups on amorphous silica is 4.9 OH per square nanometer [*Zhuravlev,* 2000].

Recovered breccias contain an average of 0.56 g of pumice. If the specific surface area of the pumice were 2.1 m^2 g^{-1} and all reactive sites were hydroxylated, then the pumice in the breccias would contain ~5 x 10^{18} surface silanol groups. If every silanols were hydrogen bonded to a water molecule, then the total mass of water in the silanol and H$_2$O monolayer would be 0.3 mg, an amount equivalent to only ~0.05% of the mass of pumice

266

in the breccias. If the specific surface area of the pumice were 1.1 $m^2 g^{-1}$, then the total mass of adsorbed water would be ~0.2 mg (under the same assumptions), an amount equivalent to ~0.04% of the mass of pumice in the breccias. Given that breccias lost 2.0 to 2.7 wt.% during TGA, a pre-impact adsorbed monolayer on pumice particles is, at most, a very minor component of the breccia's water budget.

Alternatively, breccias might have trapped water desorbed from pumice particles during impact. Once released, this water vapor (derived from the target) might be trapped in the breccias, analogous to the process proposed for water vapor derived from the projectile. The temperature required to remove an adsorbed monolayer of water is ~200 °C for amorphous silica [*Zhuravlev,* 2000]. The pumice exposed to these conditions is located beneath the point of impact and comes from a region roughly cylindrical in shape. The cylindrical region is about three projectile radii high (~9.5 mm) and three projectile radii in diameter. The density of the pumice is ~1.2 $g cm^{-3}$ [*Schultz,* 1992]. Therefore, this cylindrical region contains about 0.8 g of pumice. Using the same specific surface areas and assumptions as in the previous paragraph, an adsorbed monolayer could contribute between 0.2 and 0.5 mg of water. This amount is, at most, only 0.8% of the mass of water in the projectile. Hence, an adsorbed monolayer on pumice particles prior to impact cannot account for the unusually high water contents of the breccias.

Option 4: Post-impact addition of water. The fourth option is that breccias adsorbed water from their environment between the time of the experiments and the time of the TG analyses. Most adsorbed water should be removed by 100 °C, yet the masses of the samples changed very little below 100 °C: the breccias only lost 0.06 to 0.12 wt.% below 100 °C

(in contrast to the ~2 wt.% lost between 100 and 850 °C). Furthermore, the serpentine

equivalent calculations only considered mass losses between 100 and 850 °C. Hence, post-

impact adsorption or absorption cannot account for the high water contents of the breccias.